Investigation of the enhancement of the performance of the SIMS instruments

Marina Verruno

▶ **To cite this version:**

Marina Verruno. Investigation of the enhancement of the performance of the SIMS instruments. Accelerator Physics [physics.acc-ph]. Université Paris Saclay (COmUE), 2017. English. NNT : 2017SACLS400 . tel-01823853

HAL Id: tel-01823853
https://theses.hal.science/tel-01823853

Submitted on 26 Jun 2018

HAL is a multi-disciplinary open access archive for the deposit and dissemination of scientific research documents, whether they are published or not. The documents may come from teaching and research institutions in France or abroad, or from public or private research centers.

L'archive ouverte pluridisciplinaire **HAL**, est destinée au dépôt et à la diffusion de documents scientifiques de niveau recherche, publiés ou non, émanant des établissements d'enseignement et de recherche français ou étrangers, des laboratoires publics ou privés.

université PARIS-SACLAY

UNIVERSITÉ PARIS SUD
Comprendre le monde, construire l'avenir

NNT : 2017SACLES400

Investigation of the enhancement of the performance of the SIMS instruments

Thèse de doctorat de l'Université Paris-Saclay
préparée à L'Université Paris Sud

École doctorale n°576 Particules hadrons énergie et noyau : instrumentation, image, cosmos et simulation (pheniics)
Spécialité de doctorat : Physique des accélérateurs

Thèse présentée et soutenue à Belvaux, Luxembourg, le 06.11.2017, par

Marina S. Verruno

Composition du Jury :

M. Jean-Luc Guerquin Kern Chargé de Recherche, INSERM, institut Curie	Rapporteur
M. Gérard BenAssayag Directeur de Recherche, CNRS DR2, CEMES	Rapporteur
M. Alex Redinger Professeur associé, Faculté des Sciences, de la Technologie et de la Communication	Président-Examinateur
M. Jean-Nicolás Audinot Chargé de recherche, LIST (AINA)	Examinateur
M. Tom Wirtz Directeur de Recherche LIST (AINA)	Examinateur
M. David Dowsett Chargé de recherche, LIST (AINA)	Co-directeur de thèse
M. Serge Della Negra Directeur de Rechercher, CNRS DR1, IPNO	Directeur de thèse

Thèse de doctorat

Acknowledgments

I would like to address my first thanks to my supervisors Serge Della Negra, Tom Wirtz and David Dowsett. I am very thankful to Tom Wirtz for accepting me in his group, and for his constant support during the last four years that were very challenging but very enriching in the professional and personal level. I would like to thank Dr. David Dowsett for his guidance and to let me implement my own ideas and my own mistakes, but at the same time he provided support and council.

A special acknowledgment to Dr. Serge Della Negra for his support, interest in my work and the helpful comments and advices during my thesis, especially after “sorry, can I ask one question”, but also to teach me how to do top science without losing the sense of humour.

I would like to thank Dr. Gérard BenAssayag, Dr. Jean-Luc Guerquin Kern and Prof. Alex Redinger for being part of this thesis Jury.

Another big acknowledgment to Dr. Patrick Philipp to help me to learn how to use the Cameca IMS 4F, for his time solving the machine problems and his patience, but also for his advises and the fruitful discussions we had.

I would like to thank to Dr. Jean-Nicolás Audinot for help me to complete the experiments on the Cameca IMS 6F, and his explanations to understand many trends in SIMS machines.

I would like to thank to Dr. Hung Quang Hoang, Dr. Roch Andrzejewsky and Dr. Olivier De Castro for the CPO discussions we had, their patience and their kindness.

To my colleagues at LIST that I do not mention, I would like to thank them for the wonderful moments we spend together during this PhD journey.

To my family, specially my son Gabriel and my daughter Magali, for their patience and their understanding.

This project is supported by National Research Funds, Luxembourg (Ref. 6911468)

Table of Contents

1 Introduction

Secondary ion mass spectrometry (SIMS) is a powerful technique that has excellent sensitivity (parts-per-million/billion; ppm-ppb), high dynamic range [1], very high mass resolution [2] and has unique capability to analyse isotopic composition [3]. It is generally used to record mass spectra, for imaging but is most commonly used for depth profiling. A 3D reconstruction can be obtained by stacking several successive frames and correlating them with the depth of the crater. SIMS has become a fundamental characterization tool for nano-analysis in many fields, such as semiconductors [4], biology [5], metallurgy [6], materials science [7], cosmochemistry [8], etc..

The latest trends to obtain images with both excellent spatial resolution and chemical information is the combination of two or more techniques together in one instrument, in this manner samples can be mapped with both excellent resolution and high –sensitivity chemical information. Generally, instruments which have high-resolution imaging are giving very little chemical information, and vice versa, the instruments which has good chemical information have low image resolution. Therefore, by combining SIMS instruments that provide high chemical information, with a high-resolution technique their intrinsic limitations of the first ones can be compensated.

For high–resolution imaging the most common techniques are Electron Microscopy, the Helium Ion Microscopy (HIM) and Scanning Probe Microscopy (SPM). The Transmission Electron Microscope (TEM) can routinely provide images at the sub-A level [9] and, the Helium Ion Microscope (HIM) can achieve an edge resolution of sub-nm level [10]. Electron microscopies can be combined with extra analytical techniques like Energy Dispersive X-ray Spectroscopy (EDX), or Electron Energy Loss Spectroscopy (EELS), which are complementary to SIMS, and can be decisive in answering analytical questions in complex samples. Even though, both techniques could give chemical information, the SIMS technique has better detection limits, in some cases better spatial resolution and the ability to make isotopic and molecular measurements. Therefore, these high-resolution instruments were combined with SIMS, and the better spatial resolution is obtained by superimposing SIMS images with the high-resolution images.

However, high-performance mass spectrometers are usually very large Therefore, it is necessary to develop compact spectrometers with high performances to be added-on on these microscopes.

Several such instruments are under development at LIST. A modified TEM dedicated to be the first prototype for combining SIMS and TEM, equipped with a Gallium Focused Ion Beam (FIB) column, and a custom in-house developed SIMS mass spectrometer [11] which has a mass range of 1-30 amu and a mass resolving power (MRP) of 1500. There is also a HIM-SIMS instrument, with the SIMS extraction system and the mass spectrometer fully in-house developed [12] with mass range of 1-200

amu and MRP of 600. While this kind of MRP allows many applications, certain applications where potential mass interferences need to be resolved such as imaging isotopically labelled samples for biology or analysing semiconductor samples higher MRP is required. For example, Simply, increasing the size of the spectrometer to achieve this kind of performance is simply not possible for an add-on. A MRP between 3,000 to 4,000 is required to distinguish the most frequent mass interferences in Biology.

In order to optimize the performance of these spectrometers designed at LIST, the *first part of the thesis* was dedicated to *investigate the enhancement of the mass resolution of mass spectrometers of double focusing* configurations with charged particle optics (CPO) simulations. The MRP of a double focusing configuration is proportional to the size of the magnet. However, since the spectrometers to be added-on should have a reduced size with high-performance, in this work the proposal was to improve the MRP for a given magnet/spectrometer size or sensitivity, by replacing the standard spherical sector by the novel spheroid geometry [13], which has better focusing properties such as smaller spot size and higher transmission at the same entrance angular acceptance.

Large area analysis is an emerging field in imaging SIMS, but it is a difficult technique to implement because large images are typically created by stitching together multiple images. This leads to long analysis times for high resolution images. High resolution imaging SIMS can routinely reach spatial resolution of 50 nm (Cameca's NanoSIMS 50) [14]. However, to achieve such resolution, a small probe current (of the order of 1 pA) must be used. This usually translated into long time for analysis because is required longer bombarding times for sputtering a minimum quantity of material to see an image. For example, one complete image of marine bivalve obtained with NanoSIMS in mosaic mode, an area of 300 µm x 800 µm (3 x8 tiles with 256 x 256 pixels per tile), a raster size of 100 µm (pixel size= 390 nm), and 120 minutes per tile, means approximately two days of continuous operation [15]. The long-time analysis of the high-resolution imaging SIMS makes the technique unsuitable for large areas, in the order of centimetre [16], or 3D reconstruction. *The second part of the thesis*, was orientated to improving the *time for analysis* in imaging SIMS.

T*he reduction of the time for analysis was investigated by a proof-of–concept of multi-ion-beam system implemented in the Cameca IMS 6F*. The goal was to raster the sample with several primary micro-beams instead of one, to drastically increase the throughput of high resolution analysis. This was achieved by exploiting several features of the Cameca IMS XF instruments in a new way (the stigmatic imaging capability of the secondary optics and, the Kohler illumination mode of the primary optics).

These two modes of operation present in the Cameca IMS XF instruments plus a multi-hole-aperture, specially designed and mounted in the place of the aperture strip in the primary column allowed a proof-of-concept to be demonstrated.

1. Introduction

In Section 2, the main CPO concepts necessary to develop the simulations as well as the CPO simulation software SIMION are explained. Section 3, gives a general background of the SIMS technique and a review of most common SIMS instruments. The investigation of the enhancement of the mass resolution by CPO simulations is presented in chapter 4. Chapter 5 presents the proof-of-concept of the multi-ion-beam investigated through CPO simulations and experimentally with the Cameca IMS 4F/6F. A summary is presented chapter 6.

2 Charged Particle Optics

2.1 Introduction

In this thesis, the investigation of the improvement of the performance of the SIMS instruments is carried out, and simulations of the trajectory of charged particle optics are implemented. Prior to this, the understanding of the basic principles of the motion of charged particles by shaped electric and magnetic fields is necessary. These fields bend the trajectory of the charged particles similar to shaped optical lenses bend light rays. Electromagnetic fields with rotational symmetry can produce a stigmatic image of objects placed on or near the axis. Electrostatic and magnetic lenses have extensive applications in electron microscopy, accelerators, and any ion optical system.

The chapter begins with discussion of the *basic equations* of the charged particles and the *aberrations* present in the optical system. Later, the most common *electrostatic lenses* are described as well as some fundamental principles of the *electrostatic sectors*, with particular focus on the spherical sector. A summary of *mirrors analysers* is made, emphasizing in the novel spheroid analyser, that will be investigated in the chapter 4 in order to enhance the performance of the spectrometers used in SIMS. The principles of *magnetic deflection* are also introduced, because they are the basis for understanding the double focusing spectrometers, which will be explained in more detail in the next chapter. A brief description of CPO software used in this work (SIMION) is presented.

2.2 Charged particle optics

The evaluation of lens properties is of highest importance for designing optical systems. Initially, it is necessary to derive the potential distribution and fields in the region of interest, and later the optical properties are determined by analysing the beam trajectories. In the past, experimental methods were used, but currently, is possible to calculate easily the field of electrostatic lenses with a computer by several methods (see Section 2.7). There are two main methods to calculate the charged particle properties of the lenses: direct ray tracing, and the solution of the paraxial trajectory equation and the evaluation of aberrations integrals. The first one has the advantage that is not necessary to make assumptions a priori of the form of the aberrations and gives more accurate results when the rays are far from the axis [17]. Once the potential distribution is known the particle trajectories can be plotted and the properties are obtained after the evaluation of the influence of the field on the particles. The second method, is much faster and only requires knowing the potential distribution on the axis of rotational symmetry, but for particles far from the axis, this approach is not enough to achieve accurate imaging properties of the optical element.

2. Charged Particle Optics

To calculate the *paraxial trajectory equation* of a charged particle it is necessary to calculate the Lorentz force applied to it (eq. 2.1). For the pure electrostatic case, the equation is reduced to the value of the electric field times the charge $q\boldsymbol{E}$, the Laplace equation should be solved to obtain the potential distribution Φ when no space charge is considered. The essential equations are:

Lorentz Force:

$$\vec{\boldsymbol{F}} = \boldsymbol{q}(\vec{\boldsymbol{E}} + \vec{\boldsymbol{v}} \times \vec{\boldsymbol{B}}) \tag{2. 1}$$

Gauss Theorem for the electrostatic case:

$$\vec{\boldsymbol{\nabla}} \cdot \vec{\boldsymbol{E}} = \frac{\boldsymbol{\rho_c}}{\boldsymbol{\varepsilon_0}} \tag{2. 2}$$

Where ρ_c is the charge density and ε_0 is the electric constant.

Relation between electric field and potential [18]:

$$\vec{\boldsymbol{E}} = -\vec{\boldsymbol{\nabla}}\boldsymbol{\Phi} \tag{2. 3}$$

Combining (2.3) and (2.2) the Poisson equation is obtained:

$$\boldsymbol{\nabla^2 \Phi} = -\frac{\boldsymbol{\rho_c}}{\boldsymbol{\varepsilon_0}} \tag{2. 4}$$

If no charge is considered then, the Laplace equation is obtained:

$$\boldsymbol{\nabla^2 \Phi = 0} \tag{2. 5}$$

Therefore, by solving the Laplace equation the values of the potential can be obtained in the whole space and can be used in the equation (2. 3) to determine the electric field $\boldsymbol{E}$ to finally solve the equation of motion (2.1).

When the electric field E has axial symmetry, the lens properties are defined by the radial component of the field E_r:

$$\boldsymbol{E_r} = \frac{\boldsymbol{r\Phi''(z)}}{\boldsymbol{2}} \tag{2. 6}$$

Where $\Phi''(z)$ is the derivative with respect to z. In the paraxial approximation, also called Gaussian approximation, r is considered small and the field is proportional to the distance to the axis implying lens action. The slope of the trajectory is also considered small. Simultaneously, the velocity of the charged particle varies in z direction due to the electrostatic field in z, which makes the description of an electrostatic lens more complicated than light optics. Then, the *equation for the paraxial trajectories* for non-relativistic particles can be written as:

$$\boldsymbol{r'' + \frac{\Phi'(z)}{2\Phi(z)} r' + \frac{\Phi''(z)}{4\Phi(z)} r = 0} \tag{2. 7}$$

This equation is a linear homogenous second order differential equation, whose general solution could be written as the linear combination of two arbitrary linear independent solutions of the system.

As *m/q* is not present, particles departing with the same initial energy will follow identical trajectories, independent of the *m/q* ratio. In addition, the equation is homogeneous in Φ, which implies that changing all voltages of the electrodes by the same proportion will not change the optical properties. Finally, as the equation is homogeneous in *r* and *z*, if all dimensions are scaled by the same factor, all optical properties will also change by the same factor [17,19–21].

2.3 Aberrations

In charged particle optics, the lenses suffer from aberrations in the same way as light optics. The aberrations define the quality of the optical system. Calculation the aberrations requires going beyond first order treatment of the paraxial case and the integration of higher order terms in the trajectory equations (eq. 2.7).

There are two types of aberrations, *parasitic aberrations*, which are consequence of the imperfections of real systems such as misalignment of the optical elements, mechanical defects, etc. and *geometrical aberrations*, they are present even in perfect elements because they proceed from the higher order terms of the trajectory equation.

The *spherical aberration* is a particularly important geometrical aberration because it is present even for point objects on the axis. The refraction of the trajectories varies slightly according to the angle from the axis that particles have when they depart from the same point at the object plane. Figure 2. 1 is an illustration of this effect. The beam departing with semi angle α_0, blue colour, is focused more strongly than the beam with smaller angle, red colour, which makes its focus further from the lens, consequently they do not focus on the same point. The radius of the disc formed in the Gaussian image plane is the spherical aberration and is usually written in terms of the *third order in the semi angle*:

$$\Delta \boldsymbol{r_{sph}} = \boldsymbol{M_L C_s \alpha_0^3} \tag{2. 8}$$

Where M_L is the linear magnification, C_s is a *coefficient representing the spherical aberration* of a particular system and α_0 is the maximum half angle of the pencil rays coming from the object.

Another important geometrical aberration present in paraxial beams with imperfect axial symmetry or when the object is not on the axis is the *astigmatism.* The astigmatism is produced when the focusing force is different in the x-z and y-z planes. Therefore, the beam will be focus differently in each direction forming an image with an ellipse shape. This ellipse collapses into two separated orthogonal lines, one in x direction and the other in y direction, and at some intermediate plane, the image is a circular disk of least confusion instead of a single point. This can be corrected by adding one or more stigmators, like the primary column of the Cameca IMS XF series (Section 3.4.2). Other geometrical aberrations are: *field curvature,* is produced when an image of an object is projected on a curved surface instead

of a planar image. *Coma* is the deviation of some particles trajectories because the beam enters the lens making an angle with the optic axis, consequently, the image appears with tail on a side of the image. *Distortion* is generated when the image point is shifted radially from the paraxial position. For example, if a squared grid is considered as the object, the image of the grid with distortion can have the outer region shrinked (*pincushion distortion*) or distended (*Barrel distortion*). In general, distortion does not produce a blurring of the image. A schematic of the mentioned aberrations is in Figure 2. 2.

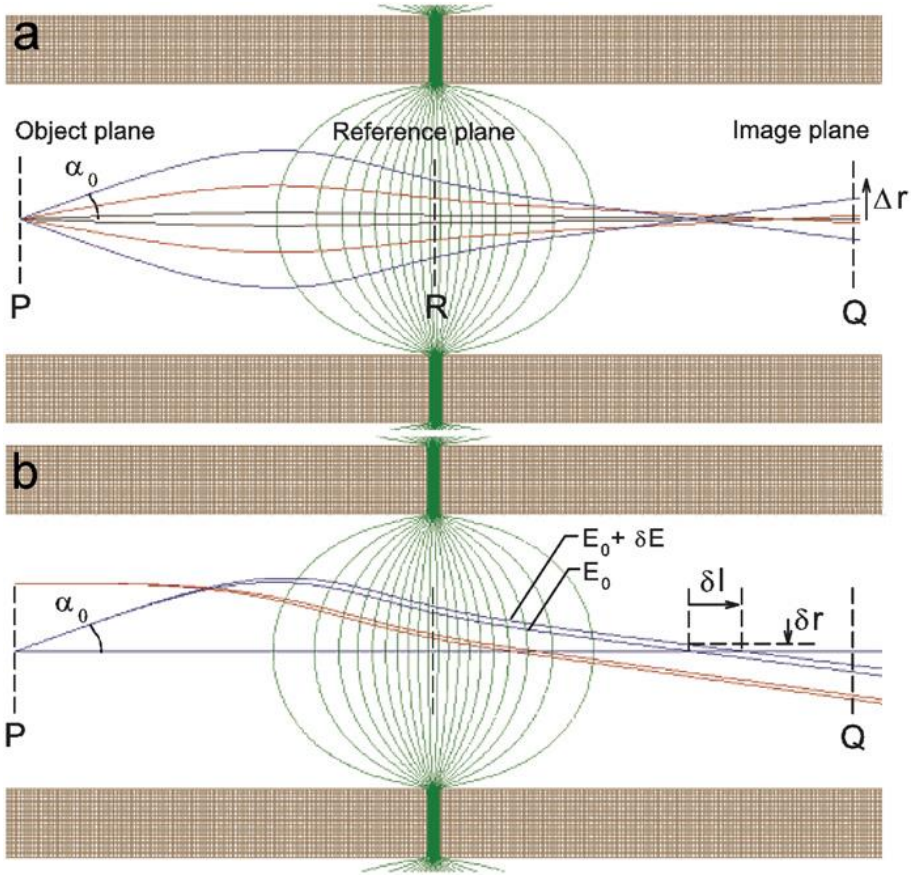

Figure 2. 1: a) representation of the spherical aberration Δr in a two elements lens at the plane Q; b) representation of the chromatic aberration in the same field strength of a) .Picture adapted from [127].

Chromatic aberration is produced when particles with slightly different energies, departing from the same point at the object plane P, are deviated according to their energy, then they get focused on distinct locations in the image plane Q. The coefficient of the chromatic aberration can be written as:

$$\Delta \boldsymbol{r}_{\boldsymbol{chr}} = -\boldsymbol{M}_{\boldsymbol{L}}\boldsymbol{C}_{\boldsymbol{c}}\boldsymbol{\alpha}_{\boldsymbol{0}}\frac{\boldsymbol{\delta E}}{\boldsymbol{E_0}} \tag{2. 9}$$

Where C_C corresponds to the chromatic aberration coefficient, which is usually used for comparison the quality of the lens, and δE is the energy difference between two rays. This can also be

expressed in terms of δl, so the dependence with the angle disappears. There are several publications where these aberrations have been computed for the most used lenses [22–24].

The *rank* of the aberration is the sum of the *order* and the *degree*. The *order* of the aberration is related with the exponential term of the geometrical aberration and the *degree* of the aberration is related with the exponent of any chromatic parameter.

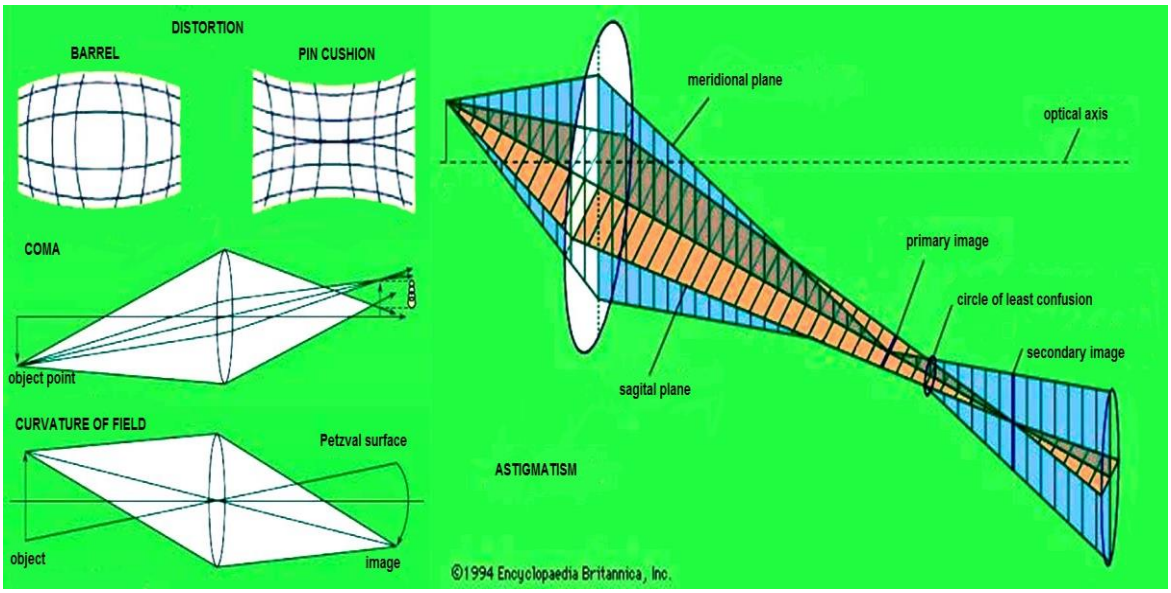

Figure 2. 2: Schematic of the different aberrations present in charged particle optics, left up: Distortion, middle Coma, down Field Curvature, right Astigmatism (picture adapted from [128]).

There are other effects that can influence the focusing of the charged particles such as the *space charge as well as* the *Boersch effect*. The beam is constituted of charged particles, where each particle produces its own field that can affect the surrounding particles; consequently, all particles within the beam interact with each other. If the distances between the particles are small compared with the time of flight (time of interaction) the repulsion induced between the charged particles have an important effect on the quality of the beam, by broadening/defocusing it. *Space charge* effect increases linearly with the beam current. It can be corrected using the system's lenses.

The *Boersch effect* arises from the statistical effects, induced by the fluctuations in the particle density, resulting in a change in the axial velocity producing energy broadening. Consequently, the system resolution is deteriorated due to the chromatic aberration. This effect cannot be corrected due to its statistical nature.

2.4 Electrostatic lenses

The electrostatic lenses can be described as a thick lens, deriving all the same equations of light optics such as the object and the image position, the magnifications and the focus position.

2.4.1 Einzel Lenses

There are many ways to arrange aperture or cylindrical lenses. The most commonly used lenses are three electrodes aligned of either tubes or disks, with central apertures, at different potentials. An example is illustrated in Figure 2. 3. When the first and the third electrodes are at the same potential (V_1=V_3) and the middle electrode at V_2, is the special case called *Einzel* lenses. The focusing action is performed by changing the beam energy when it passes through the lens, but the particle energy remains the same before and after the lens. These lenses are characterised for having two modes of operation deceleration-acceleration or acceleration-deceleration. In the first case, the two outer electrodes are at the same potential and the central electrode is at the same sign of the source voltage. This mode is preferred because it is experimentally simpler to implement: generally, the outer electrodes are grounded, and via a voltage divider, the central electrode is energised with the same sign of the source. When the value of the central electrode is similar to source voltage, high refractive index can be achieved, resulting in a short focal length. In the second case, the central electrode has opposite sign to the source, so much higher voltages are required to obtain the same refractive power. Nevertheless, it has smaller spherical and chromatic aberrations.

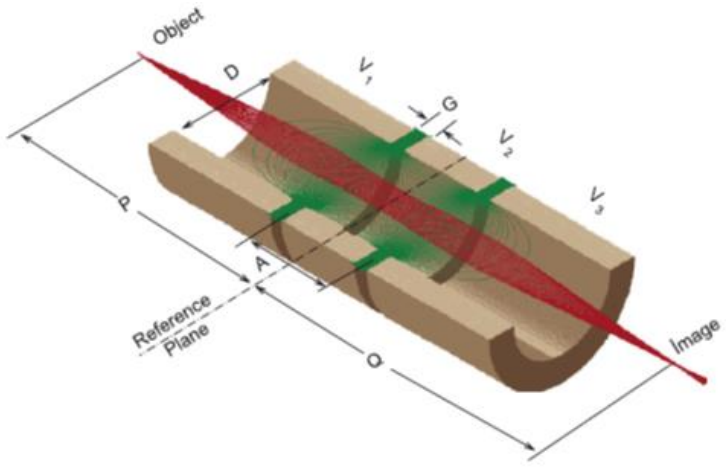

Figure 2. 3: Schematic of three cylindrical coaxial electrodes with main parameters shown. In red the beam shape and in green the equipotential lines. Image obtain using SIMION software. Image taken from [129].

The focal properties of these lenses were widely investigated [22,25–34], they vary not only with applied voltage but also with the geometry. Asymmetric lenses, i. e. lenses having at least one electrode with an asymmetric geometry, have been found to have smaller spherical aberration [29]. Most of the lenses found in the primary and secondary optics of the Cameca IMS XF instruments are *Einzel* lenses.

There are also zoom lenses that give the flexibility to maintain the same focal length but varying their magnification by using different voltages ratios and the three electrodes have different potential values.

2.4.2 Immersion Lenses

In light optics, the basic principle of an immersion lens is to fill the space between the lens and the object with an element with refractive index greater than one. In this manner, the numerical aperture of the lens is increased, bigger than one and the optical properties of the system are also enhanced. For example, in the case of microscopes the resolution is improved. An immersion electrostatic lens is similar to light optics, but instead of having a different index of refraction on each side, they have an overall accelerating or decelerating action. There is a very important difference between light optics and charged particle optics, where in the first case, the index of refraction changes abruptly at the surface of refraction, while in the second case, the index varies smoothly across the lens and may have much larger range of values. When the immersion lens is composed of three elements, the central electrode has the function of focusing the image and the magnification of the image is defined by the immersion ratio and the geometry.

An important application of these lenses is as immersion objective lenses, and advantage is that they reduce the aberration coefficients. There are two combinations, one where the specimen is in the low potential region of an accelerating lens, the case of direct imaging systems; and the other, of a decelerating lens, used for making probes. The objective immersion lenses are the base of the majority of the electron microscopes and many ion optical systems (i.e. the secondary optics of the Cameca IMS XF extracts the ions with an immersion objective).

2.5 Electrostatic Analysers

Electrostatic analysers are used essentially to measure the energy per unit charge E/q of the particles within the beam. There are classified according to the principle of functioning. The mirror type analysers use a retarding potential to reduce the velocity of the particles. They are easy to construct, but they are not suitable for obtaining energy spectra with high resolution. The deflector type analysers disperse the particles by an electromagnetic fields [35]. When the beam has energies up to several keV pure electrostatic fields are used because they are much easier to produce and magnetic fields to deflect

ions should be extremely large. Magnetic fields are used only to measure kinetic energy distributions in high-energy beams (where electrostatic potentials should be extremely high) and in electron optics.

Any electrostatic lens with curved axis can be used as an energy analyser. Therefore, there are many designs and detail study of the most used configurations can be found in literature [35,36]. These so-called sector field electrostatic analysers are widely used in the design of mass spectrometers. Double focussing configurations used cylindrical or spherical sectors. The first one used and the simplest is the cylindrical condenser, in which the electrodes are two coaxial cylinders. Distinct voltages are applied to the surfaces generating an electrostatic field that bends the particle in the centre of the circular optical axis. Cylindrical analysers are easier to produce and align than spherical shapes, but they only focus in one direction, consequently the intensity of the signal is reduced. Spherical energy analysers are preferred because they focus in the both directions: dispersive direction (r) and the perpendicular to the dispersive direction (z). They focus stigmatically, like a round lens but with curved optic axis. They are frequently used as energy spectrometers [37]. The toroidal analysers are a more general geometry that includes both spherical and cylindrical analysers as special cases. These analysers will be discused with more detail in Section 2.5.2.

An schematic of a 90° spherical analyser is shown in Figure 2. 4, where r_e is the radius of the optical axis, V_a and V_b are the inner and the outer electrode voltages respectively, D is the distance between two particles with different energy (ΔE), and α is the half opening angle.

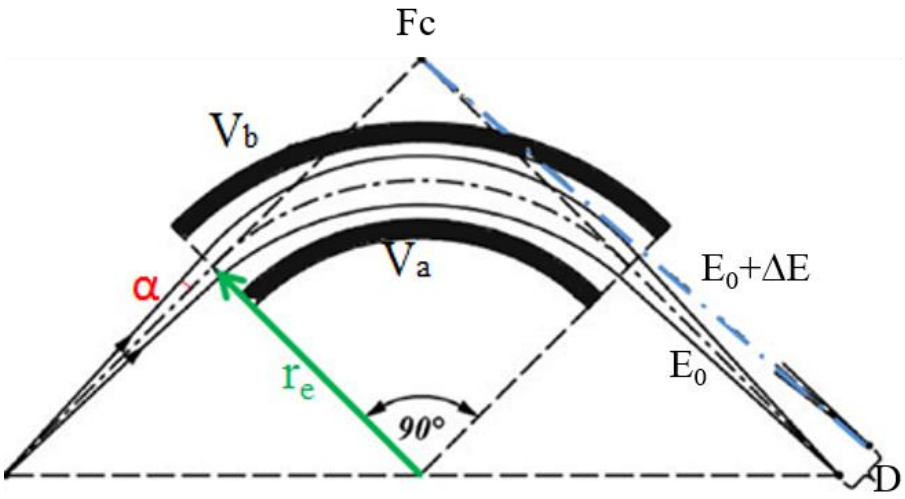

Figure 2. 4: Schematic of a 90° spherical analyser. Va and Vb are the voltages applied to the inner and outer electrodes, the optical axis at r_e, *D* is the dispersion between two particles with different energy, α is the half opening angle, Fc focus achromatic point. (Picture adapted from [21]).

Characterisation of an electrostatic analyser:

The most important parameters of an energy analyser are the *energy dispersion*, the *energy resolution*, the *trace width* and the *transmission*. The *energy dispersion D* is the displacement of the image point according to the difference from the central energy E_0. The *transmission* is the ratio between the particles registered at the exit and the particles at the entrance of the analyser.

The *energy resolution* of an energy analyser is defined as $\frac{\Delta E}{E_0}$, where E_0 is the central energy of particles transmitted through the analyser. The *energy resolution* is a measurement of the quality of the image point for two particles with different energies. The quantity ΔE is usually defined at the full width half maximum (FWHM) of the peak of the energy distribution of the beam plotted against the transmitted current. However, there is other definition called the base resolution (FBW) where ΔE_B is defined to be the half of the full width of the base resolution [36,38]. A schematic of both definitions is shown in Figure 2. 5. Mostly, a relative energy resolution given in percentage is used, and also the quantity *energy resolving power* defined as the inverse $\frac{E_0}{\Delta E}$ (also a relative a measure).

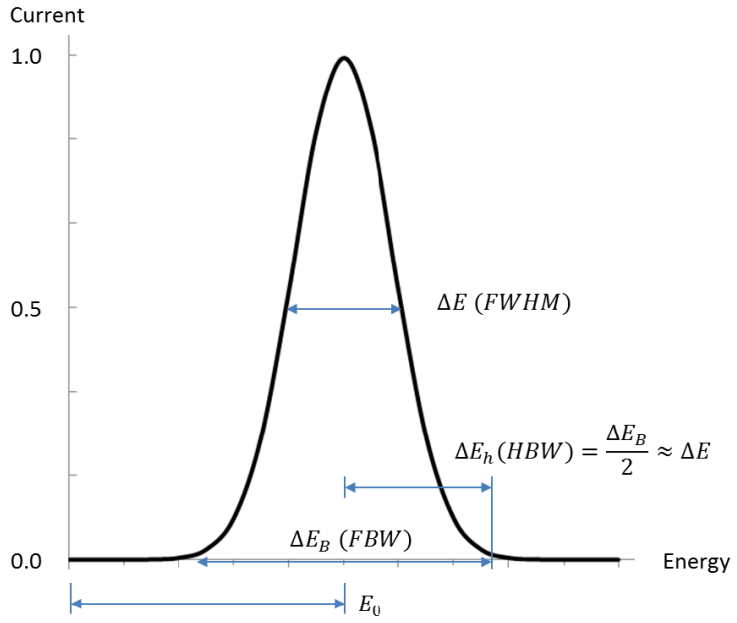

Figure 2. 5: Schematic of the different definitions of the energy resolution for a real beam with Gaussian shape. The most used is the one at the FWHM. Image taken from [130].

The *trace width W* is the width of the image due to the *energy dispersion* or, the *spherical aberration* arising from changes of the half opening angles $\Delta\alpha$, $\Delta\beta$, of the incident beam ($\Delta\alpha$ is the half

angle in the plane of the deflection, and Δβ is the half angle in the perpendicular plane). The *trace width* dependence on energy variations is mostly linear and can be characterized by the *dispersion D:*

$$\boldsymbol{D = E\left(\frac{dW}{dE}\right)} \tag{2. 10}$$

Thus, the trace width at the image for a given relative energy change can be written:

$$\boldsymbol{\Delta W = D\frac{\Delta E}{E_0}} \tag{2. 11}$$

On the other hand, if the trace width is produced by the spherical aberration ΔW_A, the relative energy resolution can be written:

$$\boldsymbol{\frac{\Delta E}{E} = \frac{\Delta W_A}{D}} \tag{2. 12}$$

There are different analytic expressions to obtain the energy resolution [36,39], in this work we will use the following expression [40]:

$$\boldsymbol{\frac{\Delta E}{E_0} = \frac{W_s}{D} + \frac{W_A}{D}} \tag{2. 13}$$

Where W_s is the width of the exit slit and W_A is the trace width due to the spherical aberration. The aberration term can be expanded in a polynomial series obtaining for the energy resolution:

$$\boldsymbol{\frac{\Delta E}{E_0} = \frac{W_s}{D} + \frac{C_{s2}}{D}\Delta\alpha^2 + \frac{C_{s3}}{D}\Delta\alpha^3 + \frac{C_{s4}}{D}\Delta\alpha^4 + \cdots} \tag{2. 14}$$

The order of focusing of the analyser is defined as the first coefficient non-zero of $\Delta\alpha^n$, and then following the rule (n-1) [40]. For *first-order focusing* the first coefficient non-zero is C_{s2} and for *second-order focusing* the first coefficient is C_{s3}. The higher the order focusing, the better the energy resolution, or higher sensitivity, which means greater angular acceptance at the same energy resolution. In general, the most popular energy analysers are *first* or *second order focusing*.

The analysis above only considered the effects of the changes in the plane of dispersion, but there could be angular changes in the perpendicular plane, as a result the transmission and the energy resolution are deteriorated. This is logically because the particles with different velocity component in that plane would be influenced differently by the field, thus a more general formula can be concluded:

$$\boldsymbol{\frac{\Delta E}{E_0} = \frac{W_s}{D} + \frac{C_{sn}}{D}\Delta\alpha^n + F\Delta\beta^2} \tag{2. 15}$$

Where C_{sn} and F are values characteristic of each particular analyser. In practice, a finer resolution, or higher resolving power, can be achieved by decreasing the slits widths, decreasing the beam opening angle and increasing the analyser dimensions.

2.5.1 The spherical analyser

Spherical deflector analysers (SDA) consist of two coaxial spherical electrodes with different voltages applied to produce an electric field to curve the particles (see Figure 2. 4).

The energy of the incident particle is $E_0=qV_0$, the voltages V_a and V_b of the inner and the outer electrode respectively, are usually chosen to keep the surface of the central radius r_e at a fixed potential such that the energy of the particles remains constant inside the sector. In practice the central equipotential is often at ground. The electric field E in the axis should be chosen in a way that the particles entering with energy E_0/q on the entrance axis will travel on circular path on the optical axis. If the particles enter the region with slightly different energies: E_0/q and $(E_0+\Delta E)/q$, they will follow different trajectories.

In order to find the dispersive and focusing properties of the spherical analyser is necessary to calculate the trajectories of the particles in the paraxial approximation (as explained in Section 2.2).

The potential and the radial electric field inside the electrodes can be written [21]:

$$\boldsymbol{V(r) = 2V_0(\frac{r_e}{r} - 1)} \qquad \boldsymbol{E(r) = \frac{-dV(r)}{dr} = 2V_0\frac{r_e}{r^2}} \tag{2. 16}$$

The equations of motion for particles outside the optical axis in the radial and vertical planes for a particle in cylindrical coordinates are:

$$\boldsymbol{m\ddot{r} = mr\dot{\varphi} - qE_r} \qquad \boldsymbol{mr^2\dot{\varphi} = C} \qquad \boldsymbol{m\ddot{z} = -qE_z} \tag{2. 17}$$

These differential equations represent an oscillation around the optic axis in both directions r and z. The equations can be integrated to obtain the equation of trajectories with a period 2π. So, the dispersive and focusing properties of the spherical sector for certain angle can deduced.

The potentials that should be applied to the electrodes to keep the middle at zero potential are [21]

$$\boldsymbol{V_a = V_0\frac{d}{r_e}\,(1 + \frac{1}{2}\frac{d}{r_e})} \tag{2. 18}$$

$$\boldsymbol{V_b = -V_0\frac{d}{r_e}\,(1 - \frac{1}{2}\frac{d}{r_e})} \tag{2. 19}$$

Where d is the gap distance. These equations are valid for negative ions or electrons, for positive ions the signs should be inverted. Thus, the deflection voltage across the electrodes is:

$$\boldsymbol{V_d = V_a - V_b = 2(\frac{d}{r_e})V_0} \tag{2. 20}$$

The image is very simple to find geometrically following Barber's rule: the object point, the image point and the centre of the sector are aligned in a straight line (see Figure 2. 4). However, the object distance should be enough to avoid that the image lies inside the analyser.

The selection of the gap distance *d* is also important, it should be wider than the beam width, so the beam does not touch the electrodes, but a small distance between the electrodes is better to reduce the effect of the fringing fields.

The most common spherical analysers are the 180° and the 90°. The first one, is called Hemispherical Deflection Analyser (HDA), and is widely used in electron spectroscopy [41,42]. It has stigmatic imaging when the source is located at the entrance of the analyser and it has the property to bend the beam 180°, so the beam "goes back" and is parallel to the original path. The second one, is mostly used as energy focusing lenses in double focusing spectrometers, such as the Cameca IMS XF and IMS 1280, combined three together like in the TOF-SIMS TRIFT [1] or like the omega filter used as monochromator in electron microscopy [20].

They are also used as energy filters in imaging systems because they make a real image of the object in the paraxial approximation.

Comparing Spherical Deflector Analysers (SDAs) with Cylindrical Mirror Analysers (CMA), they have the advantage that they usually require lower electrode potentials for transmitting particles with high energy, but they are more difficult to manufacture and align [39].

2.5.2 The toroidal analyser

The most common electrostatic capacitors are the cylindrical and the spherical analysers described above, however there are special cases where the toroidal geometry is desired because a particular dispersive or imaging property is required. In some cases, it is preferred because has better energy resolution, in other cases because it has no energy dispersion at image point. For example, they are used as analyser attachment in SEMs to measure energy spectra [40], to measure they energy of scattered ions [43], for angle detection of charged particles [43]. The toroidal sector consists of two coaxial electrodes, which are usually spherical but with different radii of curvature in the radial (R_e) and the axial planes (r_e), consequently there are two distinct points of focusing, one for the z direction (β) and the other for the radial direction (α).

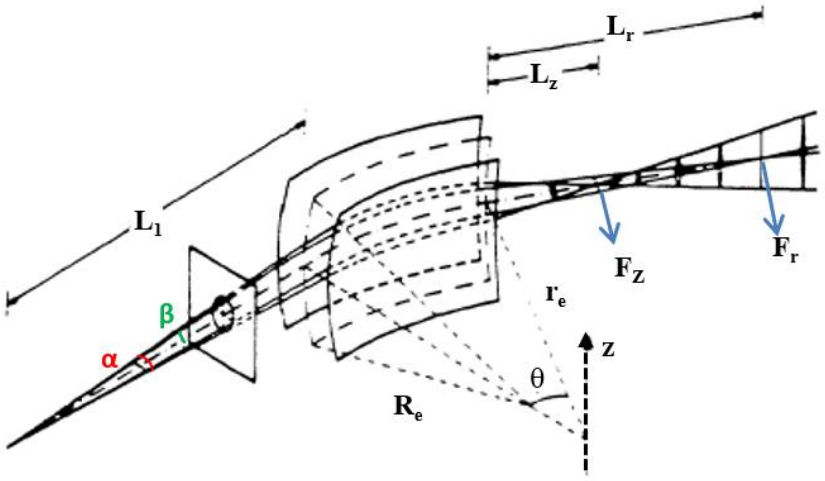

Figure 2. 6: Schematic of the toroidal sector with two different focus points. The properties in the dispersive plane are different of the perpendicular plane according to the toroidal factor: Image adapted from [21].

The toroidal factor is defined as the ratio between the optical axis deflection radius r_e and the radius R_e:

$$\boldsymbol{c} = \frac{\boldsymbol{r_e}}{\boldsymbol{R_e}} \tag{2. 21}$$

$$\boldsymbol{r_e} = \frac{\boldsymbol{r_a + r_b}}{\boldsymbol{2}} \tag{2. 22}$$

Where r_a and r_b are the inner and the outer radius of the electrodes, respectively. After expanding the potential around the optic axis and computing the focusing properties, the basic geometries are recovered, for c=0, the cylindrical deflector analyser, and for c=1, the spherical case. When c > 2 there is a strong focus in the z direction, but it is diverging in r direction. Contrary when c < 1 the toroidal has stronger focusing in r direction than in z direction.

If 1< c < 2, is possible to achieve stigmatic focusing in both directions, an intermediate axial focus is achieved inside the sector, and in the case of symmetric imaging, this focus is formed at the half of the sector angle. Figure 2. 7 illustrates the case of 180° and C=1.69 the energy dispersion is 3.2 times higher than the spherical sector of the same radius, which leads to correspondingly better energy resolution [21].

Another interesting case of application of toroidal geometry is when a radial intermediate focus is formed, the energy dispersion is zero at the image position, but is very useful to compensate the time of flight for particles with a small relative energy spread and to be inserted in time of flight mass spectrometer [44].

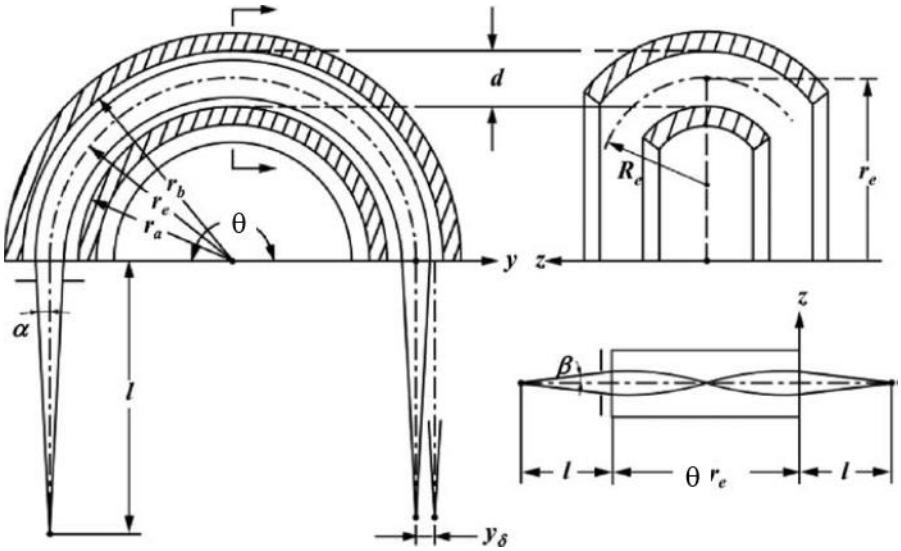

Figure 2. 7: Stigmatic imaging of the toroidal capacitor with axial intermediate focus. θ=180°; c=1.69 and dispersion =3.2 higher than spherical sector of 180°. (picture adapted from [21]).

The spheroid geometries investigated in this work present characteristics of toroidal analysers.

2.5.3 The fringing fields

When designing an energy analyser care must be taken regarding the fringing fields, where the electrostatic field decreases continuously, without a sharp cut off, so the field coming from the inside of the analyser penetrates the outside. As a consequence, the deflection of the particles should be calculated taking in to account the effective electric field boundaries, which usually do not coincide with the geometrical physical boundaries of the analyser. As a result, the resolving power of the detector decreases. Several methods are used to compensate this effect; a summary was made by Sise et al [45]. Herzog in 1935 found a combination of the aperture parameters, (the distance between the aperture and sector electrodes, the gap and the slit size, etc.) such that apertures behave as fringing field shunts and the effective field boundary coincides with the physical electrodes edges. Jost [46] proposed another geometry for fringing field shunts, which only the central part of the aperture is kept at the potential of the optical axis, specially designed for geometries that have zero object and image distances, such as the hemispherical sector and the cylindrical deflector of 127.3° (Figure 2. 8).

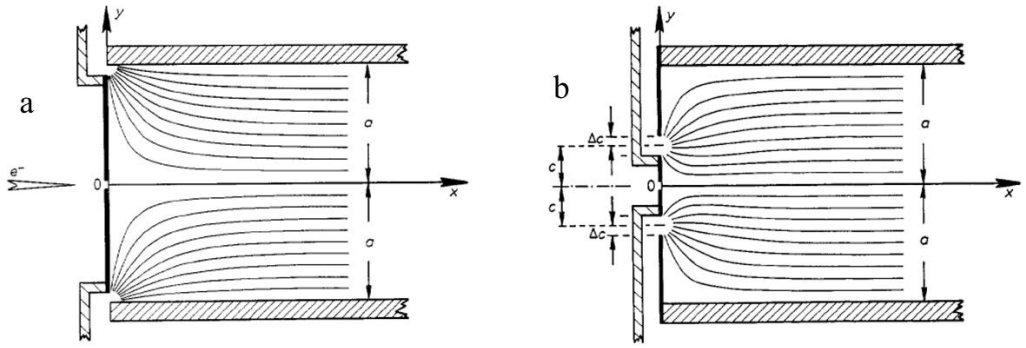

Figure 2. 8: a) Shielded parallel plate capacitor with a thin aperture and equipotential lines obtained experimentally ;b) Geometry of the Jost aperture with the fringing field obtained experimentally [46].

2.5.4 Mirror analysers

The particles entering the mirror type analysers change their energy during the trajectory inside the analyser, initially they are retarded and the re-accelerated, this is called a *retarding field*. These analysers are preferred when higher order focusing properties are desired or larger acceptance angle. Many designs of mirror analysers exist with different alternatives and characteristics depending on the application. The most common are the *parallel plate mirror analyser* (PMA), the *cylindrical mirror analyser* (CMA), the *spherical mirror analyser* (SMA) and *toroidal mirrors analysers* (TMA). We will limit our discussion to the essential concepts to understand the basic properties of the CMA, TMA and finally the novel *spheroid analysers*, because the properties of the combination of the spheroid analyser and a magnetic sector will be investigated in next chapter.

The CMA is the most commonly used analyser for electron spectroscopies such as Auger Electron Spectroscopy (AES), X-ray Photoelectron Spectroscopy (XPS) [39] it constitutes two coaxial cylinders, where the source and the exit focusing points are located on the symmetry axis of the CMA. Figure 2. 9 shows the particles entering with an incident angle φ and that are deflected back to the axis. The slits are located in the inner cylinder. The CMA focuses, as the spherical sector, in both directions; and has also a *second order focusing* for a beam at an entrance angle of 42.3° [47]. The potential of the inner electrode is the same as the source to produce a field free region.

Designing mirror analysers with a distorted cylindrical field allows new possibilities in terms of focusing properties, like changing the incident angle or improving the dispersion [48,49]. Some examples are the quasi-conical analyser [50] and the toroidal mirrors [35,51].

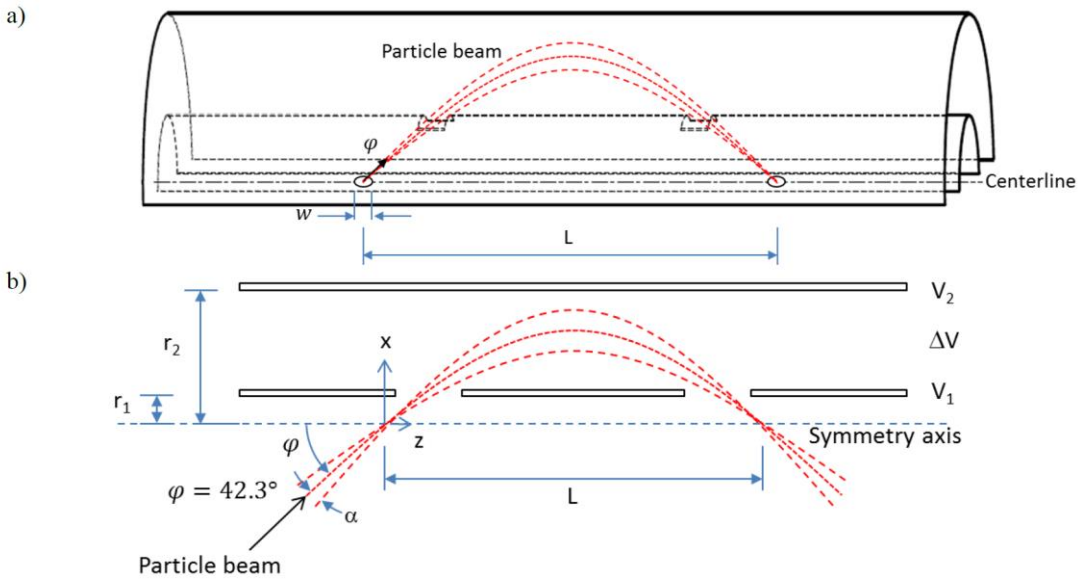

Figure 2. 9: a) Diagram of an axial focusing CMA with the source on the image located on the axis; b) cross section showing the second order focusing and the axis of symmetry. Picture taken from [130].

The *toroidal mirror analysers* (TMA) were proposed by Belov and Yavor [51], and can be considered as a further development of a distorted CMA. An example of toroidal mirror analyser is shown in Figure 2. 10, the inner electrode is a cylinder (r_1), with two circle cuts covered by grids acting as slits where the particles enter and exit the analyser, while the external electrode has a spherical shape (r_2). When the particles enter with a specific angle and energy, they can have an axis-to-axis- focusing and analyser has a *second-order focusing* [35]. Furthermore, Belov and Yavor [51] showed a *third order focusing* for geometries where the beam leaves the analyser field between the inner and outer electrodes.

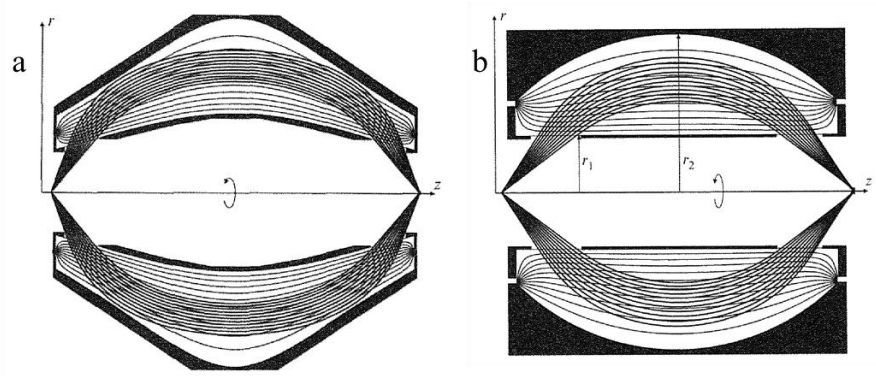

Figure 2. 10: a) Image of the quasi-conical analyser, with equipotential lines and particle trajectories; b) toroidal mirror analyser with equipotential lines and charged particle trajectories. Picture taken from [35].

2.5.5 The novel spheroid analyser

The state-of-the-art of high transmission and high resolution energy analysers are the *spheroid energy analysers* (SEA) described by Cubric [13]. The main important properties of the SEA are *the highest ordering of focusing*, 13th order of focusing was obtained by simulations; *high angular acceptance ±8°, high energy resolution*, 0.006% simulated and 0.05% measured; and *high transmission* 21% out of a 2π steradian. This design has been commercialized by Shimadzu Corporation.

Similar to the case of toroidal analysers (see 2.5.2), the SEA is a general geometry, were all other analysers are included as particular cases for certain parameters. Figure 2. 11 illustrates how the geometry is generated. The inner R_1 and the outer R_2 electrodes (red colour) have spherical shape, not concentric, rotated around the optical axis. When the red part of the electrode is rotated around the axis, geometry similar to a rugby ball is generated. Other relevant parameters are the distance to the axis of rotation to the zenith of the circles R_{01} and R_{02}, and the difference between them, R_{12}. With these parameters it is possible to make a coordinate's change and define a new space of coordinates, called the K system (Figure 2. 11b).

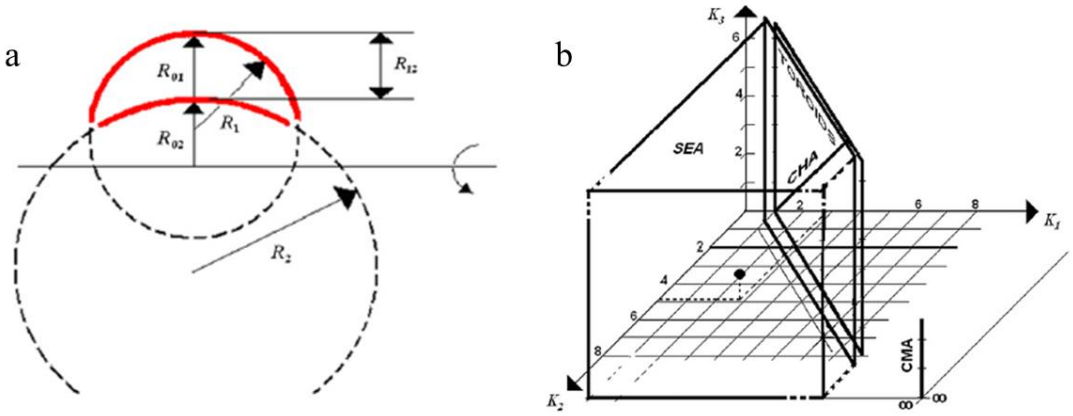

Figure 2. 11: Schematic of the main elements and parameters in the general SEA geometry; b) the new K coordinate system where all other geometries such as CHA, CMA and Toroidal are included [13].

The K parameters are defined:

$$\boldsymbol{K_1 = \frac{R_1}{R_{12}}};\quad \boldsymbol{K_2 = \frac{R_2}{R_{12}}};\quad \boldsymbol{K_3 = \frac{R_{02}}{R_{12}}} \tag{2. 23}$$

The hemispherical analyser is recovered when $K_1=1+K_2$ and $K_3=K_2$; and the CMA if $K_1=K_2=\infty$. An important condition to ensure the focusing properties of the spheroid is the selection of $R_2 > R_1$, to ensure the convergence of both electrodes, enabling very good truncation of the fringing fields. Figure

2. 12 shows a particular combination of K_1, K_2 and K_3, of the prototype built by Shimadzu Corporation [52] .

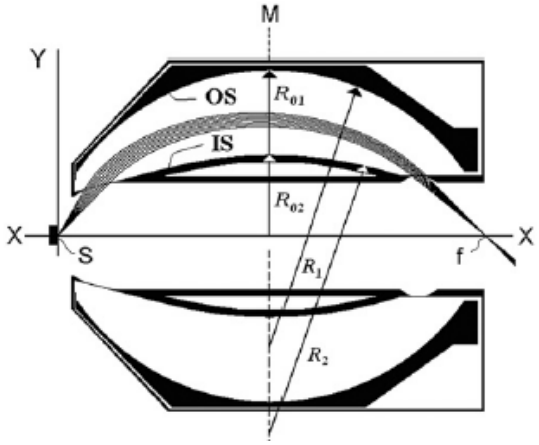

Figure 2. 12: Schematic of the Spheroid analyser built at Shimadzu Corporation. K1=2.576, K2=4.889 and K3=0.994. R1=124 mm, R2=220 mm, R02=42.5 mm and R12=45mm .Picture taken from [13].

The inner electrode is grounded while the outer electrode is energised according to the incoming particle energy. The charged particles are injected through a slit covered grid, and exit through a second grid slit, focusing on the axis equal to the CMA and TMA.

The following table compares the relative energy resolution simulated at half opening angle for two of the more popular analysers HDA, CMA and the SEA:

Semi-angle (Δα)	**HDA**	**CMA**	**SEA**
8°	0.97%	0.69%	0.007%

Table 2. 1: Summary of the relative energy resolutions in percentage of the most used analysers and the SEA obtained by simulations [53,54].

2.6 Magnetic sectors

Magnetic deflection or magnetic lenses are used when electron beams should be focused with low aberrations i.e. in electron microscopes, electron beam lithography, etc. Usually, for deflecting ions the magnetic fields must be extremely large, and electrostatic deflectors are used instead, except for mass dispersion or for focusing high ion energy beams.

As seen in Section 2.2, a charged particle that enters a uniform magnetic field $\boldsymbol{B}$ perpendicular to its trajectory experiences the Lorentz force, (eq. 2.1) and will be deflected in a circular trajectory. If we will only focus on the magnetic force, no electric field $\boldsymbol{E}$, a particle with mass m, charge q and velocity v, will be deflected following the Lorentz force law:

$$\vec{\mathbf{F}}_{\mathrm{M}} = \mathbf{q}\,\vec{\boldsymbol{v}} \times \vec{\boldsymbol{B}} = \boldsymbol{qvB} \tag{2. 24}$$

Because the particle follows a circular path with a radius r, the magnetic force compensates the centrifugal force and the following relation is obtained:

$$\boldsymbol{qvB} = \frac{\boldsymbol{mv^2}}{\boldsymbol{r}} \tag{2. 25}$$

Taking also into account the kinetic energy E_k of the ions generated in the source is equal to:

$$\boldsymbol{E_k} = \frac{\boldsymbol{mv^2}}{\mathbf{2}} = \boldsymbol{qE} \tag{2. 26}$$

Where E is the beam energy, and combining equations 2.22 and 2.23 we obtain:

$$\boldsymbol{Br} = \sqrt{\mathbf{2}\boldsymbol{E}\frac{\boldsymbol{m}}{\boldsymbol{q}}} \tag{2. 27}$$

From this equation, we can see that the deflection depends on the mass to charge ratio and the energy of the particle, thus it can be defined a mass and energy dispersion coefficient.

A schematic of the magnetic deflection for particles entering a uniform magnetic field with angle Φ is illustrated in Figure 2. 13. When the angle of deflection is small, can be approximated by L/r, where r is the radius calculated in equation (2.7) and L is the length of the field. Therefore, the deflection at the exit of the sector is:

$$\boldsymbol{y(L)} = \boldsymbol{r}(\mathbf{1} - \mathbf{cos}\,\boldsymbol{\theta}) \tag{2. 28}$$

Expanding 2.28 as power series results in:

$$\boldsymbol{y(L)} = \frac{\boldsymbol{L^2}}{\mathbf{2}\boldsymbol{r}} \tag{2. 29}$$

Therefore, to define the mass and the energy dispersion coefficients, both parameters should be changed by small quantity (γ, δ) and developed in equation (2.27) to first order:

$$\boldsymbol{r_1} = \sqrt{\frac{\mathbf{2}}{\boldsymbol{q}}}\,\frac{\mathbf{1}}{\boldsymbol{B}}\,\sqrt{\boldsymbol{V_0}(\mathbf{1}+\boldsymbol{\delta})\boldsymbol{M_0}(\mathbf{1}+\boldsymbol{\gamma})} = \boldsymbol{r_0}(\mathbf{1}+\frac{\boldsymbol{\gamma}}{\mathbf{2}}+\frac{\boldsymbol{\delta}}{\mathbf{2}}) \tag{2. 30}$$

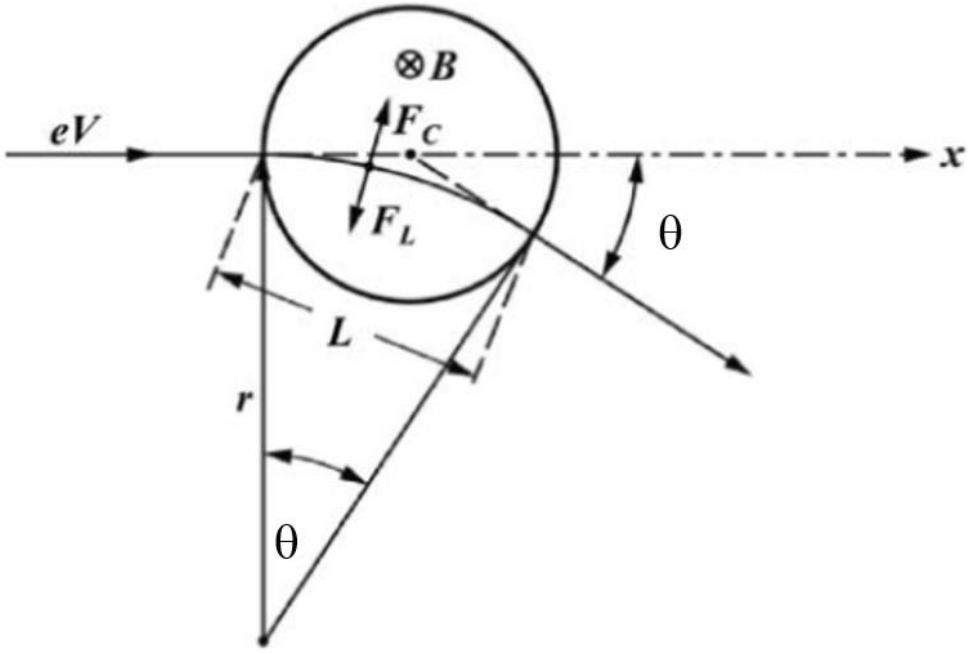

Figure 2. 13: Schematic of the magnetic deflection. Picture adapted from [21].

Finally, the deflection can be written:

$$\boldsymbol{\theta_1 = \frac{L}{r_1} = \frac{L}{r_0}\left(1 - \frac{\delta}{2} - \frac{\gamma}{2}\right)} \tag{2. 31}$$

Thus, a difference in the deflection angle can be written:

$$\boldsymbol{\Delta\theta = -\frac{1}{2}\theta_0(\delta + \gamma)} \tag{2. 32}$$

From this equation can be deduced that the dispersion factor is the same for both mass and energy. In double focusing spectrometers (see Section 3.3.3) the energy dispersion of the magnetic sector is compensated with the energy dispersion of the electrostatic sector, therefore, only the term of mass dispersion survives.

The most common application of magnetic sectors is for mass separation or mass spectrometry; thus, it is necessary to define the concept of mass resolution in analogous way as was defined for the electrostatic case the energy resolution (see Section 2.5). The mass resolution is an important parameter, which measures the capability of the instrument to distinguish between elements or compounds with close nominal mass. Theoretically, the image width of the entrance slit (s_1) should be the same of the mass dispersion and the energy dispersion, considering the magnification of the system. This yield,

when the image is symmetric (same focal distance for the object plan and the image plane), to the theoretical mass resolution is:

$$\frac{\Delta M}{M} = \frac{s_1}{r} + \delta \tag{2. 33}$$

Consequently, this expression shows that the mass resolution is limited by the energy spread. This equation highlights the conclusion discussed above, because the parameter δ is isolated and clearly can be compensated with an energy sector with the same δ but with opposite sign. Like energy deflectors, the mass resolution does not depend on the angle of the sector *Φ*. Similar to the electrostatic case, the mass resolving power (MRP) may be defined as:

$$MRP = \frac{M}{\Delta M} \tag{2. 34}$$

In practice, *M* is the mass of the species of interest and *ΔM* is the difference of mass that can be separated. Depending on the field of application *ΔM* is measured at the full width half maximum (FWHM) of the peak in a mass spectrum (TOF-SIMS), or the IUPAC [55] definition where two equally intense peaks are separated by a valley which is 10 % of the maximum peak height.

Simple sectors as described above only focus in the plane of radial dispersion, equal to cylindrical analyser. In order to have focusing in both directions, such as the spherical analyser, it is necessary to make the boundaries of the sector with certain angle ε respect to the optic axis, so the fringing fields act as a thin lens normal to the trajectory [56,57]. An illustration of the effect of the fringing field in the vertical direction is shown in Figure 2. 14.

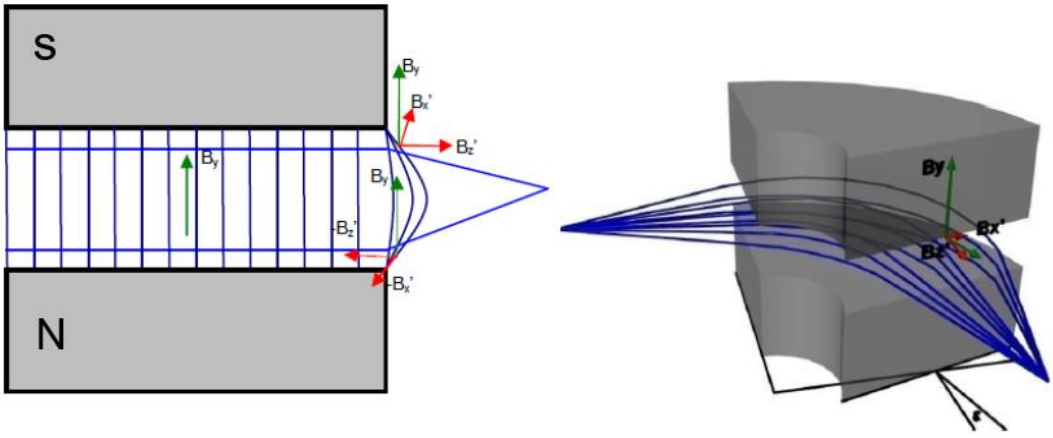

Figure 2. 14: Left, effect of the fringing field gradient is focusing the beam in the vertical plane, right example of a magnet with a tilted pole-face, with the magnetic field lines indicated between poles [131].

Figure 2. 15 shows a schematic of a symmetric sector with equal pole face angle in both faces. Similar concept is applied to the magnetic sector of the Cameca IMS XF series.

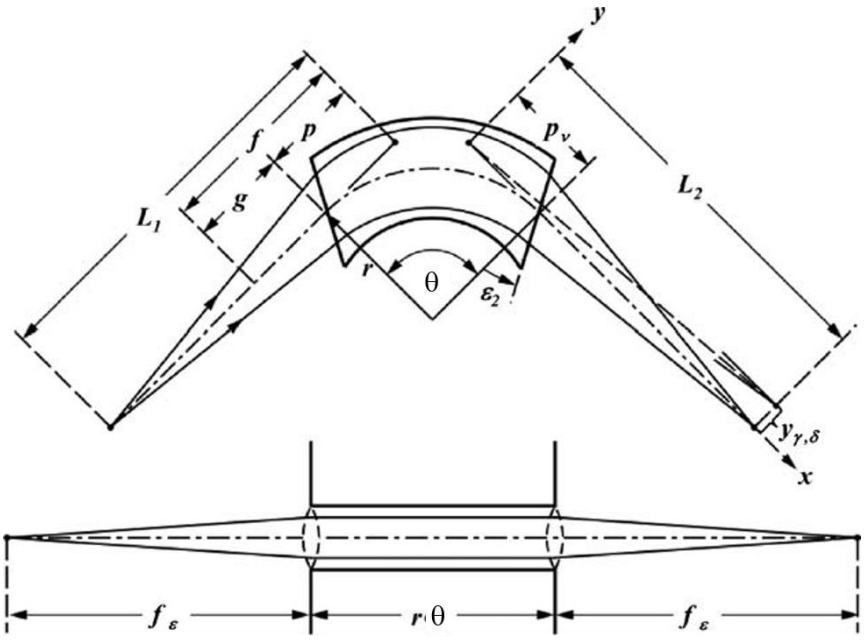

Figure 2. 15: Schematic of a symmetric stigmatic magnetic sector whit the boundaries having angle ε with the optic axis, up focusing in the deflection plane and down focusing in the axial plane. Picture taken from [21].

Another alternative to achieve focusing in z direction is to use a field gradient in the magnet, induced by non-parallel pole pieces [21]. Improvement in focusing in both directions can be achieved applying curvatures in the entrance and exit pole faces [58]. Spencer et al. obtained a two-directional focusing magnet with a second order focusing in the plane of dispersion [59].

When designing a magnet for a spectrometer or a spectrograph there are some reflections to consider. Comparable to electrostatic case, the magnetic field not only is confined to the interior of a magnet gap but also has a significant value at far distance outside the magnet. Consequently, the particles start to turn before they enter the magnet and they still continue bending after they leave the magnet, for this reason the mechanical edges do not coincide with real magnetic "faces" that the particles see [59]. Thus, it is necessary to calculate the effective field boundary (EFB), which is always curved even if the pole face boundary is straight [60]. Then the 3D field should be determined in order to find the EFB. The size and shape of the magnet is also particularly important: on one hand, the bigger the radius, the bigger the range of detectable *m/q* ions; however, on the other hand, it should have a minimum radius larger enough that the particles travel inside the gap influenced by the uniform magnetic field rather than the fringing fields. There are commercial software (TRANSPORT [61],

RAYTRACE [62], LORENTZ [61], COSY [63], etc.) available for designing magnets and calculating all the parameters such as magnification, focusing distances, energy and angular dispersion, entrance and exit angles, etc.

2.7 Software Simulation

Several computer programs have been developed for simulate systems in charged particle optics. Most of the programs are based on first or second-order finite element methods (FOFEM and SOFEM), the finite difference method (FDM), the charge density method (CDM) or the boundary element method (BEM).

The software used in this work was SIMION 8.1 [64] based in the FDM which is used to calculate the potential distribution by solving the Laplace equation using the numerical method of successive overrelaxation (SOR). The optical system is formed by potential arrays which can be 2D or 3D, depending on the symmetry of the system. The potential array consists of a grid of points in a rectangular mesh. Once each grid point of the mesh is defined as electrode or non-electrode point, the potential is approximated by a series of finite difference equations, which links the potential of that grid point with the potential of the four nearest neighbours. Once the equations are solved and the potential field is calculated, the electric field and the trajectories can be calculated integrating the system of Newton's equations with a four-order Runge-Kutta technique [20].

The advantage of this method is the speed to calculate the electrostatic field by numerical differencing and the accurate ray-tracing. In addition, the version of SIMION used in this work supports user-written programs that enable to manage programmatically different parameters of the particles and fields. For example, a special distribution for ion generation (see Section 4.4) or modify the lenses voltages to obtain the optimized optical properties etc. A drawback is that complex magnetic fields are not possible to calculate in SIMION, (i.e. non-constant permeability in 3D with magnetic vector potential).

The process to simulate an element, can be divided in three main steps: the design of the geometry and its insert in SIMION, the refining process (solve the Laplace equation) and finally apply the conditions to run the simulation of the system.

The geometry of the desired electrode can be performed in three different ways: the first one is to use directly the *modify* panel to create simple shapes. The second option is to use a geometry file (.gem) that should be written in a text editor such as Notepad++. The last option is to design the geometry with a computer-aided design (CAD) program. In the last two cases, the files must be converted to *potentials arrays* (PA).

When designing an element, it is necessary to consider the size of the PA, the bigger the size, more memory (RAM) will required, and logically more time of computer will be consumed. In addition, it is also important to define the *array symmetry*: planar (with or without mirror planes) or cylindrical; the *type of* the *electrodes*: electrostatic or magnetic. In order to reduce the memory consumption, SIMION has tools such as mirroring symmetry, where the electrodes that have at least one plane of symmetry, can be reproduced by making a mirror image on the axis of symmetry, so only half of the geometry should be design or even less if there are two axes of symmetry. The accuracy of the geometry depends on the size of the mesh, but there is always a compromise between the size of the mesch and the memory required.

After the geometry is inserted and converted into a PA, it should be refined. During this process, the Laplace equation is solved in the space between the electrodes which act as boundary conditions. There are two classes of PAs, the *basic potential array* (.PA) and the *fast adjust definition array* (.PA#). In the first group, the potential values of the electrodes are defined before the refining process. In the second group, the electrode potentials are not explicitly defined, each electrode is referenced by a number and the potentials are established after the refining process. This gives the opportunity to change the potential values of the electrodes (fast adjust) several times to simulate different focusing properties, avoiding re-refining each time. Moreover, with a user program it is possible to change the voltages while the simulation is running.

The simulation takes place on a virtual optical *Workbench*, where the PAs are load and displayed. The PAs can be positioned and oriented to build a complete system, additionally, the voltages of the electrodes can be adjusted. The particles conditions are chosen, type, number, energy distribution, position, etc. The equipotential lines may also be shown, as well as the particles trajectories. Different parameters such as energy, positions, velocities, angles, can be saved in any plane for later analysis.

2.8 Conclusions

In this chapter, the theoretical concepts of charged particle optics have been explained for the particular cases of electrostatic lenses used in this work such as immersion lenses and Einzel lenses.

A description of the electrostatic analysers with particular emphasis in the *spherical deflector analyser* (SDA) and the *spheroid energy analyser* (SEA) has been described, in order to understand their focusing properties and have the basis to compare and evaluate in chapter 4 which one performs better in combination with a magnetic deflector.

A brief description of magnetic lenses was made to have the basis for understanding the main component of sector fields spectrometers. Finally, A short explanation of the SIMION used to perform simulations in this work has been given.

3 Secondary Ion Mass Spectrometry

3.1 Introduction

This chapter covers fundamental concepts of SIMS required for the development of a SIMS instrument. Initially, an overview of the advantages and disadvantages of the technique are revised, as well as the different SIMS measurements. A short review of the sputtering and of the ionisation processes is presented, followed by key issues in SIMS such as matrix effect, quantification. Finally, the bases of the three main mass filters used in SIMS are described, including a detail explanation of the instruments used in this work.

3.2 The SIMS fundamental

3.2.1 Overview

Secondary ion mass spectrometry is a surface analysis technique with more than 50 years of development. A primary ion beam is focused onto the sample, which is normally solid, and this generates a collision cascade in the sample. Consequently, secondary particles are ejected out of the sample, this is called *sputtering*. The species ejected could be positive or negative ions, neutral atoms, molecules or electrons. The secondary ions are extracted in to the mass spectrometer, and they are separated by their mass to charge ratio. The energy of the primary ion beam typically varies from 100 eV to 30 keV [7,12].

The main advantages of the technique are the high sensitivity; it is possible to detect particles down to ppb and exceptionally parts-per–trillion (ppt), the high dynamic range, sub nanometre depth resolution, differentiation between isotopes [2] and, a lateral resolution of 50 nm .

The main drawbacks of the technique is the matrix effect which makes difficult the quantification of SIMS intensities (to convert the secondary ion counts into concentration). Additionally, mass spectra can be difficult to analyse due to mass interferences.

The applications of the SIMS technique cover a great diversity of areas, such as Materials Science, Cosmo-chemistry, Life sciences, Pharmacology, Toxicology, etc. The SIMS technique offers the possibility to obtain a mass spectrum of the sample, to make a depth profile or a chemical mapping, and 3D reconstructions. Depending on the desired measurement, the SIMS technique is divided according to the total number of primary impacts per surface area (the ion dose). For example, to analyse organic materials, the damage of the surface should be minimized to avoid excessive fragmentation of molecules, here the so called static regime; where the primary beam has low ions density per analysed

area (<10^{12} ions/cm^2) is used in order to keep the amount of fragmented molecules low. Dynamic SIMS (D-SIMS) is used to analyse the elemental and molecular distributions as a function of the depth and it is characterized by a well-focused, intense primary beam scanned over a small area (doses > 10^{17} ions/cm^2).

3.2.2 The sputtering processes

SIMS is based on the interaction between an ion beam and a solid target. When an energetic ion beam impacts on the surface of the sample different effects are produced: some of the primary ions may be backscattered; some secondary electrons can be ejected; photons can be produced, and some ions penetrate into the sample sharing part of their energy with the target atoms as electronic excitation as well as collisions (Figure 3. 1). During these collisions, the target atoms are displaced from the original positions, these first recoils, may also transfer their energy to other atoms in the sample and progressively more and more atoms are affected, forming a cascade. As consequence, some of the atoms are relocated, some particles near the surface gain enough energy to escape from the surface and some of the primary ions are implanted in the target. This is the basis of the sputtering process. The ejected particles can be ions, molecules, but the majority are neutral atoms. These particles are sputtered from the top most layers of the surface of the sample, meaning in a range of monolayers.

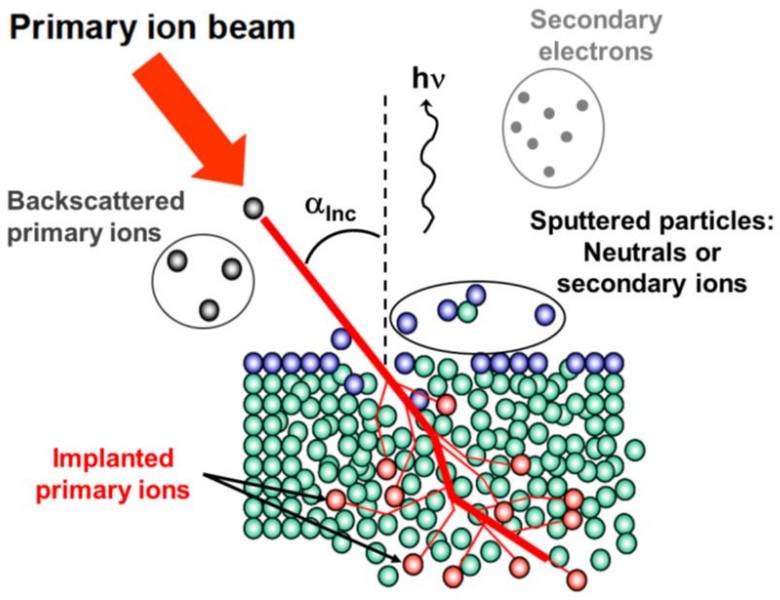

Figure 3. 1: Primary ions impacts on the solid generating a collision cascade process. Secondary ions with enough momentum are sputtered and primary ions are implanted. (adapted from [122])

The dimensions of the cascade and the range of the primary ions can be modelled and simulated by commercial software (for model binary collisions i.e. TRIM and for taking the forces from all atoms on each other Molecular Dynamics programs (MD)).

The sputter yield is defined as the number of atoms of material removed n_s ; per incident species n_i:

$$S = \frac{n_s}{n_i} \tag{3. 1}$$

Normally, the sputter yields tend to be in the range from 0.1 to 10 atoms per primary ion. The total sputtering yield depends on the mass, the energy and the angle of the primary ions, as well as on the properties of the target material such as the mass of the target atoms and the crystal orientation. The energies used in SIMS for are typically in the range of 100 eV to 30 keV.

The dependence of the sputtering yield in function of the ion energy has been studied experimentally and computationally for several ion masses and energies for some elemental substrates [65,66]. Figure 3. 2 is an example of the sputtering yield of silicon when the energy varies from 0 to 1000 keV, for different primary ions.

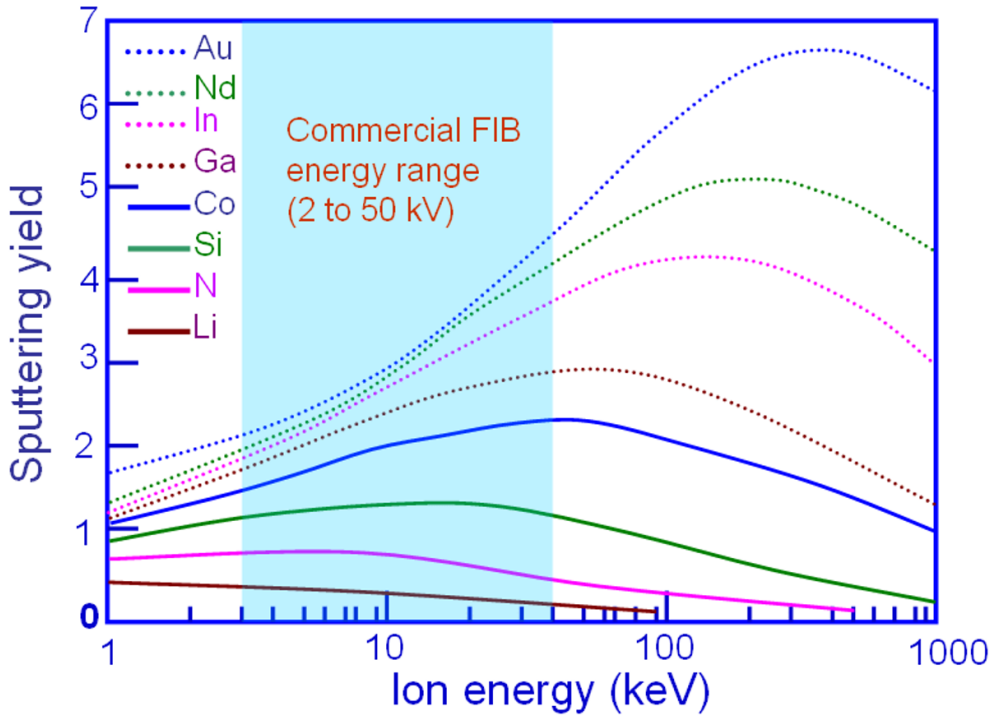

Figure 3. 2: The sputter yield of silicon as a function of beam energy. The data is shown for beams incident normally on the sample surface between 0 keV and 1000 keV .Picture taken from [132].

The yield rises smoothly, obtaining a broad maximum after 100 keV, that subsequently decreases to zero. The heavier ions have larger sputtering yields because they are stopped faster than the lighter ions when they cross the surface of the sample, transferring more energy to the top layers and allow the particles from this region to absorb the energy and get sputtered. In the case of very light elements, like helium only very small part of the energy is deposited near the surface and consequently its sputtering yield is very low.

Another parameter related to the transfer of the energy to shallower depths is the angle of incidence of the primary ions (measured respect to the surface normal). The yield increases with the angle of incidence, to a maximum around 60° to 80°, dropping to zero near glancing incidence, as the primary particles begin to be forward-scattered, thus the total amount of energy deposited in the target decreases and in consequence the sputter yield. Figure 3. 3 shows experimental data of Ne^+ and O_2^+ primary ions at 5 keV on silicon for different impact angles.

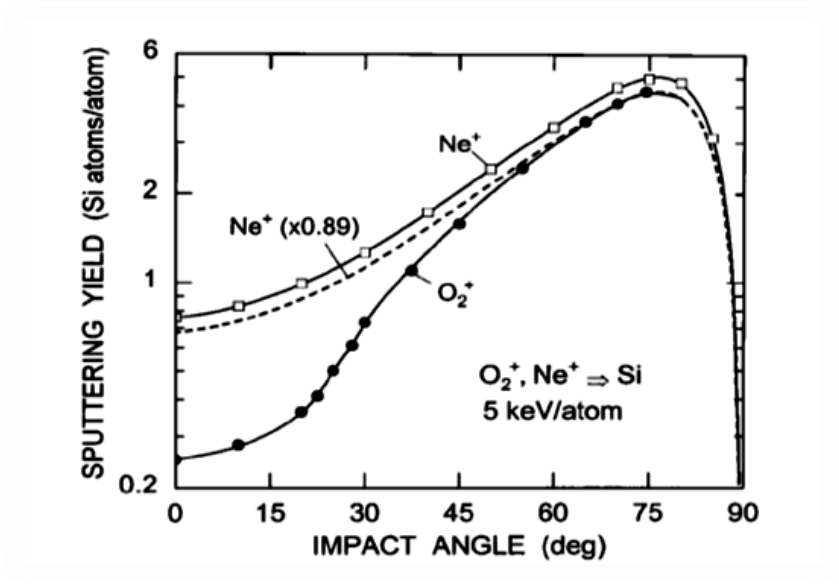

Figure 3. 3: Angular dependence of the sputtering yield of silicon under oxygen and neon bombardment at the same energy per projectile atom [133].

During the bombardment, primary ions are implanted into the sample until equilibrium is reached. Over this period of time, called the transient regime, the sputtering yield varies, as well as the concentrations of the primary ion species. When the steady state is reached, the rate of implanted primary ions is equal to the rate at which they are sputtered. This implantation modifies the sample physically and chemically, modifying the ionization probability of the sputter matter [3,7,65,67].

The dependence with the substrate compound should be analysed for each particular case because there are many factors involved such as the masses of the atoms, if the mass of the ion is similar to the

mass of the target atom, then the resulting momentum transfer is larger, if this process takes place near the surface more recoils will have enough energy to be sputtered. Furthermore, the fluctuation of the surface binding energy, (the minimum energy required to remove an atom from the surface of a solid) is the main responsible of effects such as: the bigger of sputtering yields of the pure metals with respect to their oxides compounds because they have lower binding energy; the preferential sputtering of light element like O and N from multicomponent solids, etc [1].

3.2.3 Angular and energy distributions of the sputter matter

The angular distribution of the sputtered particles depends on the composition of the target which can be a single crystal, polycrystalline or amorphous. The most accepted explanation for understanding the angular distributions and the total yield is Sigmund's theory [68], which predicts a cosine-like distribution for the sputtered atoms where random collision cascade theory applies (*intermediate mass and intermediate energy* (keV):

$$\frac{dY}{d\Omega} \sim \cos^{\nu_e} \theta_e \qquad 1 \leq \nu_e < 2, \tag{3. 2}$$

Where θ_e is the polar angle of the emitted particle. In this regime, equation (3.2) is independent of the incident angle θ_i. For glancing angles, an "over-cosine" distributions (ν_e>1) are often observed, a feature enhanced by increasing projectile energy. For energies higher than 100 keV, the angle of incidence can be increased up to 80° without changing the emission distribution [69], as a consequence of a random cascade.

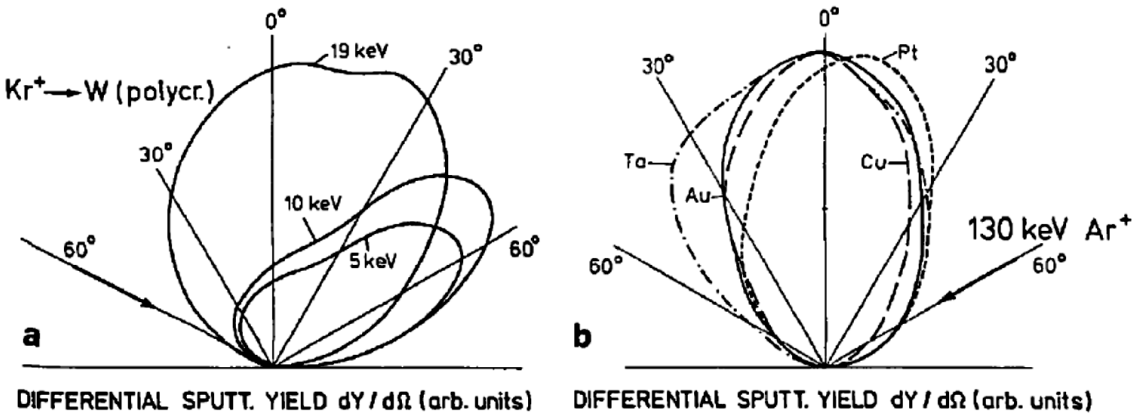

Figure 3. 4: Emission distributions from various polycrystalline targets at oblique projectile incidence. With increasing energy, ejection is determined more and more by random collision cascades, resulting in axially symmetric intensity distributions around the surface normal [69].

The memory of the primary ion momentum during the projectile-target is lost and therefore the ejection distribution is rotationally symmetric with respect to the surface normal, whatever the direction of the incoming particles. This phenomenon is observed in Figure 3. 4 where emission distribution of several polycrystalline targets at different angles of incidence and energies is plotted.

In the regime of *low-energy heavy ions* (≤ 1 keV) the emission distribution depends on the incident angle, and it deviates from the cosine law, giving higher emission at grazing angles. These are called under-cosine distributions, and are generally explained as a result of shallow cascades, where too few collisions are available to acquire momentum randomization.

The different compositions of the targets significantly influence on the angular distributions. Single crystals have a strongly anisotropic emission which is considerably enhanced along close-packed lattice directions. For polycrystalline materials, the emission distribution is a superposition of the emission distributions of the differently oriented crystallites, as well as in multicomponent materials the angular distribution can differ of each constituent [69–72].

The ions that leave the surface of the solid have some energy, which differs from one to another resulting in an energy distribution of the sputtered matter. The linear cascade theory predicts for the energy distribution the following expression:

$$\Phi(\mathrm{E}) = \Phi_{\mathrm{i}} \sec\theta_{\mathrm{i}}\, \mathrm{n}^{-2/3} \cos\phi \mathrm{L}\{\frac{\mathrm{E}}{(\mathrm{E}+\mathrm{E_b})^3}\} \qquad (3.\ 3)$$

Where Φ_i is the flux of ions, θ_i is angle of incidence, ϕ the angle between the emission direction and the surface normal, and L a constant that incorporates the cross-section for ion-target-atom collisions. The surface binding energy that atoms are bound to the surface is represented by E_b. The function $E/(E+E_b)^3$ has a peak at $E=\frac{1}{2}\mathrm{E_b}$, experimentally this value is around some eV, and at high energies it behaves like E^{-2} producing a high energy tail. This is what is called the "cascade spectrum" [21]. As an example of this Figure 3. 5 shows the energy spectra of the secondary ions and clusters obtained experimentally by Wittmaack [22], the peaks tends to get narrower for higher cluster sizes.

There is a significant difference between the energy spectra of atomic ions and cluster ions. This difference has been used to separate mass interferences problems caused by cluster ions in SIMS by the correctly choosing the appropriate energy range [73].

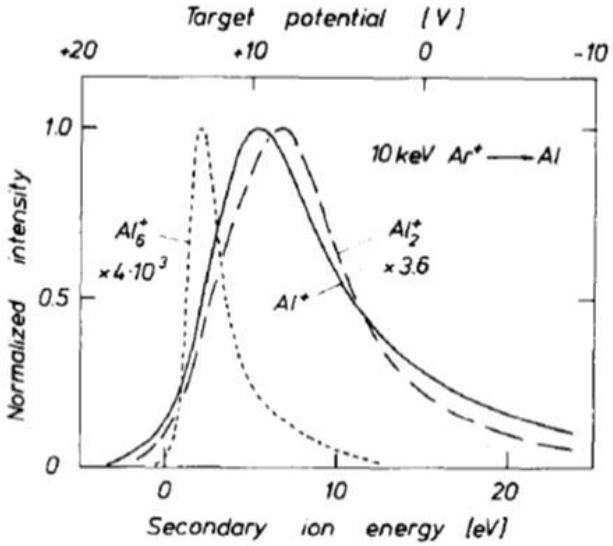

Figure 3. 5: Energy spectra of Al mono-atomic and cluster ions measured by Wittmaack [134].

3.2.4 Ionisation of the sputtered matter

SIMS only analyses the charged fraction of sputtered matter; therefore, the ionisation probability of sputtered material is a key factor. There are several models trying to explain the ionization of the sputtered atoms. During the sputtering process, the atoms that leave the surface have their electronic states perturbed because of the momentum transferred. Then, a fraction can be ionized and /or excited above their respective ground states and the valence electrons can be transferred to or from the surface during the process.

The *electron tunnelling model* can be applied for metallic and semiconductor samples. The fundamental principle is the possibility of transfer an electron as a consequence of the tunnelling effect between the atomic level of the sputtered atom and the valence band of the material.

Thus, for emmision of positive and negative ions, the ionization probability can be described as:

$$\begin{cases} \beta^+ = 1, & if\ \phi > I \\ \beta^+ = e^{-\left(\frac{I-\phi}{\epsilon_p}\right)}, & if\ \phi < I \end{cases} \qquad \begin{cases} \beta^- = 1, & if\ \phi < A \\ \beta^- \propto e^{-\left(\frac{\phi-A}{\epsilon_n}\right)}, & if\ \phi > A \end{cases} \tag{3. 4}$$

Where *I* is the ionization potential of the sputtered atom, *A* is the electron affinity of the sputtered atom, ϕ is the work function of the material, ϵ_p and ϵ_n are parameters depending on the local properties of the materials.

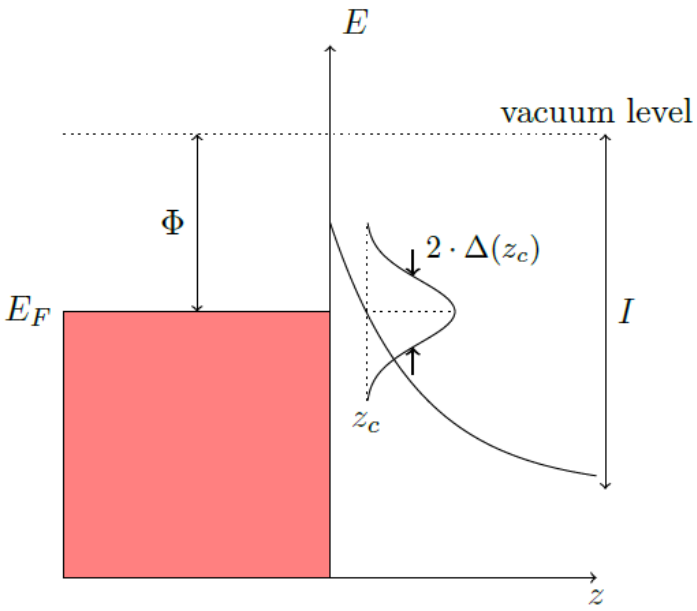

Figure 3. 6: Schematic of the energetic levels in the solid and the lowest free energy level of the sputtered atom (picture adapted from [67]).

The bond breaking model was developed by Slodzian [74,75] to explain the large secondary ion emission observed during the sputtering of ionic solids; and later, Williams [76,77] suggested that it could be appropriate for compounds like oxides, where the bonds have a partially ionic behaviour. All these concepts develop a consistent theory [78]. When an ion M^+ is sputtered, a cation vacancy X is created and can absorb the electron left, with an electron affinity A, for at least the sputtering time ($\cong 10^{-13}$ S), because during this period the electron does not necessarily occupy an equilibrium state in the solid.

Figure 3. 7 shows a potential diagram with the molecular system in a neutral covalent state M-A and the energy of the ionised system M^+-A^- as a function of separation of both components. The charge exchange can happen at the crossing point of the curves, at a distance R_c from the surface. The transition probability depends on the wave functions and shape of the curves at the crossing point, rather than the conditions of the equilibrium state. At infinite distance, the ionic curve lies above the covalent curve and the difference is equal to I-A, which means that at the crossing point the Coulomb force balances the energy in $(I\text{-}A)^{-1}$.

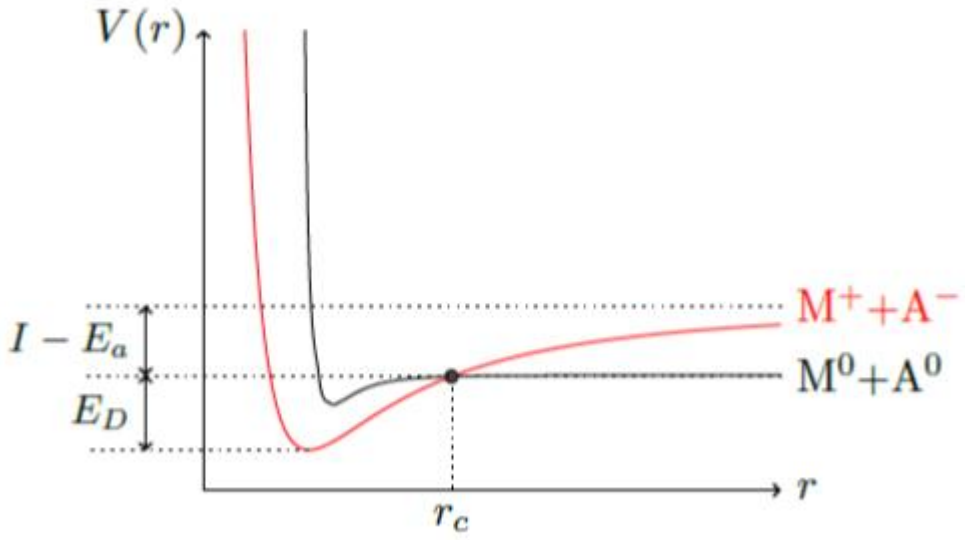

Figure 3. 7: Energy diagram showing the neutral covalent energy curve (black) and the ionic potential energy curve (red) in function of the inter-atomic distance r. *I* is the ionisation potential of the M species and E_a is the electron affinity of the species A. E_D is the energy for dissociate the molecule (Picture adapted from [67]).

3.2.5 The matrix effect and quantification in SIMS

From previous Section 3.2.4 it is clear that the ionization probability of the sputtered atoms depends strongly on the local electronic environment at the origin of the ejection. A different matrix implies a different secondary ion yield for a given species. Consequently, the secondary ion intensities do not represent the real local composition of the sample, but represents more the ionisation processes. This is called the "matrix effect" and affects the quantification in SIMS, the conversion of the secondary ion currents into concentrations of each species.

To calculate the concentration ρ_X is necessary to use the fundamental SIMS equation which calculates the number ($N_{(x)}$) of positive /negative ions detected of the type X:

$$N_{(X^{\pm})} = \left(\beta_{(X^{\pm})} T_{(X^{\pm})}\right) \rho_X(Az) \tag{3. 5}$$

Where $\beta_{(X^{\pm})}$ is the ionisation probability for this particular species (positive or negative), $T_{(X^{\pm})}$ is the transmission coefficient of the secondary ions. In a continuous sputtering, we measure the signal intensity, equivalent to the equation (3.4) but instantaneously ($\frac{dz}{dt} = \dot{z}$):

$$I_X = N_{(\dot{X^{\pm}})} = \left(\beta_{(X^{\pm})} T_{(X^{\pm})}\right) \rho_X(A\,\dot{z}) \tag{3. 6}$$

The concentration could be written then:

$$\rho_X = \frac{I_X}{\left(\beta_{(X^{\pm})} T_{(X^{\pm})}\right)(A\,\dot{z})} \tag{3. 7}$$

Since is very complicated to measure $\beta_{(X^{\pm})}$ and $T_{(X^{\pm})}$ independently, but their product *UY*, called "useful ion yield", is possible to measure using standards. The useful ion yield is defined as the ratio of the number of secondary ions detected to the number of atoms type *X* sputtered.

$$UY = \frac{N_{detected}}{N_{sputtered}} = \beta^{\pm} T \tag{3. 8}$$

If the beam parameters such as beam energy, angle of incidence, the current, are kept constant, the ionisation probability of the element depends only of the matrix. The transmission also varies from one species to another, but it is a minor effect. Thus, for quantification with the *UY* and $\dot{z}$, should be enough for converting the intensity in concentration. A drawback of this technique is that for simple quantification several standards are needed. For example, to analyse three dopants in a silicon-germanium multi-layer with five different layers, 15 standards are required.

Another common technique for quantifying is the relative sensitive factor (RSF)-method [1], is used specially in trace analysis. In this approach, the concentration of a certain element *X* is calculated from the ratio of I_X and the intensity of the matrix signal I_M. In this case is also necessary to use a standard sample to calculate the concentration, and both samples must be analysed in identical experimental conditions. The concentration can be calculated as follows:

$$\rho_X = \frac{I_X}{I_M} RSF_X \tag{3. 9}$$

The coefficient RSF_X is determined with the measurement of both samples. The advantage of this method is that variations in the primary current do not impact on the calculation of the concentration, but could be applied only to dilute dopants, which do not change their ionisation probability because of the implanted ion.

Another important approach is known as the MCs_x technique. Clusters ions of the form MCs^+ where M represents the element of interest, were observed by Ray [79] and Gao [80] after the bombardment of Cs+ as primary beam, and later with caesium flooding [81]. The detection of this clusters is a consequence of the reduction of the sample's electron work function [82]. A drawback of this methodology is that the useful yields for MCs+ are usually around 10^{-6} - 10^{-4} [83], rather below the normal useful yields SIMS, which reduced the achievable detection limit. There are other techniques, less frequently used such as Matrix Isotope Species Ratio, "MISR", convenient to use only on

homogeneous samples; the Infinity Velocity "IVM", where standards are not required, but has high error range and is not suitable for insulators [84].

3.2.6 Primary ions and reactive gas flooding

It has been shown the enhancement of positive secondary ion yields due to the oxygen flooding and that negative ion yields could be improved several orders of magnitude if alkali metals like Cs are deposited on the surface of the analysed area [85]. As mentioned above, is possible to enhance the positive (negative) secondary ion yield by rising (lowering) the work function Φ. This is achieved by bombarding the sample with reactive species and/or simultaneous flooding respectively oxygen and caesium.

Currently, the oxygen flooding is routinely used [86] and depending on the element and matrix, the useful yield can be increased by up to several orders of magnitude. The increase of the useful yield leads in an improvement of the sensitivity of the SIMS technique. Caesium flooding was first implemented in 1977 by Bernheim et al. [87], more recently improved by Wirtz et al. [88], becoming a tool used more and more frequently in SIMS. In the case of the liquid metal sources like Ga^+, is very important, because can improve the poor ionization yields (increment of the useful yield up to four orders of magnitude), and therefore is possible to benefit from the small probes sizes produced by the Gallium and obtain images with high lateral resolution and high sensitivity.

3.3 General SIMS instruments

SIMS instruments are generally composed of four main parts:

- The ion sources: for producing the primary ions
- The primary column/optics: focus the primary beam on the sample
- The mass filter system/secondary ion column
- The detection system: for detecting the filtered secondary ions and translating in the information desired (mass spectra, image)

The spectrometer's design depends on the type of mass filter used in the secondary column. The filter region is in charge of separating the secondary ions according to their mass to charge ratio *m/q*. The instruments most commercialized in SIMS are based on the following mass filters:

1. The Quadrupole mass filter
2. The time of Flight mass filter
3. The magnetic Sector mass filter

Each filter has significant different in capabilities, thus the selection of the mass filter defines the performance of the instrument, which in turn defines the area of application of the instrument. The main characteristics of a spectrometer are the mass resolution, the transmission (sensitivity), the mass range and the detection mode.

Depending on the application in SIMS the instruments can be divided in two categories: the Dynamic SIMS and the Static SIMS (presented in Section 3.2.1). In the first group, we can find the Quadrupoles and the Magnetic Sector mass filters, and in the second the Time of Flight filters. There are others mass filters such as Ion Trap, Ion Cyclotron Resonance Mass Filter, but they are mostly used in Mass Spectrometry rather than SIMS.

An essential description of the physical principle of the three main mass filters will be described in the following Sections.

3.3.1 Quadrupoles

The Quadrupoles mass filter were extensively used in SIMS from the mid-1970s through the late 1990s, they were heavily used because they have small size, great experimental flexibility (reduced extraction fields and the possibility to vary the sample angle), less expensive for purchase and maintenance than the other type of mass filters. However, they have very low mass resolution, comparatively poor detection limits, as technology demands more often high-performance analysis they have lost popularity.

A schematic of a Quadrupole is shown in Figure 3. 8. Essentially, consist of four electrically conducting electrodes of radius *r* whose axes lie parallel to the ions initial trajectory and are equal distance from each other. Two opposite rods have an applied potential of $(U + V\cos(\omega t))$ and the other two rods have a potential of $-(U + V\cos(\omega t))$; where *U* is a DC voltage, and $V\cos(\omega t)$ is an AC voltage with angular frequency ω. The AC signal generates a varying field that will only allow of specific m/q ratio pass through. After the filtration, the ions are directed into a channel electron multiplier for their detection. By adjusting the AC and the DC the secondary ions can be scanned and detected sequentially from 1 to 500 *m/q*.

The spectrometer has two modes of operation. Constant mass resolution or constant transmission; the first one, is typically applied in SIMS, but as the mass increases the transmission decreases; the second, has also a similar effect, the mass resolution varies with mass.

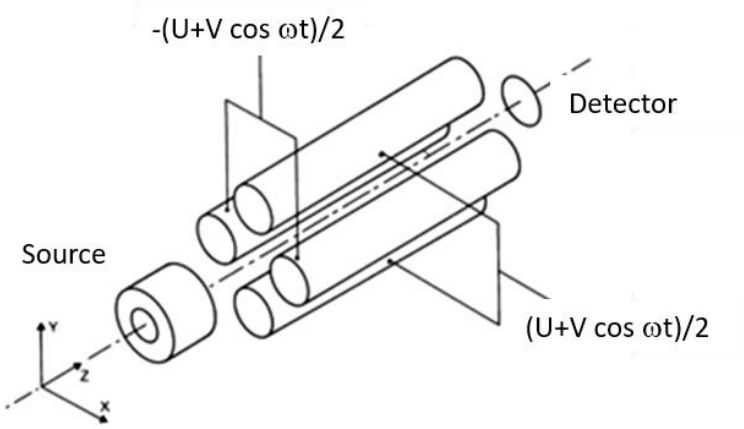

Figure 3. 8: Schematic of a Quadrupole spectrometer (taken from [135]).

3.3.2 Time of flight

Time of Flight (TOF) spectrometers were introduced shortly after the Quadrupoles and Magnetic Sectors, but their development and applications in SIMS have grown rapidly. They are most effective in Static SIMS and shallow Dynamic SIMS. Particularly in life sciences [89]. The main advantage of these spectrometers is the simultaneous detection of all secondary ions within *m/q* range. High mass range and high mass resolution are achievable with minimal loss in sensitivity. However, if it is operated in Dynamic mode the analysis time is increased and the sensitivity is reduced. Furthermore, each analysis produced large amount of data and, the mass resolution depends on the surface quality.

The Time of Flight separates the different *m/q* according to their velocity. The secondary ions are extracted with a potential V_0 and after, they pass through a drift tube, during the "flight time". Thus, the kinetic energy of the ions is:

$$E_{kin} = \frac{1}{2}mv^2 = qV_0 \tag{3. 10}$$

Where *m* is the mass, *v* the velocity and *q* the charge of the ion. Thus, for a distance *d* in a field free region, the ion mass to charge ratio can be determined as a function of the flight time *t*:

$$\frac{m}{q} = \frac{2V_0t^2}{d^2} \tag{3. 11}$$

There should be some interval of time to measure the flight time of the secondary ions. This can be achieved by two manners: by pulsing the primary ion beam or by pulsing the secondary ion beam. Most commercially available SIMS instrument pulse the primary beam in a range of frequencies from 10 to 50 kHz. To produce a pulsed beam, the primary beam is deflected across a small aperture in the primary column (Figure 3. 9). A pulse width is around 1 ns [90], and the interval time durations goes from tens

to hundred microseconds, which leads to a poor duty cycle. The secondary optics has a length of 1 to 2 m, with time-sensitive detection electronics for measuring the flight time the secondary ions. This beam is called the *analysis beam*. Under optimal conditions pulse widths of less than 1 ns are routinely achievable. The mass resolution is mostly limited by kinetic energy distribution of the secondary ions that normally ranges from a few eV with a high energy tail. The Reflectron TOF, improves the mass resolution by adding an ion mirror in the flight path of the secondary ions. Therefore, the total flight is increased without the need of longer flight tube and, a correctly tuned ion mirror, corrects the flight differences arising from small energy differences, coming from the energy distribution of the sputtered atoms. Consequently, the faster ions will spend slightly more time than the slower ones, and finally all arrive at the same time. TOFs that include this concept can obtain values of mass resolution higher than 10,000 [91].

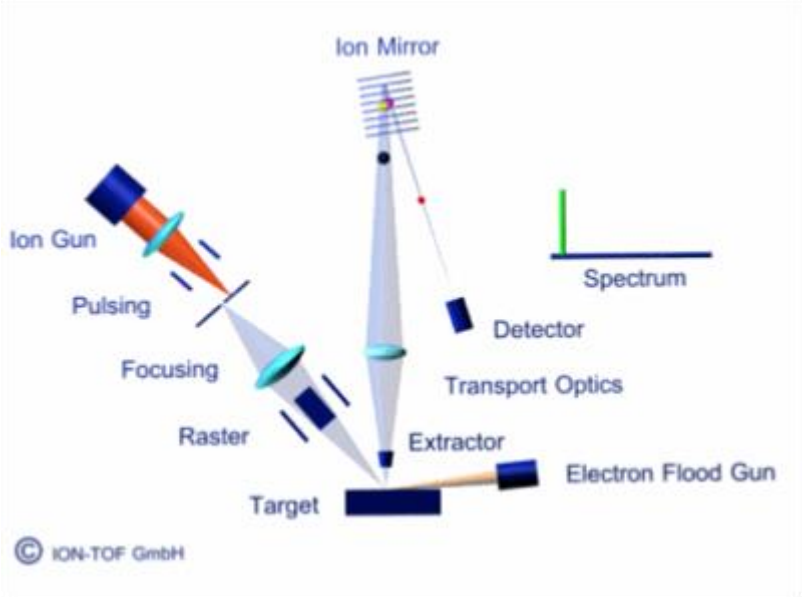

Figure 3. 9: Schematic of the ToF 5 pulsed ion beam system (picture from IonTof).

Another possibility to compensate the energy spread of the secondary ions is the use of several electrostatic analyser (ESA). The TRIFT spectrometer was designed as a stigmatic TOF ion microscope, it consists of two electrostatic lenses and a system of three hemispherical ESAs (Figure 3. 10).

When depth information is desired (similar to D-SIMS), it is necessary to implement a second primary beam to etch some volume of the sample's surface between beam cycles. The latter beam is called the *sputter beam* and O_2^+ or Cs^+ beams are most commonly used for this purpose. The drawback is that the sputtered matter cannot be recorded (only ions generated by the primary beam) and then, the detection limit cannot match the standard D-SIMS (down to 1 part per million (ppm)).

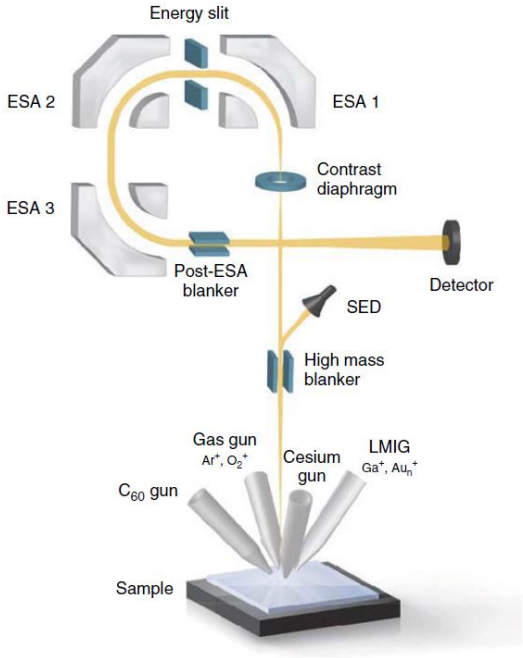

Figure 3. 10: Schematic of the Triple Focusing Time-of-Flight. TRIFT style Time-of-Flight SIMS instrument developed by Physical Electronics. It provides HMR Dynamic and Static SIMS for elemental and/or molecular distributions. (Picture adapted from [1])

The ions detectors used in TOF-SIMS are insensitive to more than one impact at a time, the time between two events can be recorded is around several tens of ns, and is called the dead time, this means that if two ions arrive within an interval shorter than the dead time, only one can be registered. This is a drawback at high signal intensity because the detection system will underestimate the real number of arrival ions.

3.3.3 Double focusing magnetic sector instruments

Magnetic Sectors mass filters are used when optimal detection limits, sensitivity and dynamic range are required in D-SIMS analysis. Detection limits less than 1 ppb are possible by depth profiling. The weaknesses of these spectrometers are: a relatively limited mass range (in SIMS); the detection limit is degraded when it is operated in high mass resolution; the relatively slow rate under which magnetic fields can be switched; the large size of the instruments.

The most common instruments use a single detector, so the detection of different masses is sequential, and is achieved by switching the magnetic field. Some designs like the NanoSIMS, IMS - 1280 and SHRIMP have multiple detectors, thus multiple masses can be acquired in parallel.

As seen in Section 2.6, the physical principle on the Magnetic Sector is based on the fact that an ion passing through a magnetic field *B* applied perpendicularly to its trajectory will experience a

deflection due to the Lorentz force, obtaining a relation between the radius the magnetic field B, the kinetic energy of the particle and the mass to charge ratio, expressed in the equation (2.27):

$$\mathrm{Br} = \sqrt{2\mathrm{E}\frac{\mathrm{m}}{\mathrm{q}}} \tag{2.27}$$

From equation, it can be concluded that: when the radius is fixed, B has to be changed sequentially, and only one combination of *m/q* may be observed, like scanning instruments, it is clear then, the magnetic field *B* is a function of *m/q*. On the other hand, when *B* is fixed, r varies for each combination of *m/q*, so the distinct particles will be focused in different places, this is the case of dispersive instruments [3,67].

As explained before, the sputtered ions have a considerable energy spread which is translated in a larger energy dispersion that deteriorates the mass resolution of the instrument (eq. 2.33). With the addition of an electrostatic sector with equal dispersion is possible to compensate the energy dispersion of the magnet, while the mass dispersion remains the same. These devices are focusing in angle but also in energy and this is the reason why they are called double focusing mass spectrometers. Figure 3. 11 shows an electrostatic sector and a magnetic sector with two beams with difference in energy of ΔV. If the magnetic sector is flipped and the energy dispersion is matched properly the double focusing condition is obtained as configurations shown in Figure 3. 12.

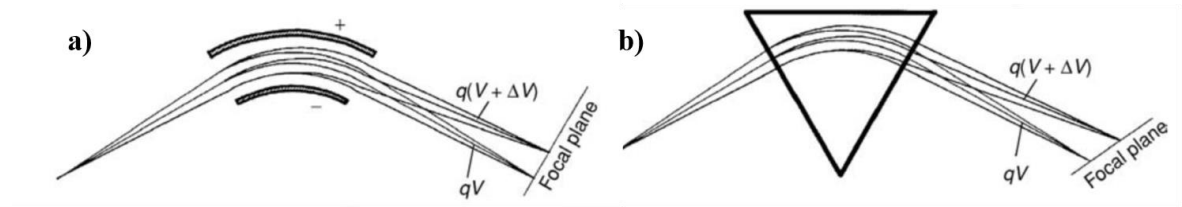

Figure 3. 11: a) Schematic of energy dispersion in an electric sector for two beams with a energy difference of ΔV, b) energy dispersion in a magnetic sector for two beams with the same energy difference. If the magnetic sector is flipped and the energy dispersion of both sectors is well matched between them, the double focusing condition is satisfied. (picture adapted from [136]).

From the beginning of the mass spectrometry several designs were implemented. Figure 3. 12, shows the most frequently used geometries of double-focusing mass spectrometers in SIMS. The Mattauch –Herzog is a configuration without a focal point between the magnetic and the electrostatic sector, the beam is almost parallel, the distance between the sectors can be short and the double focusing condition is independent of the relation magnetic/electrostatic sector radius. Detection of all masses can be done with a focal plane detector placed in the focal line [92], this means is a dispersive type. A

modified configuration is used nowadays in the Cameca NanoSIMS 50 which can detect up to 7 masses in parallel.

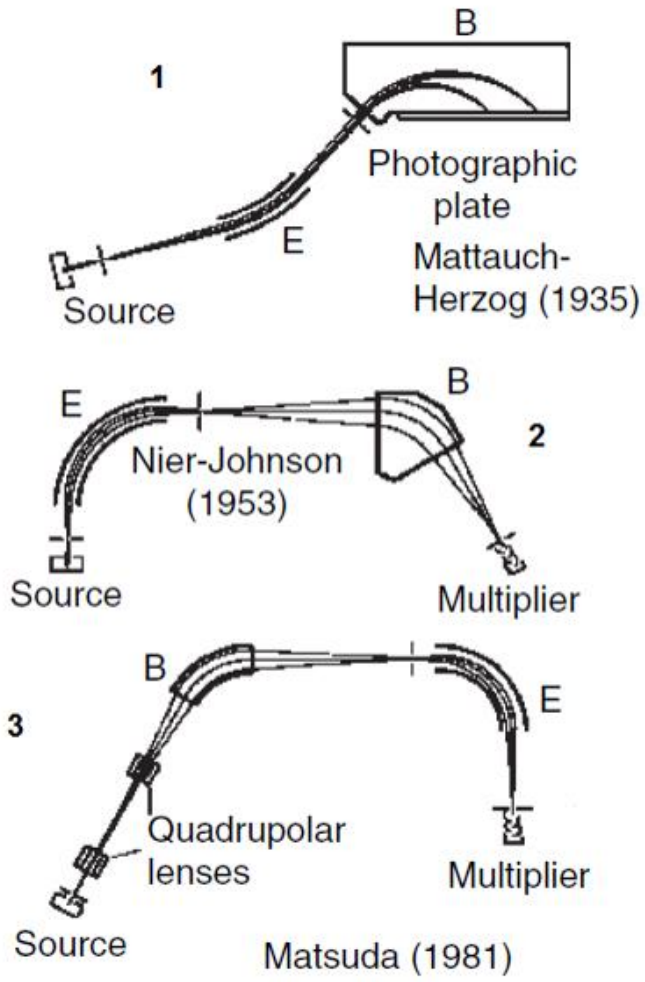

Figure 3. 12: Schematic of the three geometries most used in commercial SIMS instruments. (Picture adapted from [136]). 1) Mattauch-Herzog configuration is a dispersive type, several masses can be acquired in parallel with plane detector; 2) Nier-Johnson configuration, is a scanning type spectrometer, was the first design high-precision; 3) Matsuda design is the highest mass resolution design, used for the SHRIMP II.

The Nier–Johnson spectrometer was designed to remove the second-order angular aberrations, and therefore improve the quality of the resolution of the spectrometer. It has a focal point between sectors. Usually is used as a focal-point mass spectrometer, but over a limited mass range the angle and the energy focal lines match and can acquire several masses in parallel [93]. All the Cameca IMS XF series are based on this design.

The Matsuda design eliminates all second-order aberrations and introduced the effect of the fringing fields. A quadrupole was included between the sectors to improve the focusing perpendicular to the dispersion plane. The design of Matsuda presented the highest resolution, with resolving power up to 100,000 [94]. It is used in the commercial instruments SHRIMP II.

In chapter 4 and 5 the research is based on the first two configurations.

A summary of the main characteristics of the mass filters described above is in the following Table 3. 1:

Mass Filter	***m/q* Range**	**Transmission**	***m/Δm***	**Detection**	**Area of use**
Quadrupole	~1-300	<1%	1	Sequential	Dyn. and Static
TOF	~1-10,000	<100%	18,000	Quasi-parallel	Dyn. and Static
Magnetic Sector	~1-500	<50%	100,000	Sequential*	Dynamic

Table 3. 1: Summary of main characteristics of the three principal types of mass filters.
* Except for the Cameca NanoSIMS, IMS-1280 and SHRIMP.

3.4 Instruments used in this work

In this work charged particle simulations and experimental work were carried out on the IMS 4F and on the IMS 6F Cameca instruments. The IMS XF Cameca instruments are double-focusing mass spectrometers that combines the features of imaging ion microscope and ion microprobe.

In the microscope mode, a broad beam illuminates homogeneously the sample, and the stigmatic secondary optics projects a magnified mass filtered image onto a position sensitive detector. The immersion lens works as an *objective immersion lens* magnifying an ion image focus by the transfer lenses. The lateral resolution is controlled essentially by a contrast aperture placed in the crossover of the beam, after the transfer lenses, to limit the aperture angle of the beam and reduces the chromatic and geometrical aberrations [95]. The lateral resolution depends also on the quality of the secondary optics, and in principle, with higher magnifications, better spatial resolution (unless the contrast of the image is of poor quality.). On Cameca IMS instruments, lateral resolutions of less than 1 μm can be obtained [96–98]. This mode is also much faster because the image is acquired simultaneously; instead of scanning pixel by pixel (i.e. an image of 512 x 512 pixels, with the same transmission and the same current density, will take 2.6 x 10^5 times longer). Figure 3. 13 shows a schematic of both modes of operation.

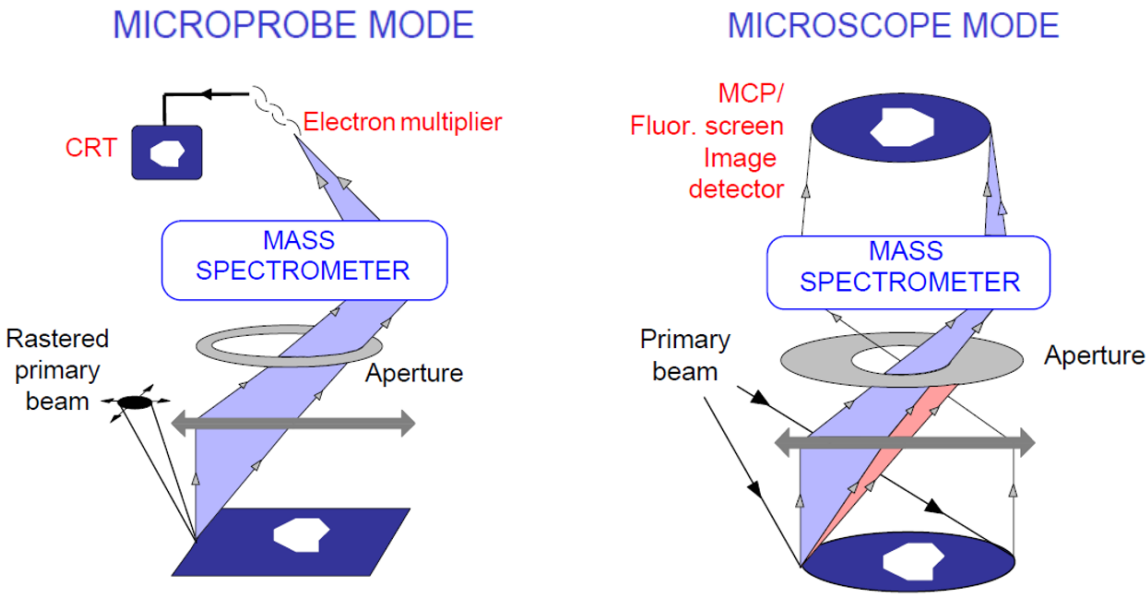

Figure 3. 13: Principle of operation of both modes of secondary ion mass spectrometers. In the microprobe mode, the beam is rastered and the ions collected in a counting system, the spatial resolution depends on the size of the probe. In microscope mode, a broad beam illuminates the sample area and make a direct image on the MCP-FS, the spatial resolution is controlled contrast aperture and the quality of the secondary optics. (Picture adapted from [137]).

In microprobe mode, the ion beam is scanned over the sample surface pixel by pixel. In this case, the immersion lens is used just to collect the secondary ions, so there are no conditions on the size of contrast aperture, consequently the lateral resolution depends on the size of the probe. In other words, the quality of the optics of the primary column. In consequence, the largest contrast aperture can be used and the transmission can be maximized. In general, the area of analysis can be divided in 128 x 128, 256 x 256 or 512 x 512 pixels, this means bigger pixel size for less number of pixels. In each case, is important to ensure that the complete area will be covered, so size of the probe should be equal to the size of the pixel. Therefore, an area of 100 μm^2 divided in 512 x 512 pixels will have pixel size of approximately 200 nm, while for same area divided in 128 x 128 pixels, the pixel size is 800 nm, this suggests that the lateral resolution in the first case should be better (~200 nm). Depending on the type of spectrometer, the ion images could be generated for one mass at a time (i.e. quadrupoles), and the masses of interest are mapped sequentially, or some masses may be mapped simultaneously (i.e. NanoSIMS 50), or in the case of the Ion-TOF time-of-flight all masses are collected in parallel.

Chapter 4 is dedicated to investigating the enhancement of the mass resolution by simulation using the secondary optics of the Cameca IMS 4F, using the microprobe capability. In chapter 5, both capabilities are exploited at the same time in order to develop the multi-ion-beam concept.

Figure 3. 14 shows a schematic of the IMS XF Cameca instrument. Positive or negative ions are generated in the duoplasmatron source and Cs+ is produced by a caesium source; both sources are mounted on two separate ports, followed by a magnet which depending on the magnetic field and polarity applied directs the beam of the selected source to the primary optics. The beam is focused on the sample and an extraction system coupled with the transfer lenses makes an image of the crossover at the entrance slit of the mass spectrometer, which is achromatic with the conjugated planes of the entrance and exit slit. Finally, the ions can be deflected to either a Faraday cup or an electron multiplier (microprobe mode) or to a microchannel plate coupled with phosphor screen followed by binoculars or a camera from outside from the vacuum (microscope mode). The main components of the instrument and their function are described below.

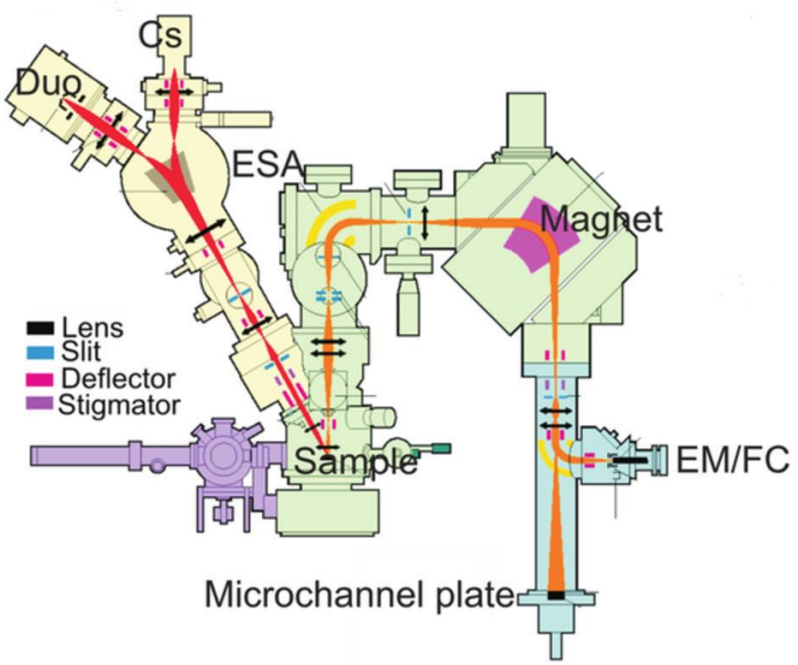

Figure 3. 14: schematic of the IMS XF Cameca instruments, including ions sources, primary optics and secondary optics and detection system. Taken from [137]

3.4.1 The ion Sources

The IMS XF has two sources connected in the primary optics: a duoplasmatron and caesium source.

3.4.1.1 The Duoplasmatron source

The duoplasmatron sources are called Plasma sources or DC Glow Discharge. They produce high current of inert gases; the most frequently used are Oxygen and Argon. Basically, there is a region where the noble gas is introduced, and electrostatic and magnetic fields are applied. The plasma is

produced by an arc maintained between the hollow cathode and anode which is kept at several hundred volts relative to the cathode (Figure 3. 15). The beam could be accelerated up to 17.5 kV, with currents up to 10 µA. The source crossover is 500 µm fixed at the exit of the source and its image at the sample varies from 0.2 to 200 µm; this means that the total reduction of the system (source primary optics) goes from 0.4 to 2500. The spot size of the beam is limited by the chromatic aberration as a consequence of the energy spread that ranges between 5 to 15 eV.

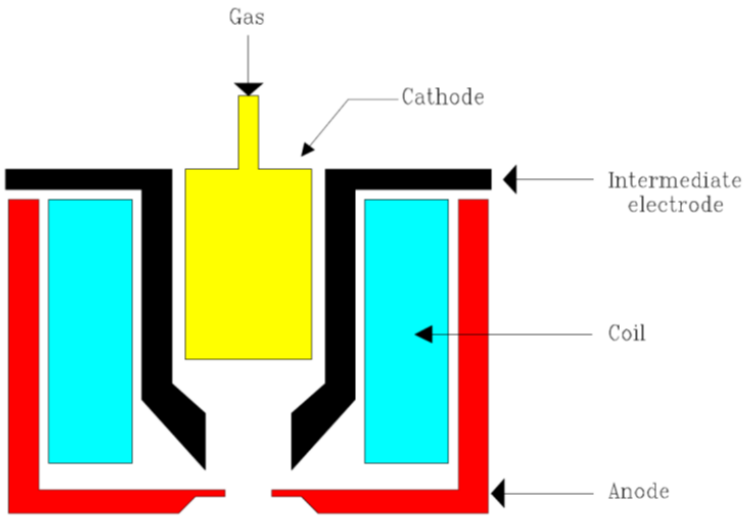

Figure 3. 15: Simplified schematic of a typical Duoplasmatron source [99]. Main parts of the source are marked: gas inlet, intermediate electrode, cathode, anode and coil.

3.4.1.2 The caesium source

The surface thermo-ionization sources are heavily used in Dynamic SIMS for producing high current density alkali ion beams, particularly Cs^+.

The caesium is contained inside a porous frit, called the *reservoir*. When this *reservoir* is heated to ~400° C, the Caesium evaporates and gets in contact with the *ionizer*, a tungsten plate at ~1100°C, producing Cs+ ions. The ions are extracted owing to the potential field applied between the *ionizer* and the *extraction electrode*. A simple design is illustrated in Figure 3. 16.

The crossover of the source has a diameter of 50 µm, but a difference of duoplasmatron source is not mechanically fixed at the exit of the source; but the is the image generate by lens 1 (L1) and acts as a source point for the magnet. Thus, its position is controlled by the voltage applied on L1 and it serves to optimize the density of the beam for different spots sizes. The maximum acceleration voltage in the IMS 6F is 12 kV,

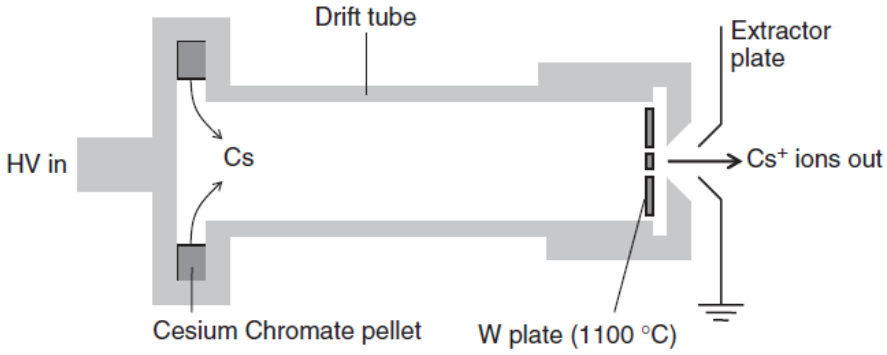

Figure 3. 16: Simplified schematic of a typical Surface Ionization source [1].

3.4.2 The primary optics

As explained above, both sources are mounted in separated ports and a primary electromagnet filters the appropriate mass depending on the field strength and the polarity (Figure 3. 17). After, three Einzel lenses are distributed along the column, L2, L3 and L4, also called the focusing lens. Each lens is also coupled with a deflector which are in charge to centre the primary beam on the optical axis. Before the middle lens (L3) there is the mass selection aperture which filters undesirable impurities of the beam and after L3 there is the diaphragm's holder which limits the opening angle of the primary beam by selecting apertures of different diameter. Following, there is an eight plate stigmator, which is used to shape the beam and, the double deflector D4, also known as beam deflector, adjust the primary beam position on the sample surface in order to raster the beam on the sample or, to deflect the beam to the Faraday cup to measure the primary current. The optics finishes with L4 focusing the beam on the sample [99].

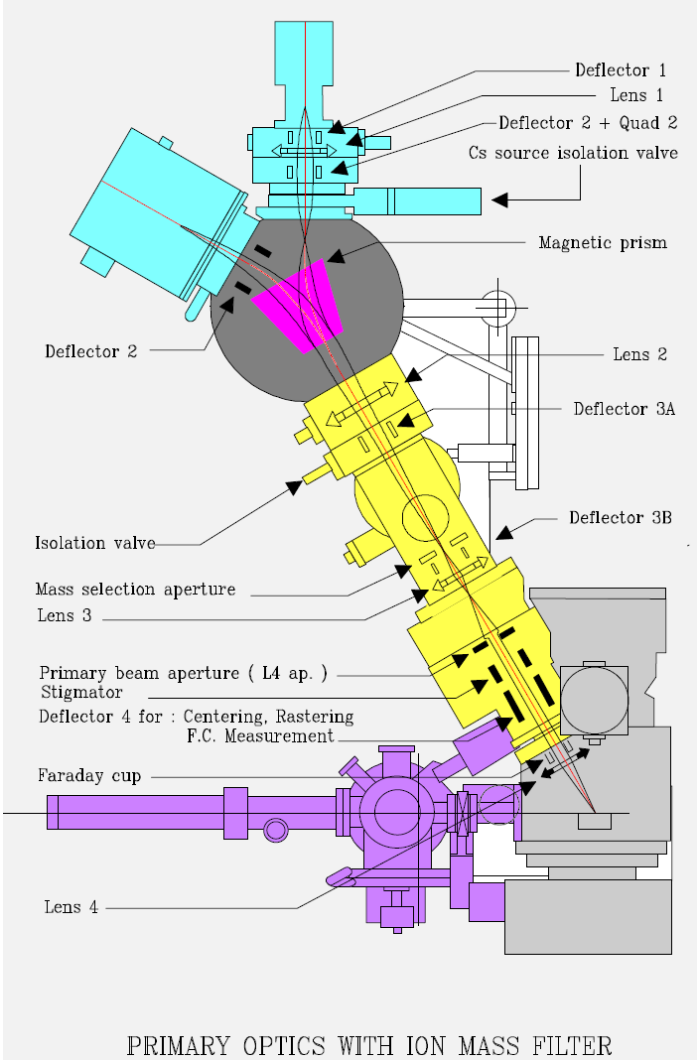

Figure 3. 17: Schematic of the primary optics of the IMS 6F Cameca instrument. The sources are drawn in blue, followed by a magnetic prism and the tree lenses L2, L3 and L4. Deflectors, stigmator and Faraday cup are also included in the yellow column. (Picture adapted from [99]).

3.4.3 The secondary optics

The sample holder can be energised at ±4.5 kV or ±10 kV, depending on the model and the application. The sputtered ions are accelerated to the immersion lens which forms a virtual image of magnification 3/4 of the sample [71]. The image acts as object for the Einzel lens of the transfer lenses system (placed behind the immersion lens) which generates a magnified real image. At the same time, a diaphragm limits the transverse energy bandwidth and the maximum ion emission angle, controlling the resolution of the image (spherical aberrations). The transfer lenses are composed of three Einzel lenses that are energised one at each time, depending of the field of view (FOV) selected. There are three possible pre-set FOV options: the small one (25-35 μm) where the last lens, LT3 is

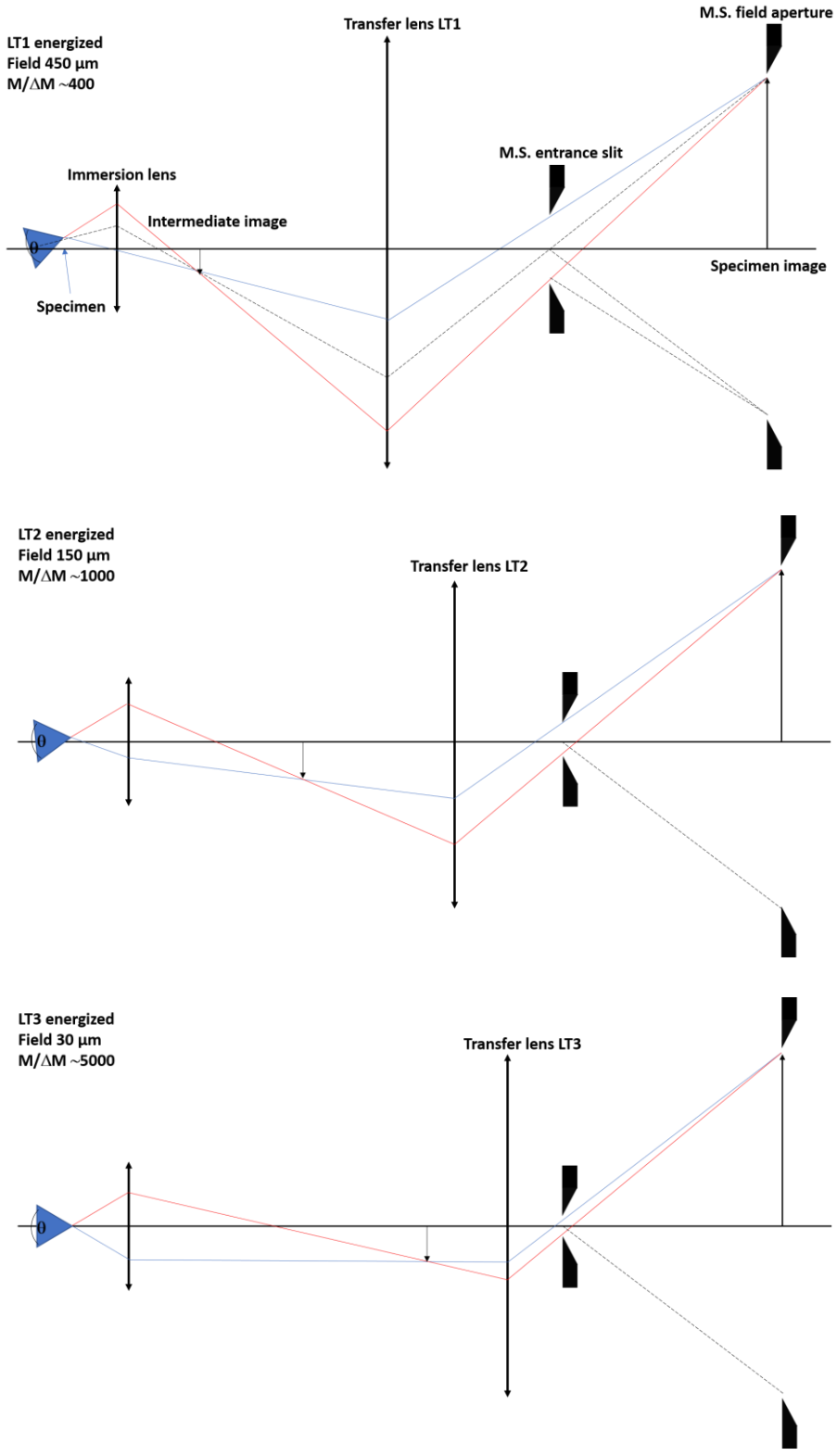

Figure 3. 18: Schematic of the transfer optics when each lens is energised. L1 corresponds to a large FOV, L2 corresponds to an intermediate FOV, most used in microscope mode and L3 is used for small FOV. The FOV is decreased at constant final image size (increasing lateral magnification), constant ion collection angle from the target and increasing mass resolution. Picture adapted from [138].

energised (Figure 3. 18). As the final image is constant in the three cases, the FOV is reduced to approximately 30 μm. In this mode of operation, the angular magnification is very high and the short focal length of the lens forms a crossover diameter very small, allowing the reduction of the slit width to obtain high mass resolution. On the other hand, when the maximum FOV is required (250 μm or more), the first lens LT1 is energised, so the angular magnification is low and the large focal length forms a big crossover diameter, therefore it is necessary to use the entrance slit wide open to let in to the spectrometer the majority of the ions. Consequently, in this mode the mass resolution is limited. The middle FOV of 150 μm is the most used in microscope mode and here the middle lens is energised. The field aperture placed at the mass spectrometer plane control the angular aperture of the ions and the FOV of the instrument [71,99–101].

These instruments also have the capability for the scanning ion probes of dynamic transfer/matching, the secondary beam is deflected when enters the transfer system, thus the virtual image seems to come from central position of the optical axis. Therefore, the field of view could be increased, theoretically, without loss in transmission or mass resolution. To reconstruct the image is necessary to know the location on the sample surface.

The spectrometer consists of two prisms: a 90° stigmatic spherical electrostatic sector (86 mm radius) and a 90° uniform magnetic field sector (127 mm radius) coupled by an electrostatic lens that ensures the system is globally achromatic with respect to energy dispersion. The image inside the spectrometer is transported as follows: the electrostatic sector forms a second magnified virtual image that is transferred by the spectrometer lens to a third virtual image inside the magnet. The spectrometer lens is positioned just behind the energy slit at the intermediate crossover between electrostatic sector and the magnetic sector. Finally, the crossover (image of the entrance slit) is formed at the exit slit while the mass filtered image of the surface is projected to MCP followed by a phosphor screen. Finally, the image can be seen by a camera outside the vacuum chamber or by binoculars.

In microprobe mode, the secondary ion beam is deflected through the Faraday cup (FC) or to the electron multiplier (EM). It is also possible to see an image of the exit slit on micro-channel plate, in this way , the limited portion of the mass spectra that is projected on the slit is visible. [100].

3.4.4 The detection system

3.4.4.1 The detection system in microscope mode

When the instrument is operating microscope mode, a direct image is projected on a micro-channel plate. The MCP is a position sensitive detector which is used to make direct ion images. The ions that impact the MCP are converted to electrons that later are converted into photons by the phosphor screen

(PS). The MCP is an assembly of small channels of approximately *10 μm* diameter where each channel is a small hollow glass tube with the inner conductive surface covered by SiO_2. When a secondary ion hits the semiconductor surface, secondary electrons are generated; these electrons are accelerated and multiplied by collision cascades inside the channel (Figure 3. 19). The *useful area*, is the ratio between the open area and the total area, is an important parameter in the micro-channel plate because is related with the number of ions that can be detected. The MCPs installed in the IMS series have a *useful area* more than *50%*.

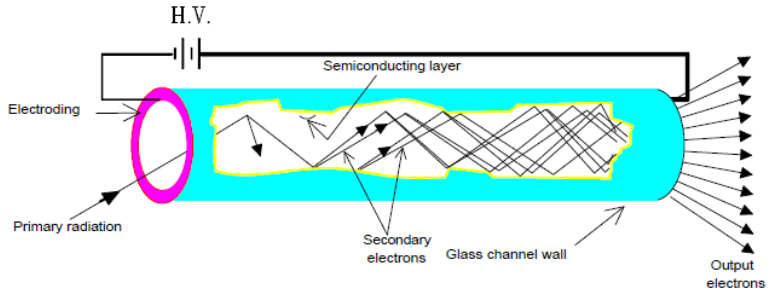

Figure 3. 19: Schematic of the electronic cascade inside one channel. (Picture adapted from [119]).

The Figure 3. 20 shows a schematic of the system MCP-PS. Generally, the gain can be adjusted according to the voltage applied to the MCP, so the number of secondary electrons could be adjustable from 10^2 to 10^4. The phosphor screen is also energised with a variable potential to maintain the acceleration region between the micro-channel plate and the phosphor screen constant at 5kV. The minimum secondary current necessary to product an image is around 10^4 c/s.

Another important parameter to consider in imaging SIMS is the lateral resolution. The lateral resolution of the MCP/PS is limited by the diameter of the micro channels and the blooming effect generated for each electron beam in the acceleration space between the exit of the face of the micro-channel plate and the fluorescent screen (pink colour, Figure 3. 20). For channels of 10 μm diameter, the blooming effect is calculated to be between 70 to 100 μm. The magnification of the analysed area on the MCP, is made by the projector lenses, that usually have six pre-set positions, for the higher magnification, the higher the lateral resolution (only true if the magnified image has sharp focus with adequate tonal contrast).

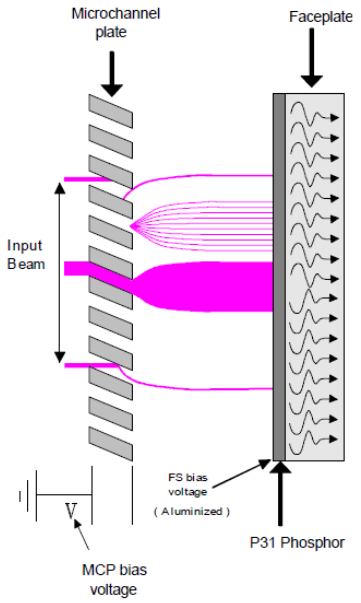

Figure 3. 20: Schematic of the complete system MCP-FS mounted on Cameca IMS XF instruments. The blooming effect is represented in pink. (Picture adapted from [119]).

Another possibility is to combine the MCP with a resistive anode encoder (RAE). The RAE generates a pulse of each event and determines the spatial position of the gravity center of the charged deposited by the electron flux and distributes to the four corners. Finally, a ion map can be done on a CRT. The advantage is that eliminates the dependence of the mass of the MCP, but the dead time is around 3 μs and limits the dynamic range.

3.4.4.2 The detection system in microprobe mode

When the microprobe mode is selected, the secondary current is deflected by an electrostatic analyser to the two types of detectors for the counting mode depending on the secondary current intensity. The combination of both the EM and FC, which count rates in the range 1 to 10^6, and 5 x 10^5 to 5 x 10^9, respectively, provides high dynamic range for the secondary intensity measurements.

The FC consists of a metallic cup into which the secondary ions are directed. When the ions impact on the interior base of the cup their charge is deposited (see Figure 3. 21). As the FC is isolated, the deposited charged can be converted from a current to a voltage with the aim of a high impedance amplifier. After, the voltage is converted in voltage/frequency, and the signal is given in counts per second (cps). A repeller is placed in front of the FC to prevent secondary electrons generated inside the cup to escape

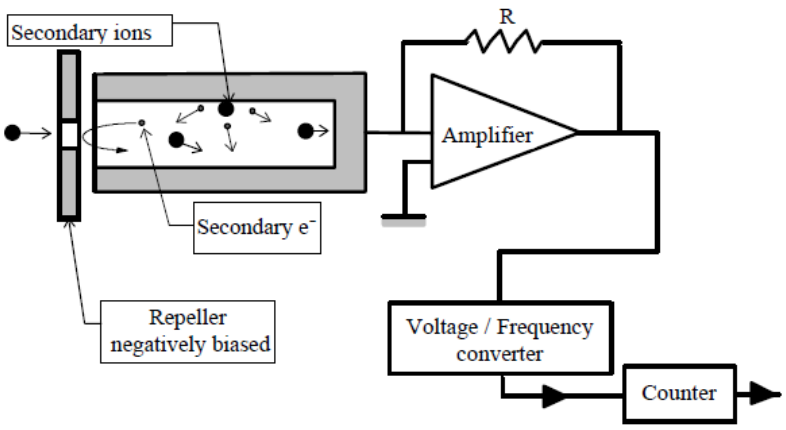

Figure 3. 21: Schematic of the Faraday Cup installed in the IMS Cameca. (picture adapted from [119]).

In the EM, the ions from the analyser are post-accelerated to a high velocity in order to improve the detection efficiency. The first electrode, called the conversion dynode is at high potential and opposite the charge on the detected ions. When an ion strikes the conversion dynode induces a secondary electron emission, that hits the different dynodes that are held at lower potential, generating a cascade effect and consequently an electric current, (Figure 3. 22). The electron multipliers can be discrete dynode or continuous dynode. In the IMS the electron multiplier is made of Cu/Be with 21 dynodes. Two parameters to take into account are the dead time and the detection efficiency (the ratio between the number of pulses counted and the ions reaching the first dynode).

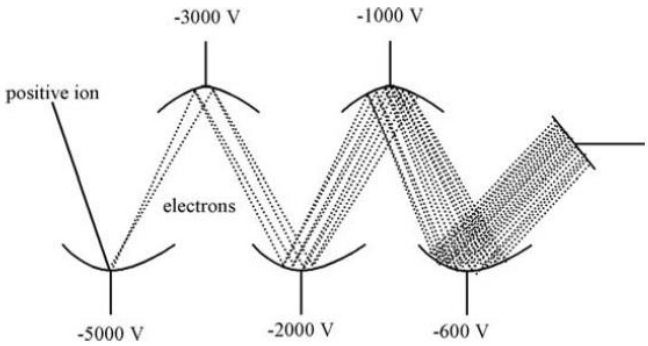

Figure 3. 22: Schematic of electron multiplier. The first dynode is a conversion dynode which converts the ions into electrons. (Picture adapted from [139]).

Table 3. 2 presents a summary of the main parameters of the Faraday cup, electron multiplier and the system:

Detector	Min/max counts Rates (cps)	Dynamic range	Dead time
FC	5 x 10^5- 5 x 10^9	10^5	~ 0 [102]
EM	~1 - 2 x 10^6	10^6	< 1 µs [1]
MCP/FS	Variable up to 2 x 10^6 [a]	10^4	10^{-7} s [b] [89]

Table 3. 2: Main parameters of the most common detectors in SIMS instruments [1].

[a] This depends on the amplification used.

[b] This value is provided no single channel is excited more frequently than once every 10^{-2}s.

3.5 Conclusions

In this chapter, basic concepts of SIMS technique were summarized. A brief survey of the fundamentals such as the sputtering process, dependences of the sputter matter, the most revelant ionization models, the matrix effect and the influence of the reactive primary ions as well as flooding are described.

The second part of the chapter summarizes the instruments used in SIMS, especially the most commonly used TOF-SIMS, Quadrupoles and Magnetic Sectors, with detail description of the instruments used in this work, the Cameca IMS XF series.

4 Study of a new electrostatic analyser for the improvement of the mass resolution in a magnetic sector spectrometer

4.1 Introduction

As seen in the introduction (chapter 1) there is an increasing necessity to develop new machines that have simultaneously high sensitivity for chemical information plus high spatial resolution. One option is to combine diverse types of high resolution microscopes with a mass spectrometer [11,12,103–105]. The limiting factor to add-on a spectrometer to the microscopes is the size and the weight of the spectrometer. The performance in terms of mass resolution of a mass spectrometer is directly proportional to the size of the magnet, and in consequence to the size of the electrostatic sector, since both sectors must match the energy dispersion. Commercial instruments such as the IMS 6F have a MRP of 10,000 which is enough for many applications which required only a few thousands to resolve the mass interferences. The performance of the add-on instruments is drastically lower. Therefore, increase the MRP from 300 to 600 or from 500 to 1000 would increase significantly the amount of applications of the machine. In order to optimized the performances of these instruments, in this work was studied the influence on the mass resolution of the double focusing mass spectrometer, by only changing the standard electrostatic sector by a novel analyser, the Spheroid Energy Analyser (SEA) which has better focusing properties. The aim was to evaluate the possibility for improving the MRP of an add-on spectrometer without significantly increasing its size. The focusing properties of this new analyser were discussed in Section 2.5.5.

By selecting an electrostatic sector with such high order of focus, the energy resolution is better than the standard spherical sector, the focus point position does not change with second or third-order variations in the input angle. Thus, for sectors of similar radius (approximately similar dispersion) the sector will have better energy resolution, meaning that it will have smaller spot size which allows the use of smaller slit after the electrostatic sector. Consequently, better energy selection can be made producing better mass resolution with the same transmission. On the other hand, if the opening angle at the entrance is much higher than the standard sector, keeping the energy slit with the same width than the spherical analyser, more particles are transmitted, meaning an increasing in sensitivity.

In this chapter, the performance of the two widely used double focusing spectrometers configurations, the Mattauch-Herzog (the instruments designed at LIST are based on this principle), and Nier-Johnson (a configuration extensively used in commercial instruments), with the spheroid

geometry were analysed, and compared with the performance when the standard spherical sector was used.

First, the spheroid shape with the same parameters (K_1=2.756, K_2=4.889 and K_3=0.944) reported in Cubric's work [13] was reproduced using SIMION and the main focusing properties were evaluated. To circumvent some artefacts arising from the fact that SIMION uses a square mesh to reproduce geometries, the *boundary matching technique* was applied. Later, a performance comparison between the standard spherical sector and the spheroid geometry in a Mattauch-Herzog and Nier-Johnson configurations is presented.

4.2 Preliminary simulations

The spheroid geometry was reproduced using SIMION in the same way described in the literature [13] and the optical properties were obtained and compared with the literature ones. Figure 4. 1 is an illustration of the spheroid analyser reproduced in this work. The fact that the crossover is not exactly on the axis reveals that the geometry was slightly different to that Cubric's work. This is because the spheroid geometry has very complicated shapes at the entrance and at the exit. A small difference in the field distribution inside the sector produces a meaningful change in the size and position of the focus.

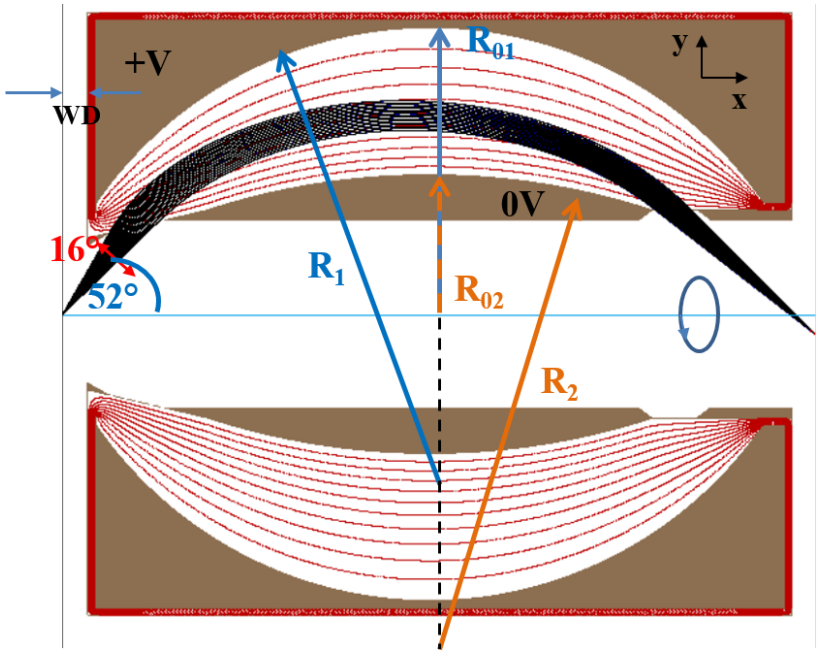

Figure 4. 1: Schematic of the spheroid geometry with the main parameters. The particles -in black- depart with 16° opening angle, from 44° to 60°, the equipotential lines are in red. V=300 V; R1=124 mm; R_2=220 mm; R_{02}=42.5 mm; R_{01}=87.5mm, particle energy=645 eV, WD=7.6 mm. The crossover is not on the axis.

Figure 4. 2 shows a cross section of the entrance slit for both analysers, where the small difference between both entrances slits is difficult to observe. For example, there is a thin straight line at the entrance of the sector (blue oval) that simulations showed that varying its length the field inside the sector is significantly modified that the focus width and position are significantly affected. In this simulation, a grid size of 10 μm per grid unit instead of 100 μm was used, what gives one more order of accuracy to model the geometry. Nevertheless, as the entrance grid is not aligned with the square mesh, it is modelled as a "staircase" rather than a smooth line. As a result, the particles that reach the different steps are deflected slightly differently and consequently the scattering of the particles broad the crossover at the landing position.

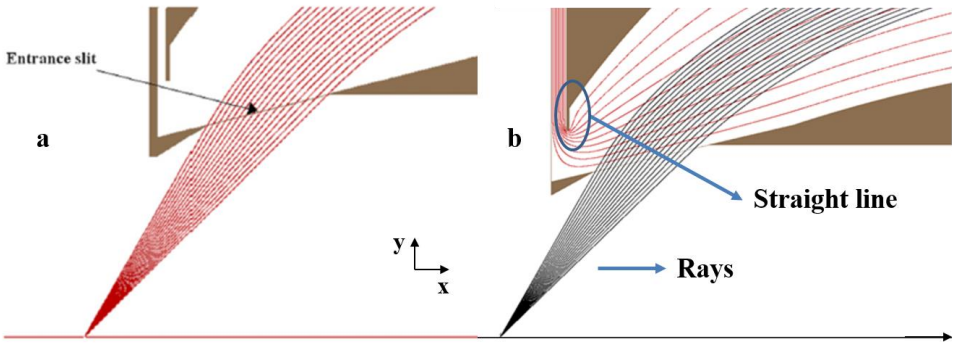

Figure 4. 2: Comparison between the cross section of SIMION entrance slit model with a set of trajectories spanning the angular range from 44° to 60° , a) reproduced from [13]; b) modelled in this work; the trajectories are in black and the equipotential lines in red. Little differences in the straight line represents significantly changes in the field distribution inside the sector.

Figure 4. 3 shows a comparison of the effect described in the literature and the results obtained in this work. In figures 4.3.c/d the oscillations are observed at the landing position, while in literature

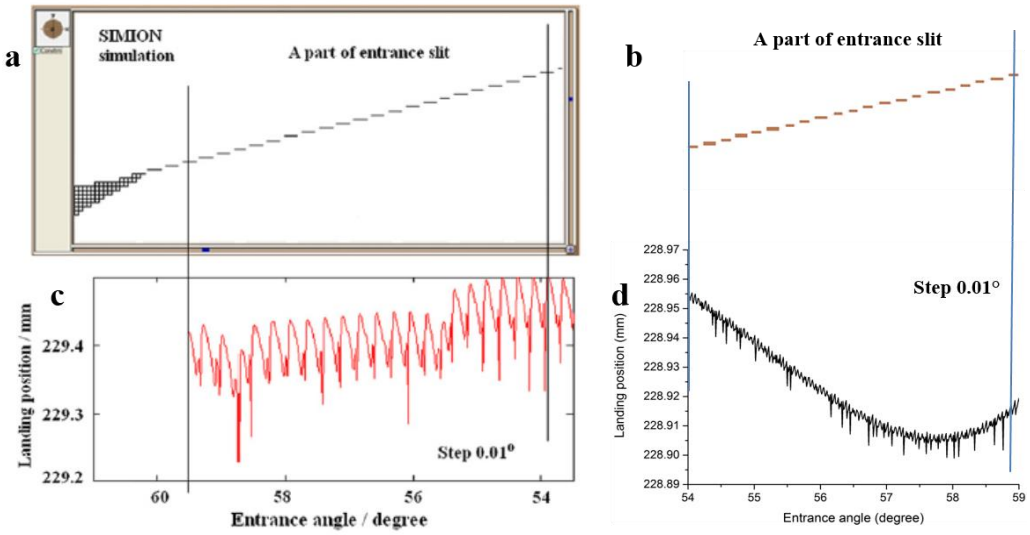

Figure 4. 3: Cross section of small portion of the entrance slit, a) reproduced from [13] and b) reproduced from this work. In both cases the staircase is observed. c) Landing positions of electrons following trajectories angularly spaced by 0.01° at the entrance, broadening 300 μm reproduced from [13]; d) similar simulation with positive ions angularly spaced by 0.01°, (V/E=0.45) broadening around 60 μm, five times smaller than [13].

particles at the focus position are reported to be scattered over 300 μm, in this work the broadening obtained was approximately 60 μm.

The scattering in this work is five times smaller because the smaller mesh size generates smaller steps, which is translated into a reduction of the effect of the broadening. In order to reproduce high order focusing is necessary to solve this effect. In theory, by reducing the grid size the effect could be reduced, but this is impracticable because of the huge amount of computer resources it would require. Instead, the *boundary matching technique* was implemented in SIMION to solve this problem and will be explained later in Section 4.2.1.

Figure 4. 4 shows a relative energy difference of 0.05% obtained at full angular acceptance of 16° in two cases. In the first case, picture b, two bunches of ions were flown with 645 eV and 645.3325 eV, and 1° step, obtaining a distance centre to centre of 0.093 mm exactly as literature. In the second case, the angular step was 0.1° in literature and 0.01° in this work. The images c and d present both simulations, on picture d, the two bunches of particles are completely separated, while on picture c the two bunches are resolvable only at FWHM even though the step is one order of magnitude less. This is a consequence of the smaller mesh size which provides better simulation accuracy.

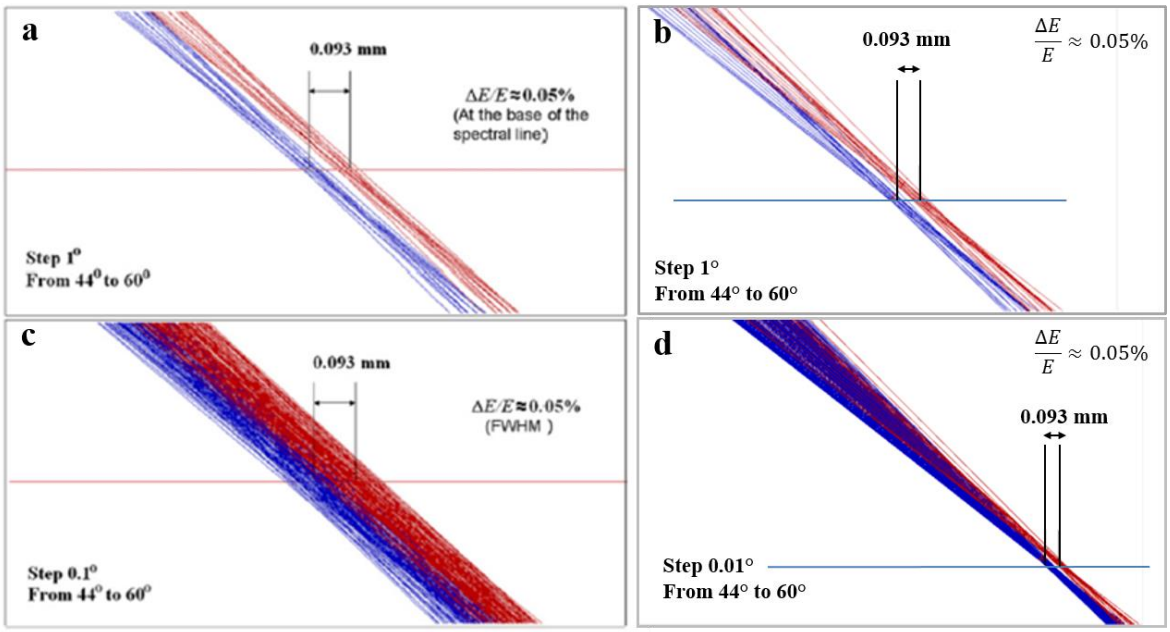

Figure 4. 4: Two bunches of electron trajectories with a relative energy difference of ΔE/E=0.05% at the focus. a) The full angular range of each bunch is 16°, 16 trajectories per bunch, reproduced from [13]; b) reproduced in this work; c) 160 trajectories per bunch, resolvable at the FWHM, reproduced from [13]; d) 1600 trajectories per bunch clearly resolvable, consequence of finer mesh.

As seen in 2.2.3 the energy resolution can be calculated as:

$$\frac{\Delta E}{E_0} = \frac{W_s}{D} + \frac{C_{s2}}{D}\Delta\alpha^2 + \frac{C_{s3}}{D}\Delta\alpha^3 + \frac{C_{s4}}{D}\Delta\alpha^4 + \cdots \qquad (2.9)$$

The order of focus n of an analyser is calculated as the first nonzero coefficient C_{sn} of the above equation. This means for a second-order focusing the coefficient C_{s2} must be zero, but C_{s3} is not. In this work, the estimation of the order of focusing is slightly different from the standard definition and follows the concept introduced in Cubric's work. In his work, the fitting was done with *all* coefficients, and the grade of the polynomial is selected by the polynomial which better fits the function. By using the same criteria of the calculus of the order of focusing the results can be compared. The positions of the particles at the focal plane were plotted against the entrance angle and the best fit was with a fourth order polynomial with all coefficients, illustrated in Figure 4. 5. The simulation conditions were: working distance (WD) of 7.6 mm, outer electrode voltage of 300 V, energy of 645 eV (V/E=0.46), a point source and the entrance angle of 52° with an angular spread of 16° in steps of 0.1°.

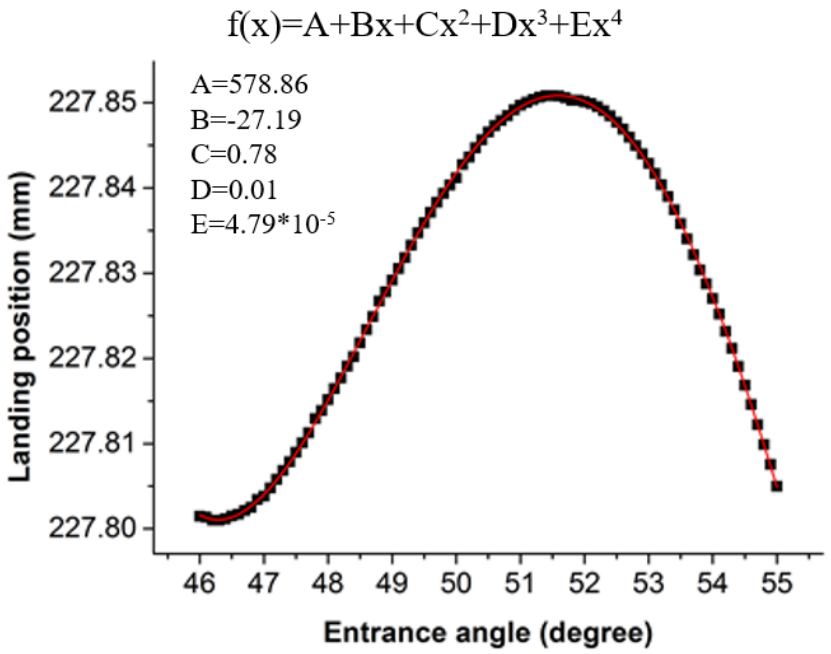

Figure 4. 5: Black squares: landing position versus the incident angle for WD=7.6 mm, mid angle 52° and V/E=0.46, in red the fitting curve with fourth grade.

Consequently, the analyser has presence of third focusing order, so in order to obtain the high order focusing properties, it is necessary to circumvent the effect of the stepwise appearance of the mesh, thus the boundary matching technique was implemented in SIMION.

4.2.1 Boundary matching technique

The boundary matching technique is used to match the potential values between different potential arrays that are overlapped within the SIMION workbench. This ensures that the potential varies smoothly and continuously when the ions/electrons pass from one PA to another. The idea was to design a smaller PA which reproduces the geometry of the entrance slit and it is aligned with the mesh, thus a straight line is obtained instead of the staircase (see Figure 4. 6).

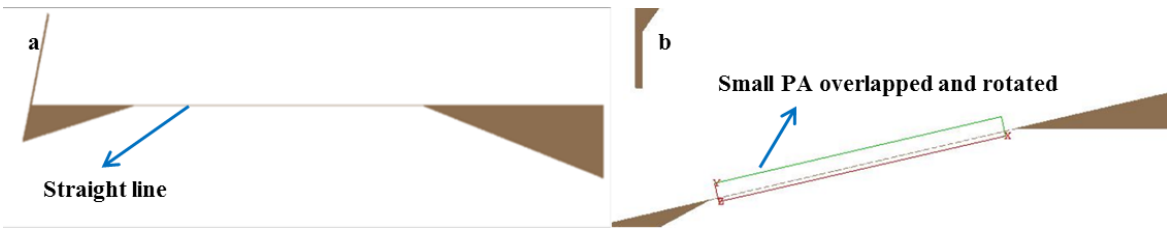

Figure 4. 6: a) geometry of the entrance slit reproduced aligned with the mesh, b) the small PA is overlapped with the big PA. The PA is rotated to match with orientation of the entrance slit.

This potential array is inserted in the workbench, rotated and overlapped in the position of the entrance slit. The potentials should be continuous across all the edges between the PAs. In Figure 4. 6 and in Figure 4. 7 the sides of the small PA have red and green colours. They are one grid unit thick, so they are completely transparent for the ions, this means that ions can go through the PAs without noticing. The potential values obtained in the big PA are recorded where the sides of the small PA overlaps. The edges of the small PA can be used as virtual electrodes therefore they can have potential values at their grid points.

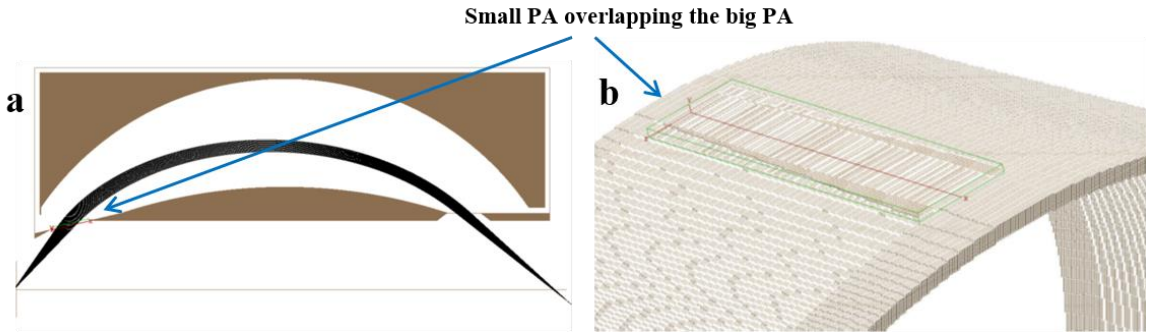

Figure 4. 7: a) Cross section in XY plane of the small PA -entrance slit- overlapping the big PA; b) 3D zoom of the place where the small PA is inserted in the big PA. The green lines are the edges of the small PA and where the potential is smooth and continuous.

These potential values are calculated from the ones stored from the big PA. Because the small PA is rotated, the grid points do not coincide with the grid points of the big PA, so an interpolation technique is used to calculate the values of the small PA from the values of the big PA.

Once all the values are calculated on the sides, SIMION can determine the potential values within the small PA. In this manner by *boundary matching technique*, the potential values of the big PA are matched with the values of the small PA.

In the simplest case when two 2D PAs are matched, the verification of the correct overlapping is very easy, just by observing if the equipotential lines on the sides coincide. One example of this case is shown in Figure 4. 8, where a boundary matching technique was applied between 2D PAs overlapped with different density of grid units. In more complex cases, such as different dimensional matching 2D-3D with rotation, SIMION cannot display the equipotential lines for checking. Thus, to verify a correct matching different parameter can be analysed such as: the jumps in the potential, the behaviour of the different components of the velocity (Vx, Vy, Vz), energy discontinuities, etc., when the particle crosses the edges between the PAs.

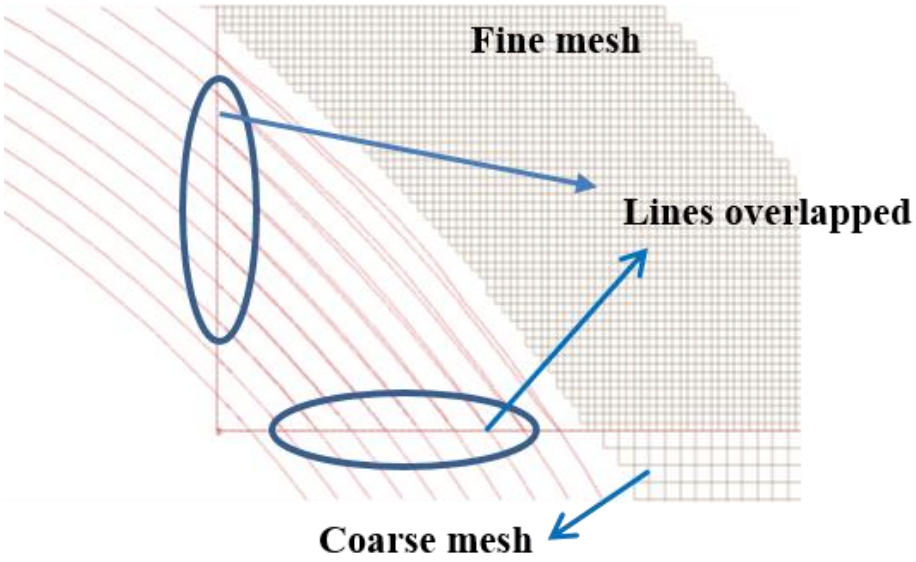

Figure 4. 8: Image of 2D PAs with different density mesh. The equipotential lines of both PAs are overlapped.

Figure 4. 9 shows the equipotential lines immediately after the entrance slit; when the entrance slit has the staircase the equipotential line is curved, but after the boundary matching technique it is a straight line.

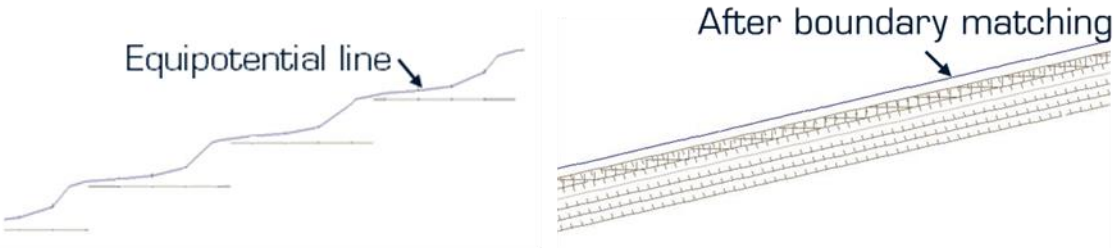

Figure 4. 9: a) SIMION workbench image of the entrance slit with curved equipotential line (staircase); b) straight equipotential line after boundary matching.

Figure 4. 10 shows the landing position of the ion plotted against the entrance angle with and without the staircase. The reduction of the spot size is approximately 10 μm, which is only 15% of improvement. Indeed, this result is a consequence of the fact that the total width of the spot is a combination of the intrinsic focusing properties of the analyser and the oscillation arising from the stair effect. The difference between the two curves is due to the oscillation contribution, which is around 10 μm.

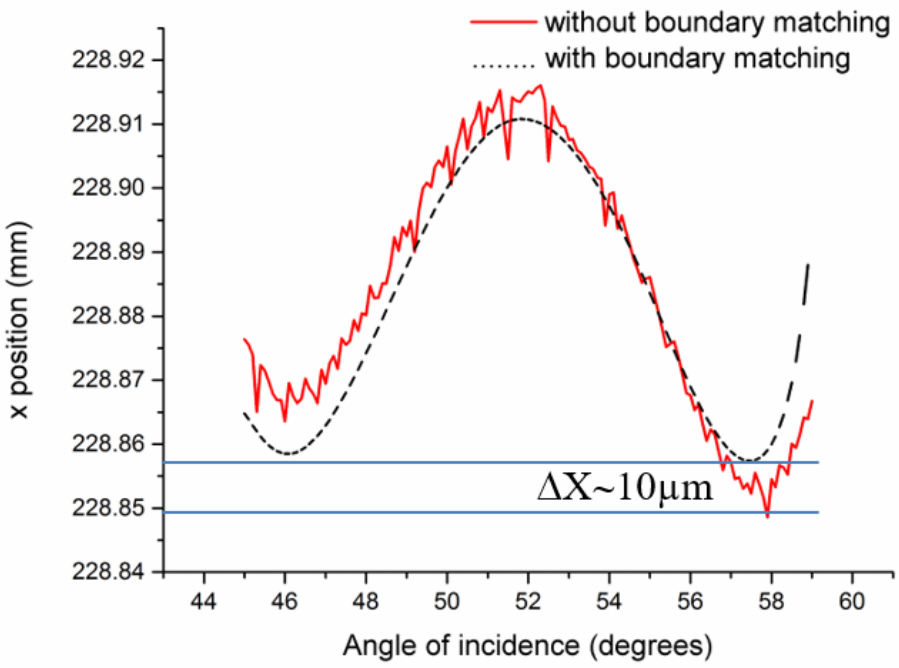

Figure 4. 10: Landing position versus the incident angle for WD=7.6 mm, mid angle 52° and V/E=0.45, black dot line after boundary matching, red line without boundary matching.

4.2.2 Higher order focusing

An electrostatic sector with higher order of focusing, essentially means an analyser with better focusing properties. Particularly, if the spot size after the sector is smaller than standard sectors, the spot size after the magnet can also be smaller, implying a smaller FWHM, and therefore, a higher MRP (Figure 4. 11).

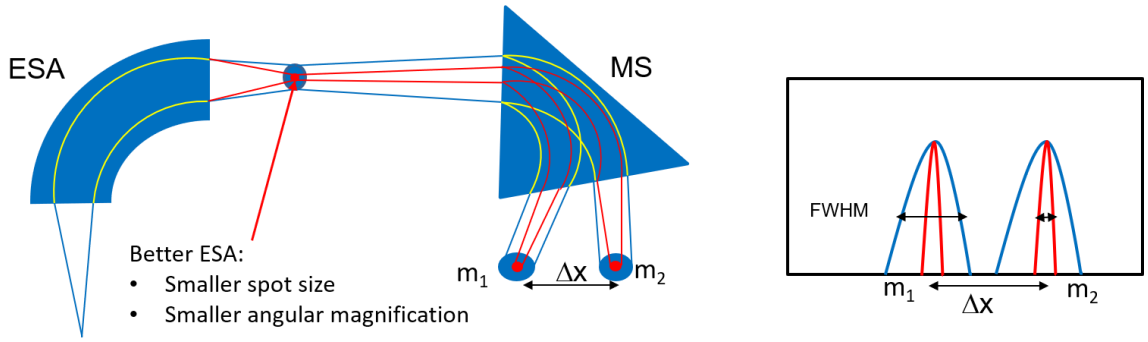

Figure 4. 11: Schematic of a double focusing mass spectrometer showing the effect of a smaller spot at the exit of the ESA on the spot size at the exit of the magnet. On the right side a schema how the FWHM is reduced implying higher MRP.

In addition, if the spot size at the exit remains equal to those ones obtained with the standard electrostatic sectors, but the entrance opening angle is larger, more ions could be collected, enhancing the transmission and subsequently the sensitivity (Figure 4. 12).

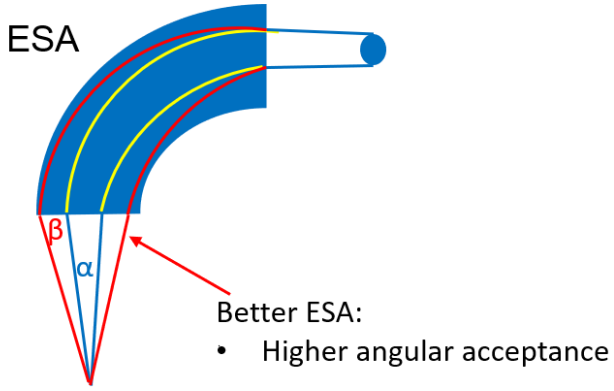

Figure 4. 12: Schematic of better ions collection when the ESA accepts higher entrance opening angle.

In order to obtain higher order focusing the analyser should be tuned to optimum conditions. The working distance, the particle energy and the entrance angle were scanned sequentially through different values and the crosses over sizes were evaluated at the focus point. The combination with the smallest value was selected as optimized spheroid parameters. The conditions for the best focusing were α=50.8°, WD=8.6 mm and V/E=0.45. These conditions are different from those reported by Cubric. (Table 4. 1). The reasons are due to the minor differences between the entrance and the exit slit and that the software used to simulate the optimized values were different. In this work, the software used was SIMION 8.1, while in Cubric's work initially was SIMION 7.0 and the optimized values were obtained with BEM.

	Spheroid modelled in this work	Spheroid modelled by Cubric
Spot size	8 μm	10 μm
Shape of the curve	With a relative max.	flat
WD/Mid angle	8.6 mm/50.8°	11.6 mm /47
Opening angle	9°	12°
Mean X position (L)	230 mm (not on the axis)	238 mm (on the axis)
Outer potential/Mean	0.45	0.41

Table 4. 1: Conditions for higher order focusing for both analysers.

Even though the conditions are not the same, when the entrance angle is reduced from 16° to 9°, a curve with only a width of 8 μm is obtained as it is shown in Figure 4. 13b; in Cubric's work the opening angle was reduced to 12°. The curve was best fitted with a fourth order polynomial. The energy resolution was calculated in an equivalent manner to that in Cubric's work: the energy dispersion was normalized to the mean of the landing position L=230 mm, being D=0.57; the spread in the landing positions was $\Delta Z \approx 8$ μm for the angular range of 9°.

The estimation of the energy resolution was done at the crossover position,

$$\frac{\Delta E}{E}\% \approx 100\frac{\Delta Z}{DL} = 0.006\ \% \qquad (4.\ 1)$$

This is better than the value reported in Cubric's work of 0.007%, this is because the resolution at the crossover plane is somewhat better than the resolution at base of the spectral line (where the value of the literature was obtained).

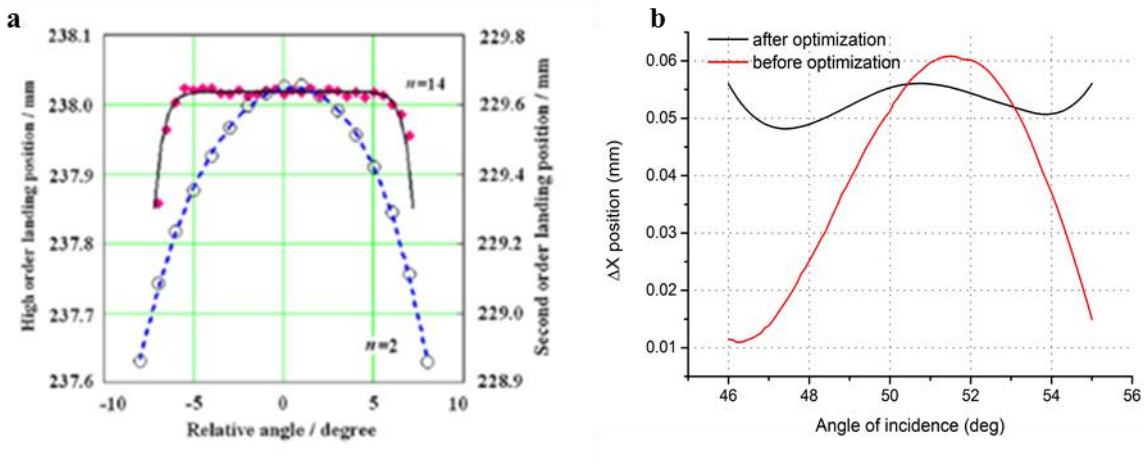

Figure 4. 13: a) Results reproduced from [13], the red dots represent the high order focusing and the full curve in black is the best least square fit 14th order polynomial; b) the red curve without any optimization neither boundary matching, and the black curve with boundary matching and optimized parameters. Both curves present the variation in the position, meaning the size spot.

4.2.3 Model with real grids

In Cubric's work the spheroid was built with the entrance an exit slits covered with thin tungstens wires of 50 µm diameter tightened longitudinally across the slits. In order to investigate the effect of the real grids in the optics of the analyser, the entrance and the exit grids were modeled as thin wires of different diameters tightened longitudinally, always keeping 90% transmission per grid, which is the maximum values obtained in real grids [91]. The entrance and exit slits were designed separately in small PAs that later were overlapped on the big PA and the boundary matching technique was applied. An schematic of the wires simulated is shown in Figure 4. 15a.

The spot size was calculated at the focus point as the Full Width 50 (FW50), which is a circle obtained of a cross section perpendicular to the beam at the focus point that contains the 50 % of the particles. This was implemented each time the spot size was calculated by CPO simulations. In most cases FW50 is different from FWHM it is typically used to enable comparison of beams with different distributions where the FWHM would provide a misleading comparison.

In order to calculate the FW50 of the crossover, the ion velocities and positions are recorded in a plane perpendicular to the beam in the field free region (X_1, Y_1, Z_1). As the beam has certain angle with the SIMION axis the optical path is not aligned with X axis, so firstly, the system must be rotated to be

aligned with the beam centre and direction before the extrapolation of the trajectories. A rotation matrix is used for this purpose:

$$\begin{pmatrix} X_1' \\ Y_1' \\ Z_1' \end{pmatrix} = \begin{pmatrix} \cos\gamma & \sin\gamma & 0 \\ -\sin\gamma & \cos\gamma & 0 \\ 0 & 0 & 1 \end{pmatrix} * \begin{pmatrix} X_1 \\ Y_1 \\ Z_1 \end{pmatrix}$$

Where γ is the angle between the X axis and the beam, in SIMION is called the elevation angle and could be recorded in the same plane where positions and velocities are recorded.

Secondly, with the new coordinates, the trajectories can be extrapolated along the optical path in the free field region and the coordinates of the new plane (X_2', Y_2', Z_2') at certain distance from the original recorded plane can be obtained with the following equations and the Figure 4. 14 is a geometrical description of them:

$$X_2' = X_1' + \Delta X'$$

$$Y_2' = Y_1' + \Delta Y' = Y_1' + \sqrt{(\Delta X'^2 + \Delta Z'^2)} \cdot \tan\beta$$

$$Z_2' = Z_1' + \Delta Z' = Z_1' + \Delta X' \cdot \tan\alpha$$

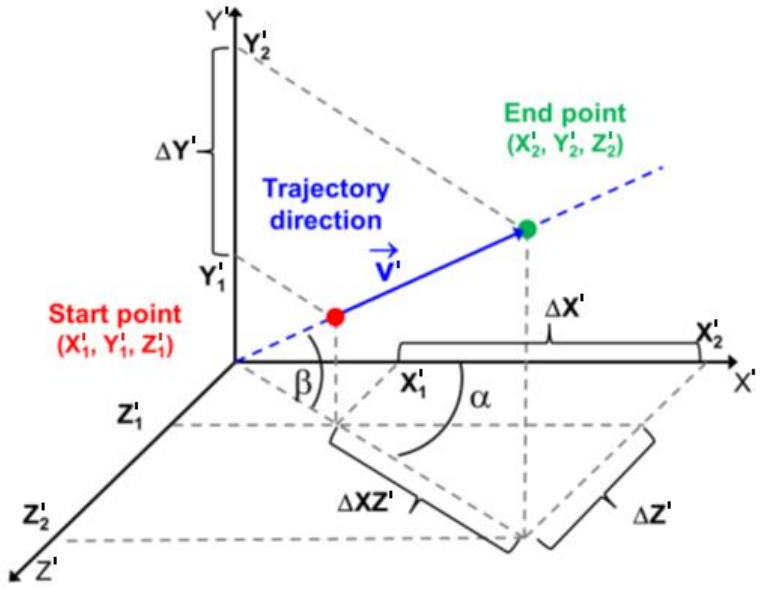

Figure 4. 14: Geometrical description of the projected trajectories in the rotated coordinate system (picture adapted from [122]).

The $\tan\beta$ and the $\tan\alpha$ can be expressed in velocities terms as they do not change in the free field region. The direction of the beam is now aligned with X' axis, by varying ΔX' in small equidistant steps

along the optical path, several new planes (X_2', Y_2', Z_2') can be obtained. In each plane, the distance to the axis can be calculated and the radius is obtained. The minimum radius of all the planes which contains the 50 % of the particles is the FW50. Finally, a rotation back to recover the SIMION coordinates (X_2, Y_2, Z_2) can be done with the inverse of the previous matrix.

Figure 4. 15b shows the dependence of the FW50 versus the size of the wire and transmission. Simulations conditions: source 100 µm diameter, 10,000 particles each case were flown from a circle with a cone distribution of 2° half angle around the main entrance angle of 50.2°, the particle energy was 4,500 eV, without energy spread.

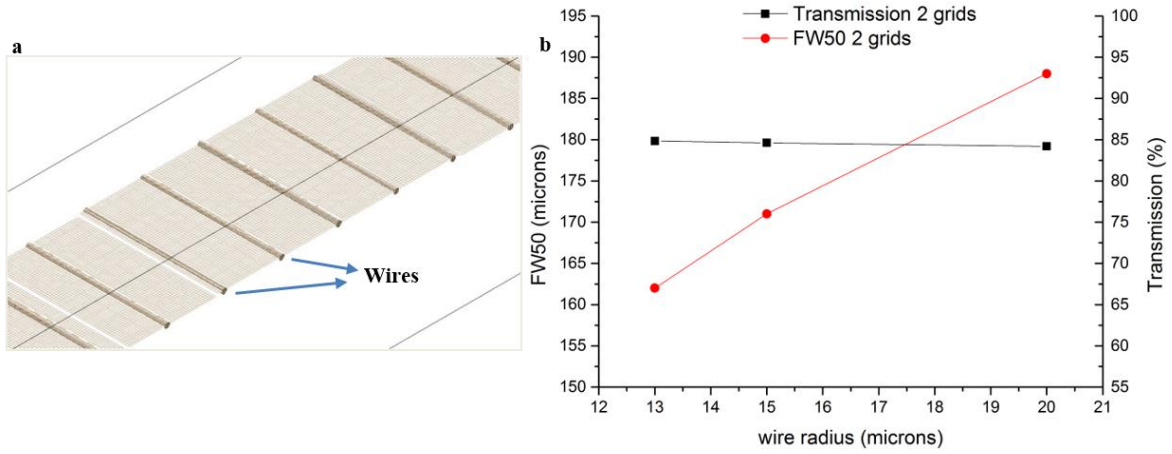

Figure 4. 15: a) Image of grid of the entrance slit with wires of 13µm radius and 90% transmission. The scale of the pa was 0.004 mm/GU b) Transmission including both grids in black and, the dependence of the FW50 with the radius in red. While the transmission was keep constant, the minimum FW50 was obtained for wires of 13 µm, 4 times smaller than Cubric's work.

Figure 4. 15b shows that the best FW50 is obtained for wires with a diameter of 13 µm instead of wires of 50 µm. The 13 µm was selected for being one of the smallest standard diameter fabricated [106].

The FW50 of the spheroid with real grids is 25% bigger than the spheroid with ideal grids. However, in Section 4.2.6 can be seen that the optics behavior is similar to the spheroid with ideal grids. This analysis is very important because it gives an approximation of the degradation of the optical system.

4.2.4 The hybrid

Most of the electrostatic sectors found in double focusing mass spectrometers are used in deflecting mode, they are used as a lens to bend the trajectory and match the dispersion. The spheroid works in

retarding mode, so to evaluate the spheroid geometry in deflecting mode, it was modified with a third electrode connected to ground potential for shielding. In this manner, the sector can work in deflecting mode and the field surrounding will be the same field nearby the magnet, so the beam coming out from the sector will not be influenced by external fields, allowing a correct coupling with magnet. Thus, the outer potential was connected to positive voltage and the inner electrode to a negative voltage as seen in Figure 4. 16 . The asymmetric shapes of the entrance and exit slits were removed; the shape is completely symmetric and ideal grids cover the entrance and exit slits.

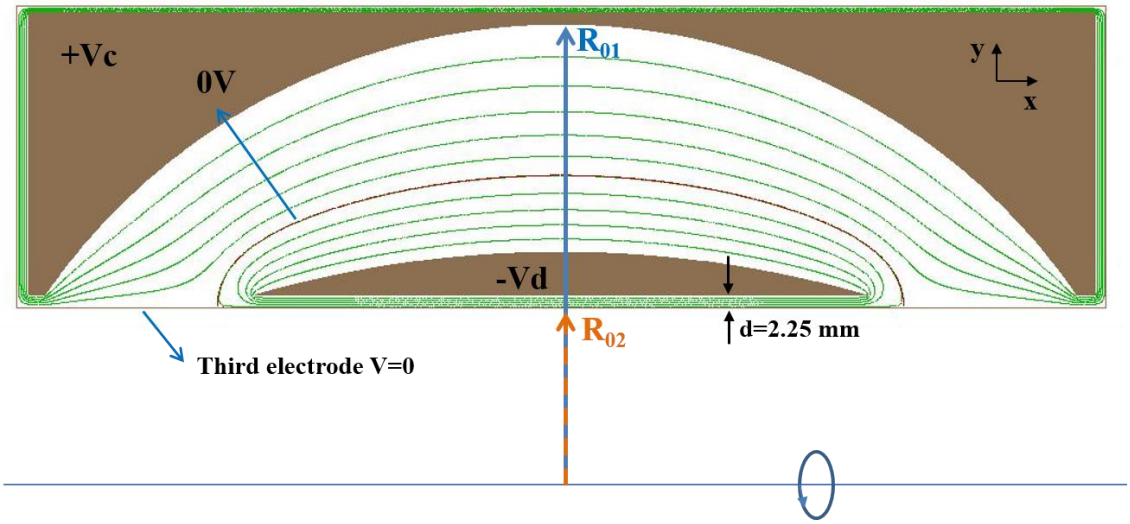

Figure 4. 16: Schematic of the Hybrid with symmetric entrance and exit slits and the third electrode. Potentials on the electrodes are settled to deflect positive ions. The radius has same values as the Spheroid: R1=124 mm; R_2=220 mm; R_{02}=42.5 mm; R_{01}=87.5mm.

This is an ideal designed, in practice for building the analyser some modifications should be done, such as round the edges of the electrodes to avoid arcing and increase the distance between the third electrode and the inner electrode to have values around 1 kV/mm.

4.2.5 Simulation of the Spherical electrostatic sector

A spherical sector with a mean radius equal to 64 mm similar to the mean radius of the spheroid and hybrid (65 mm) with rotational symmetry, similar as the spheroid geometry, was designed in order to make performance comparisons as a single sector and in combination with a magnet.

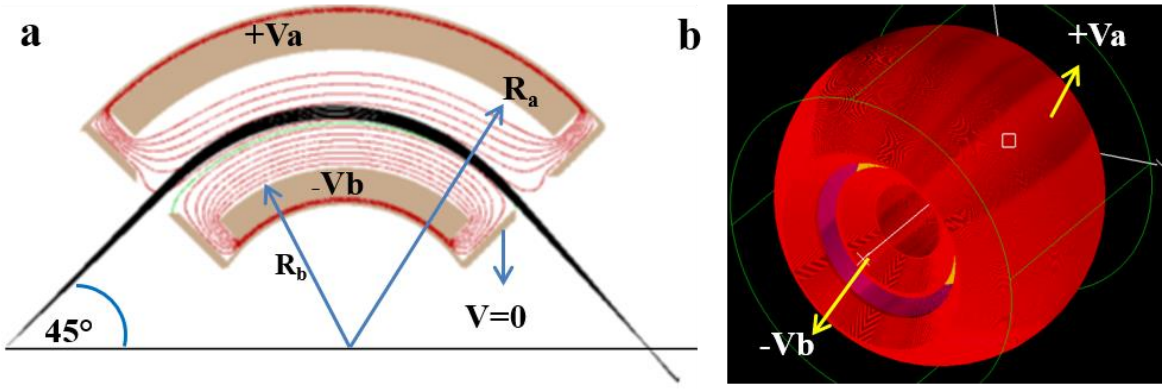

Figure 4. 17: a) A cross section in XY plane of a ninety-degree spherical sector with 3D rotational symmetry. b) 3D image of the sector designed.

The spherical sector simulated was based on a geometry found in the literature [35]. The slits have the following Herzog parameters: distance between electrodes and slits d=0.4 g_0; size of the aperture 2h=g_0 (R_a=80 mm; R_b= 48 mm, gap size 2g_0=16 mm; d=6.4 mm; h=4 mm). The outer potential was 2,300 V and the inner potential was -2,000 V and the mean energy of the ions was 4,500 eV. (Figure 4. 17).

4.2.6 Response of the different analyser according to the source radius

The previous simulations were performed with a point source to compare the spheroid simulated in this work and spheroid modelled in Cubric's work. In ion optics, especially in SIMS, the collected secondary ions come from a finite area. In order to evaluate the performance of the spheroid geometries for these applications, the first simulation investigates the dependence of the spot size defined as FW50 at the focus point on the source size, or the aperture radius which is the same in this case.

Therefore, the spot size for distinct size apertures was calculated and Figure 4. 18 presents the results for the different analysers modelled in this worked (standard spherical sector, spheroid geometry reproduced in this work with real grids, spheroid geometry with ideal grids and hybrid with ideal grids), for a focused beam. Focused beams are beams that focus at exit of the energy sector - are used for example in Nier-Johnson spectrometers. In each case 10,000 particles were flown from a circle with a cone distribution of 2° half angle around the main entrance angle, the particle energy was 4,500 eV, without energy spread. Figure 4. 19 shows that for all spheroid designs as the aperture size increases, the FW50 also increases exponentially, whereas for the spherical sector the FW50 is approximately constant. Consequently, for aperture radius smaller than 50 the spheroid geometry performs better than the spherical sector. Surprisingly, the hybrid shows the smaller FW50 than spheroid which was claimed to have presence of 13th order focusing. In the case of IMS XF Cameca series the aperture radius would

represent the contrast aperture size, meaning that for the common diameter sizes of 20 μm, 50 μm, and the spheroid geometries would be the better option.

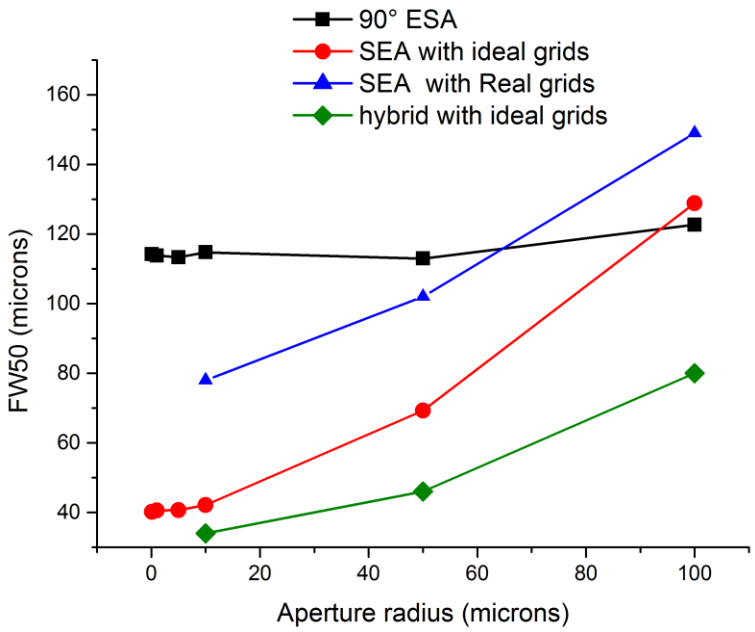

Figure 4. 18: FW50 at the focus point versus the aperture radius. Spheroid designs have a pronounced slope while the spherical sector remains approximately constant. Spheroid geometries have smaller FW50 for aperture radius less than 50 μm.

The Matauch-Herzog configuration requires a parallel beam at the exit of the electrostatic sector, so the evaluation of the size of a parallel beam at the exit of the electrostatic sector containing the 50 percent of the particles was calculated for the four sectors mention above. In order to obtain a parallel beam at the exit of the electrostatic sector a practical method is to use the principle of reversibility. Firstly, a parallel beam is introduced to the analyser, obtaining at the exit a focus point, the position coordinates are stored and later from this point in the inverse direction a parallel beam is simulated , generating the new coordinates for the source position. In the case of the spherical and hybrid sectors is very simple, but as the spheriod is not symmetric, finding the correct source position to obtain a parallel beam at the exit of the sector is a more complex process. The analysis of the convergence of the envelope beam and FW50 is required. Figure 4. 19 shows a parallel beam at the exit of both analysers, the blue line is the envelope of the beam, which in both cases has practically no slope; while the green and red lines represent the size of the 50% of the particles through the optical path. The spherical sector has a decrease of 0.3%, while the spheroid has an increase of 1%. This value was evaluated acceptable for considering the beam at the exit of the spheroid geometry as parallel.

Moreover, the red line shows that the FW50 reachs a minimun size around x=155 and after the beam widens inside and envelope that seems to remain aproximately constant.

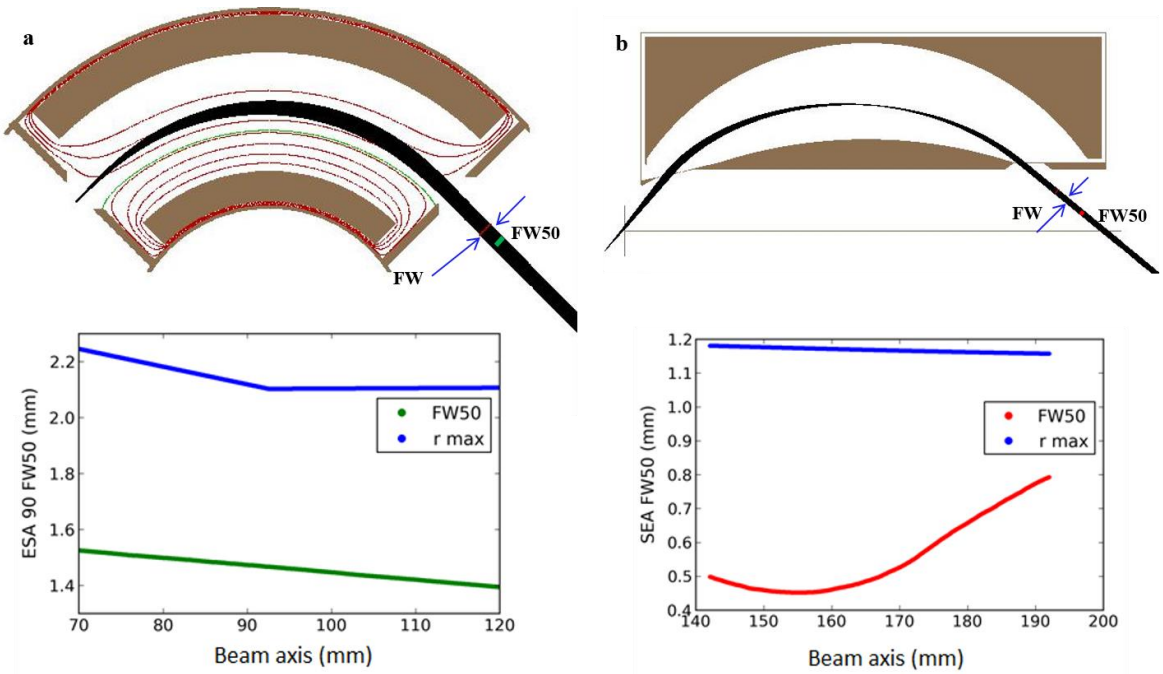

Figure 4. 19: Schematic of the parallel beam at the exit of the sectors, the blue lines represent the full width of the beam, a) green line represent the size of the beam containing 50 % of the particles, the slope decreases 0.3%; b) red line represents the size of the beam across the optical path and the slope increases 1%.

Figure 4. 20 shows the minimum size containing 50 percent of the particles for the previous analysers, all spheroid designs have a constant value for aperture radius for the whole range between 0 and 100 μm; aproximately four times smaller FW50 that the spherical case. Once again, the spheroid geometry appears to perfom better than the spherical sector.

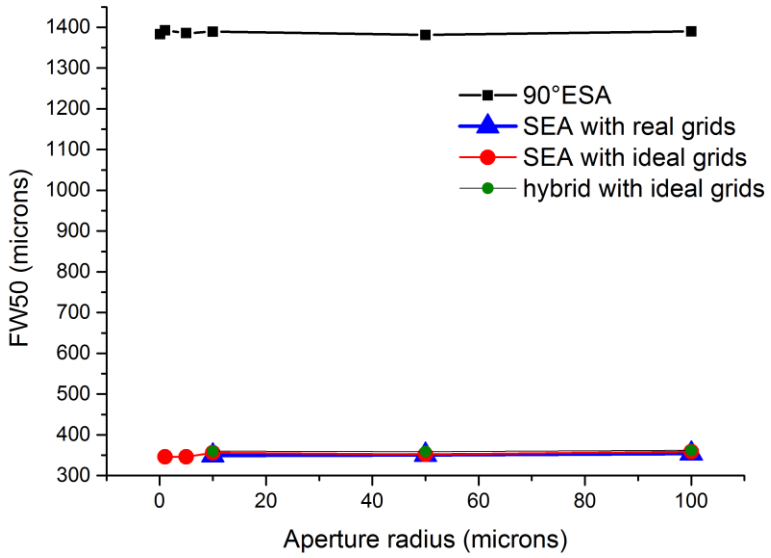

Figure 4. 20: FW50 versus the aperture radius. Spheroid designs have constant behaviour as well as the spherical but 4 times smaller FW50.

4.2.7 Comparison of the performances in retarding energy field mode

The three analysers, the spheroid, the hybrid and the spherical sector were compared under the same conditions. A retarding field was applied in the three cases, where the central energy was to make the 4,500 eV and two more beams with ± 0.45 eV (the energy difference represents 0.01% of the central energy). The total angular spread was 8° (half opening angle of 4°) and a point source. The central angle for the spheroid was 50.8°, 52° for the hybrid and 45° for the spherical sector (Figure 4. 21).

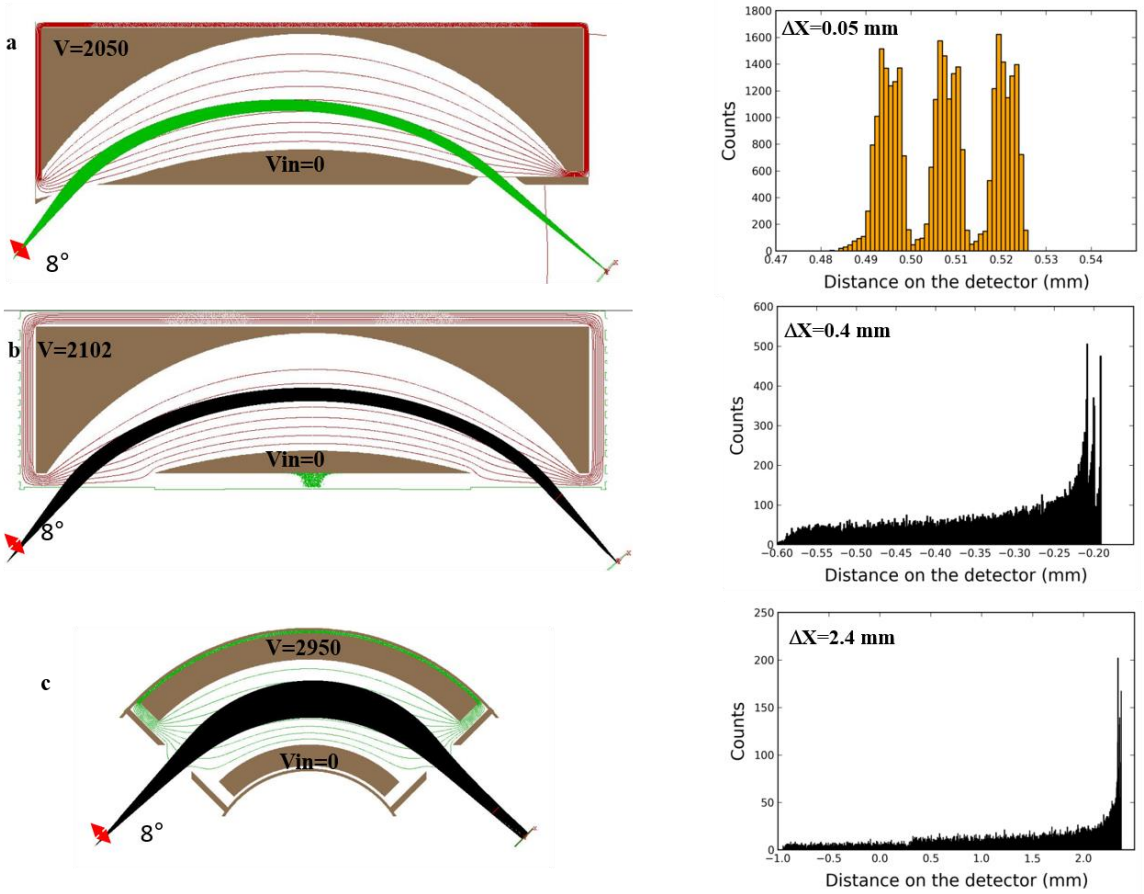

Figure 4. 21: Schematic of the three analysers with three energies with 0.01% of difference, total angular spread of 8°and a point source. The histograms are obtained at detector plane. a) spheroid total width of 0.05 mm and $\frac{\Delta E}{E}$ =0.006%; b) hybrid analyser total width of the beam is 0.4 mm with three peaks distinguished and $\frac{\Delta E}{E}$ =0.36%, c) spherical analyser in retarding mode total width on the detector 2.4 mm and $\frac{\Delta E}{E}$ =1.76%.

Figure 4. 21 illustrates the three cases, the image on the right is a histogram in one dimension recorded on a detector placed on the FW50 position. The three energies are clearly resolvable for the spheroid geometry; for the hybrid, the total width is 0.4 mm, with three peaks one side of the detector and the spherical analyser has a total width is 2.4 mm, where the peaks are difficult to distinguish and the counts per peak are approximately 3 times lower than hybrid. The energy resolution calculated for the spheroid was 0.006%, for the hybrid was 0.36% and 1.76% for the spherical sector.

From these simulations, it can be concluded that the spheroid analyser has the best performance in retarding mode, and the hybrid performs better than the spherical sector.

4.2.8 Comparison of the performances in deflecting energy field mode

A comparison between the hybrid and the spherical sector was made in deflecting mode. For the same beam conditions, main energy 4,500 eV ± 0.45 eV and total angular spread of 8°. The central angle for the hybrid was 44.63°, and 45° for the spherical sector. The outer potentials were calculated to obtain an optical path exactly in the middle of the gap.

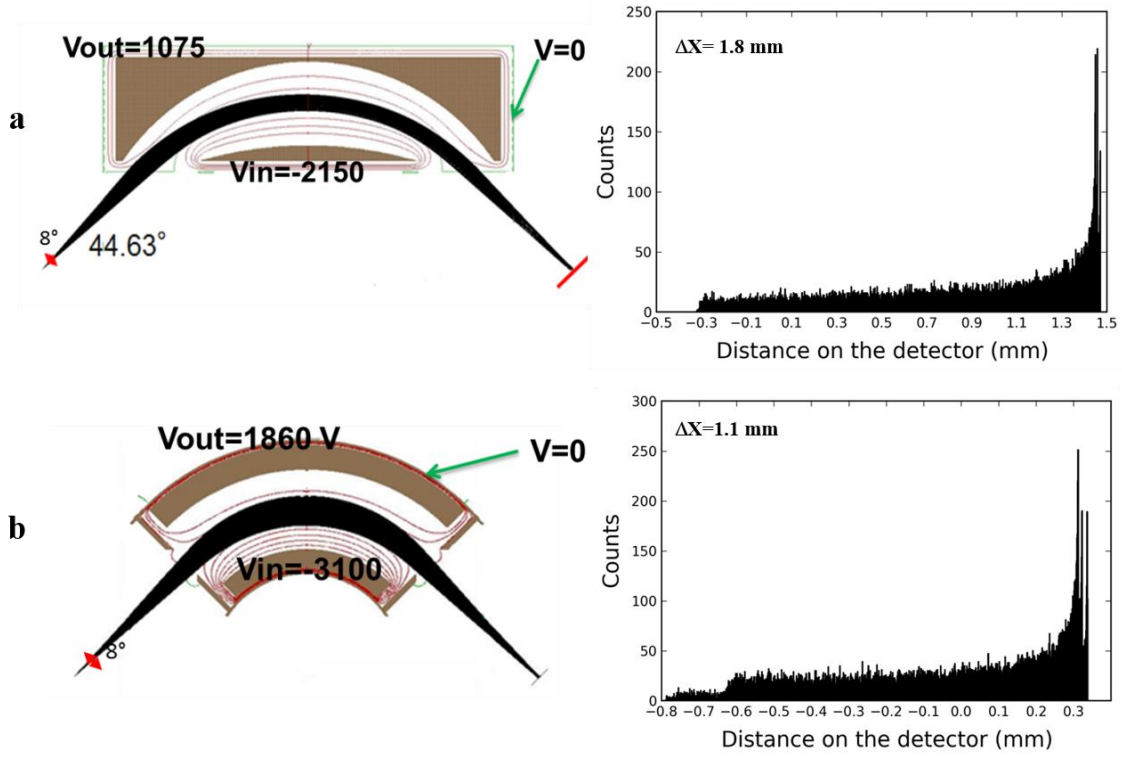

Figure 4. 22: Schematic of hybrid and spherical analysers with the optical path exactly in the middle of the gap in deflecting mode; a) the total width is 1.8 mm $\frac{\Delta E}{E}$ =1.56%; b) the total width is 1.1mm $\frac{\Delta E}{E}$ =1.07 %. The spherical sector has better energy resolution than hybrid.

In both cases the focus point was calculated using the extrapolation technique described in this section and the detector plate was inserted perpendicular to the beam in the crossover. The total width of the beam at the crossover, where the detector was placed was 1.8 mm for the hybrid and 1.1 mm for the spherical, the total counts per peak are of the same order, but in the spherical case the three peaks can be observed. This result seems to be in contradiction of the ones presented in Figure 4. 18, in fact in that moment was considered the size of the beam including only the 50 % of the particles, which is located only in the peak region. Figure 4. 22 illustrates the sectors with the optical path exactly in the middle of the gap, and on the right, the histograms in one dimension on the detector plate.

The energy dispersion was calculated exactly in the same way for all the analysers; 11 particles were simulated with an increment of 1 eV keeping constant the angle (fixed at the main entrance angle) and the particles positions were stored at the detection plane. Figure 4. 23 represents an example of the distance between the particles with different energy at the detector plane.

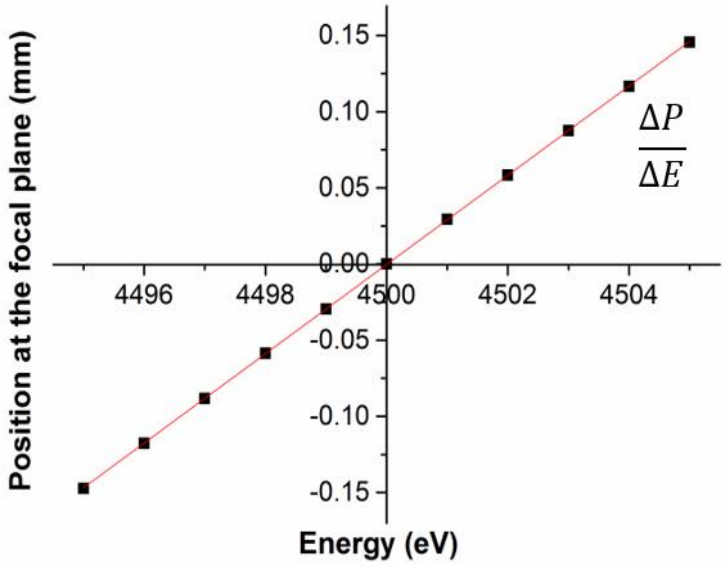

Figure 4. 23: Energy dispersion of the spherical sector in deflecting mode, the Y axis represents the detection plane in mm, and the X axis is the particle energy. The slope of the line gives the dispersion per eV that the particles are separated on the detector.

The energy resolution calculated for the hybrid was 1.56 % and 1.07% for the spherical. Table 4. 5 summarizes the main properties of the three analysers simulated in this work. The spherical sector properties included were for the deflecting mode (best case). The mid radius of the spheroid and hybrid was calculated at the middle of the gap in the centre of the analyser, being approximately 65 mm, since the radius of curvature is not constant. The bending angle was calculated by adding the main entrance angle and the exit angle formed between the particle trajectory and the X axis. The opening angle was ±4° (equivalent to a total opening angle of 8°) centred at the main entrance angle.

	Spherical	**spheroid**	**Hybrid**
Mid Radius	6.4 cm	6.5 cm*	6.5cm*
Bending angle	90°	93°	104°

Opening angle	±4°	±4	±4°
ΔE/E	1.07 %	0.006%	0.36%
Dispersion	0.03mm/eV	0.029 mm /eV	0.024 mm/eV
Transmission	100%	81%	81%

Table 4. 5: Table of the main characteristics of the analysers simulated in this work.

The energy resolution for the spherical sector was calculated as described in Section 3.2.3. (equation 3.9), only considering the second order for spherical aberration:

$$\frac{\Delta E}{E_0} = \frac{C_{S2}}{D}\Delta\alpha^2 \qquad (4.\ 2)$$

Where the C_{S2} is the coefficient associated with the spherical aberration, *D* is the normalized dispersion and $\Delta\alpha^2$ is the half opening angle. The C_{S2} was obtained by fitting the trace width with a second order polynomial and *D*, the normalized dispersion, with a linear fit. In order to obtain the trace width, particles from 41° to 49° with steps of 0.1 were simulated, and their positions were recorded at the detection plane. Then, the distance between the particles was calculated and normalized to the distance L=187.7 mm and plotted in function of the angle spread (in radians). The second order polynomial was used to fit the trace width and the coefficient was C_{s2}=1.67.

Figure 4. 24 illustrates the trace width as a function of the angular spread and the fitting curve is shown in red. The difference between the sides of the parabola reflects the difference of the potential distribution between the upper part of the gap and the lower part of the gap. This effect starts to be significant from half opening angles larger than 2° (0.035 radians). The dispersion coefficient *D* was calculated using a similar process as described for the dispersion, but in this case the fitting was made for normalized dispersion versus the relative energy spread as depicted in Figure 4. 25. The slope of the linear fit corresponds to *D*, in this case is equal to 0.742.

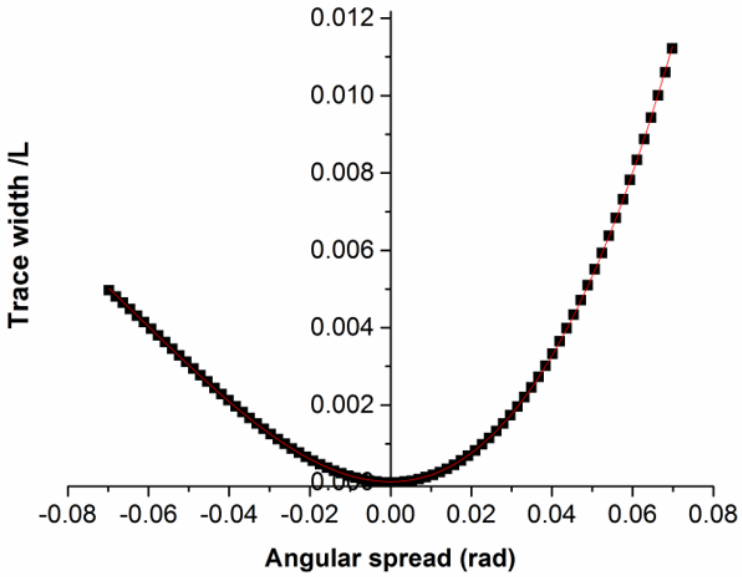

Figure 4. 24: Black spots are normalized positions at detection plane of the particles with different entrance angle. Red line is a second order polynomial fitting.

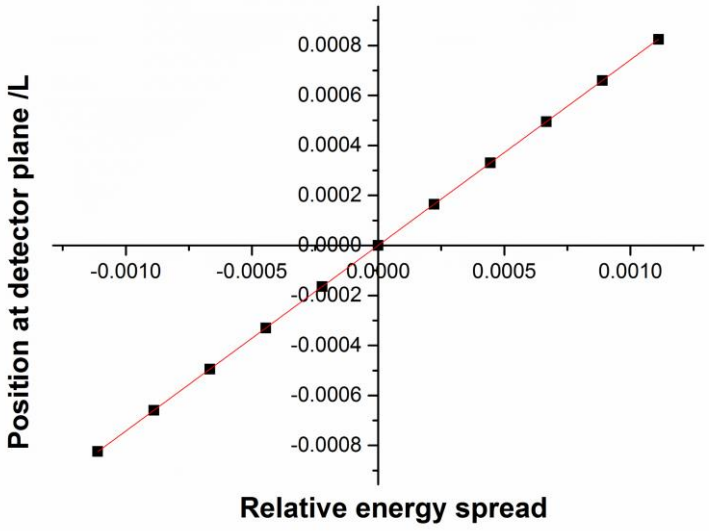

Figure 4. 25: Normalized dispersion versus the relative energy spread. Red line corresponds to the linear fit with slope equal to 0.742.

The hybrid resolution in both modes was calculated in the same manner as that for the spherical sector described above, giving 0.36% in retarding mode and 1.56 % in deflection mode. The last value

implies that hybrid is not better than the spherical sector in deflecting mode; this is true only if the optical path is exactly on the middle of the gap. If the outer potentials are slightly changed, keeping the central energy 4,500 eV, moving the zero equipotential near the inner electrode, the particles fly through an equipotential line with a positive value, recovering similar characteristics that in the retarding mode. For example, an energy resolution of 0.53% is obtained when the outer value was 1650 V and the inner was -1050V. This is 3 times better energy resolution than having the optical path in the middle of the gap, and is two times better than the spherical sector. For this reason, hybrid with these values was chosen for comparison with the spherical sector in a Mattauch-Herzog configuration.

The transmission of the spherical sector was 100 % and the simulations for the spheroid and hybrid were made in ideal case were the transmission was 100 %, but in practice the total transmission can be estimated approximately 81%, after the beam pass through two grids with 90 % of transmission each one as described in 4.2.3.

4.3 Comparison between spheroid geometry and standard spherical sector based on a Mattauch –Herzog configuration

The Mattauch-Herzog configuration is a compact mass spectrometer design, particularly interesting as an add-on to ion microscopes [11,12] because its compact design allows both a reduced size and the detection of several masses in parallel. Several such spectrometers are under development at LIST. In this Section, the electrostatic sector and the magnetic sector were combined based on the Mattauch-Herzog concept. A comparison was made between the performances of the two configurations: one including the standard spherical sector and the other with the spheroid geometry. The mass resolution of both systems was calculated.

Initially, both electrostatic sectors were combined with a simple rectangular magnet with a constant magnetic field ($\vec{B} = 0.8$ T) perpendicular to the dispersive direction, simulated in SIMION as it shown in Figure 4. 26. The conditions of the simulation were 10,000 ions, mass 200, a source circle of 100 μm radius with a cone distribution of 2° half angle around the main entrance angle, the particle energy was 4,500 eV, without energy spread. Figure 4. 26 shows a clear focus point in spherical sector configuration, but not in the spheroid configuration. In the XZ plane (Figure 4. 27) the focusing properties of both sectors are evident, the spherical sector has very weak focus in this plane, the beam is almost parallel, while the spheroid has a very strong focus point which produces a huge dispersion of the beam in Z direction. Even though the focusing properties in the dispersion plane are more relevant for the mass spectrometer, huge dispersion in Z plane is not desired because, depending on the size of gap, a part of the beam will hit the walls of the magnet and the transmission will be drastically reduced.

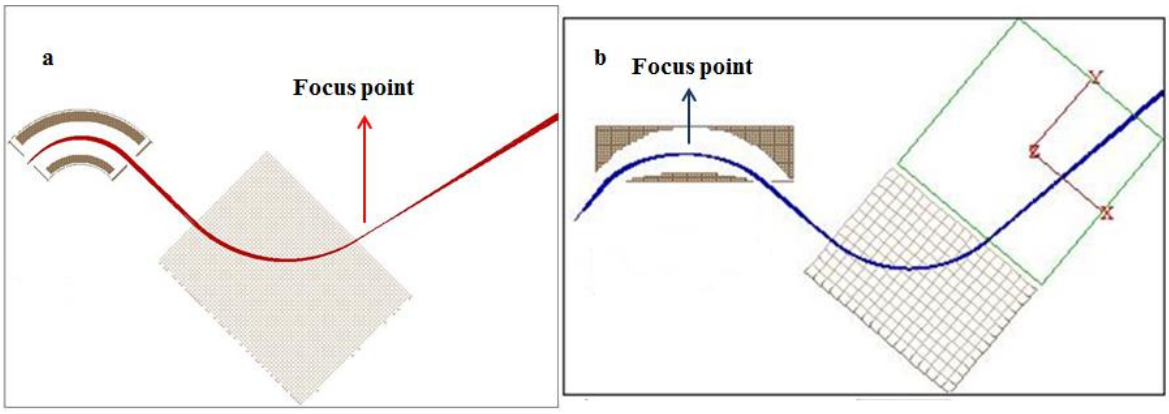

Figure 4. 26: a) Schematic of spherical sector combined with the magnet with a clear focus point after the magnet, b) spheroid sector with the same magnet at the same distance equal conditions for the ions, the focus in the xy plane is not obvious.

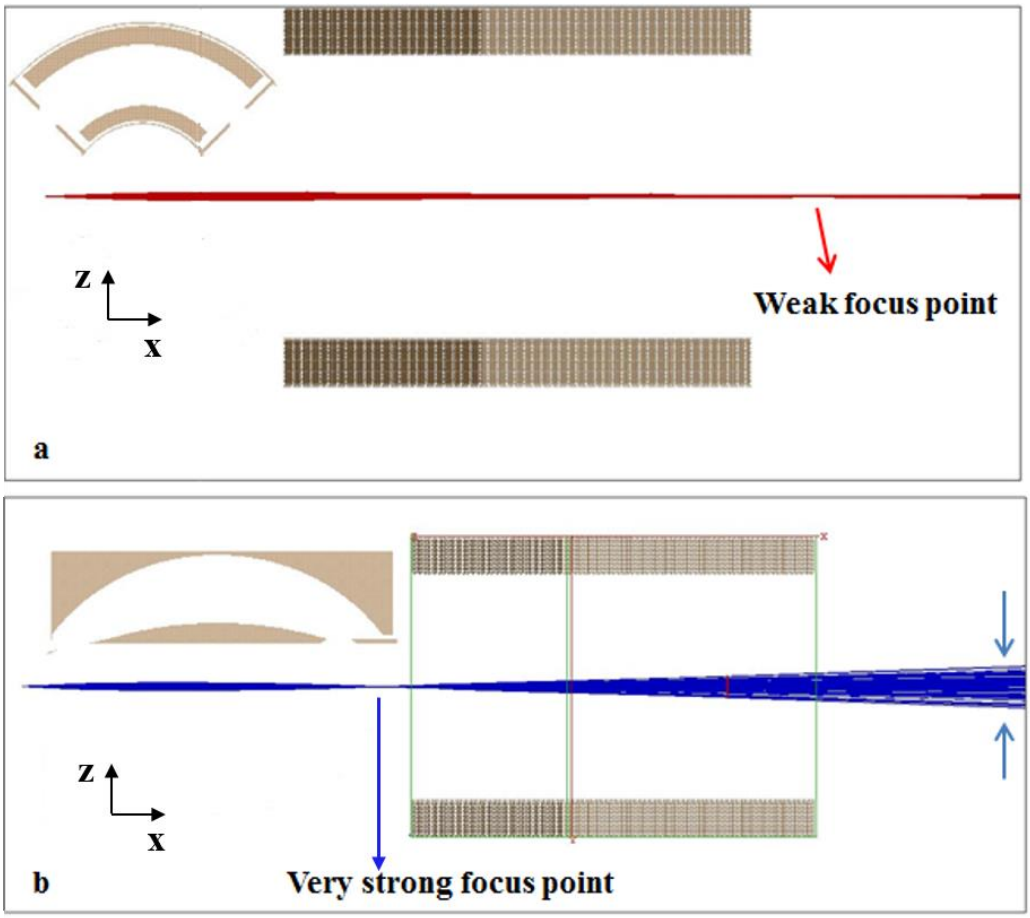

Figure 4. 27: a) Schematic of spherical sector combined with the magnet XZ plane almost parallel, b) spheroid sector with the same magnet in XZ plane with a very strong focus and subsequently high Z values at the exit of the magnet.

In order to reduce this effect two measures were taken. Firstly, optimizations to parallelize the beam coming out from the spheroid sector were done, and secondly, a more sophisticated magnet was introduced in order to use the magnet fringing fields to converge the beam in Z direction, enhancing the focusing properties in the dispersion plane.

4.3.1 Analysis of parallel beam

Previous images (Figure 4. 26 and Figure 4. 27) show that this spheroid geometry could be compared to toroidal sectors described in Section 2.5.2 where the dispersion plane has different focusing properties than the perpendicular plane. A possibility to modify the component of the velocity in Z direction is to vary the distance of the inner electrode to the axis of rotation. In order to investigate the different options to make the beam more parallel the hybrid design in deflection mode was chosen because its symmetry simplifies the investigation and the optimization process. Several simulations varying the distance from 10 mm to 100 mm in steps of 10 mm, were carried out to find the optimum distance to the axis of rotation. The evaluation criteria was to find the condition when the beam inside a 5 mm gap did not hit the plates of the magnet, this value was equal to R_{02} plus 80 mm, equivalent to K_3=3.39 instead of 1.61, represented in Figure 4. 28. With this condition, the focus in the XZ plane was not only much weaker but was also the position displaced to the right, approaching to the profile obtained with the spherical sector. The sector was also reduced to the half size in order to keep the width of the beam in Z direction less than 5 mm, which was the size gap of the magnet used in the followings simulations.

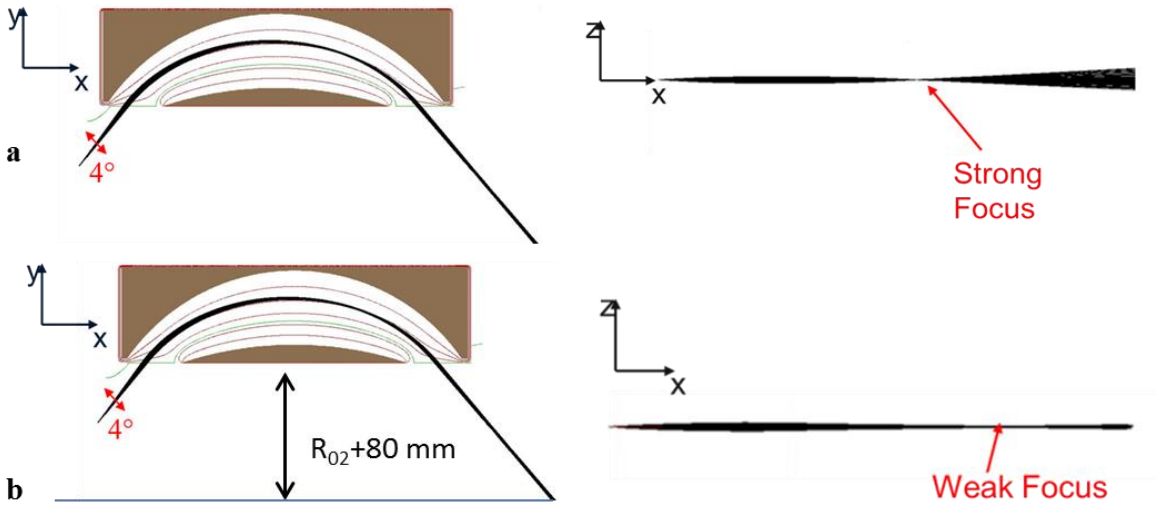

Figure 4. 28: a) Schematic of the initial configuration of the spheroid geometry with strong focus in XZ plane; b) Modified spheroid with 80 mm more to the axis X of rotation, and consequently a weaker focus point in XZ plane.

Figure 4. 29 illustrates the cross section of the beam for the three analysers, spherical, hybrid, and the modified hybrid, near the exit of the analyser and at 200 mm from the exit of the analyser. The beam coming out from the spherical is elliptical with semi axis of 2 mm in Z direction and 1.5 mm in Y direction; further the beam is compressed in Z direction and the distribution in Y direction is not uniform, concentrated around the spot and with tail. In the case of the hybrid, the spot at the exit of the analyser is half size in Z plane and 6 times smaller in the Y direction; however, at further distance the Z direction is 15 times bigger than the spherical and at least two times broader in Y direction. Finally, the modified hybrid has approximately the same size as the spherical in Z direction at the exit but still has six times smaller size in Y direction; at further distance, the beam is three times bigger than the spherical in Z and two times in Y plane, but appears to be more uniformed distributed. The modified hybrid seems to be an intermediate state between the spherical and the spheroid geometry where the Z size was controlled with more separation from the axis of rotation.

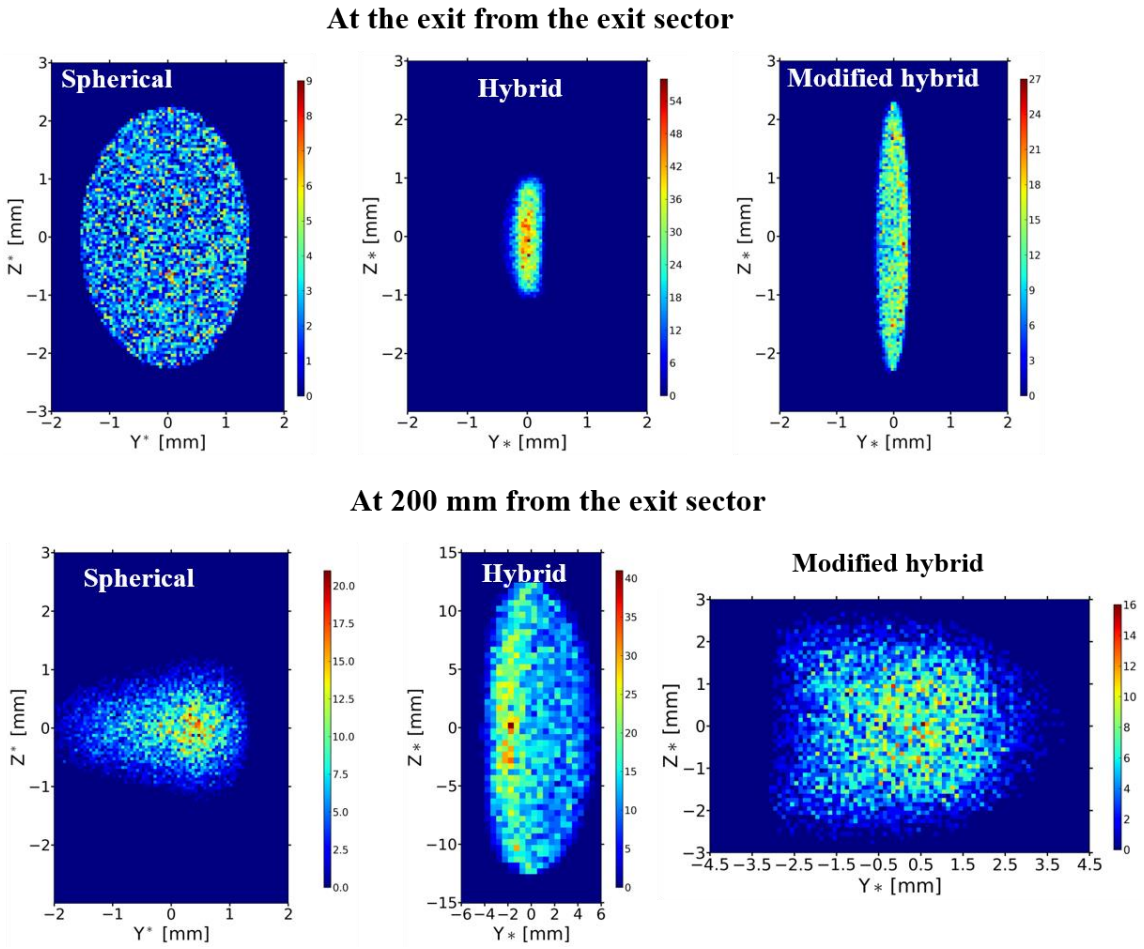

Figure 4. 29: Top: Cross section of the beam at the exit of the sector for the three analysers spherical, hybrid and hybrid plus 80 mm; bottom: cross section of the beam at 200 mm from the exit of the sector.

4.3.2 Comparison of the performances in the final arrangement

As explained in Section 4.3, a magnet with more sophisticated focusing properties was introduced in order to exploit the lens effect of the fringing fields and optimize the conditions for the evaluation of the spheroid geometry based in the concept of the Mattauch-Herzog configuration.

The magnetic sector used in this section was designed and optimized at LIST [107]. It was created with flexibility to vary the entrance and the exit pole face angle and the total bending angle of the magnetic sector to find the optimized parameters to obtain the combination that gives the best mass resolution. The best hybrid result was obtained with the combination of entrance pole angle 50°, exit pole angle -52° and bending angle 75°. The magnetic field applied was 0.8 T and the gap distance was 5 mm.

The distance between the magnet and the electrostatic sector was optimized keeping the parameters found before starting from a minimum distance of 180 mm, to avoid the PAs of the sectors to overlap, to 370 mm, in steps of 10 mm. In each case the mass resolving power was numerically integrated over the mass range 1-238 and the largest value was considered the optimized configuration. Both configurations one with the modified hybrid and one with the spherical are illustrated in Figure 4. 30 and Figure 4. 31 respectively.

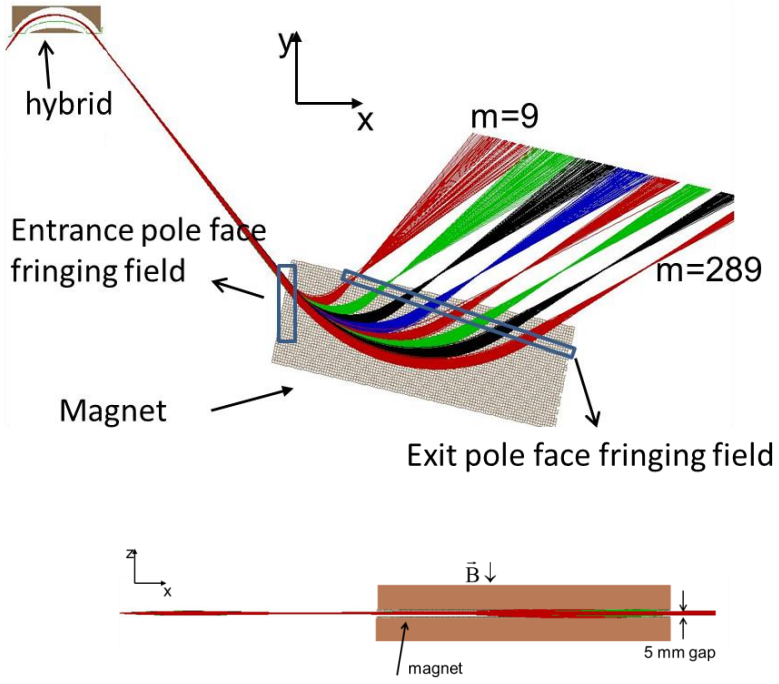

Figure 4. 30: Schematic of both planes of the combination of hybrid sector and the magnet. Entrance and exit pole face fringing fields are remark in blue squares. The different colours show the masses from 9 to 289 with clear focus after the magnet.

In both cases eight groups of particles with different masses were simulated (9, 25, 49, 81, 121, 169, 225 and 289 amu), represented with different colours. The simulation conditions were 2000 particles for each mass, a circle of 100 μm radius with a cone distribution of 2° half angle around the main entrance angle, the particle energy was 4,500 eV with a Gaussian energy distribution with an energy spread of 10 eV. Both planes XY and XZ are shown in the picture as well as two rectangles representing the entrance pole face fringing field and the exit pole fringing field.

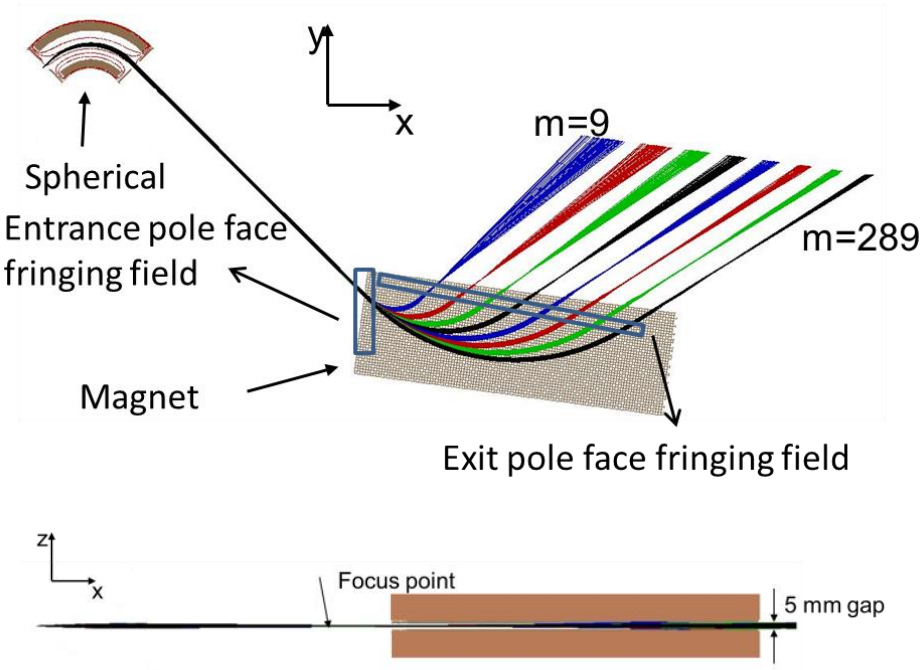

Figure 4. 31: Schematic of both planes of the combination of spherical sector and the magnet. Entrance and exit pole face fringing fields are remark in blue squares. The different colours show the masses from 9 to 289 with clear focus after the magnet.

The process to calculate the mass resolution or the resolving power was developed at LIST and is divided in four steps:

First, the focus point of each mass at the exit of the magnet is calculated. The focal plane is obtained by fitting the positions of the focuses points with a straight line which has included errors in 2D (i.e. X and Y, Figure 4. 32).

Second, the histogram for each mass should be reconstructed in the focal plane coordinates as shown in Figure 4. 33 a) shows the mass spectrum of the hybrid configuration, while b) shows the mass spectrum of the spherical configuration. For masses smaller than 200 amu the peaks of the spherical sector are higher than the hybrid peaks implying a slightly better mass resolving power for the spherical sector in this mass range (Figure 4. 34).

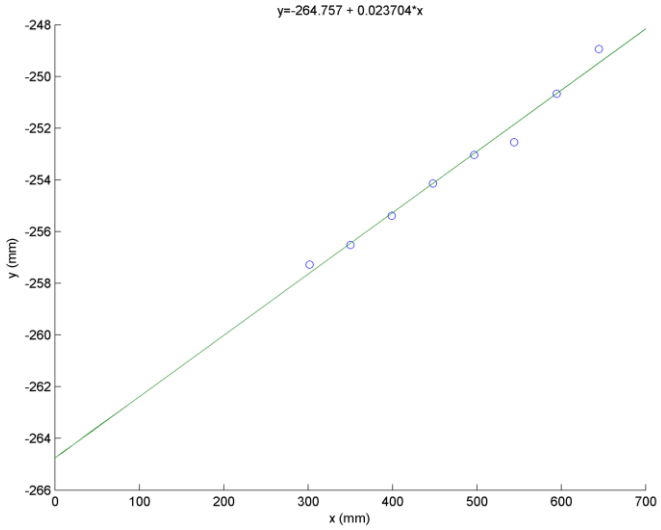

Figure 4. 32: Example of the focus positions of the 8 masses for the spherical configuration fitted with a straight line, which represents the focal plane at the exit of the magnet in the XY plane.

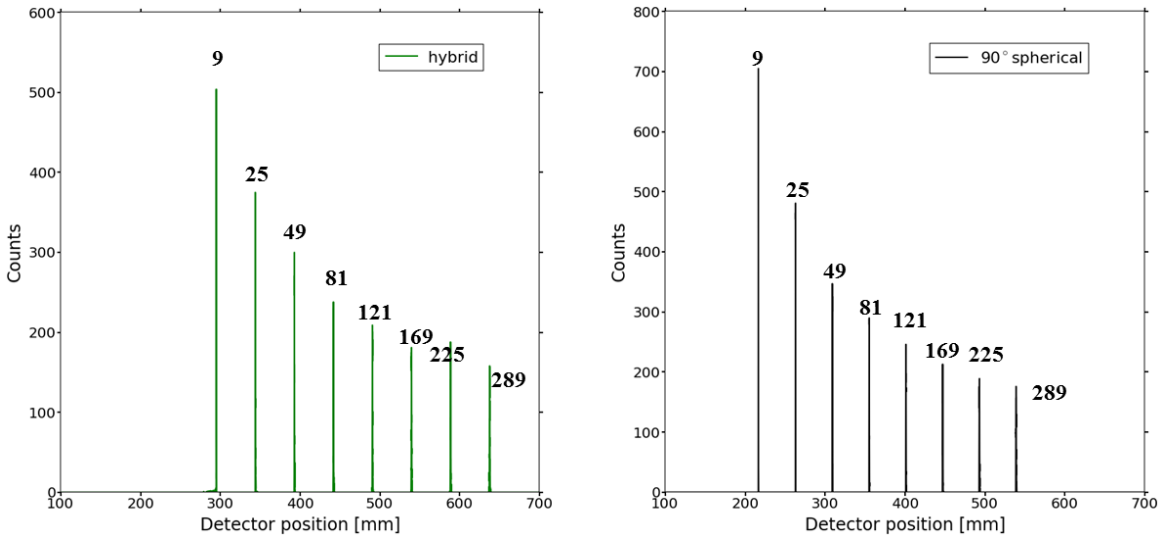

Figure 4. 33: a) Mass spectrum for 8 masses for the configuration with the hybrid, b) mass spectrum for the configuration with the spherical. The spherical configuration has slightly higher peaks. The position on the detector is also slightly different, meaning that the crossover of each mass is in a different position for each sector.

Third, the peak position of each mass peak is plotted against the mass and later is fitted with curve:

$$X' = A \cdot \sqrt{M} \qquad (4.\ 3)$$

Where A is fitting constant. The relation between positions and masses can be expressed by the following relation:

$$\frac{M}{\Delta M} = 0.5\,\frac{X'}{\Delta X'} = 0.5\,\cdot\frac{A\cdot\sqrt{M}}{\Delta X'} \qquad (4.\ 4)$$

Where ΔX' can be calculated by fitting each mass peak with a Lorentizian curve to determine the FWHM. Finally, the mass resolution or its inverse, the mass resolving power, can be obtained and plotted for each mass.

Figure 4. 34 shows the MRP for both systems. In black the spherical analyser and in green the hybrid. Even though both systems have similar resolving power, the spherical sector is slightly better for masses smaller than 200 amu. This is a surprising result showing that even though the hybrid has better energy resolution than the spherical, the whole arrangement performs better with the spherical sector.

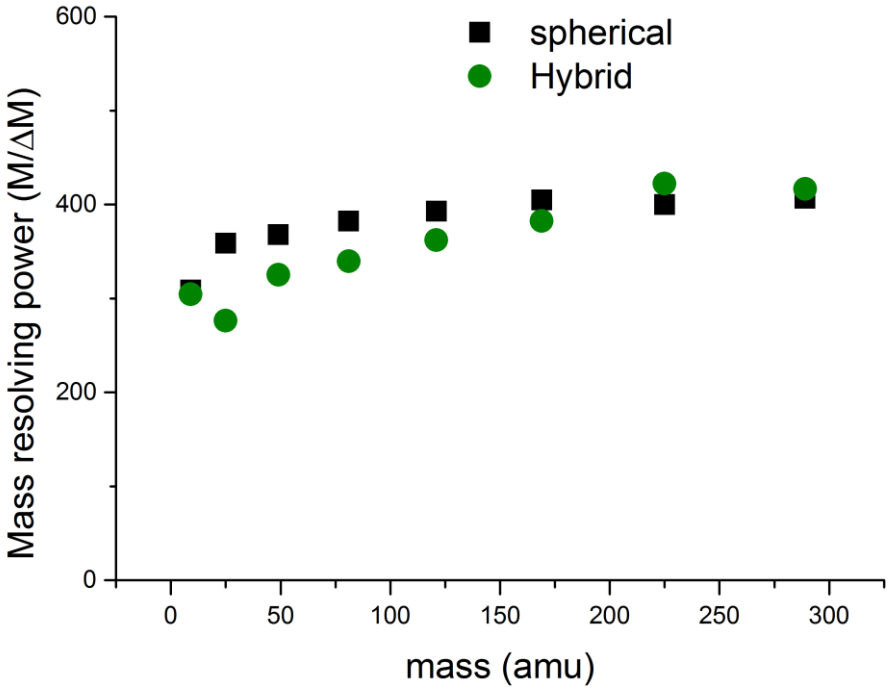

Figure 4. 34: Mass resolving power of both configurations with modified hybrid and spherical sector. Both configurations perform similar, but spherical is slightly better for masses lower than 200 amu.

4.3.3 Analysis of double focusing condition

In order to discuss further the results obtained above, the condition of double focusing was investigated in both configurations. Two groups of particles were simulated, the first one keeping the energy constant at 4,500 eV and varying the opening angle in steps of 0.01° for a total opening angle of 4° and the second group, was simulated keeping the mean entrance angle fixed and the energy was varied in steps of 0.1 from 4495 to 4505, at mass 68, the central radius of the magnet. Figure 4. 35 shows the results for both configurations, the black colour represents the particles of the first group, while the red colour represents the second group. When the crossover of both groups coincides, the double focusing condition is satisfied. Figure 4. 35shows this is the case for the spherical sector, if not, the focus in angle and the focus in energy do not match and the double focusing condition is not satisfied.

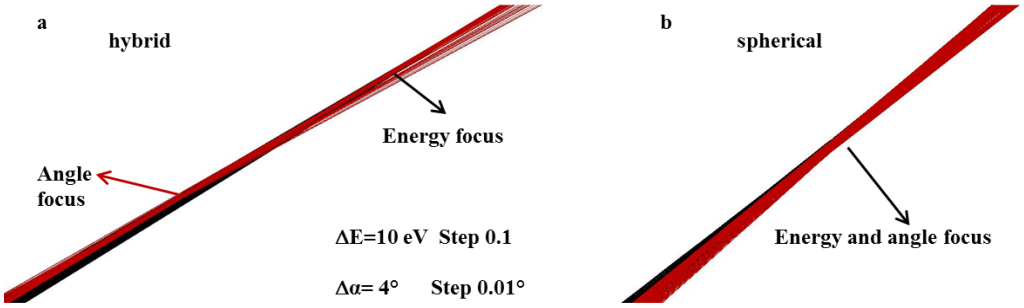

Figure 4. 35: Schematic of the double focusing condition, in both cases the particles were simulated for mass 68 amu and the energy spread was 10 eV in steps of 0.1 eV, the total opening angle was 4° in steps of 0.01°, a) for the hybrid configuration the positions of both focuses are at different places, b) both focusses are at the same place.

The study of the double focusing condition was completed with the investigation of the matching between the dispersion of the magnet the dispersion of the electrostatic sector. In order to obtain the magnet dispersion, the back tracing method was used from the focus point in the focal plane and the magnetic field had opposite sign. The central trajectory of the magnet, mass 68, was selected for this purpose. The dispersion of the magnet was equal to 0.036 mm/eV, while the dispersion of the modified hybrid was 0.012 mm/eV, one third of the magnet dispersion. This is a result of reducing the size of the hybrid to the half to match the 5 mm gap of the magnet.

A quick simulation to investigate the behaviour of both configurations, without taking into account the energy spread, was done to analyse the angular focus. The conditions were the same as before, except that the energy spread was zero.

Figure 4. 36 shows the mass resolving power in this case, here the hybrid shows slightly better mass resolving power for low masses, but subsequently the mass resolving power grows until it is obtained twice the value of the spherical sector. This result shows the potentiality to have better mass resolution with the spheroid geometries if the system is built with a properly energy dispersion matching.

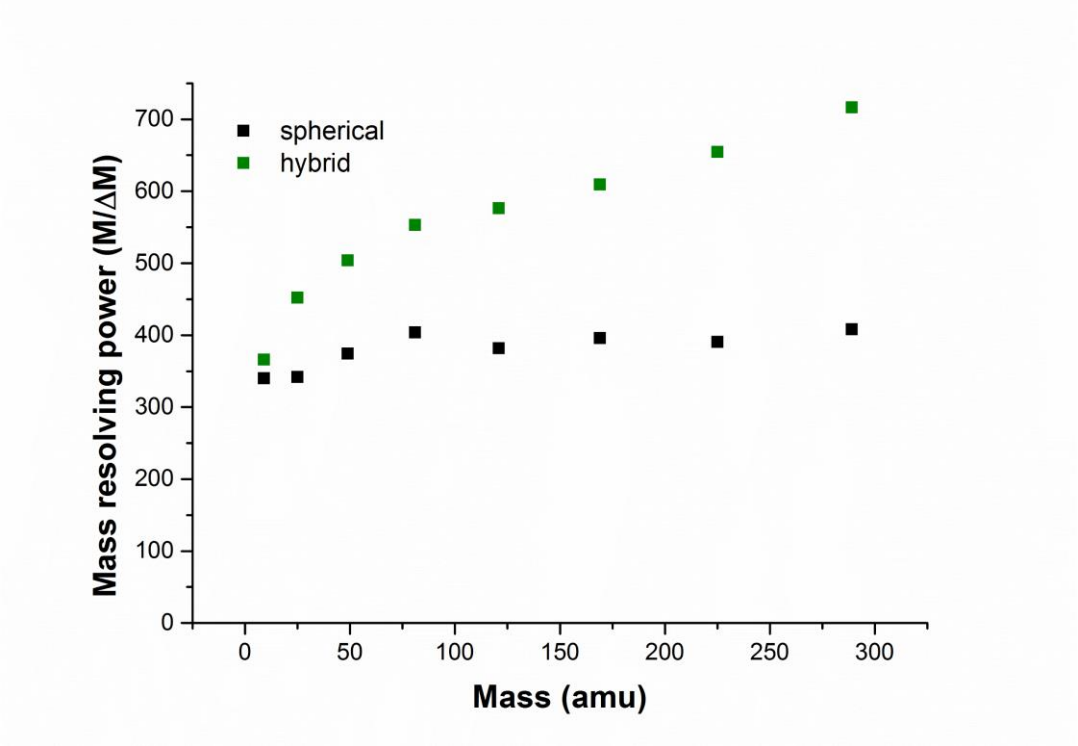

Figure 4. 36: Mass resolving Power obtained without energy spread. The spheroid has slightly better values for low masses, but for the highest masses the values are twice the spherical. This opens the possibility to obtain better mass resolution for the hybrid configuration if the energy dispersion is well matched.

4.4 Comparison between spheroid geometry and standard spherical sector based on a Nier-Johnson configuration

In this Section, the spheroid geometry was investigated in a double focusing spectrometer based on the Nier-Johnson configuration. This spectrometer, contrary to the Mattauch–Herzog configuration, is designed with focus beam at the exit of the electrostatic sector. A model of the secondary optics of the Cameca XF series spectrometer was provided to LIST by J. Lorincik. In this case the spheroid sector reproduced previously was chosen for the comparison because has better focusing properties than the hybrid for the focus to focus beam.

4.4.1 Comparison in the IMS 4F Cameca

Figure 4. 37 shows a SIMION's workbench picture of the standard secondary optics of the Cameca IMS XF series used in this work. The main components were explained in Section 3.3, here they are just numbered, from the sample to detection system. The magnet is a dummy potential array, the straight line is the trajectory of the particles simulated by a user program, a transfer matrix that estimates the position of the particles at the entrance and at the exit of the magnet. The dotted line, represents the real curved trajectories of the particles in the magnetic field.

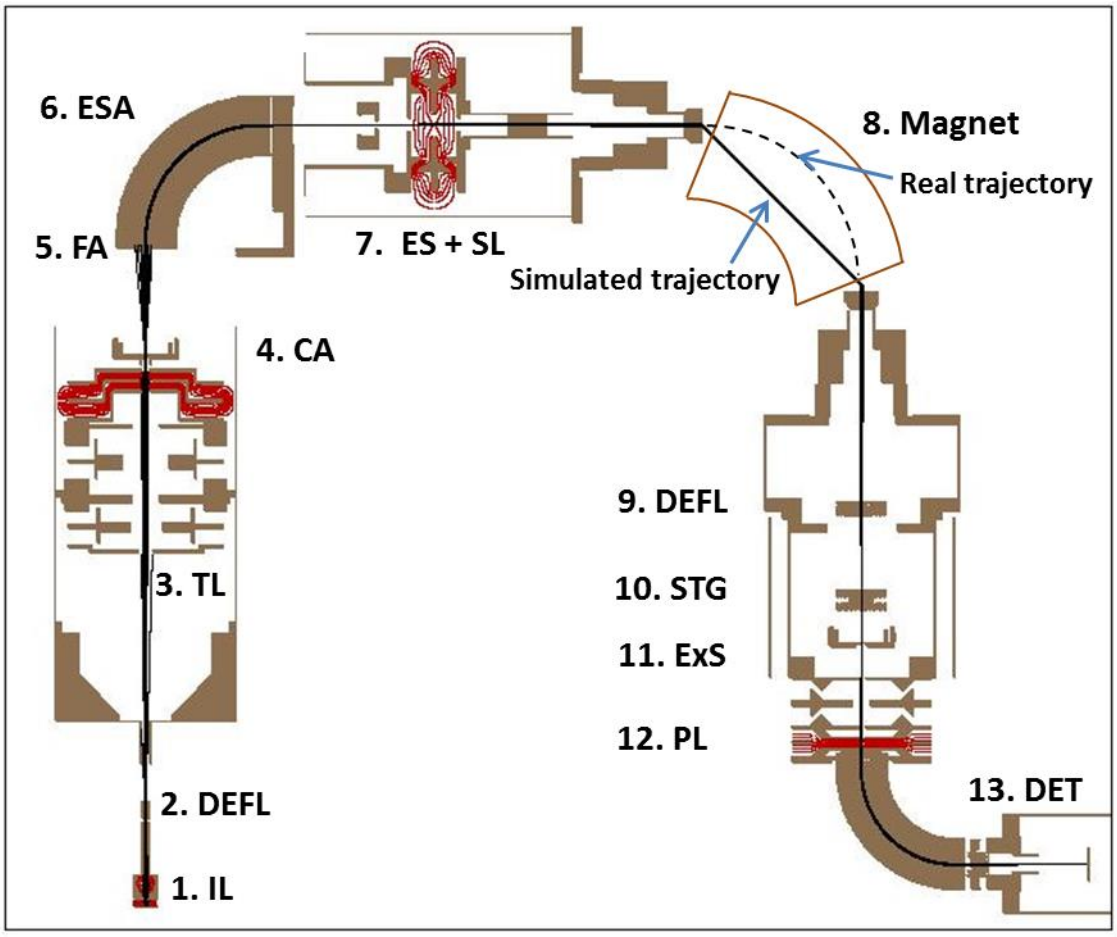

Figure 4. 37: SIMION's workbench picture of the model of the Cameca IMS XF secondary optics. The main parts are highlighted with numbers and names.

The spheroid geometry was placed instead of the spherical sector and the optics before the spheroid was tilted 3° because the spheroid total bending angle is 93°. The contrast aperture acts as a source for the spheroid, and the focus point after the spheroid coincides with the position of the energy slit equal as the spherical case (Figure 4. 38).

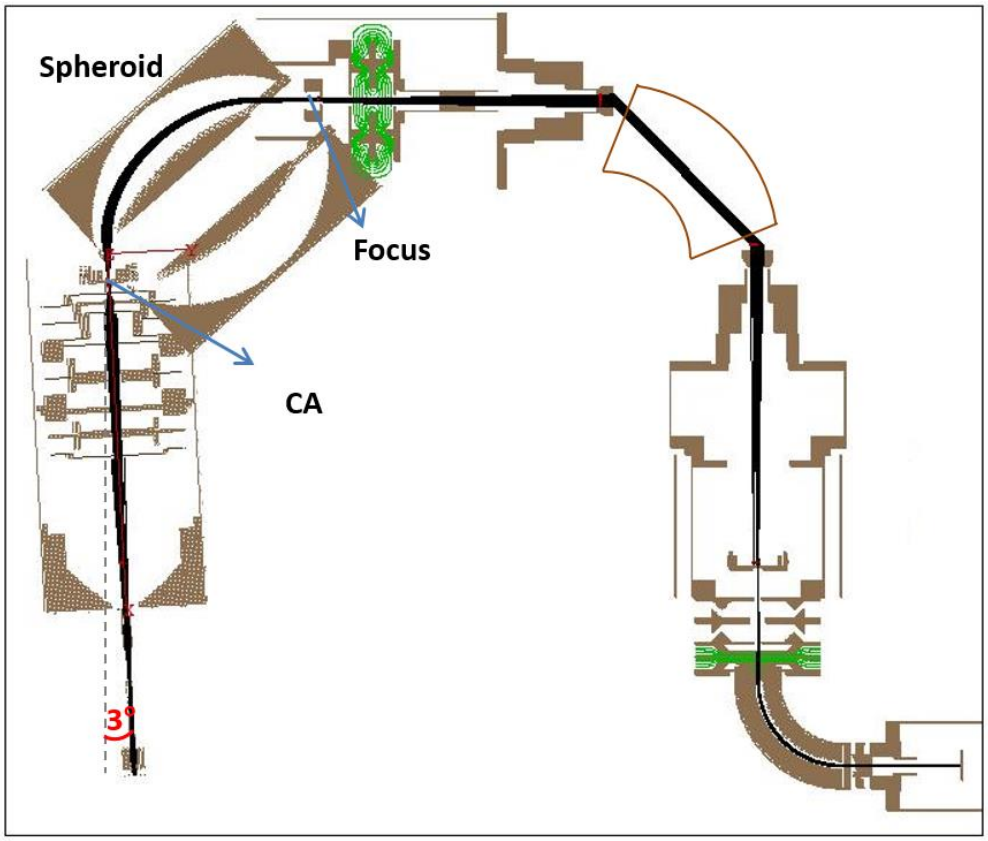

Figure 4. 38: SIMION's workbench picture of the model of the Cameca IMS 4F secondary optics with the spheroid. The optics before the spheroid was tilted 3°, the CA acts as a source for the spheroid which focus the beam at the energy slit.

The spherical sector described in chapter 3 was also simulated in this configuration for comparison (Figure 4. 39). The position of the focus is also at the position of the energy slit equal to the cases above. The opening angle in the three cases was measured and adapted to be the same in the three cases. The original designed has a round aperture in front of the shunts that limits the opening angle to 1.7° when the CA aperture of 50 µm was used. In this work there is no aperture to limit the entrance opening angles which are 10.4°; and 9.2° for the spherical sector and the spheroid respectively. To have the same conditions in the three cases the spherical sector designed in this work was modified, closing the entrance and the exit shunts to limit the opening angle to 1.7° as shown in Figure 4. 40 The opening angle in the spheroid configuration was limited by introducing a round aperture before the entrance grid.

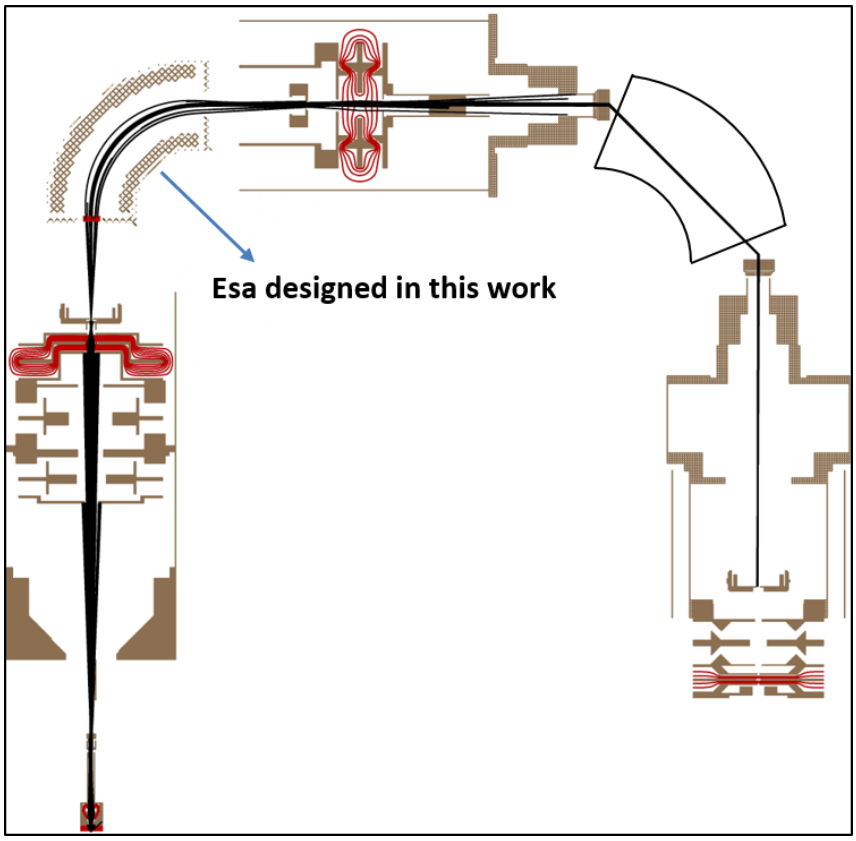

Figure 4. 39: SIMION's workbench picture of the model of the Cameca IMS 4F secondary optics with the spherical designed in this work.

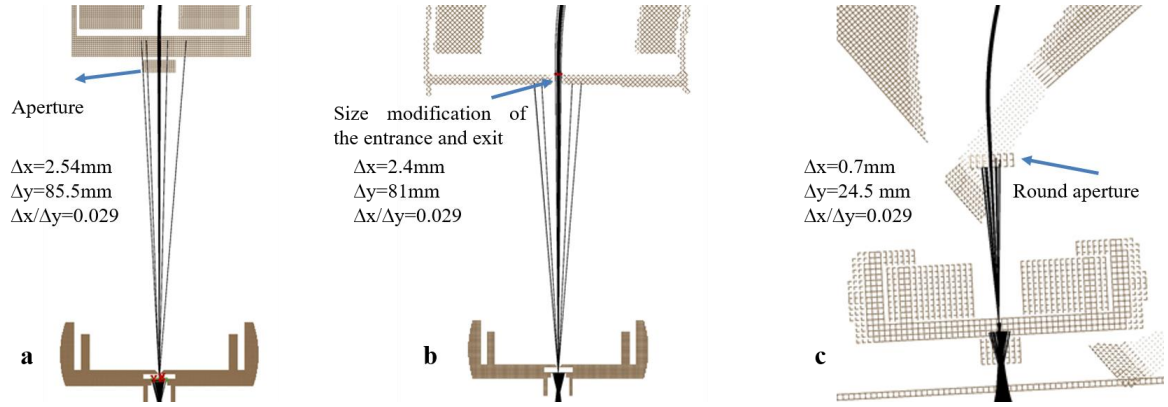

Figure 4. 40: a) XY cross section of the SIMION workbench showing the beam path between the contrast aperture and the electrostatic sector; a) the original design includes a round aperture which limits the opening angle to 1.7°; b) schematic of the spherical designed in this work with a reduced entrance and exit shunts to limit the opening angle to 1.7°; c) schematic of the spheroid configuration a with round aperture that limits the opening angle to 1.7°.

In all cases the particles were generated programmatically by a user program using a Monte Carlo method to reproduce the sputtering phenomena, including the energy and angle distribution of the particles. The initial positions, angles and energy are generated using a random function. The initial kinetic energy distribution of the secondary ions can be expressed in terms of the surface binding energy *U* and the energy (written as random variable):

$$\mathrm{E} = \frac{\mathrm{U}\cdot\left(\mathrm{rand\ E}+\sqrt{\mathrm{rand\ E}}\right)}{(1\text{-}\mathrm{rand\ E})} \tag{4. 5}$$

Producing energies according to the equation 3.3 theory (see Section 3.2.3). The polar emission angle, in SIMION is the complementary angle of the elevation angle, was simulated with a cosine distribution:

$$\varphi = \cos^{-1}(\mathrm{rand}\ \alpha) \tag{4. 6}$$

Where *rand α* is the variable that generates random values between 0 and 1.

The following parameters were chosen for the simulation: 50,000 particles for each mass, masses 17 and 17.02, the beam raster area 1 μm, the surface binding energy *U*=4 eV, spectrometer lens 2,850 V, only the first transfer lens was energised at 4,234 V, sample voltage 4,500 V, immersion lens voltage 3,208 V, contrast aperture 50 μm, no field aperture, energy and exit slits wide open. All voltages were taken from [108] and are in agreement within 4% with the values measured at the IMS 4F spectrometer at LIST.

Initially, the FW50 only in one dimension was calculated to identify the focus position after the magnet of the three configurations. Figure 4. 41shows the minimum one-dimensional FW50 calculated in one dimension, in the X direction. The original design has a range of minimum values when y varies between -380 and -370 mm, with a minimum value of 0.005 mm at y=-373 mm; the configuration with the spherical sector designed in this work presents a broader range of lowest values between -380 and -360 mm with a minimum value of 0.014 mm at y=-373 mm; while the spheroid shows a very narrow region around y=-382 mm with the highest value 0.04 mm. A higher beam width implies that the spheroid sector will have a broader peak, which means a lower mass resolution. Thus, in order to understand the beam propagation and find the y value where each configuration has the best mass resolution several cross sections were measured, between y values that go from -343 to -413 mm. be worse in the spheroid case, because the beam is broader in X direction than the other cases (Figure 4. 42) The histograms in 1D in the focus point position were plotted and the mass resolution in the three cases was calculated.

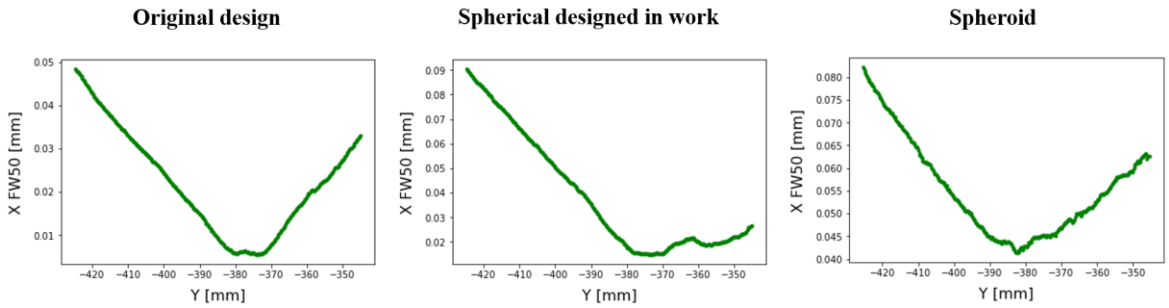

Figure 4. 41: FW50 only calculated in one dimension, in the dispersion direction. The original design has approximately 10 mm range where the values are minimum (0.01 mm), the spherical designed in this work has 20 mm width (lowest values than 0.02 mm) and the spheroid is a region very narrow around y=-382 with a value of 0.04 mm. This suggests that spheroid configuration will have a worse mass resolution.

The histograms in the dispersion plane show a FWHM for the original case of 0.02 mm, resulting in a MRP of 13,076 and a total transmission of 2.8% of the initial particles. The spherical designed in this work has a FWHM of 0.02 mm, giving a MRP of 13,076 and total transmission of 2.7%; however, the height of the peaks are two thirds the height of the original design. The spheroid configuration has a FWHM of 0.08 mm, giving a MRP of 3,178 and total transmission of 5%. These results show that the configurations with the spherical sectors perform four times better that the spheroid configuration (Figure 4. 43).

This result shows that the spherical sector performs better in both cases than the spheroid in a Nier-Johnson configuration, which was not expected because the spheroid has two orders of magnitude better energy resolution. A reason for this is that the beam propagates differently after the focus point at energy slit. The difference in the focus points coming out from the spheroid in XY plane and in XZ plane remains through the optics generating a mismatching in the angle focus of the spectrometer.

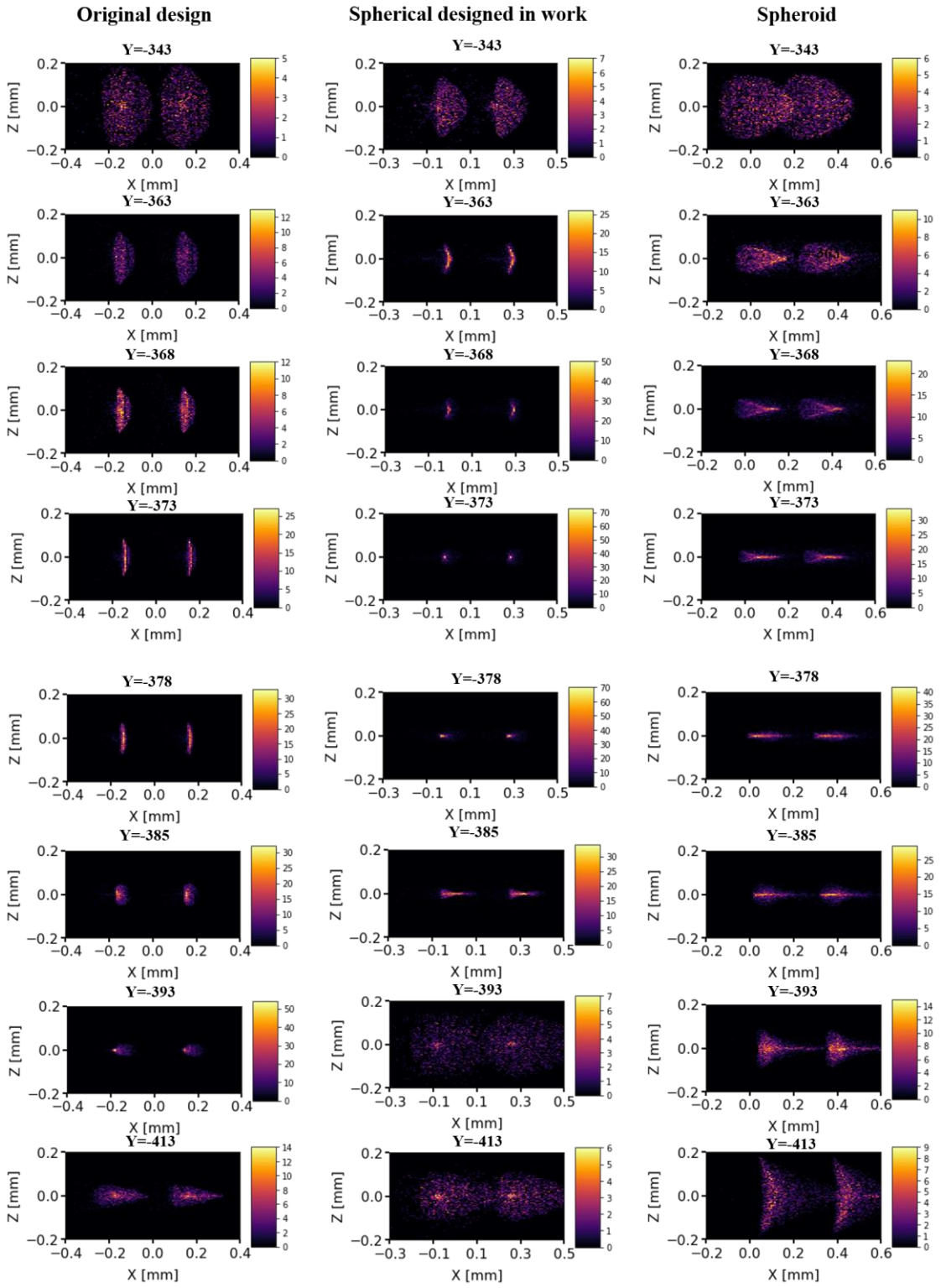

Figure 4. 42: Cross section of the beam at different Y positions: -343; -363; -368; -373; -378; -385 (at exit slit); -393; -413; for the three configurations. The spherical configurations go from big oval shape to a vertical line, a dot, a horizontal line to end dig oval shape horizontally aligned. The spheroid configuration goes from the big oval to the horizontal line without having a vertical line, limiting the value of the mass resolution.

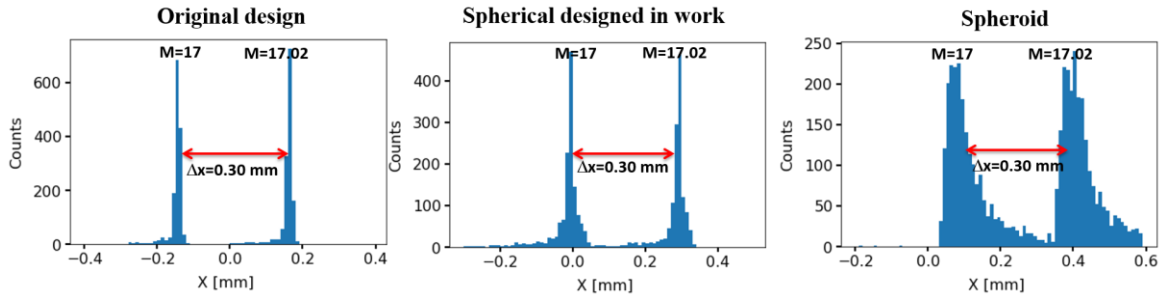

Figure 4. 43: Mass spectrums obtained in the focal plane of each configuration. The original design has the focus plane at y=-378 mm, M/ΔM=13,076; the spherical sector designed in this work has its focal plane at y=-368 mm, M/ΔM=13,076, equal to the original design. The spheroid configuration has its focus at y=-393 mm and M/ΔM=3,178. The mass resolution of the spheroid configuration is four times smaller than the configurations with the spherical sector.

4.5 Summary and conclusions

- The spheroid geometry was reproduced in this work to be evaluated in a double focusing mass spectrometer. The spheroid reproduced showed of 3rd order focusing and not 13th as reported in literature. The conditions for higher order focusing were different from literature. However, for a total opening angle of 9° the spot size was 8 μm and the energy resolution was 0.006%, compared to the literature, with 12° opening angle and spot size of 10 μm. The differences between the two models come from the fact that the geometry of the spheroid is very asymmetric at the entrance and some parameters were not reproduced exactly. In addition, the CPO program used in this work was SIMION, while in literature the simulation was done initially with SIMION and then with BEM, consequently the grids were simulated in a different manner, thus the optical properties vary from one model to other.
- A new model of the spheroid geometry with a third electrode in order to couple with the magnet and work in deflecting mode, named hybrid, was designed.
- A standard 90° spherical sector was also simulated to be compared with the previous geometries in different conditions. The response of all the analysers to different source sizes was evaluated for focus to focus beam and for a focus to parallel beam, and in both cases spheroid geometries perform better than the standard spherical sector for source sizes smaller 100 μm.
- A table comparing main characteristics of the three analysers in their best conditions for focus to focus beams was calculated. In retarding mode, the spheroid geometry has better energy resolution, 0.006% while in deflecting mode, the hybrid had better energy resolution when the optical path was not at the central position 0.53%.

- A comparison with the spheroid and spherical sectors in combination with a simple magnet based on Mattauch-Herzog configuration was performed. The spheroid geometry had very strong focus point in XZ plane producing a big dispersion in Z direction, thus the beam was not parallel in this direction, affecting the focus in the XY direction. To circumvent this effect and beneficiate from the better properties of the spheroid, several modifications were introduced. The magnet was changed to a magnet with fringing fields to focus the beam in the Z direction and to enhance the focusing in the dispersion plane. The spheroid was changed to the hybrid analyser, in which the distance to the axis of rotation was modified obtaining a weaker focus in the XZ plane and the size was reduced to the half in order to have a beam entering into the magnet gap smaller than 5 mm.
- The final comparison between the half size modified hybrid and spherical sector with a magnetic sector with fringing field showed that mass resolving power of both configurations was similar from masses 300 to 400, but slightly better for spherical sector for masses lower than 200 amu. The energy dispersion of the magnet and the half hybrid do not coincide, the dispersion of the first one is three times bigger that the half size hybrid. A simulation done without energy spread showed that the hybrid configuration performs two times better than the spherical configuration for high masses. This suggests that designing a system where the double focusing condition is optimized, the mass resolution could be enhanced by only changing the electrostatic sector.
- A comparison in a Nier-Johnson type spectrometer, the secondary optics of the Cameca IMS XF series was made between three configurations: the original configuration, a configuration with the spherical sector designed in this work and an arrangement with the spheroid. The size of the entrance and exit shunts was modified in the spherical sector designed in this work, and a round aperture was incorporated in front of the grid to limit the opening angle in the three cases to be the same 1.7°. The mass resolution of the spherical configurations was 13,076 and a total transmission of 2.7-2.8%. The height of the peaks of the configuration with spherical designed in this work was two times the height of the original design.The mass resolution of spheroid configuration was 3,178 and total transmission of 5%. These results show that the configurations with the spherical sectors has four times better mass resolution, however the sensitivity was two times larger for the spheroid case.
- The analysis of the beam propagation after the magnet showed that the beam in the spheroid configuration was rotated 90°, harming the mass resolution. The behaviour of the beam after the spheroid is complex to understand. The difference in the focus points coming out from the spheroid in XY plane and in XZ plane remains through the optics generating a mismatching in the angle focus of the spectrometer.
- The spheroid analyser is a more complex geometry to design and build than the spherical sector, but combined with a proper magnet in a configuration especially designed for its optics, could result in spectrometers with better mass resolution and sensitivity.

5 Surface Analysis by SIMS with a Multi-Ion Beam

5.1 Introduction

Imaging SIMS has become an indispensable analytical tool in many fields, including material sciences, biology, cosmo-chemistry, geosciences, to mention some. The state-of-the-art in high resolution imaging SIMS, is the Cameca NanoSIMS 50, with high spatial resolution, values down to 50 nm [109]. There is an emerging technique TOF with clusters ions, that can achieve lateral resolution also down to 50 nm [110]. Nevertheless, in the last two cases the main drawback is that high resolution imaging requires very small size probes, which usually means very low primary currents, in the order of pico-amperes or less and the area of analysis is sometimes limited to to small fields of view. For example, the maximum FOV of the NanoSIMS is 50 x 50 μm^2. The small current leads to long acquisition times and small FOVs require many images to be stitched together to form a mosaic leading to stitching errors and intensity variations form image to image. These issues make the NanoSIMS (or TOF-SIMS with clusters) unsuitable for large area imaging or 3D reconstruction. One application for large area imaging is the mapping of biological systems e.g. entire rat brains. The size of the entire rat brain is more than 3 cm^2 [12]. To be imaged with high resolution imaging techniques, the tissue should be scanned through 30.000 x 30.000 μm^2, which means 600 tiles of 50 x 50 μm^2. If each tile consists of 512 x 512 pixels, equivalent to 100 nm probe size (not the smallest probe), and with a dwell time per pixel of 5 ms/pixel, each tile image will take 21.8 min, then the scanning time of the complete tissue will be 218 hrs (9 days), only for one complete surface image. For a 3D reconstruction will be necessary several layers of the sample (scans), for a minimum of 10 layers, the total acquisition time will be equivalent to 90 days of continuous operation. In conclusion, a machine that can perform high resolution imaging SIMS for larger areas or 3D imaging, in an acceptable time, is still really missing.

Previously, the only way to reduce the analysis time has been through the development of high brightness sources in order to increase the primary currents and keeping the small probe size. Here in this work, the aim is to develop a multi-ion-beam, where instead of only one beam, several ion beams with probe characteristics comparable to the NanoSIMS probe, scan the sample simultaneously.

The concept of multi-beam was first introduced in the electron beam community to improve the throughput of the electron beam for pattern generation [111] and is also used for electron beam lithography for the production of nanotechnology [112], but this is the first time that a multi-ion-beam system was investigated for SIMS analysis. When the sample is scanned by n-beams, the scanning time is reduced by n-times. Taking the previous example of the brain tissue, if the sample would be rastered by 100 beams, the analysis time would be 100 times shorter, approximately 2.2 hours for a 2D image, and the 3D reconstruction would take less than a day. In consequence, analyses that currently seem

unfeasible could be done in a few hours, what creates a fully new world of opportunities in the nano-analytics field.

In this chapter, the fundamental concepts of the technique of multi-beam will be explained (5.2) as well as results from initial simulations (5.3) and the experimental results (5.4) that support the proof-of-concept of the multi-ion-beam for SIMS imaging.

5.2 Fundamental concepts:

The concepts of multi-beams were introduced in the community of electron beam systems which try to develop devices for different fields such as microelectronics [113–115], micro fabrication [116] and material science. They demand an ever-increasing spatial resolution and throughput in electron optical systems. However, the better was the spatial resolution, the worse was the throughput because the probe current is proportional to the square of the source image in the probe [117]. In consequence, the electron beam community has been developing different multi-beam systems with different approaches, which can be divided in to 4 categories (Figure 5. 1):

a) multi-axis systems: an array of sources each with a corresponding optical column;
b) multi source, single column system: an array of sources that are delivered to a single optical column;
c) single source, single column system: multiple beams are created from one single source and delivered to a single column; and
d) single source, multicolumn systems: multiple beams are created from one source and each is delivered to a corresponding optical column [117] .

In this work, the model single source- single column (c) was chosen because the machines available to proof the concept of the multi-ion-beam at LIST´s laboratory, have this configuration, (Cameca IMS 4F and IMS 6F).

The Cameca IMS XF instruments are especially convenient to make a proof-of-concept of multi-ion-beam in SIMS imaging because they have two modes of operation that usually are implemented independently: the microscope mode and microprobe mode. As explained in chapter 3, in the microprobe mode, a finely focused primary beam (hundreds of nm to few μm) is rastered across the sample surface while the secondary ions transmitted through the spectrometer are correlated electronically with the position of the primary beam and an image with spatial resolution around the probe size is obtained. In the microscope mode, the primary beam is much broader (40 μm or larger), all points are simultaneously imaged within the FOV in real time, making the acquisition time extremely

fast. The image resolution is limited by the secondary optics which is lower than the resolution in microprobe mode.

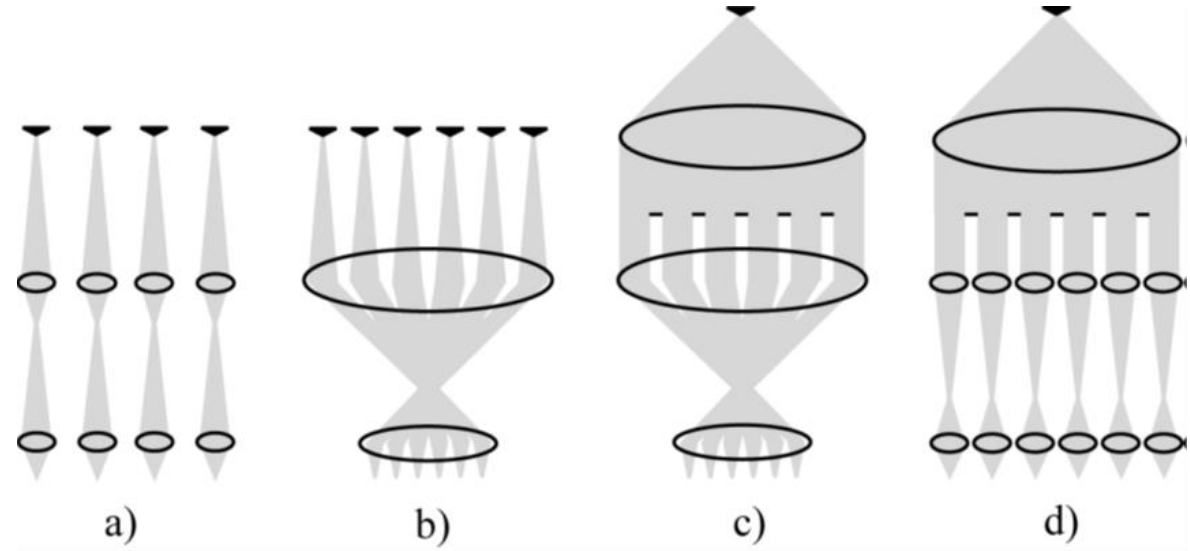

Figure 5. 1: Schematic of the four possible combinations to obtain multi-beams reproduced from (1); a) multi-axis systems; b) multi source, single column system; c) single source, single column system; d) single source, multicolumn systems. The option c was used in this work.

Combining both modes simultaneously, a new hybrid mode is created, which enables with the aid of a multi-hole aperture to generate the multi-ion-beam system. By using the microscope mode, the primary optics is settled in Köhler illumination, making an image of the multi-hole-aperture on the sample. In addition, the stigmatic secondary optics focus the multi-ion-beam on a position sensitive detector (MCP) that reproduces the contribution of each beam in space. The microprobe capability provides the function of the beam raster, so the multi-ion-beams generated in the primary optics and focused on the sample, can be scanned over the sample at the same time, exactly in the same way as one microprobe.

When microscope mode is on, the aperture strip is illuminated homogenously (Köhler illumination), and a demagnified image of the aperture is projected on to the sample. If the standard aperture with a simple circular hole is replaced by an aperture with several small holes, then several micro beams will be generated and focused on the sample that can be scanned across it, like the microprobe mode (Figure 5. 2).

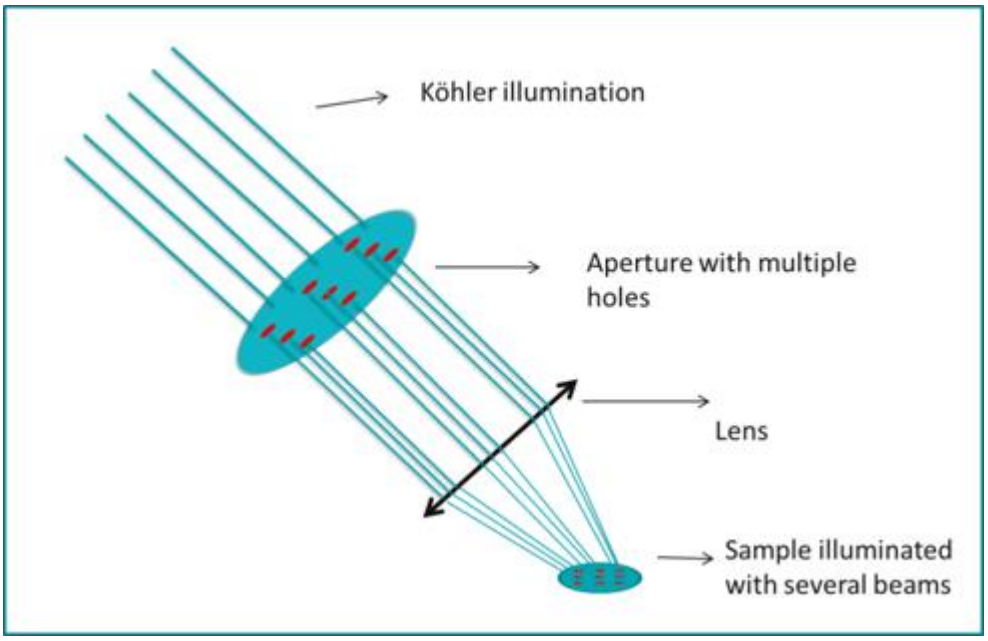

Figure 5. 2: Schematic of the generation of the multi-ion-beam by the illumination of the multi-hole aperture with the Köhler illumination. Several beams are focus on the sample and later are rastered.

The Figure 5. 3 shows the comparison between scanning an area with one beam (a) and the same area with nine beams (b). The length covered by one of the nine beams is one third in both directions (horizontal and vertical) of the single beam. Translating this into scan time, each beam of the multi system will spend one ninth of scan time compared to the single beam, as the 9 beams are scanning at the simultaneously, the total area is covered 9 times faster. Consequently, for N beams, the acquisition time will be 1/N, what it means that the time analysis will be reduced N times.

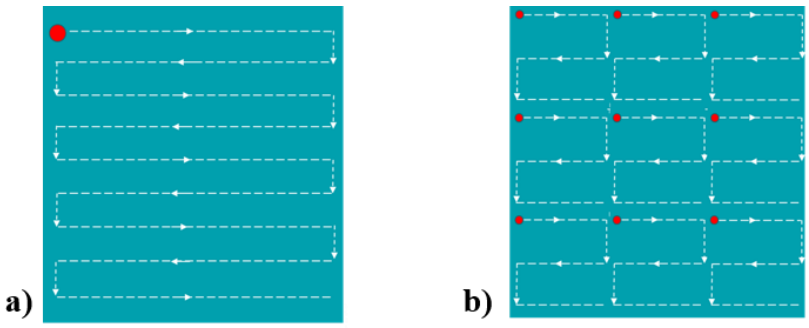

Figure 5. 3: Schematic of the beam scanning; a) raster certain area with one beam; b) raster the same area with nine beams. The time spent for rastering the same area with nine beams is one ninth of the time rastering with one beam.

5.3 Simulations:

The objective of the simulations was to make a preliminary investigation of the performance of the multi-ion-beam that flows through the mass spectrometer, to analyse the minimum distance between the spots on the sample that could be clearly distinguished on the microchannel plate and to investigate the limitations of the technique.

This information provides a first understanding of the feasibility of the multi-ion-beam concept, the potentiality of the technique and set an initial basis for the design of the multi-hole aperture.

Similar to chapter 4, the simulations were carried out using the model of the secondary optics of the IMS Cameca 4F in SIMION. As the spectrometer worked in microscope mode, the images (data) were recorded on the detector (in practice the MCP). The following parameters were chosen for the simulations: ion mass 17, surface binding energy Us=4, ESA voltages +500V and -547 V, spectrometer lens voltage 2,850 V, second transfer lens voltage 4,324 V, sample voltage 4,500V, immersion lens voltage 3,208 V and contrast aperture 50 and 400 μm, no field aperture. The measured values on the IMS 4F at LIST where within 4%. The projector lenses values were measured in the instrument and implemented in the simulation, for the different magnifications the values in image mode were:

Pre-set	Second lens (V)	First lens (V)
1	4115	4342
2	4151	4141
3	4185	3967
4	4222	3773
5	4292	3580
6	4363	3380

Table 5. 1: Values of the voltages of the projector lenses measured at the IMS 4F at LIST. The different pre-sets give bigger images on the MCP/FS.

Initially, the secondary emission coming from one single spot of 1 µm diameter was simulated to understand the main characteristics of the physical principles involved. The simulation conditions were: 50,000 particles departing from a full circle of 1 µm diameter following the cosine law of secondary emission, generated by the Monte Carlo method explained in chapter 4. The spot was in the centre of the optical axis, (0,0). Figure 5. 4 shows a 2D histogram of the image recorded at the detector place, with a line scan fitted with a Lorentzian function due to the tail of the function. This tail indicates a limitation in the lateral resolution, when the spots are closed the tails overlap increasing the background noise and reducing the quality of the image of each spot. This is an intrinsic limitation for the lateral resolution in the secondary optics of the IMS 6F.

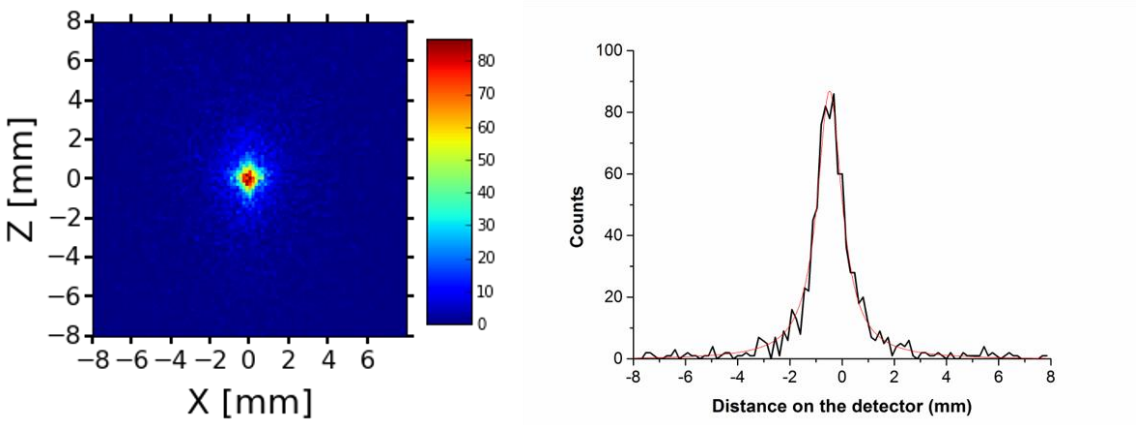

Figure 5. 4: Left: 2D histogram recorded on the detector of one spot on the sample with 1 µm diameter, right: line scan in black and Lorentzian fitting in red of the left image. The peak is centred on X=-0.59 and the FWHM= 1.23. Magnification 6.

Afterwards, the emission of the secondary ions was simulated coming from the sample as nine different spots arranged in a square matrix all of them equidistant. A layout is depicted in Figure 5. 5. The spots were full circles of 1 µm diameter, 20,000 ions were generated from each spot per run, (total of 180,000 ions). The distance between centres was reduced from 10 µm, 5 µm and 3 µm, the contrast aperture was 50 µm (Figure 5. 6 to Figure 5. 11).

The images show a 2D histogram obtained of the recorded positions of the particles hitting the detector (MCP). The information presented is spread in 16 mm in X and Z directions, with 100 bins in each direction, a total number of bins of 10,000. The size of the beam corresponds to 0.16 mm. A line scan of the middle row was done in each case and was fitted with a Lorentzian curve as before.

Figure 5. 6 is pattern of 3 x 3 beams separated 10 µm, centre to centre, the line scan shows that the spots can be resolved only at FWHM.

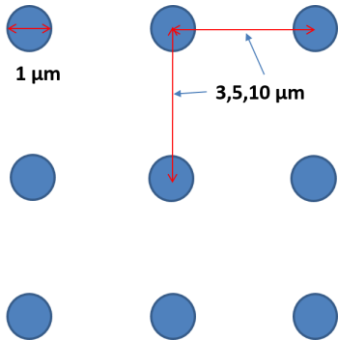

Figure 5. 5: Schematic of the matrix of spots where the secondary ions depart from the sample. Nine beams of 20,000 particles equidistant separated centre to centre: 10, 5 and 3 µm.

However, Figure 5. 7 is the same pattern but the projector lens setting used in this case was 4 (overall magnification approximately 300), the line scan shows that spots are resolvable at the base. Figure 5. 8 shows a pattern 5 µm centre to centre, in magnification 4, the spots are much closer, but the peaks are resolved at 25 % of the base. Following the same pattern, but increasing the projector lenses to number 5 (overall magnification approximately 400), Figure 5. 9 shows that the spots are more separated. When the pattern was changed to spots separated 3 µm centre to centre, the distance of spots on the detector is also reduced, the tails overlap and the peaks are resolvable at the 35 % of the height (Figure 5. 10). Changing the projector lenses to number 6 (overall magnification approximately 500), do not improve the quality of the image, the peaks are resolvable only at FWHM.

Finally, a simulation in a nano-scale was done to evaluate the performance of the system. The particles were simulated from spots of 200 nm, in the maximum magnification in two cases: contrast aperture was 50 µm and 400 µm (Figure 5. 12- Figure 5. 13). In both cases the total number of ions the spatial resolution was the similar to the case of probes of 1µm, this implies a limitation in the Cameca secondary optics, even if the probes are reduced in size, enlarging the relative distance, the lateral resolution was not better due to the tail of the function.

Figure 5. 14 shows the superposition of three times one spot separated by 2 mm, similar to the line scan of the middle row of Figure 5. 11 . This is another example to illustrate the contribution of the tail to the lateral resolution.

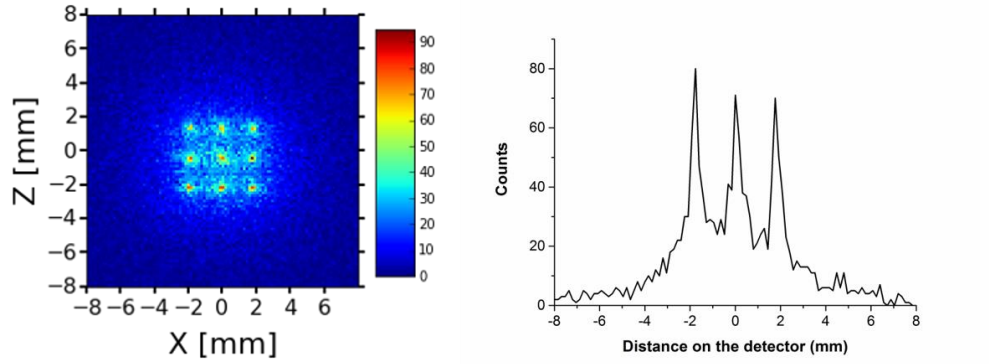

Figure 5. 6: Left: 2D histogram recorded on the detector of 9 spots on the sample with 1 µm diameter, separated **10 µm;** right: line scan of the middle row. Peaks centred on X_1=-1.78 FWHM=0.65, X_2=0.05 FWHM=0.85, X_3=1.8 FWHM=0.51. **Projector lenses pre-set 3**.

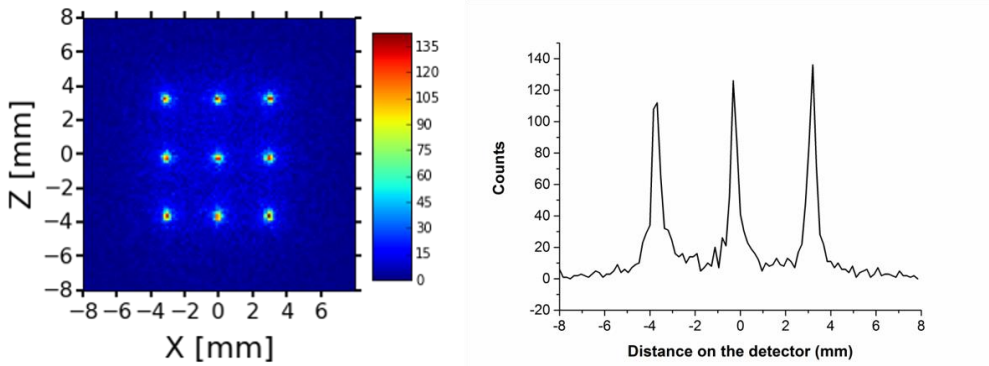

Figure 5. 7: Left: 2D histogram recorded on the detector of 9 spots on the sample with 1 µm diameter, separated **10 µm;** right: line scan of the middle row. Peaks centred on X_1=-3.73 FWHM=0.42, X_2=-0.27 FWHM=0.35, X_3=3.17 FWHM=0.36. **Projector lenses pre-set 4**.

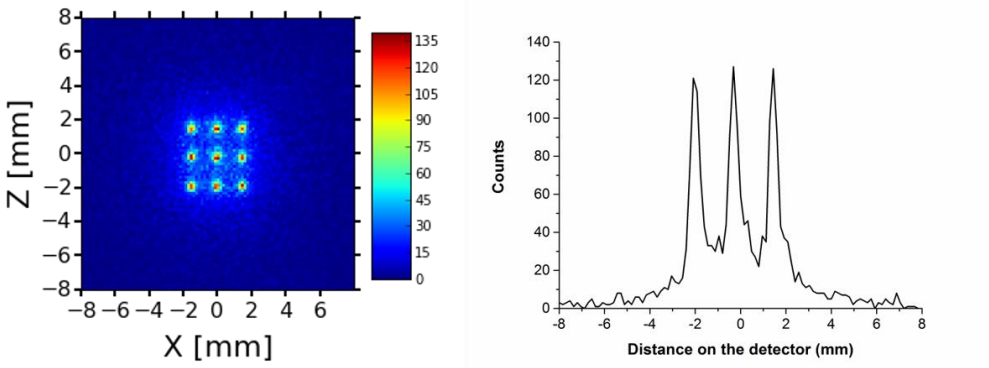

Figure 5. 8: Left: 2D histogram recorded on the detector of 9 spots on the sample with 1 µm diameter, separated **5 µm;** right: line scan of the middle row. Peaks centred on X_1=-2 FWHM=0.47, X_2=-0.29 FWHM=0.56, X_3=1.44 FWHM=0.5. **Projector lenses pre-set 4.**

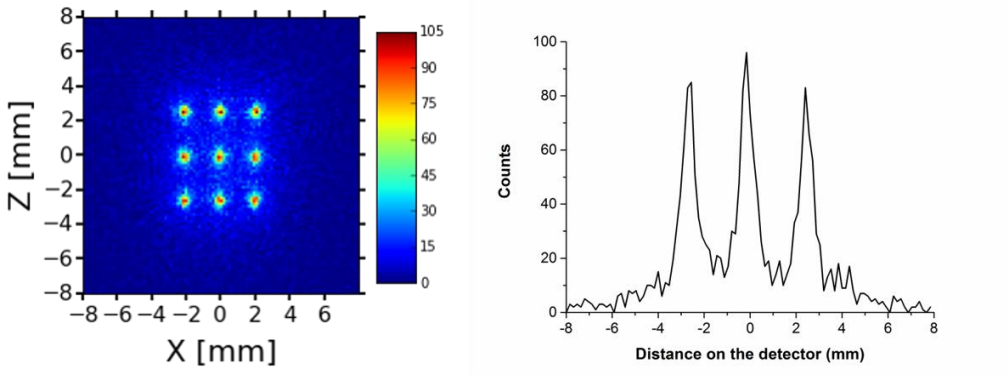

Figure 5. 9: Left: 2D histogram recorded on the detector of 9 spots on the sample with 1 µm diameter, separated **5 µm;** right: line scan of the middle row. Peaks centred on X_1=-2.66 FWHM=0.68, X_2=-0.15 FWHM=0.68, X_3=2.44 FWHM=0.67. **Projector lenses pre-set 5.**

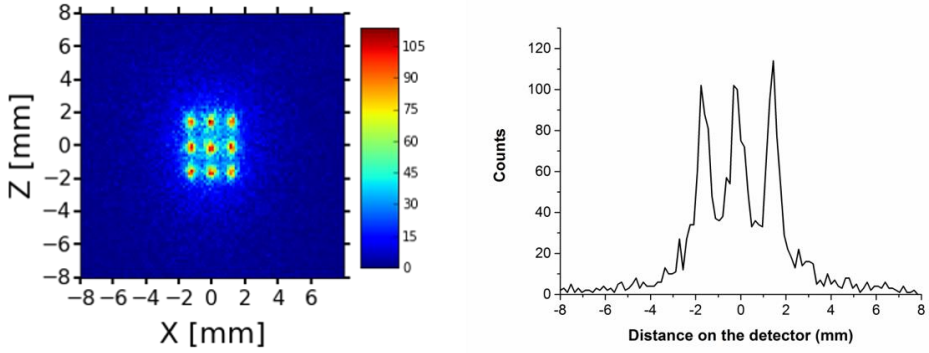

Figure 5. 10: Left: 2D histogram recorded on the detector of 9 spots on the sample with 1 µm diameter, separated **3 µm;** right: line scan of the middle row. Peaks centred on X_1=-1.67 FWHM=0.64, X_2=-0.17 FWHM=0.76, X_3=1.41 FWHM=0.56. **Projector lenses pre-set 5**.

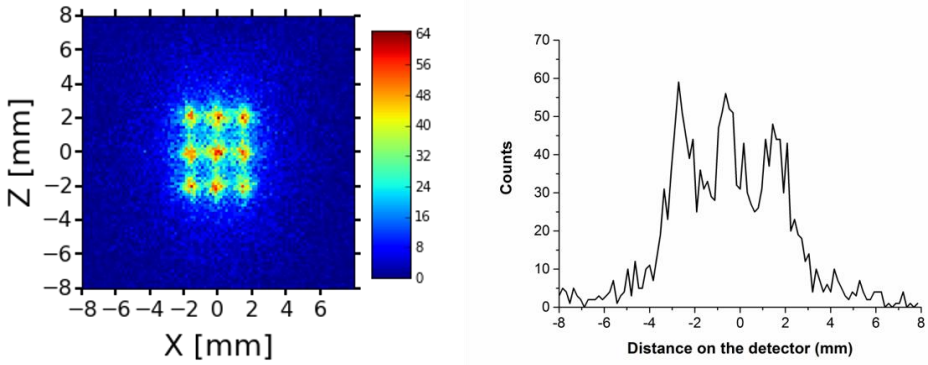

Figure 5. 11: Left: 2D histogram recorded on the detector of 9 spots on the sample with 1 µm diameter, separated **3 µm;** right: line scan of the middle row. Peaks centred on X_1=-2.62 FWHM=1.21, X_2=-0.59 FWHM=1.24, X_3=1.57 FWHM=1.55. **Projector lenses pre-set 6.**

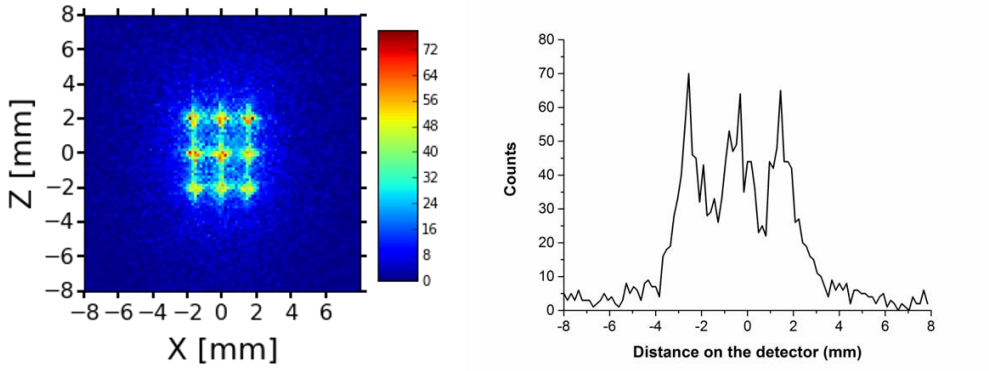

Figure 5. 12: Left: 2D histogram recorded on the detector of 9 spots on the sample with 200 nm diameter, separated 3 μm; right: line scan of the middle row. Peaks centred on X_1=-2.57 FWHM=1.11, X_2=-0.49 FWHM=1.42, X_3=1.51 FWHM=1.18. **Projector lenses pre-set 6**. CA=50μm

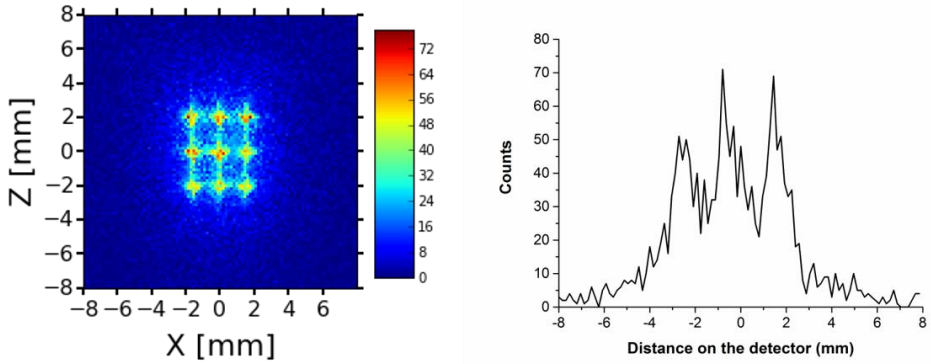

Figure 5. 13: Left: 2D histogram recorded on the detector of 9 spots on the sample with **200 nm** diameter, separated **3 μm;** right: line scan of the middle row. Peaks centred on X_1=-2.57 FWHM=1.2, X_2=-0.59 FWHM=1.31, X_3=1.53 FWHM=01.09. **Projector lenses pre-set 6**. **CA=400μm**.

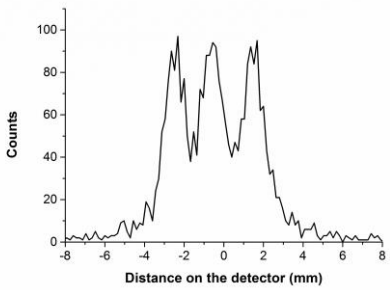

Figure 5. 14: Peaks centred on X_1=-2.62 FWHM=1.11, X_2=0.59 0 FWHM=1.23, X_3=1.57 FWHM=1.20. **Projector lenses pre-set 6**.

In summary:

- The best situation is when the spots are separated 10 μm on the sample and the zoom position is in magnification 4, where the relation Δx/FWHM is 9.88, more than three times of any other combination of magnification and distances and peaks are resolvable at the base.
- When the spots are closer in the sample, the magnification of the projection system should be increased to resolve the spots.
- When the magnification is maximum, the minimum distance between spots to be resolvable is 3μm. Even if the spots are reduced in size (200 nm), the distance centre to centre do not correspond to 3 diameters spot size, instead correspond to 15 diameters, a relative distance higher than the optimal case, the resolution has practically no improvement.
- There is a limitation in the lateral resolution and distance between spots, because the resolution is not improved by reducing the probe size as in the microprobe mode.
- The simulation done with one spot showed the behaviour of the tail of the peak, and by superimposing three of these peaks Figure 5. 14 the effect of the tail makes a background that reduces the quality of the image.
- Moreover, and Figure 5. 13 shows that the size of the contrast aperture did not influence in the number of ions detected neither in the resolution. This is logical because the FOV is 9 μm, smaller than the FOV illuminated with the second transfer lens 150 μm, energised when microscope is on.
- The transmission of the system was approximately 30 percent.
- The pattern obtained on the detector shows that the multi-ion-beam technique is feasible in the secondary optics of the IMS XF instruments.

5.4 Experimental conditions:

The set up consisted of the Cameca IMS 4F/6F instruments with a modified detection system comprising the standard MCP and phosphor screen coupled to a fast digital camera. A schematic of the complete system is illustrated in Figure 5. 15. The camera is made by EO Edmund, model EO-0813C 1/322 CCD colour USB Camera (1/3", 1024 pixels, size of the pixel 4.65 x 4.65 μm, 8-bits pixel depth, 1-30 fps, resolution of 0.8 megapixels) [116]. The lens is a Computar TV Lens of 25 mm diameter, 1:1.3 (fstop =1/3) [118]. The detection system is then the combination of the MCP/FS plus the lens/camera. The intrinsic resolution of the MCP/PS system for 150 μm FOV is 400 nm [119]. The dynamic range is 256, limited by the 8 bits camera. The efficiency of the system is smaller than 50 %, mainly limited by the MCP useful area.

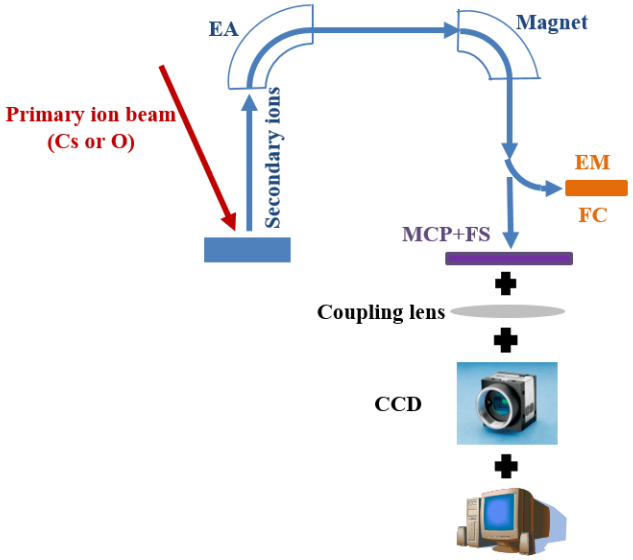

Figure 5. 15: Schematic of the setup used to proof the concept of the multi-ion-beam in imaging SIMS.

The aim of the experiments was to complete the proof-of-concept of the multi-ion-beam for SIMS imaging. For that purpose, the experiments were divided in two stages. Initially, the beam in Köhler illumination was characterized to acquire the necessary information for designing the multi-hole aperture. Secondly, the multi-ion-beam generated by the multi-hole aperture mounted in the primary column of the Cameca IMS 6F was evaluated.

5.4.1 Acquisition of the images:

The detection system in the IMS 4F and in the IMS 6F Cameca instruments is composed by the original MCP/PS. At the back of the phosphor screen a CCD camera is coupled by a lens as described in 5.4. The parameters that could be varied in this system are the potential applied to the microchannel plate, and the settings of the camera e.g. time frame, colour management, etc.

The acquisition of an image with this detection system can vary from short time frames (30 f/s) to longer exposure (1f/s). For high fluency of secondary ions, the first option represents the physical phenomena quite accurately, but when the secondary current is below 10^4 c/s the time exposure should be longer to accumulate enough information of each pixel and the image can be reproduced completely. However, another way to increase the time exposure of each pixel of the image is to modify the raster frequency. The standard IMS 4F/6F have the possibility to choose between 20 kHz or 2 kHz. For example, by minimizing the frame rate, exposure time of one second, and using the lower scanning frequency (2 kHz), enhancing the green contrast of the camera and increasing the gain of the microchannel plate, it is possible to have intense and clear images for few thousand counts per second.

Figure 5. 16 shows the difference in intensity for an aperture of 20 μm scanned through 90 μm at frequency of 20 kHz, while the right image is the scanned through 100 μm at 2 kHz, which the colour is more intense due to low frequency (longer dwell time per pixel).

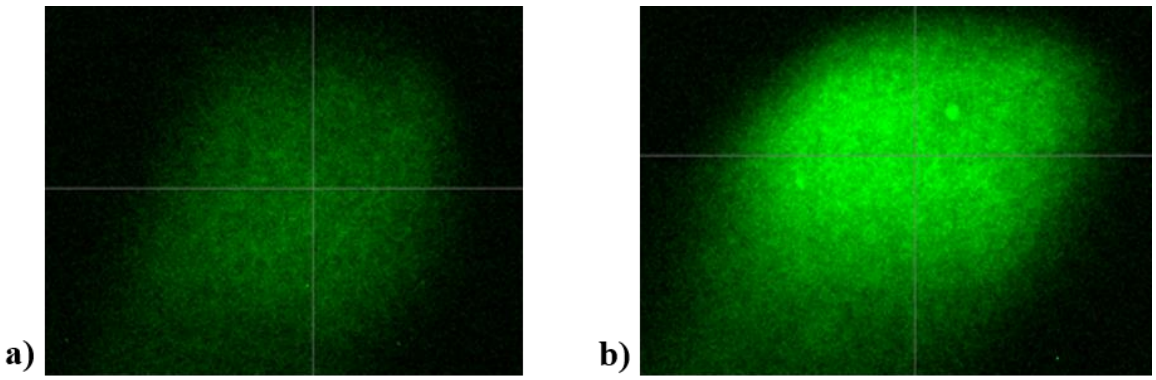

Figure 5. 16: a) 20 μm aperture rastered 90 μm at 20 kHz; b) 20 μm rastered over 100 μm at 2kHz. The image rastered at 2kHz is brighter due to longer dwell time per pixel.

The fact that the gain of the MCP cannot be measured, limits the possibility to calibrate and the quantify the images.

5.4.2 Characterization of the Oxygen Duoplamastron and Caesium sources in Köhler illumination

The main parameters of the beam in Köhler illumination relevant to the design of the multi-hole aperture are the *homogeneity* and the *intensity* of the beam.

The experiments were done in the Cameca IMS 4F where it was possible to characterize the Oxygen beam (O_2^+) coming from the Duoplasmatron source in the Köhler illumination mode. The ions were extracted at 10 kV and the sample holder was biased at 4.5 kV, thus the energy of the ions was 5.5 keV. The standard process to obtain Köhler illumination in the Cameca IMS XF instruments requires the alignment of the primary column optimizing the current and after, turn down to zero the voltage of the middle lens of the column and align the aperture. When the middle lens is turned off, no intermediate image is generated, and the rays remain quasi parallel until the aperture strip, thus an image of the aperture is produced on the specimen with the aid of the focus lens (Figure 5. 17). By moving slightly, the voltage of the focus lens is possible to adjust the beam diameter, within a certain range. The sputtered secondary ions extracted by the immersion lens (in positive mode), are focused through the spectrometer on the channel plate, and a magnified image of the sample is observed on the screen.

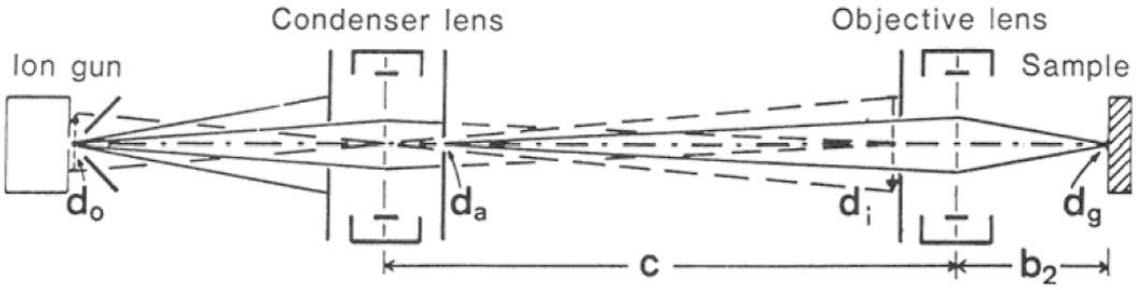

Figure 5. 17: Schematic of the optics of the primary column in Köhler illumination/beam shape mode. The condenser lens (L2 in IMS 6F) images the source (d_0) to the objective lens aperture, while the objectives lens (L4 in IMS 6F) images the condenser aperture d_a to the sample surface. The objective aperture size is chosen to define the size of the spot on the sample. Since the spot is an image of a round aperture, the size or the shape of the source has no influence. (image taken from [140]).

The size and shape of the beam was always estimated with a standard grid of AlCu, which has a pitch size of 25 μm (Figure 5. 18).

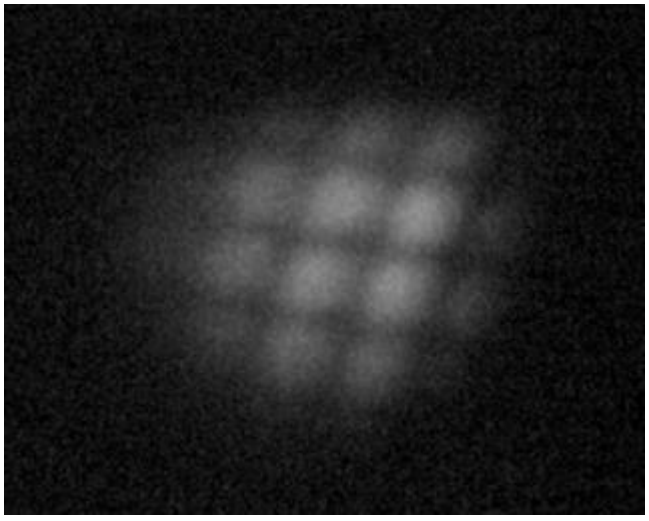

Figure 5. 18: Image of Al^+ obtained when the intermediate lens was off and a 200 μm aperture was used. Field of view (FOV) =150 μm and contrast aperture CA=50 μm. The shape is round, and the diameter is minimum 100 μm (demagnification 2) and edges are defocused.

A *homogeneous* Köhler illumination should produce an image of the aperture with well-defined edges. In Figure 5. 18 the limits are not clear. For this reason, it was necessary to determine a methodology to evaluate the homogeneity of the beam and to define the best conditions to optimize the

Köhler illumination. A TEM grid of 50 mesh size (hole of 420 μm and bar of 80 μm) was mounted over the aperture of 1 mm with the aim to adjust the focus lens and other parameters such as stigmators, deflectors, primary magnetic field, etc. to obtain a sharp image of the central cross. Figure 5. 19 shows the aperture holder with three slots for apertures for mounting apertures with varied sizes, the hole with the cross corresponds to the TEM grid.

Figure 5. 19 : Aperture holder with three slots for 3 apertures, the hole with the cross corresponds to the 1mm aperture with the TEM grid superimposed.

Figure 5. 20, shows two images obtained with this aperture, the image on the left (5. 20a) has sharper cross and edges than the image on the right (5.20b). Line scans were also acquired in both directions to analyse the *uniformity* of the beam. The normalized line scans corresponding to Figure 5. 20a (with sharper edges) illustrate a more uniform illumination where all the peaks seem to be of the same height even though the signal is low and consequently the signal to noise ratio is higher than Figure5.20b. On the other hand, on the border of Figure 5. 20b the illumination has some diffusion and its corresponding line scans also show different intensities from quadrant to quadrant of 40 %, representing a beam profile like the Gaussian shape. Furthermore, Figure 5. 20b was obtained with a secondary current of three orders of magnitude higher than Figure 5. 20a, comparable to microprobe mode. In addition, an integration of the intensity over a square of equal size in each quadrant showed that the illumination was 2 times more uniform for the setting in Figure 5. 20a.

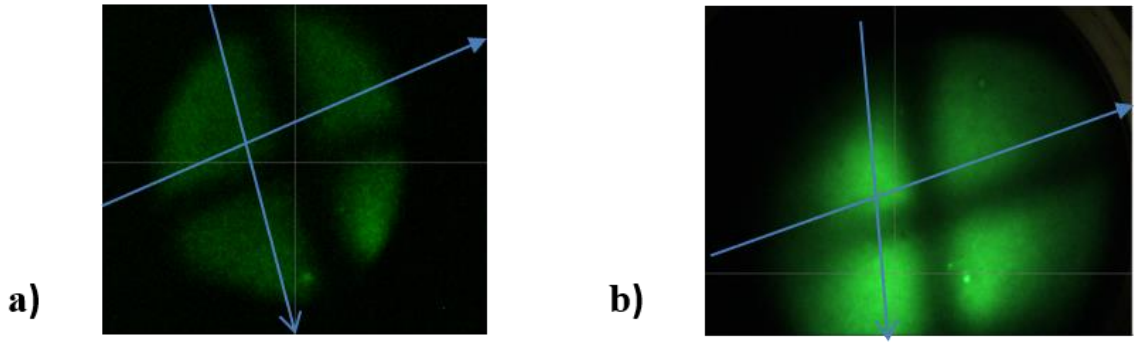

Figure 5. 20: Images of the In+ signal obtained from an InP wafer. Contrast apeture 400um FOV 250 um all slits open. a) Ip 1nA and Is 2.6e5c/s raster frequency 2kHz b).Ip 110 nA and Is 1.7e8 c/s The blue arrows indicate the direction of the line scans in Figure 5.2.1. The settings used for a) produce a slightly more uniform illumination, but much lower signal.

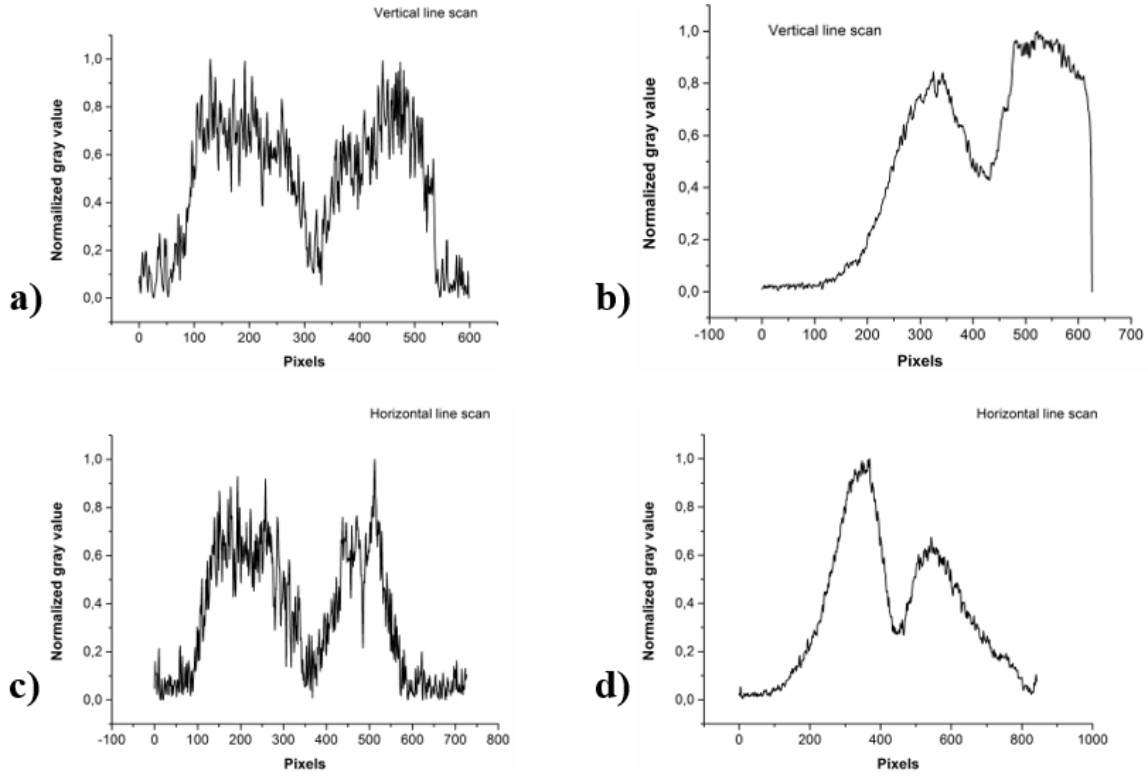

Figure 5. 21: a) and c) Normalized line scans of the image 5.20a. The peaks have similar height implying that the illumination is uniform, but the signal to noise ratio is high. b) and d) Normalized line scans of the image 5.20b, the difference between heights is about 40 %, representing a non-uniform illumination.

The intensity of the beam was investigated for apertures with different diameters, 20, 50, 200 and 1000 μm and craters were made in silicon and InP wafers and subsequently they were measured with the profilometer Tencor p-15.

Results for 200 μm and 20 μm apertures are shown below for two different alignments of the beam on InP matrix. The images presented in this work correspond to InP because the useful yield of the InP matrix was two orders of magnitude higher than the silicon wafers, providing images of better quality. The results showed the difficulty of obtaining nice Köhler illumination with this machine.

- ***Results for the 200 μm aperture:***

Figure 5. 22 shows the image of the In^+ signal on the screen of the 200 μm aperture for two different settings for obtaining Köhler illumination. Figure 5. 22a was made in similar conditions of Figure 5. 20a, when uniform illumination was obtained. The normalized line scan of Figure 5. 23.a shows high noise to signal ratio while that the line scan of the Figure 5. 23b does not remind a "hat shape" but Gaussian type shape. However, any of both cases can be consider as a Köhler illumination. Even though in the case of Figure 5. 22a the illumination appears to be uniform, only a part of the dynamic of the camera was used, generating an image that appears flat and homogeneous.

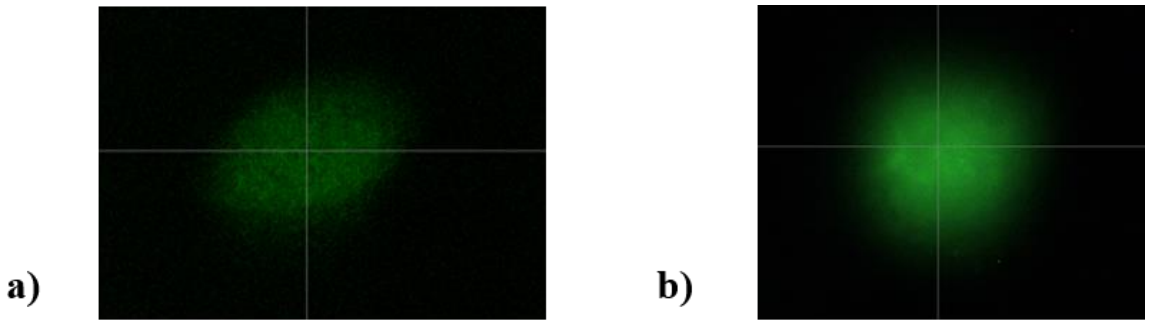

Figure 5. 22: Image of the 200 μm aperture, a) I_p=0.5 nA and I_s=2x 10^{+4} c/s, b) I_p=17 nA and I_s=1 x 10^{+8} c/s. Contrast aperture 400 μm and FOV 250 μm. All slits open. a) represents a slightly more homogeneous illumination, one characteristic of Köhler illumination, b) has a bright centre surrounded by decreasing intensity.

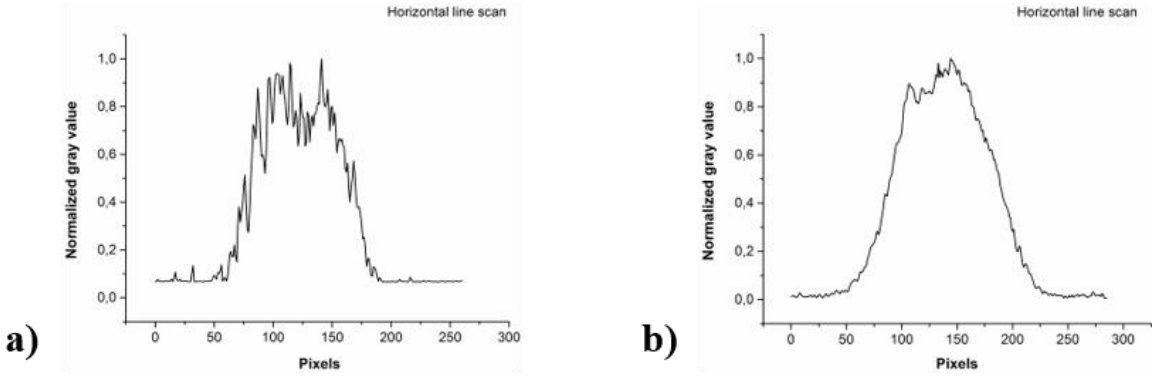

Figure 5. 23: a) Line scan of the image above with hat shape corresponding to more uniform illumination, b) line scan of the image 6b with a shape resembling a Gaussian curve.

Craters were eroded in InP using the 200 μm aperture and their profiles were extracted with the profilometer. They were elliptical with short axis equal to 150 μm and the long axis equal to 200 μm and a depth smaller than 0.8 μm for the case a. The long axis of the crater was equal to the diameter of the aperture; implying that the image has no demagnification in one direction. The crater made in the case b, was round with a diameter of 89.5 μm, meaning a demagnification factor more than two. The profile was characteristic of a Gaussian beam shape. The depth was around 5 μm, 6.25 times deeper.

- ***Results for the 20 μm aperture:***

In the case of the aperture of 20 μm it was possible to see an image on the screen only when the illumination was Gaussian type (condition of Figure 5. 20b) where the primary current was 338 pA and the intensity of the secondary signal was 4 x 10^{+4} c/s. In the case (Figure 5. 20a) where the illumination appeared to be more homogeneous, the primary current was two orders of magnitude lower, being 4 pA, and consequently the secondary signal was also two orders of magnitude lower equal to 3 x 10^{+1} c/s, not being enough to ions to generate a visible image in the system formed by the MCP and the phosphor screen, which needs a fluency of the order of 10^4 ions per second (Figure 5. 24) . Or in case of currents of thousands of counts it should be concentrated in a small area.

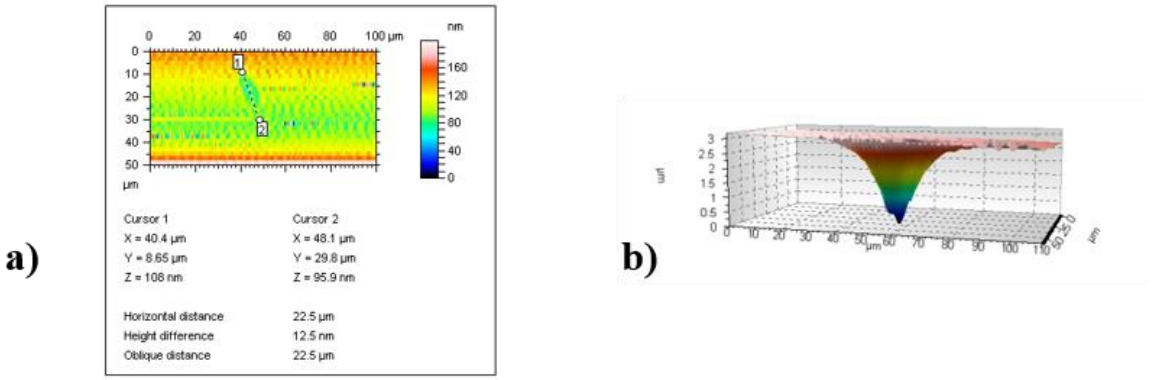

Figure 5. 24: a) Profile of the crater made with the conditions in a, short axis=10 µm and the long axis=22 µm, sputtering rate=4 nm/min, b) profile of the crater made with the conditions in Figure 5. 20, short axis=19.2 µm and the long axis=41 µm, sputtering rate= 72 nm/min

The experimental results obtained with the IMS 4F Cameca spectrometer indicate that in the case of more uniform illumination, not only the primary intensity was very low but also the secondary current. Consequently, the number of ions reaching the microchannel plate were not enough to observe an image with the aperture of 20 µm or smaller. Furthermore, these results do not coincide with the results founded by Hervig et al [120]. In that work, they made craters on NIST 610 using Köhler illumination through an aperture of 200 µm in Cameca IMS 3F and IMS 6F. The conditions of the experiment were quite similar to the conditions that were used in this work: maximum transmission of secondary ions through the mass spectrometer (contrast aperture equal to 400 µm diameter and fully opened entrance and exit slits), but the primary beam was O^- and the net energy beam was 8 keV. In that experience, they obtained flat bottomed craters with more than three times demagnification and primary currents between 4.5 to 10 nA. In this work, the primary current was not only one order of magnitude lower 0.5 nA with O_2^+, but also the craters had practically no demagnification. These differences could arise from some mechanical misalignment in the primary optics of our IMS 4F.

In order to increase the primary current, have a uniform illumination and avoid any error that could come from the machine misalignment, the following tests were made with the Cameca IMS 6F, also at LIST.

A new set of craters and images were made with a Caesium source at 10 kV extraction voltage and the sample voltage was at 4.5 kV, (total energy of 5.5 keV). The conditions were for maximum transmission and the apertures imaged had diameters of 115, 264 and 447 µm. The craters were made in InP and measured with the profilometer. The images of each aperture presented in the Figure 5. 25 were made using always the same AlCu grid. Profiles of the three apertures are shown in Figure 5. 26.

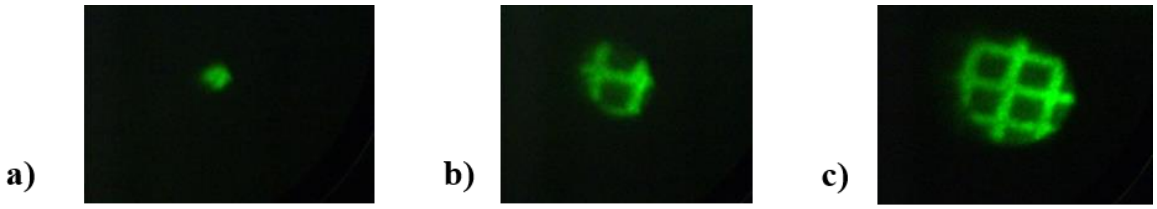

Figure 5. 25: Image on the screen: a) aperture of 115 μm, screen estimation of the size around 25 μm, b) aperture of 264 μm, screen estimation of the size around 50 μm, c) aperture of 447 μm, screen estimation of the size around 75 μm, primary current 7 nA. In all cases the contrast aperture was 400 μm, all slits open and the secondary currents higher than 10^7 c/s.

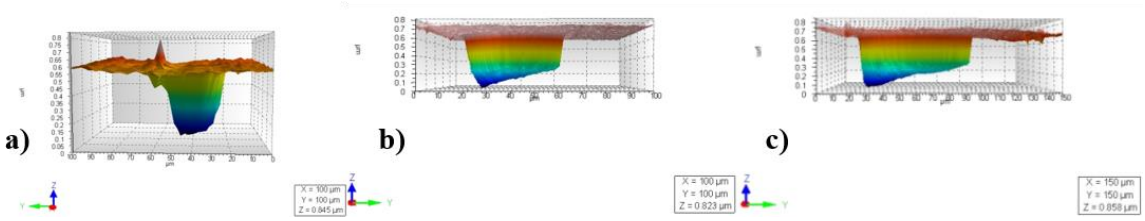

Figure 5. 26: Profiles of the craters made with the conditions mentioned in figure 5.26, a) short axis=37.7 μm and the long axis=40.3μm, sputtering rate=9.71 nm/min**;** b) short axis=49.2 μm μm and the long axis=56.8 μm, sputtering rate=15.1 nm/min; c) short axis=80 μm and the long axis=90 μm, sputtering rate=12.35 nm/min.

The images obtained with IMS 6F have very well-defined edges, the sizes of the images of the apertures are 3 to 4 times smaller than the original size of the aperture and the walls of the craters are steep-edged. Moreover, the primary currents were in the range of the nano-amperes. All these values are in agreement with the ones cited by Hervig et al. Therefore, as the results obtained with the IMS 6F are much more coherent with what was expected, it was decided to use this information for designing the multi-hole aperture and, also to continue the experimental test with this machine.

5.4.3 Design of the multi-hole aperture

The standard apertures of the Cameca instruments consist of a circular aperture with certain profile (Figure 5. 27a) usually made of molybdenum and mounted on the diaphragm holder, secured by a thin gold foil (Figure 5. 27).

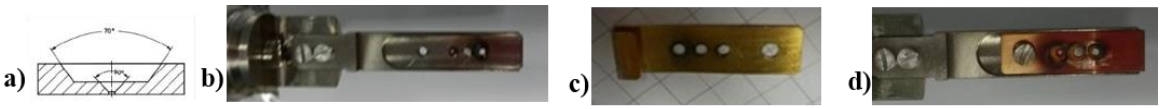

Figure 5. 27: a) profile of the standard apertures used in the IMS 4F and 6F (image obtained from catalogue Agar scientific); b) empty diaphragm holder; c) thin alloy foil for secure; d) ensemble of the pieces in b and c. The standard apertures are mounted on the holder and covered with the golden foil for security.

In order to determine the best design for the multi-hole aperture, that will replace the standard aperture (one circular hole); it was necessary to analyse the following parameters:

1 The minimum diameter of the aperture required to observe a secondary ions image.
2 The minimum distance between holes.
3 The maximum number of holes.
4 The distribution of the holes.

1. The total ion current can be related to current density by integrating the current density over the area where the ions are flowing:

$$I = \int \Phi^* dA = \Phi^* \pi r^2 \quad (5.1)$$

Hence, the ion current that arrives on the sample depends on the radius of the aperture, the smaller the hole, the less current arriving to the sample, therefore there will be a minimum aperture diameter to generate an image on the screen.

2. The distance between holes depends on the demagnification of the image on the specimen. The demagnification in the IMS XF Cameca instruments could vary from 1 to 5. The accuracy of the raster system is around 3-5 μm, this implies that the minimum raster size between holes should be 30 μm. This means that the distance between holes on the aperture should be from 30 to 150 μm.

3. The recommended FOV for the microprobe mode is 150 μm to limit the aberration in the secondary optics and to obtain images with good lateral resolution (1 μm [119]). Consequently, there is a maximum number of holes that could be fitted in the FOV, apertures between 3 x 3 and 4 x 4 holes could be adjusted in this FOV, depending on the distance between the holes and the demagnification.

4. The distribution of the holes was proposed to be in a square matrix along with the edge of the thin foil.

Considering the four points mentioned above, the multi-hole apertures were designed in a single thin foil of stainless steel similar to the alloy foil with three slots, the first is an aperture of 200 μm, the second is a multi-hole aperture with 9 holes of 50 μm diameter, arranged in a matrix of 3 x 3 separated 150 μm centre to centre, and the third one has 9 holes of 20 μm diameter, also arranged in a matrix of 3 x 3 separated 100 μm centre to centre (Figure 5. 28a/b). A parameter to consider is the ratio between the aperture diameter and the thickness of the foil. Standard apertures have a ratio 1:1 with profile similar to Figure 5. 27. The three apertures were drilled as follows: the first one of 200 μm diameter was drilled with standard profile, and the multi-hole apertures were drilled inside a standard profile with 2 mm of external diameter and 1.5 mm of internal diameter, which thickness is 50 μm. Thus, the holes of 50 μm have 1:1 ratio, while the holes of 20 μm have a ratio of 1:2.5. The size of the holes was selected to be sure to have enough current to see images on the screen, considering previous measurements.

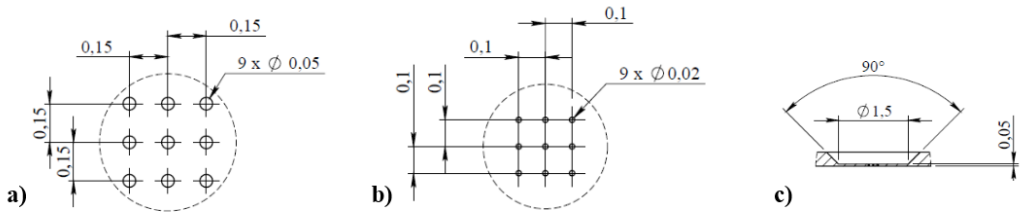

Figure 5. 28 a) Schematic of the multi-hole aperture with 50 μm diameter separated 150 μm centre to centre; b) schematic of the multi-hole aperture with 20 μm diameter separated 100 μm centre to centre; c) profile of the circle containing the matrix with the nine apertures.

Figure 5. 29 is a photo of the aperture ready to be mounted on the primary column of the IMS 6F. The big hole is for screwing the aperture to the holder. The small hole corresponds to the aperture of 200 μm and the other two are the bigger areas including the matrix of holes.

Figure 5. 29: Photo of the thin foil with the aperture of 200 μm, and the two multi-hole apertures described in Figure 5. 28.

5.4.4 Results using the multi-hole aperture

Finally, the multi-hole aperture was mounted in the Cameca IMS 6F to complete the proof-of-concept of the multi-ion-beam SIMS imaging. The aperture was illuminated in Köhler mode with the Caesium beam extracted at 10 kV and the sample holder was always energised at 4.5 kV, thus the mean energy of the ions was 5.5 keV. Images of the grid with the different apertures were acquired with spectrometer settled in $^{133}Cs^{+}$, for raster sizes from 0 to 50 µm and craters were made for the three set of apertures in InP that were subsequently analysed with the profilometer. Below, there is a summary of the main results obtained:

- ***Results from 6F with Cs^{+} source for apertures of 200 µm, 9 x 50 µm and 9 x 20 µm (raster 0):***

Figure 5. 30a corresponds to the image of the 200 µm aperture, made on the AlCu grid. The size of the spot can be estimated around 50 µm. Figure 5. 30b/c are images taken with the profilometer on InP wafer; in both images it can be seen that there is a deeper zone, which means that the illumination was *not uniform.*

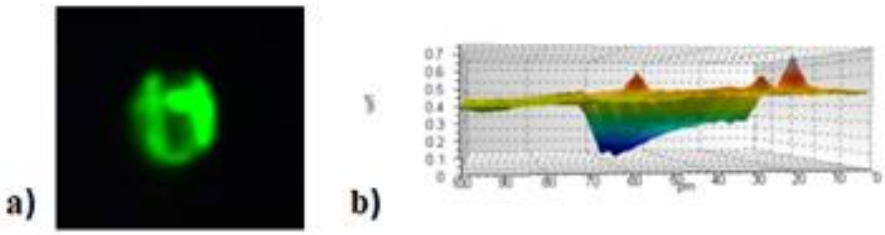

Figure 5. 30: a) Image on the screen of the 200 µm aperture on the grid ($133Cs^{+}$) diameter size estimated 50 µm, I_p=120 pA, I_s=6 x10^3 c/s; b) profile of the crater. CA 20 µm. Demagnification of the system approximately 4.

The same behaviour is observed also in Figure 5. 31b/c, measurements done with the multi-hole-aperture 9 x 50 µm and Figure 5. 32b/c, done with the multi-hole aperture 9 x 20 µm. This suggests that the properties of the beam are not affected by the multi-hole aperture. Moreover, the area of each hole was measured independently with the profilometer in both cases, the sizes of the 9 x 50 µm holes had a mean of 135.44 µm^2 with a standard deviation of 16.45, and for the aperture of 9 x 20 µm, the mean was 67.3 µm^2 with a standard deviation of 15.82. In both cases, there was no difference between central hole and any other hole. This implies that the off-axis aberrations are negligible for a multi-hole aperture with a general diameter of 475 µm (from hole to hole in diagonal).

The distance between holes made with the 9 x 50 µm aperture was 27 µm, the mean diameter of the hole was 10 µm, the demagnification factor is nearly 5. For the holes made with the 9 x 20 µm aperture the distance between them was 18 µm and the mean diameter of the holes was 5 µm, a demagnification factor around 4-5. The measurements of the holes with small sizes such as 5 µm become to be inexact because the accuracy of the needle of the profilometer is 2 µm.

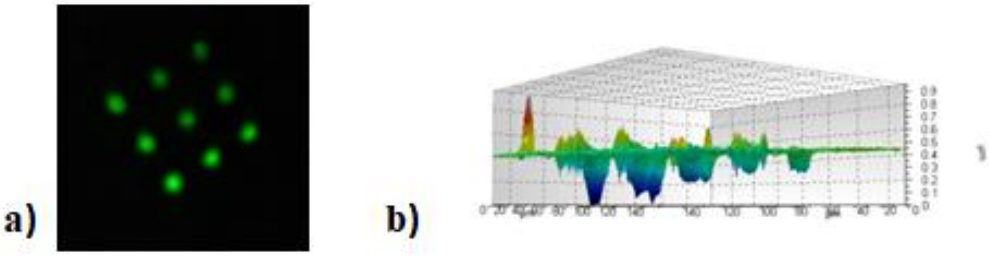

Figure 5. 31: a) Image on the screen of the 9 x 50 µm aperture on InP (using $_{133}Cs^{+}$), I_p=80 x pA, I_s=6 x10^3 c/s; b) profile of the craters. The height of each hole differs a 100% from the deepest to the shallow ones. CA 20 µm. *Demagnification 5*.

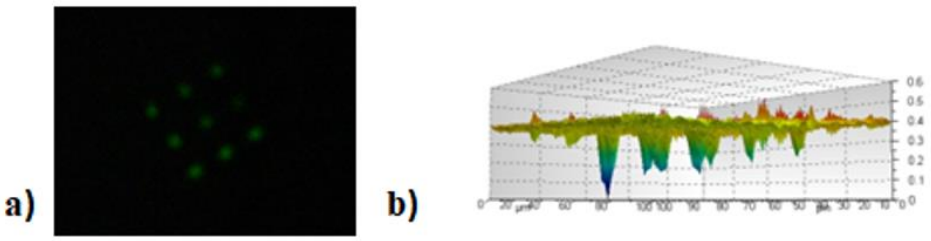

Figure 5. 32: a) Image on the screen of the 9 x 20 µm aperture on InP (using $_{133}Cs^{+}$), I_p=20 pA, I_s=2 x10^3 c/s; b) profile of the craters. The height of the craters also differs a 100 % from the deepest to the shallow ones. CA 20 µm. *Demagnification 4.5*.

The difference in the intensity observed on the screen from spot to spot could be due to main three factors: first, the illumination is not homogeneous; second, the system MCP/FS has regions with different erosion, influencing in the brightness of the image. This effect could be corrected if the intensity of the whole area is measured (using a homogeneous sample) and with a software for image processing the intensities can be systematically levelled (i.e. in the places where the MCP/FS is degraded, certain intensity is added). Third, the sample is not homogeneous. Thus, for the development of the multi-ion-beam is necessary to work with known uniform samples.

- ***Results from 6F with Cs^+ source for the multi-hole aperture 9 x 20 μm rastering the beam:***

Figure 5. 33a shows the image on the screen when the raster was 15 μm. The raster size is smaller than the distance between the spots on the sample equal to 18 μm, that is why there are black spaces between the bright spots. Figure 5. 33b/c have been made with the profilometer; both pictures show that the raster with the nine beams works identically as one beam, and the craters are square with flat bottoms.

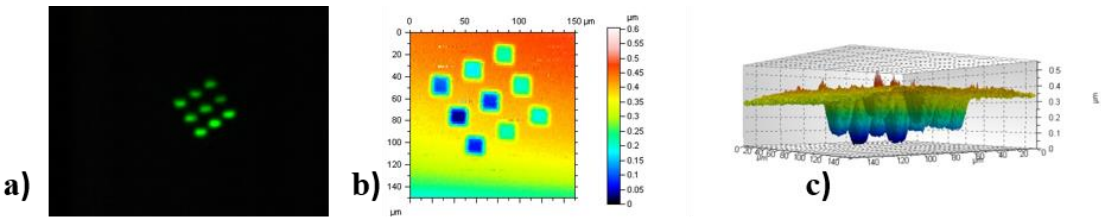

Figure 5. 33: a) Image on the screen of the 9 x 20 μm aperture on AlCu grid (using $_{133}Cs^+$) raster =15 μm, I_p=20 pA, I_s=2 x10^3 c/s; b) profilometer top image of the squares craters; c) profile of the craters. CA 20 μm. Even if the beam if rastered the difference in height between the craters is up to 100 %.

As the raster size increases, the sample area gets fully covered and the image of the AlCu grid is obtained on the screen. Figure 5. 34d shows images of four different raster sizes 15 μm, 20 μm, 30 μm and 50 μm, where the grid is observed.

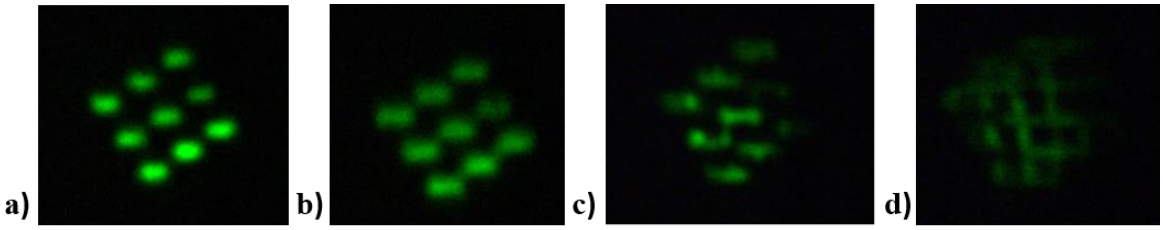

Figure 5. 34: a) Image on the screen of the 9 x 20 μm aperture on AlCu grid (using $_{133}Cs^+$) raster =15 μm; b) raster =20 μm; c) raster =30 μm; d) raster =50 μm.

The results show that the multi-ion-beam are transmitted successfully across the complete instrument, primary and secondary optics, as it was predicted by the simulations (5.3). However, the matrix of the holes shows a rotation around 30° to 35° in the craters analysed with the profilometer and in the images too. This means that the multi-hole aperture orientation is not aligned with raster and consequently, when the system is scanned the image reconstruction is not well matched. For smaller

raster sizes, some black regions were observed, and for bigger sizes some regions were over scanned, consequently the information of the image is not representing properly the sample (Figure 5. 34). For doing a good image of the sample the orientation of the multi-hole aperture should be aligned with the raster system.

During the Köhler illumination the multi-hole aperture was difficult to align because the Ceasium source showed multiple points of emission, for this reason it was decided to make more tests using the Duaoplasmatron source with O_2^+. The extraction voltage was 15 kV when the sample holder was at 4.5 kV, this means that the ions had an energy of 10.5 keV on sample surface.

- ***Results from 6F with O_2^+ source for apertures of 200 μm, 9 x 50 μm and 9 x 20 μm (raster 0):***

Figure 5. 35a corresponds to the image of the 200 μm aperture, made on the AlCu grid. The size of the spot can be estimated around 50 μm. Figure 5. 35b/c are the images of the measurements taken with the profilometer on InP wafer; the hole was deeper than the profilometer settings, so the bottom could not be measured. Figure 5. 36c has similar effect, but it is possible to observe that one of the holes has a very sharp triangular shape, suggesting that this is the shape for the holes of Figure 5. 35c and Figure 5. 36c.

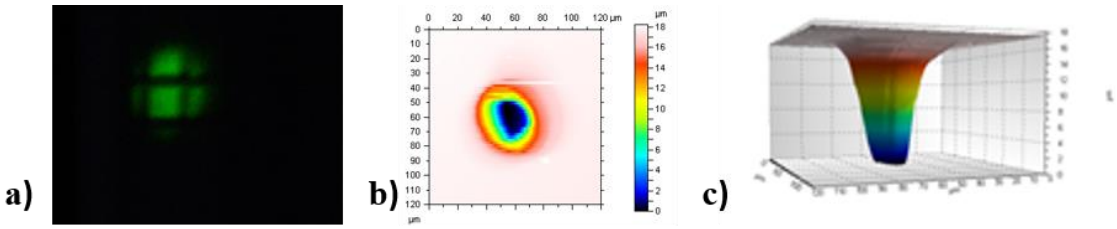

Figure 5. 35: a) Image on the screen of the 200 μm aperture on the grid $_{27}Al^+$ (using O_2^+), diameter size estimated 50 μm, I_p=23 nA, I_s=10^9 c/s; b) profilometer top image of the crater on InP long axis=50 μm, *demagnification 4*; c) profile of the crater. Ca 20 μm **(**the crater was deeper than the profilometer settings).

Figure 5. 36a corresponds to the image of the 9 x 50 μm aperture, made on the AlCu grid. The size of the spot can be estimated from the screen to be nearly 25 μm. Figure 5. 36b/c are the images measurements taken with the profilometer on InP wafer; the distance between holes is 32 μm, so the demagnification factor is 5, however, the hole's shape is elliptical, and the long axis measures 32 μm, meaning that the reduction of the size is not proportional to the system demagnification (only 1.4 times), reflecting a significant non-desired effect when each individual hole is image. This shows a clear difference in behaviour between the Caesium source and the Duoplasmatron source when the beam is

going through holes of 50 µm or less. This effect is increased when the size of the aperture gets smaller. Figure 5. 37b/c show the images of the measurements made with the profilometer on the InP with the 9 x 20 µm aperture, the shape of the holes is much more elliptical with a long axis with 36 µm and the short axis with 25 µm and the distance between holes is 21 µm. The demagnification factor is 4 for the complete optics, but once again, the size of the holes is not proportional to the demagnification factor, having a magnification instead of demagnification. This result agrees with those obtained with the IMS 4F (Figure 5. 24b). One possible cause for this effect is due to the scattering of the ions that go through the holes, so when the size of the hole is reduced the effect is increased, in consequence the projection of image on the sample is enlarged. In the case of the Duoplasmatron, the effect is considerably higher because the O_2^+ is four times lighter than Cs^+ and the rays that arrive at the aperture are not perpendicular, but they have some angle (illumination with Gaussian shape) [121]. In addition, the energy dispersion (ΔE) of the duoplasmatron is higher (5-20 eV) than the Caesium source (0.2-0.5 eV) [122], giving two orders of magnitude higher energy spread to the ions. In addition, the spherical aberration is larger in the duoplasmatron source, generating ions with larger angle spread, enhancing the scattering of the ions that arrive at the aperture with wider angles.

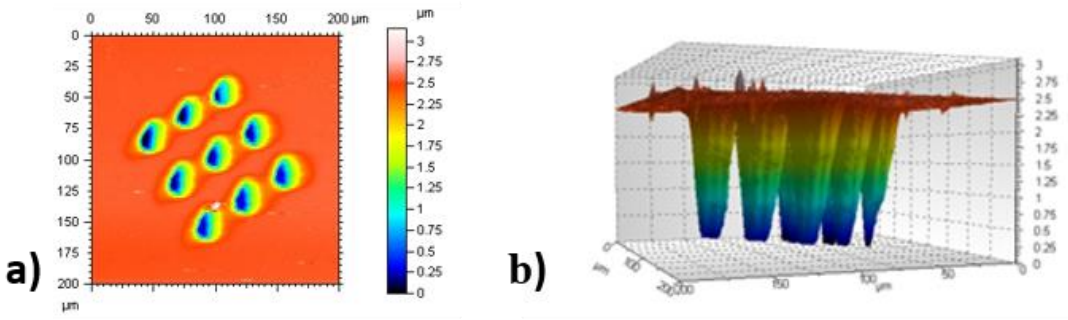

Figure 5. 36: a) profilometer top image of the crater on InP long axis=32 µm, system demagnification 5, *hole size reduction factor1.5*; b) profile of the crater. CA 20 µm (the crater was deeper than the profilometer settings). There is no agreement between the demagnification of the system and the size of the hole.

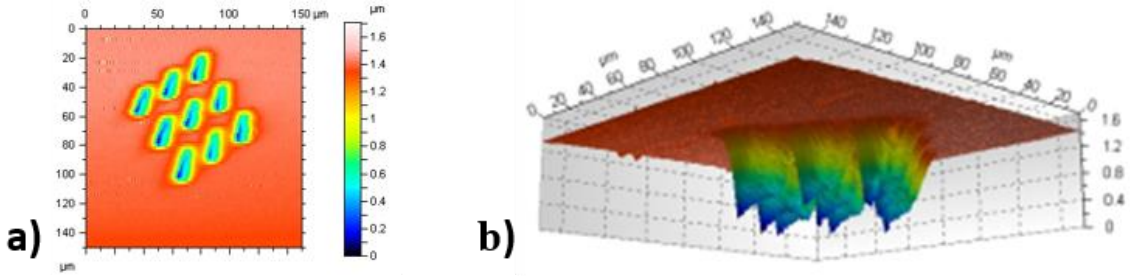

Figure 5. 37: a) profilometer top image of the crater on InP long axis=36 μm and short axis=25 μm, *demagnification of the system 4, hole size is bigger than the aperture hole*; b) profile of the crater. Contrast aperture 20 μm. There is no agreement between the demagnification of the system and the size of the hole.

The primary current was measured on the sample holder externally using a pico-amperemeter. The values of the primary currents with oxygen were always two orders of magnitude larger than with caesium and this was also reflected in the secondary currents. These results imply that potentially the size of the holes of the aperture could be reduced until 1 μm, so with 3 or 4 times demagnification, it would be able to reach the sample with probes with few hundreds of nanometres with enough current. However, the reduction of the size of the holes not only is not constant for each aperture size, but also it is inversely proportional to the size of the aperture. For example, in the case of the 200 μm aperture, the measurement was around 50 μm, i.e. 4 times smaller; for the 50 μm aperture the mean diameter was 35 μm (1.4 times smaller) and for the 20 μm aperture, the holes were elliptical, with the long axis equal to 35 μm and the short axis around 22 μm (this represents no change in size in one direction and 1.75 times magnification, bigger size, in the other direction). The fact that the aperture of 20 μm has no reduction of the size, as the results shown also in Figure 5. 24, obtained with the IMS 4F, could limit the possibility to obtain nano-probes by using the duoplasmatron source.

Finally, the last measurements, were carried out with a re-designed multi-hole aperture. The goal was to make images of the sample with the matrix of holes aligned to the scan axis to obtain correct images and with smaller holes to investigate the practical limitations of the techniques.

The parameters of the new multi-hole the aperture were re-defined:

1. The size of the holes selected should be big enough to produce beams with high enough current to produce enough secondary ions to generate an image on the screen. The required secondary current to activate the phosphor screen is at least 10^3 counts per second (depending on the density ions/mm^2). One possibility to enhance the amount of the secondary current could be modify the settings of the spectrometer, for example changing the contrast aperture, but this is at the expense of the quality of the image, what is desired for a good lateral resolution.

The secondary current also depends on the amount of primary current. Therefore, there were made analyses of the amount of primary current regarding the aperture size. According to the measurements with both sources, an estimation of the current per hole was made assuming that the illumination was uniform and each beam coming from the multi-hole aperture has the same current. The estimation of the primary current coming from smaller holes, was done according to the ratio between areas of the holes and currents. The following Table 5. 2 summarizes the values obtained during the experiments and the values projected for apertures with more amount and smaller holes.

Standard measurements in NanoSIMS use probes of the order 1.5 pA, thus probes with smaller values will be difficult to see in this system. Table 5. 2 shows that apertures with 1 µm hole are below this reference value and for this reason it was decided to make apertures with 5 and 10 µm.

Apertures	**9 x 20 µm (real) pA**	**16 x 10 µm (estimated) pA**	**16 x 5 µm (estimated) pA**	**16 x 1µm (estimated) pA**
Total Cs^+	20	8.8	2.2	0.09
I per beam Cs^+	2.2	0.55	0.13	0.005
Total O_2^+	2700	1200	300	12
I per beam O_2^+	300	75	18.75	0.75

Table 5. 2: Table of measured primary currents and projected ones to evaluate the size of the hole for the second multi-hole aperture.

2. The pitch between holes depends on the demagnification of the projection of the aperture with multi-holes, which relies on the value of the focus lens. From the experiments mention above, the demagnifications varied approximately from 3 to 5 for the caesium source. Another important parameter to consider, which really limits the number of holes that could be included is the accuracy of the raster size, which for these machines is between 3 to 5 µm. This implies that the minimum raster size should be around 30 µm to keep at least an accuracy of 10%. If the distance between centre to

centre of the aperture is 80 µm, for demagnification 3 the distance between holes on the sample will be approximately 26 µm, for demagnification 4 will be 20, this value will have 15% of accuracy. Furthermore, the maximum FOV is 250 µm, so the total image should be included in this range.

3. The measurements of the surface of the holes made in Figure 5. 31 showed a 12% of difference in size between them. Line scans of the 4 external spots and the central one on the screen image were performed in two perpendicular directions to analyse the roundness of the spots and the size variation. The roundness of the spots was measured as the difference between the size in both direction. For the central hole, the difference was around a 5%, and for the external holes, the maximum difference was 13%. This means that the difference between the external holes and the central is 8 % or less. The difference in size between the external holes and the central hole was 10% in both directions. Consequently, for a multi-hole aperture with diagonal of 475 µm the contribution of the off-axis aberrations to the roundness and the size was lower than 10 %. Therefore, for an aperture for 4 x 4 holes, the total width will be 3 x 80 µm=240 µm plus 1 diameter (max. 20, then 260 µm), meaning a diagonal of 340 µm, so the off-axis aberrations will be less significant than in the first case.

4. The images on the screen show that the matrix was rotated around 30° to 35° degrees respect to the raster axis. This rotation corresponds to the angle of insertion to the primary column of the holder diaphragm. To align the multi-ion- beam system with the raster axis the matrix of holes was rotated 30° with negative sense. Figure 5. 38 shows the angle that the holder aperture makes with the Z axis, which generates the tilt of the matrix.

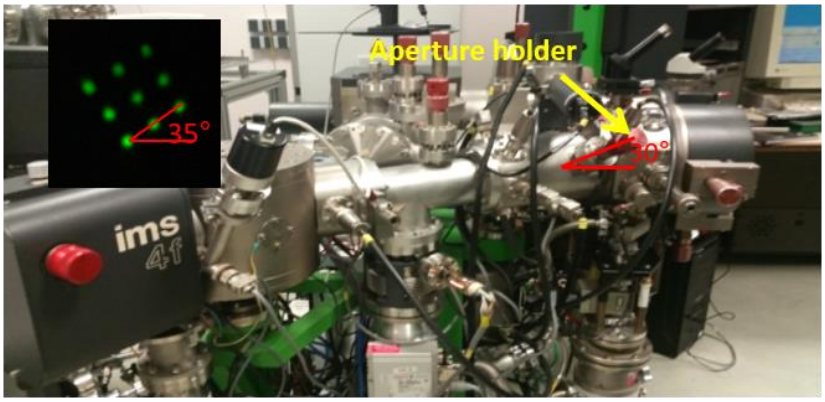

Figure 5. 38: Schematic of the angle rotation on the screen and the angle of insertion of the aperture holder marked on the IMS 4F.

The re-designed multi-hole aperture was made again with a thin foil of stainless steel, with an aperture of 200 µm, a rotated matrix of holes of 16 x 11.33 µm and a rotated matrix of 16 x 8.33 µm. The general profile follows the profile described in Figure 5. 28, the matrixes of holes were made at

LIST with a dual-beam (HELIOS). The thickness of the thin foil in the region of the matrix was 10µm, giving a ratio of 1:1 and 1:1.25 respectively. Figure 5. 39a shows the profile of the aperture, b shows the image of one of the holes of 11.33 µm and, c shows an image of one hole of 8.33 µm.

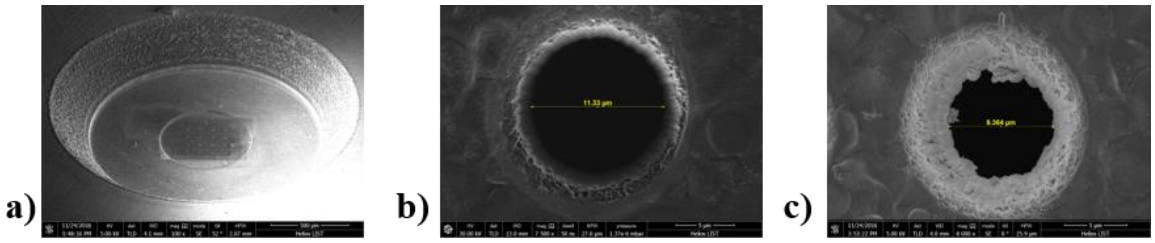

Figure 5. 39: Images of the multi-hole aperture made at LIST with dual-beam; a) profile of the complete aperture with a matrix of 4 x 4 holes; b) aperture of 11.33 µm; c) aperture of 8.33 µm.

The measurements were done with the caesium source extraction voltage 10 kV, sample holder 4.5 kV). The images were made on InP wafer, and the magnet was tuned for $^{133}Cs^{+}$. Below are presented the results for the multi-hole apertures 16 x 10 µm, 16 x 5 µm, with raster sizes from 0 to 50 µm.

- ***Results from 6F with Cs^{+} source of the apertures of 16 x 11.33 µm and 16 x 8.33 µm (raster 0):***

Figure 5. 40a shows the image of the 16 x 11.33 µm aperture, the image was taken with 9 frames per second (fps). Figure 5. 40b/c are the measurements on InP wafer, image c is the profile of the first row, the distance between holes is approximately 28 µm, representing a demagnification 3, and the mean diameter of the holes is 4.5 µm, which means a reduction of the size of the hole is also 3.

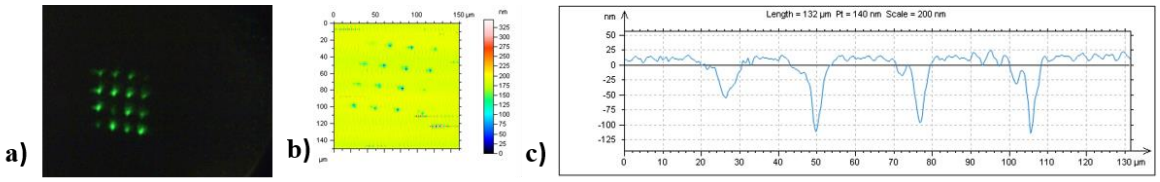

Figure 5. 40: a) Image on the screen of the 4 x 4 of 11.33 µm aperture on InP taken with 9 fps, Ip=38 pA, $I_s=10^5$ c/s; b) Image of the surface taken with the profilometer; c) profile of the first row mean diameter of the surface of the hole 4.5 µm *demagnification 3*.

Figure 5. 41 shows the same information for the aperture of 16 x 8.33 µm, the mean distance between holes is 26 µm and the mean size of the holes is 4 µm. In this case the reduction of the hole size was 2 but the demagnification of the system was 4.

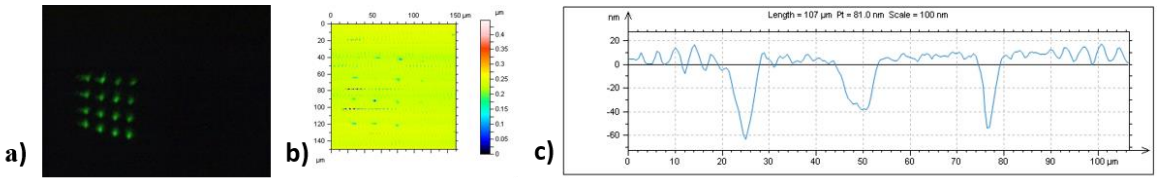

Figure 5. 41: a) Image on the screen of the 4 x 4 of 8.33 µm aperture on InP taken with 1 fps, Ip=6 pA, I_s=1.5 x 10^4 c/s; b) Image of the surface taken with the profilometer; c) profile of the fourth row mean diameter of the surface of the hole 4 µm, *hole reduction 2, system demagnification 4*.

This result shows that for holes with 8 µm diameter, the Caesium source presents also scattering effects. Limiting the minimum size of the holes for the aperture.

- ***Results from 6F with Cs^+ source of the apertures of 16 x 11.33 µm and 16 x 8.33 µm rastering:***

Figure 5. 42 presents the images of the screen of the AlCu grid made with the 16 x 11.33 µm aperture rastered with 15 µm, 25 µm and 50 µm, the last raster size recovers a complete image of the grid. Depending on the raster size the acquisition time of the camera was increased to have images with better quality. Figure 5. 43 presents the images on the screen of the grid made with the 16 x 8.33 µm aperture rastered the same distances as in Figure 5. 42, but the image of the grid is poorer reconstructed and have diffused edges than the images made with the aperture of 11.33 µm. This low-quality image is because the intensity of the secondary ions per beam was very low (lower than 10^3 c/s), so the signal to noise ratio is higher. Since this image was acquired with the longest time, the quality could not be improved.

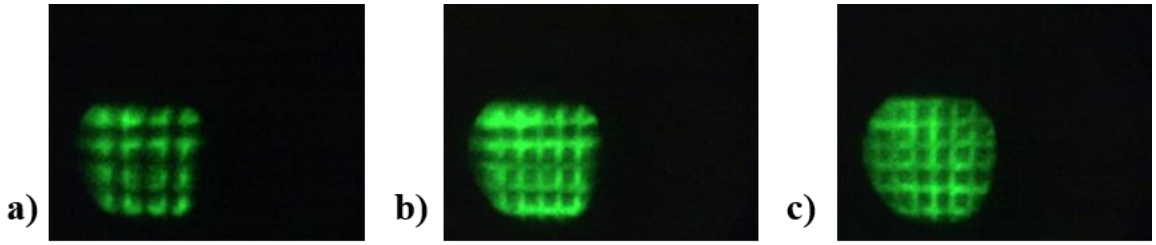

Figure 5. 42: Images of the grid with different raster sizes made with the 16 x 11.33 µm multi-hole aperture; a) 15 µm (10 fps); b) 25 µm (3 fps); c) 50 µm (3 fps).

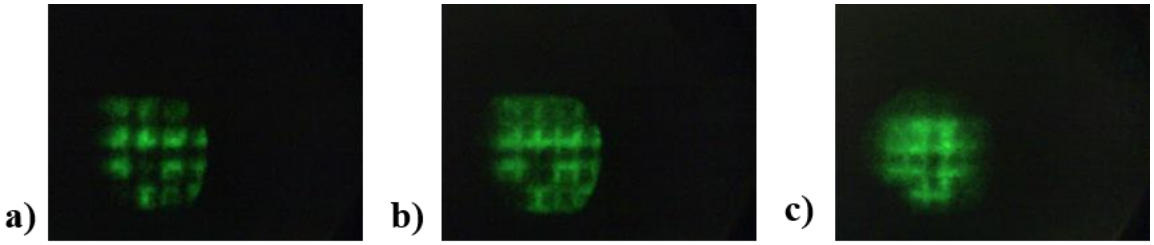

Figure 5. 43: Images of the grid with different raster sizes made with the 16 x 8.33 µm multi-hole aperture a) 15 µm (3 fps); b) 25 µm (2 fps); c) 50 µm (1fps).

5.5 Conclusions

- The results obtained from simulations and experimentally demonstrate that the multi-ion-beam is feasible technique to do SIMS imaging.
- With the aperture of 9 x 20 µm, 9 multi-ion-probes were generated with 5 µm diameter and 2,2 pA per beam. With the aperture of 16 x 11.33 µm, 16 beams of 5 µm diameter were generated with 2.35 pA per beam. With the aperture of 16 x 8.33 µm and 16 beams with 4 µm diameter with 0.375 pA per beam.
- The craters suggest that the illumination with both sources was *not homogeneous*. When the experiments were made with the caesium source, the craters had difference in height that varies 100 %. For the experiments done with the apertures 9 x 20 µm and 9 x 50 µm the craters had a slope in the bottom, from left to right varying 100%, even when the beam was rastered. When the apertures with 16 x 10 µm, and 16 x 5 µm were used the difference in height was also a 100%, but with a random distribution. The craters made with the Duoplasmatron source, showed a Gaussian profile for apertures larger than 50 µm, and a significant scattering effect, that produces magnified beams instead of demagnified beams for apertures smaller than 20 µm. This limits the possibility to generate Nano-beams with this type of Duoplasmatron sources.
- The intensity of the primary current was not constant through the different days of measurements in Köhler illumination when the Caesium source was used. The following table summarizes the differences:

Measurements	**Primary current**
Aperture diameter 264 µm **(Figure 5. 27b)**	1.5 nA

Aperture diameter 200 µm **(Figure 5. 32)**	0.12 nA
Aperture diameter 200 µm **(measurement with the last aperture)**	0.7 nA
Aperture diameter 200 µm **Maximum current registered (bad image)**	9 nA

Table 5. 3: Primary current values measured in different days in Köhler illumination with the caesium source.

- This difference in current implies that the illumination was not homogenous, and depends critically on the alignment of the aperture.
- The huge variation in the values of the primary current in Köhler illumination produces an inaccurate estimation of the minimum hole size that could be used. Furthermore, the variation in the current produces images of varied intensities, preventing to evaluate the multi-ion-beam precisely. This variation proceeds from the operating condition of the IMS 6F and is not a limitation of the technique.
- During the alignment of the multi-hole aperture with the caesium source in Köhler illumination, it was observed in some cases a multi-emission beam generating more images than expected and make the aperture alignment difficult.
- There is a challenge in the reduction of the hole size in the multi-hole aperture. For apertures of 8.33 µm the demagnification was a factor 2 for the holes but still a factor 3 for the complete optic system, suggesting that effects such as scattering can play a significant role, limiting the demagnification of the beam size. To circumvent this effect, the aperture profile of each hole should be like the standard ones (Figure 5. 27a) and the ratio of the aperture should be 1:1. So for making apertures with 1 µm diameter, the thickness should be 1 µm, reducing drastically the life time of the multi-hole aperture. A solution to this problem will be having a system with much higher demagnification factor, and a more parallel and homogeneous beam.
- This work was a proof-of-concept of the multi-ion-beam for imaging SIMS and showed that the multi-ion-beam system could be a powerful technique. Most of the limitations and difficulties found were regarding the conditions of the operation of the Cameca IMS 6F. For nano-scale probes a new system should be designed. A multi-beam-source with higher brightness and more homogenous

illumination should be used and a new detection system with larger dynamic range and better lateral resolution should be designed.

6 Conclusions and Outlook

Secondary ion mass spectrometry instruments should be improved to satisfy the demands of trends in fields such as nanotechnology, biology, materials science, etc, that require analytical tools that could map samples with not only with excellent lateral resolution, high mass resolution and high-sensitivity chemical information, but also with shorter analysis time.

In this thesis both problems were investigated. The first point was addressed investigating the enhancement of the performance of a double focussing mass spectrometer. To reduce the analysis time, a multi-ion-beam system for SIMS analysis was investigated and a proof-of-concept was done in the Cameca IMS 6F. In the following sections, the main conclusions and the outlook will be given.

6.1 Conclusions

6.1.1 Study of a new electrostatic analyser for the improvement of the mass resolution in a magnetic sector spectrometer

The improvement of the mass resolution in a double focusing mass spectrometer was investigated in the commonly used configurations: the Mattauch-Herzog and the Nier-Johnson by replacing the standard spherical sector by a novel spheroid geometry which has better focusing properties. Initially three analysers were designed using SIMION software: a spheroid similar to the literature; a hybrid, a modified spheroid with a third electrode and symmetric entrance and exit, and a 90° spherical sector. Their main focusing properties were compared, for parallel beams and focused beams, in retarding and deflecting mode. The spheroid geometries always showed better focusing properties.

Two designs were analysed to evaluate the performance of the spheroid geometries in the Mattauch-Herzog configuration: one with a simple combination with electrostatic sector and a basic magnet and the other one with a more sophisticated magnet designed at LIST. The investigation includes a comparison for each design with the spherical sector. A model of the secondary optics of the Cameca IMS XF was used as a Nier-Johnson configuration to compare the mass resolution of the original design with the spheroid and the spherical designed in this work.

- The spheroid geometry was simulated in this work by reproducing the design published by Cubric [13,52]. All the radii were exactly the same values, however the entrance and exit grids shape are very asymmetric and can be slightly different from the literature. Consequently, the spheroid reproduced had 3rd order focusing and not 13th as reported in literature. The conditions for higher order focusing were different from literature: the opening angle was 9° instead of 12°, the spot size was 8 μm (not 10 μm) and the energy resolution was 0.006%, (0.007% in literature). Except for the

opening angle, the other parameters were better than literature, which made sense to continue with the investigation. Another possible reason to have differences is the fact that for the high order of focusing the CPO program used in literature was different from SIMION and based on BEM technique. A new model of the spheroid geometry with a third electrode in order to couple the magnet and work in deflecting mode, named hybrid, was designed. In summary, the spheroid geometry presented in literature is a complex geometry, where any small detail of the entrance and exit grids can affect significantly the focusing properties of the analyser.

- Even if the spheroid and the hybrid geometries had smaller FW50 than the standard 90° spherical sector for source sizes smaller 100 µm, their spot size increase exponentially when the source size increase, so for Nier-Johnson configuration apertures or slits before the electrostatic sector should be less than 100 µm. (i.e. in the secondary optics of the Cameca IMS XF the CA should be 50 µm or 20 µm).
- The spheroid geometry had the best energy resolution of the three analysers, 0.006%, followed by the hybrid in retarding mode 0.36% and in deflecting mode out of central path 0.53%. The spherical sector was better than the hybrid in deflecting mode when the beam goes exactly through the central path 1.07% while the hybrid had an energy resolution of 1.52%. Therefore, the comparison in the Mattauch-Herzog was done between the spherical in deflecting mode and the hybrid in deflecting mode out of the central path.
- When the electrostatic sector was combined with a constant magnetic field perpendicular to the dispersion plane, the configuration with the spherical sector presented a smaller crossover, which means better mas resolution. The reason was that the spheroid geometry had a very strong focus point in XZ plane producing a big dispersion in Z direction. Therefore, a magnet with fringing fields to focus the beam in Z direction and to enhance the focusing in the dispersion plane replaced the constant magnetic field, and the spheroid was changed by the hybrid analyser, which distance to axis of rotation was modified obtaining a weaker focus point in the XZ plane and the size was reduced to the half to have a beam entering the magnet gap smaller than 5 mm. The MRP was around 300 for masses smaller the 49, and 400 for higher masses, for configurations with both sectors.
- An analysis of the double focusing condition showed that the focus in angle and in energy were not at the same place and the energy dispersion of the magnet was three times the value of the half size modified hybrid. An evaluation of the performance of both configurations without energy spread, showed that the hybrid configuration performs two times better than the spherical configuration for high masses. This suggests that if the double focusing condition is optimized, the mass resolution could be enhanced by only changing the electrostatic sector in a Mattauch-Herzog configuration.
- An evaluation of the mass resolution was done using the secondary optics of the Cameca IMS XF, a Nier-Johnson type spectrometer. Three configurations were compared: the original, one with the

spherical sector designed in this work and one with the spheroid. To make the comparison exactly in the same conditions of original design opening angle 1.7°, the central part of the entrance and exit shunts was reduced in the spherical sector designed in this work, and a round aperture was incorporated in front of the entrance grid of the spheroid to limit the opening angle to 1.7°. The MRP of both spherical configurations was 13,076 and a total transmission was 2.7-2.8%. The height of the peaks of the configuration with spherical designed in this work was two third times the height of the original design. This arise from the differences between both spherical sectors, essentially the gap distance, but also a round aperture in the original case compared a rectangular aperture in the other case, distances between shunt and electrodes. The MRP of spheroid configuration was 3,178 and total transmission of 5%. These results show that the configurations with the spherical sectors has four times better mass resolution, however the sensitivity was two times better for the spheroid case.

- The analysis of the beam shape after the magnet showed that the beam in the spheroid configuration seems to be rotated 90°, not obtaining a vertical line at any position, instead was obtained a horizontal line, affecting the size of the beam in the dispersive plane, degrading the mass resolution.
- The beam behaviour after the exit of the spheroid is complex. The difference in the focus points coming out from the spheroid in XY plane and in XZ plane remains through the optics generating a mismatching in the angle focus of the spectrometer.
- The spheroid analyser is a more challenging geometry to design and build than the spherical sector, the transmission is also lower because of the grids, but results in the Nier-Johnson configuration showed two times larger transmission values. Furthermore, the results showed that combining the spheroid in configuration based on the Mattauch-Herzog concept, with a magnet designed especially for the spheroid optics, could result in spectrometers with better mass resolution or sensitivity.

6.1.2 Surface Analysis by SIMS with a Multi-Ion Beam

A multi-ion-beam system was investigated by simulations and tested experimentally in a Cameca IMS 6F. The transport of nine beams, departing from the sample with 1 µm diameter arranged in a square matrix 3 x 3, through the secondary optics of the spectrometer was analysed. The simulations were carried out for varied distances between holes of 3 µm, 5 µm and 10 µm and for different magnification values.

Later a characterization of the beam in Köhler illumination with duoplasmatron O_2^+ was done in the Cameca IMS 4F. Because the results were not as good as expected, a second characterization with the Caesium source was done in the IMS 6F, obtaining results in agreement with literature. A multi-

hole aperture was designed according to the beam characteristics and subsequently was mounted in the instrument to complete the proof-of-concept. The nine beams were transmitted successfully through the complete instrument, primary and secondary optics. The following conclusions can be drawn from the simulations and the experimental results:

- The results obtained from simulations and experimentally demonstrate that the multi-ion-beam is feasible technique to do SIMS imaging.
- The secondary optics of the Cameca IMS XF showed in the simulation that the minimum distance between the beams arriving at the sample should be 3 µm, independently of the size of the beam diameter (1 µm or 200 nm) and the values of the contrast aperture (50 µm or 400 µm). The best condition was for beams separated 10 µm at the sample and magnification 4.
- The intrinsic limitation to the lateral resolution in the secondary optics arose from the fact the background contribution of each beam behaves like a Lorentzian function and the limitations of the detection system.
- The size of the minimum size of the holes obtained with the aperture 9 x 20 µm was 5µm diameter and with 2,2 pA per beam. With the second aperture 16 x 11.3 µm, the size of the holes was also 5 µm diameter with 2.35 pA per beam. These current values correspond to beam sizes of 1 µm diameter, which means one order of magnitude smaller than standard operation for these sizes (Nakashima 2012).
- The spots obtained with the Duoplasmatron (O_2^+) showed an incoherence between the demagnification of the complete aperture and the size of the holes. For the 50 µm aperture the demagnification of the system was 4 while the reduction of the hole was only 1.5. This effect was increased when the size of the aperture was reduced to 20 µm. The demagnification of the system still was 4, but the size of the beam was increased and became elliptical. This effect was also observed with the caesium source for the apertures with 8.33 µm diameter. The system demagnification was 4 and the reduction of the hole was 2. A possible explanation for this effect is the scattering of the ions inside the hole of the aperture. The effect is significantly larger with the duoplasmatron because the species (O_2^+) are five times lighter that the $_{133}Cs^+$. Furthermore, the energy spread of the source is two orders of magnitude larger than the energy spread of the caesium source, producing a beam with bigger chromatic aberration through the system. The spherical aberrations are also larger in the duoplasmatron source, therefore, the ions coming out from the source have larger energy spread and angle spread enhancing the scattering effect.
- The analysis of the craters shape suggested that the illumination of both sources was *not homogeneous*. In several measurements, the craters produced with the caesium source presented a variation in height of 100 %. The craters made with the duoplasmatron source, showed a Gaussian profile for apertures larger than 50 µm, and for apertures smaller than 20 µm while the overall hole

pattern is correctly demagnified, the individual spots are actually larger. As described above, this may be caused by higher scattering at the edges of the apertures as the effect was worse for the lower mass O2+ ions than Cs+. This limits the possibility to generate nano-beams with this type of duoplasmatron sources in this mode of illumination.

- Another issue observed in the Cameca instrument was that the intensity of the primary current of the caesium source was not constant through the different days of measurements in Köhler illumination, the variation was of one order of magnitude for the same aperture. This could be because of the difficulty to align the multi-hole aperture. during the alignment of the beam, it was observed multi-emission when the first lens of the primary column was adjusted, consequently several beams were overlapped mixed with the images of the multi-ion-beam. Furthermore, the precision of the current measurements indicates a fluctuation of the beam and of the measurement system. This variation in the current reflects that the illumination was not homogeneous.
- The huge variation in the values of the primary current in Köhler illumination produces an inaccurate evaluation of the technique, because the image changes the intensity and the resolution of the image is affected. Moreover, the variation could lead to wrong estimation of the minimum size hole that could be used. This variation proceeds from the operation condition of the IMS 6F and is not a limitation of the technique.
- A challenge of the technique will be the reduction of the hole size in the multi-hole aperture. For apertures of 8.33 µm the demagnification was a factor 2 for the holes but still a factor 4 for the complete optic system, suggesting that effects such as scattering can play a significant role, limiting the demagnification of the beam size. To circumvent this effect, the aperture profile of each hole should be like the standard ones (Figure 5. 29a) and the ratio of the aperture should be 1:1, meaning that apertures with 1 µm diameter should be 1 µm thin, reducing drastically the life time of the multi-hole aperture. A solution to this problem will be having a system with higher demagnification factor, and a more parallel and homogeneous beam.
- This work was a proof-of-concept of the multi-ion-beam for imaging SIMS and showed that the multi-ion-beam system could be a powerful technique. Most of the limitations and difficulties found were regarding the conditions of operation of the Cameca IMS 6F. For nano-scale probes a new system should be designed. A multi-beam-source with higher brightness and homogeneous illumination should be used, apertures with the standard profile and proportions should be made, a new detection system with better dynamic range and lateral resolution should be designed.
- The technique will face new challenges for nano-scale probes: The correct pitch between the beams to obtain a good lateral resolution: in the Cameca IMS XF the minimum limit was 3 µm (by simulations). But also, an accurate and precise raster to scan each region with correct size, and do not over or under raster certain regions of the sample. The off-axis aberration can start to play a more significant role, the apertures should be design with the profile shown in (Figure 5. 28). The

demagnification system should be more powerful than 5, to avoid making apertures very thin (short life time) and the size of the hole will not be so small and the scattering phenomenon will be reduced. The detection system should have a good detection efficiency and the crosstalk should be reduced to the minimum.

6.2 Outlook

6.2.1 Study of a new electrostatic analyser for the improvement of the mass resolution in a magnetic sector spectrometer

The results obtained in chapter 4 showed that the spheroid geometries have better focusing properties than the spherical sector. However, when the sector is combined with the magnet this does not necessarily translated in better performance. From the conclusions it was deduced that there is still a potentiality that the spheroid sector can improve the performance in double focusing mass spectrometers. To complete the investigation it is necessary to make a new design based on the Mattauch-Herzog configuration, optimizing the double focusing condition, and adding a magnet with fringing fields especially design for the spheroid optics.

6.2.2 Surface Analysis by SIMS with a Multi-Ion Beam

The results obtained with the simulations and experimentally showed that the multi-ion-beam technique could become an important tool in the field of imaging SIMS. However, it is necessary to improve the actual system to produce a dedicated instrument for multi-ion-beam.

The main components to improved will be the primary optics and the detection system. Since it is fundamental to have high intensity currents and homogenous illumination, a better option will be to use a model with multiple sources and a single column (fig Figure 5. 1b). This concept simplifies the optics because it is not necessary to make an independent column for each source, reducing the size of the instrument and allowing to incorporate more sources. The real challenge in this configuration is to obtain an array of sources with high stability, high brightness and low energy spread. It should deliver also species like caesium or oxygen, because they enhance the secondary ion yields. One possibility to obtain a multi-ion source based on the concept proposed by Kruit [111,123,124] where an electron beam coming out from a Shottky source is divided by an aperture array that divides the beam in 100 beams plus an microlens array which produce 100 images sources and a blanket array which deflects each beam. A possible source could be the Hyperion plasma source that can deliver for example O_2 and Ar, with one order of magnitude better brightness, with less energy spread (5-6 eV) [125].

6. Conclusions

The actual detection system has very limited capabilities the detection efficiency is limited to open area of the MCP, which is less than 50%, a low dynamic range limit by standard camera of 8 bits (total dynamic range of 256) limiting high resolution images in SIMS where the dynamic range is in order of 10^9, a medium/low spatial resolution, the MCP/FS system in microscope mode for 150 FOV is 1 µm and time response limited to the phosphor decay [84].

A more adequate detection system could be an arrangement of miniaturize electron multipliers, who's dynamic range is 10^6, the spatial resolution could be similar to the NanoSIMS, nanometre resolution. Each electron multiplier should be synchronised in time with the raster position on the sample, therefore for an arrangement of 25-30 beams, each raster region corresponds to a single EM, so each detector only counts the information coming from one beam. The principles are the same that are used for microprobe imaging, but with several EM.

The challenge would be for 100 beams, thus a funnel type MCP which has an open area of 90% could be combined with different devices such as a resistive anode encoder or an active pixel detector like the Timepix detector [125] or an MCP with a cross strip read out .

7 Appendix : Résumé français de la thèse

7.1 Introduction :

La Spectrométrie de masse des ions secondaires (SIMS, Secondary Ion Mass Spectrometry) est une technique puissante qui a une excellente sensibilité (parties par million/milliard ; ppm/ppb), une grande dynamique de détection [1], une très haute résolution en masse [2] et qui dispose d'une capacité unique pour l'analyse isotopique [3]. Cette technique est largement utilisée pour l'analyse des surfaces et permet aussi de déterminer la composition des échantillons et d'obtenir des images ioniques de leur surface et de la distribution des constituants en profondeur. Il est possible de construire des images 2D et 3D de la composition des échantillons avec une résolution spatiale de quelques dizaines à centaine de nm sur la surface et à l'échelle nanométrique en profondeur. Le SIMS est devenu un outil fondamental de caractérisation nanométrique dans de nombreux domaines, tels que les semi-conducteurs [4], la biologie [126], la métallurgie [6], la science des matériaux [7], la cosmochimie [8], etc...

Malgré tous ces avantages plusieurs aspects peuvent être améliorées dans le cadre de l'imagerie SIMS tels que : la résolution spatiale latérale (autour de 50 nm), le temps d'analyse, la résolution en masse, la gamme dynamique, la sensibilité. Certains de ces points ont été étudiés dans cette thèse. Les dernières tendances pour obtenir des images avec la meilleure résolution spatiale avec le SIMS consistent à combiner deux ou plusieurs techniques dans un seul instrument. L'imagerie des échantillons allie simultanément une très haute résolution spatiale et une grande sensibilité entre espèces chimiques. En effet, les images à très haute résolution donnent habituellement peu d'informations pour différencier les espèces chimiques et vice versa.

Ainsi, en combinant des microscopes tels que TEM, HIM, SEM à fort pouvoir de résolution avec l'imagerie par spectrométrie de masse (MSI, Mass Spectrometry Imaging), les limitations intrinsèques des premiers pourraient être compensées par l'apport du second. Cette combinaison d'images multimodales est une avancée technique récente appelée « microscopie corrélative ». Toutefois, les spectromètres de masse de haute performance sont très encombrants et il est nécessaire d'optimiser leur conception pour développer des modèles plus compacts.

Le laboratoire LIST tient compte de ces contraintes pour développer plusieurs types d'instruments. Le premier est réalisé autour d'un TEM dédié pour être le premier prototype combinant SIMS et TEM [11]. Il est actuellement équipé d'une colonne ionique focalisée de Gallium (Focus Ion Beam, FIB) et d'un spectromètre de masse magnétique. Le second instrument associe les techniques HIM et SIMS

[12]. Dans ce cas, le faisceau dédié initialement à l'imagerie est utilisé pour la spectrométrie de masse. Le développement consiste à fabriquer le système d'extraction et le spectromètre de masse.

Afin d'optimiser les performances, la ***première partie de la thèse examine les possibilités d'améliorations de la résolution en masse des spectromètres de masse à double focalisation*** avec des simulations d'optique de particules chargées (CPO). Le but était de remplacer le secteur sphérique standard par une nouvelle géométrie avec un sphéroïde qui possède de meilleures propriétés de focalisation. Ceci doit permettre d'améliorer la résolution en masse et la sensibilité.

La deuxième partie de la thèse, porte sur l'amélioration du *temps d'analyse* dans le cas d'imagerie avec le SIMS. Les hautes résolutions en imagerie SIMS peuvent atteindre voire être inférieures à 50 nm. Cependant, c'est au détriment de l'intensité du faisceau car pour obtenir une sonde nanométrique, l'émittance doit être réduite. Cette nécessité conduit à des courants de l'ordre du pA ou moins, qui impose des temps d'analyse longs pour pulvériser une quantité minimale de matériaux pour obtenir une image ionique. Par exemple, une image complète des bivalves marins obtenus avec l'instrument NanoSIMS de Cameca en mode mosaïque, une superficie de 300 µm x 800 µm (3 x 8 carreaux avec 256 x 256 pixels par tuile), une taille de trame de 100 µm (taille du pixel = 390 nm) et un temps de 120 minutes par tuile, demandera environ deux jours de fonctionnement continu [15]. Ces temps d'analyse font de l'imagerie SIMS haute résolution une technique inappropriée pour l'analyse des grandes surfaces, de l'ordre du centimètre [16] , ou la reconstruction 3D.

Dans ce travail, ***la réduction de temps d'analyse a été abordée en mettant en œuvre le concept de multi-faisceau d'ions dans le Cameca IMS 6F du laboratoire***. Le but est de bombarder l'échantillon avec plusieurs nano-micro faisceaux primaires, afin d'accroître considérablement le débit d'analyse en haute résolution. Cela pourrait se faire en combinant les deux modes de fonctionnement présent dans les instruments de Cameca IMS 4F/6F (microscope et microsonde ionique) en l'associant à un collimateur multi-trous spécialement conçu et monté dans la colonne primaire.

7.2 Etude d'un nouvel analyseur électrostatique pour l'amélioration de la résolution de masse de spectromètre magnétique :

Ce nouvel analyseur de type sphéroïde [13,52] présente à la fois une excellente focalisation au 13ème ordre, une dimension du faisceau focalisé 10 fois plus petite et une acceptance angulaire 4 fois plus élevée que celles de l'analyseur sphérique. Ces caractéristiques pourraient conduire à réaliser des spectromètres de taille équivalente, en préservant une meilleure résolution en masse et une meilleure sensibilité.

Les caractéristiques de cet analyseur ont été évaluées avec le logiciel SIMION, la géométrie du sphéroïde a été reproduite à l'identique de celle décrite dans la littérature. Les propriétés optiques obtenues ont été comparées avec celles de la littérature. L'analyseur de sphéroïde reproduit dans cet ouvrage est légèrement différent de celui réalisé par Cubric car celui-ci est développé pour l'analyse en énergie des électrons (Figure 7. 1a). Son adaptation comme analyseur en spectrométrie de masse présente certaines difficultés au niveau de la forme de l'injection et de la sortie du sphéroïde. Concernant la simulation, l'introduction des grilles a nécessité quelques approximations et adaptations. Une taille de grille de 10 µm (à la place de 100 µm) a été employée pour obtenir une meilleure précision pour modéliser la géométrie. La grille d'entrée est modélisée comme un « escalier » plutôt que d'une surface lisse pour permettre son alignement avec la maille carré. Ainsi, les particules qui atteignent les différents échelons sont déviées un peu différemment, et par conséquent la dispersion des particules élargit le « crossover » au point de focalisation. L'élargissement obtenu était d'environ 60 µm tandis que dans la littérature il est de 300 µm (sans optimisation) (Figure 7. 1b).

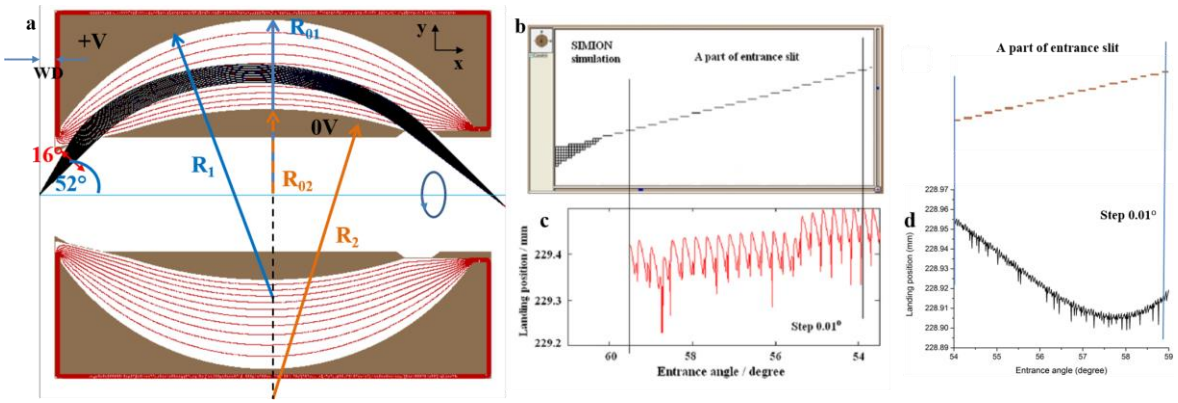

Figure 7. 1: a) Schéma de la géométrie sphéroïde avec les paramètres principaux. Les particules - en noir - partent avec un angle d'ouverture de 16 °, de 44 ° à 60 °, les lignes équipotentielles sont en rouge. V = 300 V ; R1 = 124 mm ; R2 = 220 mm ; R02 = 24,5 mm; R01 = 87,5 mm, énergie des particules = 645 eV, WD = 7,6 mm. Le crossover n'est pas sur l'axe. b) Section transversale de la petite partie de la fente d'entrée, a) reproduite de [13] et b) reproduite dans ce travail. Dans les deux cas, l'escalier est observé. C) Crossover des électrons suivant des trajectoires angulairement espacées de 0,01 ° à l'entrée, élargissant 300 µm reproduit à partir de [13]; D) simulation similaire avec des ions positifs espacés angulairement de 0,01 °, (V / E = 0,45) s'élargissant autour de 60 µm, cinq fois plus petit que [13].

La *technique « boundary matching technique »* a été implémenté dans SIMION pour résoudre le problème de l'escalier, parce que cela détériorait la taille du faisceau focalisé. Cette technique est utilisée pour ajuster les valeurs de potentiel entre différents tableaux de potentiels de SIMION qui se chevauchent. Cela garantit que le potentiel varie en douceur et continuellement quand les ions/électrons

passent d'un PA à l'autre. L'idée était de concevoir un petit PA reproduisant la géométrie de la fente d'entrée, alignée avec la maille. Une ligne droite est alors reclassée au lieu de l'escalier.

Après l'implémentation de cette amélioration la réduction de la taille du faisceau focalisé était environ 10 μm, ce qui ne représente que de 15 % d'améliorations. En effet, ce résultat est une conséquence du fait que la largeur totail du faisceau est une combinaison des propriétés intrinsèques de focalisation de l'analyseur et de l'oscillation résultant de l'effet d'escalier. Dans la littérature, ce problème a été résolu à l'aide d'un logiciel CPO différent (basé sur la technique de «boundary element method BEM »), combiné avec le processus d'optimisation pour obtenir un dispositif plus performant de focalisation.

Afin d'obtenir un ordre supérieur de focalisation, l'analyseur doit être ajustés parfaitement. La procédure a été identique à celle de la littérature et, les conditions obtenues sont : α= 50,8 °, WD =8,6 mm, V/E = 0.45 et angle d'ouverture de 9 °. Ces conditions sont différentes de celles obtenuees par Cubric : α= 47 °, WD = 11,6 mm, V/E = 0,41, angle d'ouverture de 12 °. Les raisons sont dues à des différences mineures entre les fentes d'entrée et de sortie et au logiciel utilisé pour simuler les valeurs optimisées.

La courbe a été mieux ajustée au niveau de la zone de focalisation ; elle était du quatrième ordre polynomial, alors que pour le concept introduit par Cubric [13], le sphéroïde était au troisième ordre de focalisation. La résolution en énergie a été calculée de manière équivalente, au travail de Cubric elle est de0,006 % ce qui est légèrement mieux que la valeur des travaux de Cubric qui est de 0,007 %.

Tous les secteurs électrostatiques étant utilisés comme déflecteur du faisceau dans les spectromètres de masse à double focalisation, le sphéroïde a pu être modifié pour fonctionner en mode de déviation en ajoutant une troisième électrode reliée à la masse du dispositif. Il a été nommé hybride. Les formes asymétriques des fentes d'entrée et de sortie ont été supprimées ; la forme est totailment symétrique et des grilles idéales couvrent les fentes d'entrée et de sortie (Figure 7. 2b).

En outre, un secteur sphérique (Figure 7. 2a) avec un rayon moyen égal à 64 mm identique au rayon moyen du sphéroïde et de l'hybride (65 mm), avec une symétrie rotationnelle, semblable à celle du sphéroïde, a été conceptualisé afin de faire des comparaisons de performances entre les trois analyseurs seuls et associés avec le secteur magnétique. Les fentes ont les paramètres Herzog suivantes : distance entre les électrodes et les fentes d = 0,4 g_0 ; taille de l'ouverture de 2h = g_0 (R_a=80 mm ; R_b=48 mm, gap taille $2g_0$=16 mm ; d=6,4 mm ; h=4 mm). Le potentiel extérieur était de 2300 V, le potentiel intérieur était de -2000 V et l'énergie moyenne des ions est de 4500 eV.

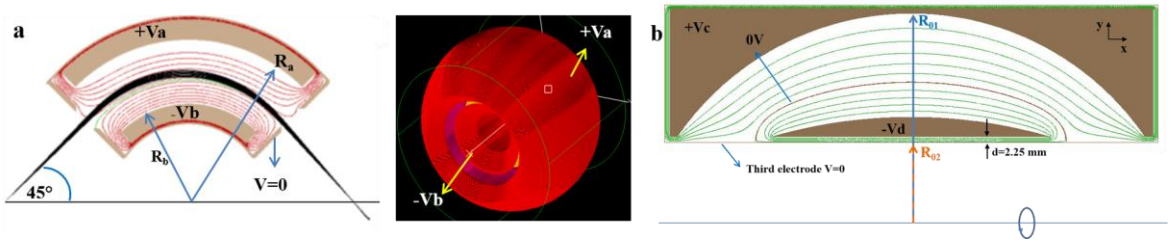

Figure 7. 2: a) Une coupe transversale dans le plan XY d'un secteur sphérique de 90° avec une symétrie de rotation en 3D. b) Schéma de l'hybride avec des fentes d'entrée et de sortie symétriques et la troisième électrode. Les potentiels sur les électrodes sont réglés pour dévier les ions positifs. Le rayon a les mêmes valeurs que le Sphéroïde : R1 = 124 mm ; R2 = 220 mm ; R02 = 24,5 mm; R01 = 87,5 mm .:

Plusieurs caractérisations ont été faites avec les trois analyseurs pour comprendre leurs propriétés de focalisation. Tout d'abord, la largeur à mi-hauteur FW50 a été obtenue en fonction de la taille de la source.

Premièrement, la taille de la source couvrait un large éventail d'une source ponctuelle jusqu'à une source de 100 µm de diamètre, le sphéroïde et l'hybride ont donné des tailles de faisceaux plus petites que le secteur sphérique. Des études et résultats similaires ont été obtenus avec des faisceaux parallèle (configuration du spectromètre de masse type Mattauch-Herzog) et focalisé (configuration du spectromètre de masse type Nier-Johnson) à la sortie du secteur électrostatique

Deuxièmement, les trois analyseurs, le sphéroïde, l'hybride et le secteur sphérique ont été comparés dans les mêmes conditions suivantes : un champ de ralentissement a été appliqué, où l'énergie centrale était de 4 500 eV et deux autres faisceaux avec une différence d'énergie ± 0,45 eV (la différence d'énergie représente 0,01 % de l'énergie centrale). L'écart angulaire total était de 8° et une source ponctuelle. L'angle au centre du sphéroïde a été de 50,8 °, 52° pour l'hybride et de 45° pour le secteur sphérique. La résolution en énergie a été de 0,006 % pour le sphéroïde; de 0,36 % pour l'hybride et de 1,76 % pour le sphérique. Sans équivoque, la géométrie sphéroïde a une meilleure résolution en énergie.

Une comparaison entre l'hybride et le secteur sphérique a été effectuée en mode de déflection. Les conditions sont les mêmes que précédemment. L'angle central pour l'hybride était 44,63 ° et 45° pour le secteur sphérique. Le potentiel externe a été calculé pour que les trajectoires soient exactement au milieu des électrodes. La résolution en énergie pour le secteur sphérique était de 1,07 % et de pour 1,56 % l'hybride. Cela implique que l'hybride n'est pas plus performant que le secteur sphérique en mode de déflection. Si le potentiel externe est légèrement modifié, pour que les trajectoires des particules de 4500 V passent plus près de l'électrode intérieure, dans ce cas nous retrouvons des caractéristiques semblables au mode retardateur, soit une résolution en énergie de 0,53 % avec un potentiel de 1,650 V

pour l'électrode externe et 1050 V pour l'électrode interne. La résolution en énergie est alors améliorée d'un facteur 3 et deux fois meilleur que celle du secteur sphérique.

Finalement, une comparaison entre les performances des spectromètres de masses type Mattauch-Herzog, avec le sphéroïde et le sphérique a été réalisé. Au départ, les deux secteurs électrostatiques ont été combinées avec un aimant rectangulaire simple et un champ magnétique constant (B=0.8T) perpendiculairement à la direction de dispersion. Les conditions de la simulation étaient : 10,000 ions de masse 200, une source circulaire de 100 μm de diamètre avec une distribution angulaire de 4°, l'énergie de la particule était de 4,500 eV, sans dispersion d'énergie. Il a été observé que le secteur sphérique a une faible focalisation et donne un faisceau presque parallèle dans le plan XZ, tandis que le sphéroïde a un très fort effet de focalisation ce qui produit une énorme dispersion du faisceau dans la direction Z et donc dégrade la résolution de masse. Pour réduire cet effet deux dispositions ont été prises : premièrement, le faisceau a été parallélisé en ajoutant 80 mm à la distance de l'électrode intérieure par rapport à l'axe de rotation. Ainsi la focalisation dans le plan XZ était beaucoup plus faible avec un décalage du faisceau vers la droite permettant un résultat plus proche de celui de l'analyseur sphérique. Deuxièmement, un aimant plus sophistiqué, conçu au LIST, avec 0,8 T et des champs correctifs a permis la convergence du faisceau dans la direction Z et l'amélioration des propriétés de focalisation dans le plan de dispersion. Le secteur magnétique a été également réduit de moitié pour garder la largeur du faisceau dans la direction Z à moins de 5 mm, respectant ainsi l'écart de taille des aimants utilisés dans les simulations. Huit masses différentes ont été simulées (9, 25, 49, 81, 121, 169, 225 et 289 u) avec les mêmes contions que précédemment et une dispersion d'énergie de 10 eV. Les deux systèmes ont un pouvoir de résolution similaire, les valeurs variaient de 300 pour les masses inférieures à 50 et environ 400 pour les masses plus élevées, le secteur sphérique est légèrement meilleur pour les masses inférieures à 200 u.

Pour comprendre ce résultat, la condition de double focalisation a été analysée, montrant un décalage de la position de focalisation en angle et en énergie, et aussi une valeur de dispersion de l'énergie 3 fois plus petite que la dispersion de l'aimant. Une simulation rapide sans dispersion d'énergie a montré un pouvoir de résolution en masse deux fois plus grand que pour la configuration hybride. Ceci indique qu'il est possible avec un aimant qui s'ajuste correctement à la géométrie sphéroïde, d'obtenir une meilleure résolution en masse que celle d'un spectromètre de la même taille avec le secteur sphérique.

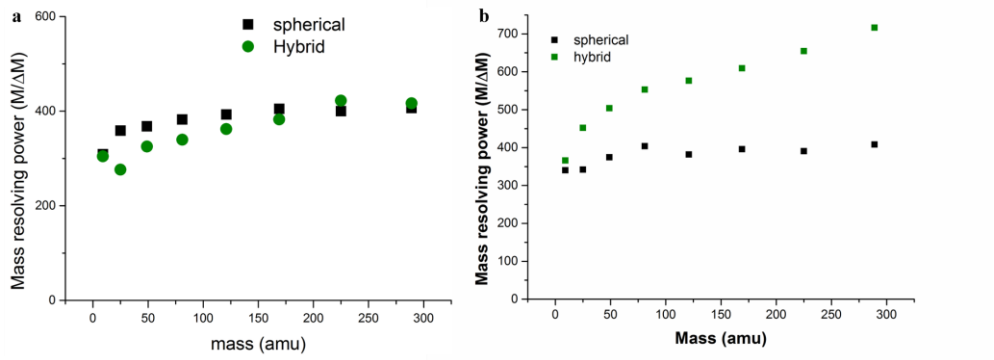

Figure 7. 3: a) Puissance de résolution de masse des deux configurations avec un secteur hybride et sphérique modifié. Les deux configurations se comportent de manière similaire, mais la sphérique est légèrement meilleure pour les masses inférieures à 200 u. b) Résolution de la puissance de masse obtenue sans propagation de l'énergie. Le sphéroïde a des valeurs légèrement meilleures pour les masses faibles, mais pour les masses les plus élevées, les valeurs sont deux fois sphériques. Cela ouvre la possibilité d'obtenir une meilleure résolution de masse pour la configuration hybride si la dispersion de l'énergie est bien adaptée.

Les dernières simulations ont permis une comparaison entre les performances des spectromètres de masses type Nier-Johnson, équipés soit avec le sphéroïde soit avec le secteur sphérique. Enfin, les deux analyseurs sphéroïde et sphérique conçus au cours de ce travail ont été insérés dans un modèle de l'optique secondaire du spectromètre Cameca XF séries fourni au LIST par J. Lorincik [108]. Une comparaison de la résolution en masse à la sortie de l'aimant a été realiseé pour les trois configurations dans les conditions suivantes : 50,000 particules pour chaque masse, masses 17 et 17.02, une surface de 1 µm, une énergie de liaison de surface U= 4 eV, le potentiel appliqué sur la lentille du spectromètre 2,850 V, seulement la dernière lentille de transfert a été mise sous tension à 4,234 V, la tension de l'échantillon 4,500 V, la tension de la lentille d'immersion 3,208 V , diaphragme de contraste 50 µm, aucun collimateur de champ, les fentes de sélection en énergie et de sortie grandes ouvertes. Toutes les tensions proviennent de [5] et sont en accord autour de 4 % des valeurs mesurées dans le spectromètre de 4f IMS du LIST. Dans tous les cas, les particules ont été générées par un programme utilisant une méthode de Monte Carlo pour reproduire la distribution en énergie et angulaire des particules suite au phénomène de pulvérisation. L'angle d'ouverture dans les trois cas a été mesuré et adapté pour être le même, 1,7 °. Pour cette raison, le secteur sphérique conçu dans cet ouvrage avait une réduction de l'espace de la partie centrale à l'entrée et à la sortie, et l'angle d'ouverture du sphéroïde était limité en introduisant un collimateur rond devant la grille d'entrée.

Le pouvoir de résolution en masse pour les deux configurations de secteur sphérique était de 13,076 et une transmission de 2,7-2,8 %. Cependant, la hauteur des pics pour le sphérique conçus dans ce travail était de deux tiers de la hauteur de la conception originale en raison de la différence d'espace

vide entre eux. Le pouvoir de résolution en masse de configuration avec le sphéroïde était de 3,178, quatre fois plus petite, mais la transmission totale était de 5 %, deux fois supérieure à celle des configurations sphériques.

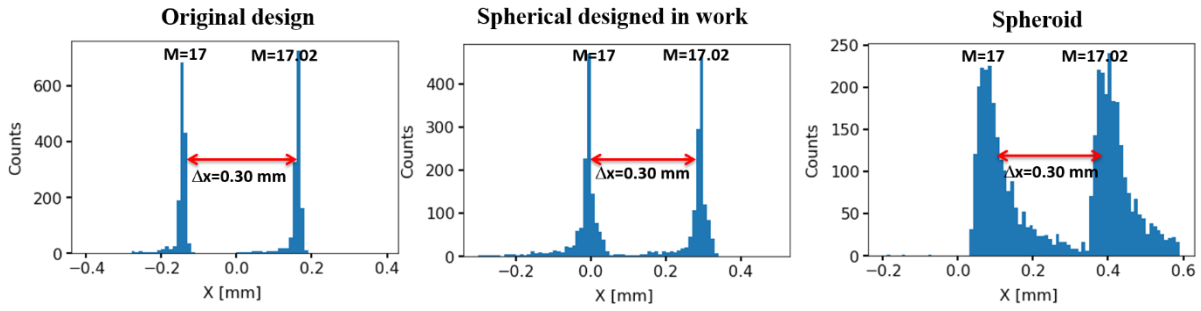

Figure 7. 4: Spectres de masse obtenus dans le plan focal de chaque configuration. La conception originale a le plan de focalisation à y = -378 mm, M / ΔM = 13,076; Le sphérique conçu dans ce travail a son plan focal à y = -368 mm, M / ΔM = 13,076, égal à la conception originale. La configuration sphéroïde se focalise à y = -393 mm et M / ΔM = 3,178. La résolution en masse de la configuration sphéroïde est quatre fois plus petite que les configurations avec le secteur sphérique.

7.3 Analyse de surface par SIMS avec un Multi-Faisceau d'ions :

Les instruments de Cameca IMS XF sont particulièrement commodes pour réaliser des tests du concept de multi-faisceau d'ions pour le SIMS parce qu'ils possèdent deux modes de fonctionnement, généralement implémentées indépendamment, le mode microscopie et le mode de la microsonde. Dans le mode de la microsonde, un faisceau primaire finement focalisé (plusieurs centaines de nm à quelques µm) balaye la surface de l'échantillon tandis que les ions secondaires transmis par le spectromètre de masse sont corrélés avec la position du faisceau primaire et une image avec une résolution spatiale proche de la taille de la sonde est ainsi obtenue. Dans le mode microscope, le faisceau primaire est beaucoup plus large (40 µm ou plus), tous les points sont imagés simultanément dans le champ visuel en temps réel, rendant le temps d'acquisition très rapide. La résolution d'image est limitée par l'optique secondaire qui est plus faible que la résolution du mode microsonde.

En combinant les deux modes simultanément, un nouveau mode hybride est créé, à l'aide d'une platine de collimateurs constituée de plusieurs trous montés dans la colonne principale, qui génère le système multi-faisceau. En utilisant le mode microscope, l'optique principale est réglée suivant le mode de Köhler, ce qui donne une image du collimateur « multi-trou » sur l'échantillon. En outre, l'optique secondaire stigmatique concentre le multi -faisceau sur un détecteur sensible en position (MCP) qui

donne la contribution de chaque faisceau dans l'espace. L'électronique de la microsonde fournit la fonction de balayage en trame du faisceau, donc le faisceau multiple d'ions traversant l'optique principale et axé sur l'échantillon, peut balayer l'échantillon exactement de la même manière qu'un faisceau de microsonde et ainsi imager la cible.

Les performances du faisceau multiple qui passe dans le spectromètre de masse (optique secondaire) ont été d'abord étudiées au moyen de simulations CPO. La distance minimale entre les faisceaux sur l'échantillon permettant une séparation nette au niveau de la détection par les galettes à micro canaux a été déterminée. Les conditions de ces simulations étaient 50,000 particules avec un diamètre de 1 µm généré par la méthode de Monte-Carlo centrées sur l'axe optique, (0,0). Un balayage en ligne de l'image enregistrée sur le MCP, était reproduit par une fonction lorentzienne pour tenir compte de la queue de la fonction. Cela conduit à une limitation de la résolution latérale, lorsque la distance des faisceaux au départ de l'échantillon se rapproche, le chevauchement de ces queues de faisceaux augmente le bruit de fond et réduit la qualité de l'image pour chaque spot. Il s'agit d'une limitation de l'optique secondaire de l'IMS 6F.

Dans une seconde étape, l'émission des ions secondaires provenant de l'échantillon a été simulée comme neuf différentes sources équidistantes disposées dans une matrice carrée. Les spots étaient des surfaces circulaires de 1 µm de diamètre, 20,000 ions ont été générés pour chaque spot, (total de 180,000 ions). Les distances entre les centres sont : 10 µm, 5 µm, 3 µm, le diamètre du diaphragme de contraste était de 50 µm et les tensions des lentilles de projection ont été ajustées dans chaque cas pour trouver la meilleure combinaison. Celle-ci correspond à des spots séparés de 10 µm sur l'échantillon et un grandissement de 4.

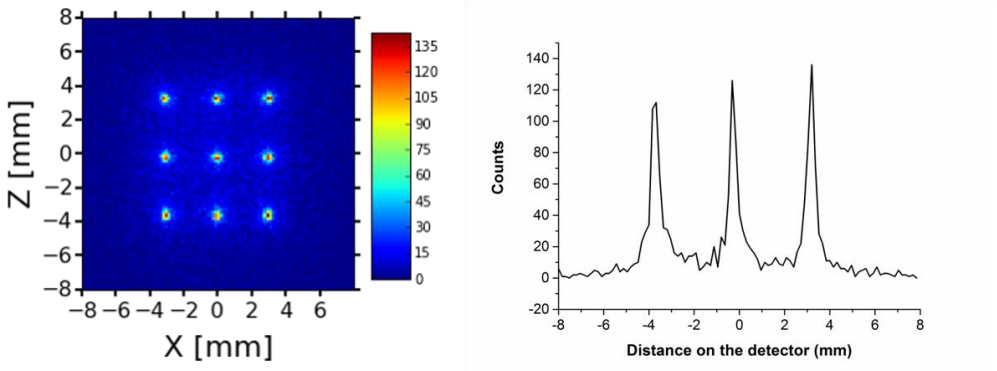

Figure 7. 5: A gauche : l'histogramme 2D a enregistré sur le détecteur concernant de 9 points sur l'échantillon avec 1 µm de diamètre, séparé 10 µm; À droite: analyse par ligne de la ligne du milieu. Les pics sont centrés sur X1 = -3,73 FWHM = 0,42, X2 = -0,27 FWHM = 0,35, X3 = 3,17 FWHM = 0,36. Magnification 4.

Lorsque le grossissement était maximal, la distance minimale entre les taches sur l'échantillon était de 3 µm pour être séparées. Une réduction de la taille des spots à 200 nm, n'a conduit qu'à une amélioration faible. Cela signifie qu'il y a une limitation dans la résolution latérale et la distance entre les spots. En outre, il faut noter que la variation du diamètre du diaphragme de contraste entre 50 µm et 400 µm n'a pas d'influence sur le nombre d'ions détectés, ni la résolution. La transmission du système est d'environ 30 pour cent Le résultat de la simulation montre que la technique de faisceau multiple est réalisable avec l'optique secondaire des instruments de type IMS XF.

Les expériences ont été effectuées initialement avec l'IMS 4F et ensuite avec l'IMS 6F. Les dispositifs expérimentaux sont constitués du spectromètre SIMS, plus d'un système d'acquisition composé d'une caméra CCD couplée avec une lentille, connecté à l'arrière de l'écran phosphorescent, monté au LIST avec les composants de base utilisés pour les mesures de routine. La gamme dynamique est de 256, limitée par la dynamique de la caméra qui est de 8 bits et l'efficacité du système qui est inférieure à 50 %, principalement limitée par la surface utile du détecteur MCP.

Une évaluation de l'illumination de Köhler a été faite avec la source de césium et des ions de 5,5 keV d'énergie. Les images obtenues avec IMS 6F ont des bords bien définis, les images des ouvertures sont 3 à 4 fois plus petites que la taille d'origine des ouvertures et lors des expériences de pulvérisations utilisant ces faisceaux les parois des cratères sont réellement à bord franc. Il faut noter que les courants primaires étaient de l'ordre du nanoampère. Toutes ces valeurs sont en accord avec ceux cités par Hervig [120].

Une fois que le faisceau et l'optique ont été caractérisés, les collimateurs avec plusieurs trous ont été réalisés dans une seule feuille mince d'acier inoxydable. Le premier avait une ouverture de 200 µ, le second des multi-trous, 9 trous de 50 µm de diamètre, disposés en une matrice de 3 x 3 séparés de 150 µm centre à centre, et le troisième a 9 trous de 20 µm de diamètre, également disposées en une matrice de 3 x 3, séparé 100 µm de centre à centre. Ces collimateurs ont été montés sur la colonne primaire dans la position habituelle des collimateurs standards.

La taille et la forme des faisceaux mesurées sur l'écran sont en accord avec la taille et la forme des cratères réalisés dans une cible d'InP et mesurées avec un profilomètre. La démagnification du système était d'environ 5 pour les trois ouvertures. L'illumination n'était pas homogène, car les hauteurs des cratères variaient d'un côté à un autre de près de100 %, systématiquement, dans les trois cas. La matrice des trous avait une inclinaison de 30° à 35° par rapport à l'axe du balayage, donc lorsque les faisceaux étaient balayée l'intensité dépendait de la région visualisée. La taille des trous obtenus par pulvérisation dans une cible InP a été mesurée pour les deux collimateurs de multi-trous et dans les deux cas, il n'y avait aucune différence entre les différents trous et le trou central. Cela indique que les aberrations hors axes sont négligeables pour une ouverture couvrant plusieurs trous sur un diamètre total de 475 µm.

Les résultats montrent que le faisceau multiple a été transmis avec succès à travers l'instrument complet, optique primaire et secondaire, comme il a été prédit par les simulations.

Une évaluation du faisceau multiple a été effectuée avec la source duoplasmatron pour des ions O_2^+ accélérés 15 keV, pour obtenir une énergie de 10,5 keV. Les résultats pour les trois ouvertures, ont montré que le système faisceau multiple a aussi été transmis avec succès également dans ce cas. Cependant, on a constaté une incohérence entre la démagnification du système et la réduction de la taille du faisceau. Ainsi, pour l'ouverture de 200 µm, la démagnification était égale à 4, pour le collimateur avec des trous de 50 µm de diamètre, la démagnification du système était de 5, mais la taille des spots sur l'échantillon avait une réduction de 1,5 seulement, et pour les multi-trous de 20 µm de diamètre, la démagnification du système était de 4, mais la taille du spot sur l'échantillon a été plus grande que le diamètre du trou du collimateur, pas démagnification. Une cause possible de cet effet est due à la diffusion des ions qui passent par les trous, cet effet augmente quand les trous diminuent en taille et en conséquence, l'image sur l'échantillon est élargie. Dans le cas du duoplasmatron, l'effet est considérablement plus élevé car l'O_2 est quatre fois plus léger que le Cs et les trajectoires qui arrivent sur les ouvertures ne sont pas perpendiculaires à la surface, le faisceau n'est pas parallèle la distribution angulaire observée sur les cratères obtenus par pulvérisation, a une forme gaussienne. Ce sont les caractéristiques de la source qui sont la cause de ces effets, la dispersion en énergie (ΔE) de la source duoplasmatron est plus élevée (5 à 20 eV) que la source de césium (0,2-0,5 eV), et l'aberration sphérique est plus grande.

Les dernières mesures ont été réalisées avec de nouveaux collimateurs multi-trous qui avaient des diamètres de trous plus petits, 8 µm et 11 µm, respectivement, dans une matrice de 4 x 4, tournée de 30° pour être aligné avec l'axe de balayage, avec le source de césium. Les résultats ont montré le bon alignement du système multi-ion-faisceau avec cet axe. Par ailleurs, le même effet qu'avec la source duoplasmatron a été observé pour le trou de plus petit diamètre (8 µm), où la démagnification du système était de 4 et l'image du trou est réduite de seulement un facteur 2. Des images de la grille d'AlCu ont été obtenues avec le système multifaisceaux. Les images ont été acquises par balayages avec différentes tailles de trous, 15 µm, 25 µm et 50 µm. L'image était complètement reconstruite pour les plus grandes ouvertures, mais dans le cas d'images générés par la plus petite ouverture de multi-trous, l'image a une résolution inférieure, en raison de la faible intensité des faisceaux. Cela signifie que le 6F IMS présente actuellement une limitation pour continuer à développer ce concept dans ces conditions.

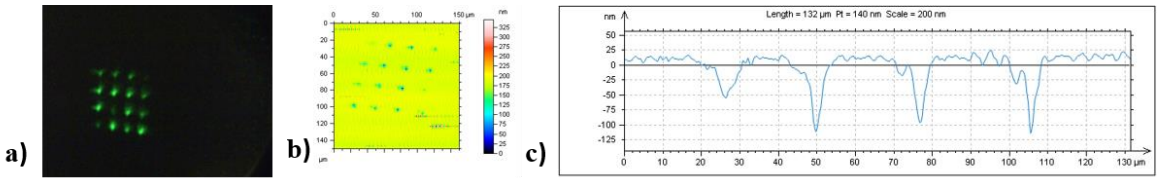

Figure 7. 6: A) Image sur l'écran de 4 x 4 de 11,33 µm d'ouverture prise avec 9 fps, Ip = 38 pA, Is = 10^5 c / s; B) Image de la surface prise avec le profilomètre; c) profil de la première rangée, diamètre moyen de la surface du trou de 4.5 µm démagnification 3.

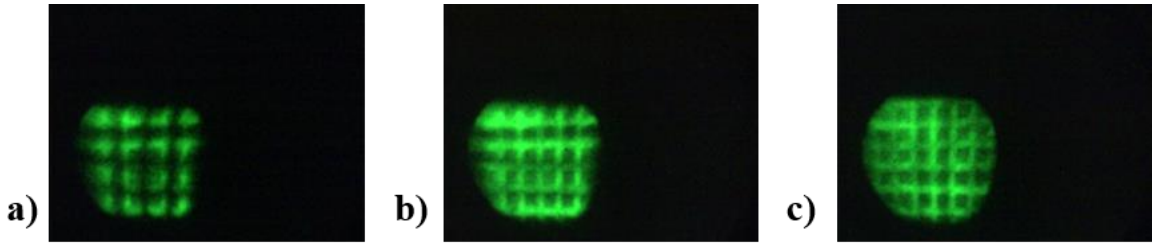

Figure 7. 7: Images de la grille avec différentes tailles de balayage réalisées avec l'ouverture multi-trous 16 x 11,33 µm; A) 15 µm (10 fps); B) 25 µm (3 fps); C) 50 µm (3 fps).

7.4 Conclusions et perspectives :

- La géométrie sphéroïde a été simulée dans ce travail en reproduisant le principe publié par Cubric [13] à l'aide de SIMION. Toutes les dimensions étaient identiques, sauf la forme de grilles d'entrée et de sortie très asymétrique et peut être légèrement différente de la littérature. La conséquence est que le sphéroïde reproduit a une focalisation au 3 rd ordre de focalisation et pas 13ème tel qu'il est rapporté dans la littérature. Les conditions d'ordre supérieur de focalisation différaient légèrement de ceux de la littérature : l'angle d'ouverture a été 9° au lieu de 12 °, la taille du spot était de 8 µm et non de pas 10 µm et la résolution en énergie était de 0,006 % (0,007 % dans la littérature). Les différences découlent du fait d'une part des différents logiciels CPO et des différences dans la modélisation des grilles d'entrée et de sortie de l'analyseur. Une modification supplémentaire a été apporté pour fonctionner en mode de déviation qui consiste à ajouter une troisième électrode connectée à à la masse du dispositif. Ce troisième modèle a été baptisé hybride. La comparaison des résultats des simulations a montré que la géométrie du sphéroïde donnait la meilleure résolution en énergie avec une précision de 0,006 %, suivie de celle de l'hybride. La résolution de masse a été similaire pour l'hybride modifié et pour le secteur sphérique dans la configuration Mattauch-Herzog. Cependant, la condition à remplir pour l'utilisation en double focalisation n'est pas obtenue. Les simulations sans dispersion d'énergie montrent que la configuration hybride a 2 fois

plus de pouvoir de résolution, ce qui reflète la possibilité d'obtenir les meilleures performances du spectromètre si la condition est optimisée et si l'aimant est adapté aux propriétés optiques du sphéroïde. L'évaluation dans une configuration de Nier-Johnson, a montré que le faisceau a été apparemment tourné à 90°, en dégradant la résolution en masse (quatre fois plus petite que pour les configurations sphériques) puisque que les points de focalisation en XY et XZ ne sont pas à la même position. Toutefois, la transmission est deux fois plus grande que celle de la configuration sphérique. Par conséquent, les résultats montrent une grande potentialité de concevoir un spectromètre à double focalisation avec une meilleure résolution en masse ou sensibilité en changeant le secteur sphérique par le sphéroïde et en le combinant avec un aimant aux champs appropriés à l'optique du sphéroïde.

- Un système de faisceau multiple a été étudié par des simulations et testé expérimentalement dans un Cameca IMS 6F. Les résultats obtenus à partir des simulations et des expérimentions ont montré que le -faisceau multiple est une technique utilisable pour l'imagerie SIMS. Dans la simulation, l'optique secondaire de Cameca IMS XF a montré que la distance minimale entre les faisceaux en arrivant sur l'échantillon devrait être de 3 µm, indépendamment de leur diamètre (1 µm ou 200 nm) et des valeurs du diaphragme de contraste (50 µm ou 400 µm). La meilleure condition a été obtenue pour des faisceaux séparés de 10 µm sur l'échantillon et un grossissement de 4. La limitation intrinsèque de la résolution latérale dans l'optique secondaire est due à la contribution du fond de chaque faisceau qui se comporte comme une fonction Lorentzienne et aussi des limitations du système de détection. Avec un collimateur constitué de16 trous de 11.3 µm, la taille de chaque faisceau a été de 5 µm de diamètre avec un courant de 2,35 pA. Ces valeurs correspondent aux tailles de microfaisceau de 1 µm de diamètre, ce qui signifie que le courant a un ordre de grandeur inférieur à l'intensité d'un faisceau de la même taille. Toutefois, les valeurs d'intensité mesurées changent jusqu'à un ordre de grandeur en raison des difficultés à aligner l'ouverture des multi-trous et l'incertitude de mesures. L'illumination n'était pas homogène, et les effets de diffusion ont été observées pour les deux sources lorsque la taille des ouvertures a été réduite. Les effets étaient plus nets pour la source duoplasmatron parce que les ions produits présentent une dispersion en énergie jusqu'à 2 ordres de grandeur plus grande et aussi en raison de la plus grande aberration sphérique, dispersion angulaire, ce qui ne permettra pas d'utiliser les sources duoplasmatron pour la production de faisceau multiple en illumination de Koehler. Ces effets de diffusion apparaissent avec la source de césium à partir des ouvertures de trou de 8 µm de diamètre. L'analyse de la forme des cratères suggère que l'illumination des deux sources n'était pas homogène. Dans plusieurs cas, les cratères produits avec la source de césium ont présenté une variation de hauteur de 100 %, tandis que les cratères réalisés avec la source duoplasmatron ont montré un profil gaussien (cratères sans fond plat). Ce travail était une preuve de faisabilité du concept de faisceau multiple pour l'imagerie SIMS et il a montré que ce système pourrait être une technique puissante. La plupart des limitations et

difficultés rencontrées portaient sur les conditions d'exploitation du IMS 6F. Pour générer des sondes nanométriques, un nouveau système devrait être conçu. Une source de faisceau multiple avec plus de luminosité et une illumination homogène devront être utilisée, il faudrait que les trous des collimateurs aient un profil standard, un nouveau système de détection avec une meilleure gamme dynamique et résolution latérale doit être conçu.

8 References

[1] P. van der Heide, Instrumentation Used in SIMS, John Wiley & Sons, Inc., 2014.

[2] T.R.Ireland, SIMS Measurement of Stable Isotopes, in: P.A. d. Groot (Ed.), Handb. Stable Isot. Anal. Tech. Vol., Elsevier, 2004: p. 652.

[3] P.C. Zalm, Secondary ion mass spectrometry, Vacuum. 45 (1994) 753–772.

[4] S. Hibbert, D. Johnson, Applications of secondary ion mass spectrometry (SIMS) for the analysis of electronic materials, Semicond. Sci. Technol. 7 (1992).

[5] C. Lechene, F. Hillion, G. McMahon, D. Benson, A.M. Kleinfeld, J.P. Kampf, D. Distel, Y. Luyten, J. Bonventre, D. Hentschel, K.M. Park, S. Ito, M. Schwartz, G. Benichou, G. Slodzian, High-resolution quantitative imaging of mammalian and bacterial cells using stable isotope mass spectrometry, J. Biol. 5 (2006) 20. doi:10.1186/jbiol42.

[6] F. Degréve, N.A. Thorne, J.M. Lang, Metallurgical applications of secondary ion mass spectrometry (SIMS), J. Mater. Sci. 23 (1988) 4181–4208. doi:10.1007/bf00551909.

[7] D.S. McPhail, Applications of Secondary Ion Mass Spectrometry (SIMS) in Material Science, J. Mater. Sci. (2006) 873–903.

[8] T. Stephan, TOF-SIMS in cosmochemistry, Planet. Space Sci. 49 (2001) 859–906. doi:10.1016/S0032-0633(01)00037-X.

[9] R.F. Egerton, Physical Principles of Electron Microscopy. An Introduction to TEM, SEM, and AEM., Springer US, 2005.

[10] R. Hill, F.H.M. Fridur Rahman, Advances in helium microscopy, Nucl. Instruments Methods Phys. Res. A. 645 (2011) 96–101.

[11] S. Eswara Moorthy, D. Dowsett, T. Wirtz, Correlative Microscopy Using TEM and SIMS: Parallel Ion Electron Spectrometry (PIES) for High-Resolution, High-Sensitivity Elemental Mapping for Applications in Materials Science and Biology, Microsc. Microanal. (2014).

[12] T. Wirtz, P. Phillip, D. Dowsett, SIMS on the Helium Ion Micrsocope: A powerful tool for high-resolution high-sensitivity nano-analytics, in: A.G. Gregor Hlawacek (Ed.),

Helium Ion Microsc., Springer International Publishing, 2016.

[13] D. Cubric, N. Kholine, I. Konishi, Electron optics of spheroid charged particle energy analyzers, Nucl. Instruments Methods Phys. Res. Sect. A Accel. Spectrometers, Detect. Assoc. Equip. 645 (2011) 234–240.

[14] A. Benninghoven, Secondary ion mass spectrometry, SIMS IX: proceedings of the Ninth International Conference on Secondary Ion Mass Spectrometry (SIMS IX), the Hotel Yokohama and the Sangyo-Boeki Center Building, Yokohama, Japan, 7-12 November, 1993, Wiley, 1994.

[15] C.P. Lechene, Y. Luyten, G. McMahon, D.L. Distel, Quantitative Imaging of Nitrogen Fixation by Individual Bacteria Within Animal Cells, Science. 317 (2007) 1563–1566.

[16] L.J. Gamble, C.R. Anderton, Secondary Ion Mass Spectrometry Imaging of Tissues, Cells, and Microbial Systems, Micros. Today. 24 (2016) 24–31. doi:10.1017/S1551929516000018.

[17] P. Grivet, P.W. Hawkes, A. Septier, Electron Optics, Elsevier Science, 2013.

[18] A. Septier, Focusing of Charged Particles, Elsevier Science, 2013.

[19] H. Rose, Geometrical Charged-Particle Optics, Springer Berlin Heidelberg, 2013.

[20] J. Orloff, Handbook of Charged Particle Optics, Taylor & Francis, 1997.

[21] H. Liebl, Applied Charged Particle Optics, Springer Berlin Heidelberg, 2008.

[22] F.H. Read, A. Adams, Electrostatic cylinder lenses II: Three element einzel lenses, J. Phys. E. 5 (1972) 150.

[23] A. Renau, Geometric aberrations in electrostatic lenses: I. A simple and accurate computer model, J. Phys. E. 19 (1986) 284.

[24] A. Renau, Geometric aberrations in electrostatic lenses: II. Aberration coefficients and their interrelations, J. Phys. E. 19 (1986) 288.

[25] A.B. El-Kareh, M.A. Sturans, Analysis of the 3-Tube Symmetrical Electrostatic Unipotential Lens, J. Appl. Phys. 42 (1971) 1870–1876. doi:10.1063/1.1660460.

[26] O. Sise, M. Ulu, M. Dogan, Multi-element cylindrical electrostatic lens systems for focusing and controlling charged particles, Nucl. Instruments Methods Phys. Res. Sect. A Accel. Spectrometers, Detect. Assoc. Equip. 554 (2005) 114–131.

[27] A. Adams, Electrostatic cylinder lenses II: Three element einzel lenses, J. Phys. E. 5 (1972) 150.

[28] A. Adams, Electrostatic cylinder lenses III: three element asymmetric voltage lenses, J. Phys. E. 5 (1972) 156.

[29] F.H. Read, Calculated properties of electrostatic einzel lenses of three apertures, J. Phys. E. 2 (1969) 679.

[30] G.H.N. Riddle, Electrostatic einzel lenses with reduced spherical aberration for use in field-emission guns, J. Vac. Sci. Technol. 15 (1978) 857–860. doi:10.1116/1.569613.

[31] O. Sise, N. Okumus, M. Ulu, M. Dogan, Computer simulation of electrostatic aperture lens systems for electron spectroscopy, J. Electron Spectros. Relat. Phenomena. 175 (2009) 76–86.

[32] D.W.O. Heddle, M. Kurepa, The focal properties of three-element electrostatic electron lenses, J. Phys. E. 3 (1970) 552.

[33] A.B.E. kareh, M.A.Sturans, Analysis of the 3-Tube Asymmetrical Electrostatic Unipotential Lens, J. Appl. Phys. 42 (1971) 4902–4907. doi:doi: 10.1063/1.1659872.

[34] G.F.Rempfer, Unipotential electrostatic lenses: Paraxial properties and aberrations of focal length and focal point, J. Appl. Phys. 57 (1985) 2385–2401. doi:10.1063/1.334347.

[35] M. Yavor, Electrostatic energy analysers, in: P.W. Hawkes (Ed.), Adv. Imaging Electron Phys. Opt. Charg. Part. Anal., Elsevier Science, 2009: pp. 213–258.

[36] D. Roy, D. Tremblay, Design of electron spectrometers, Reports Prog. Phys. 53 (1990) 1621.

[37] E.M. Purcell, The Focusing of Charged Particles by a Spherical Condenser, Phys. Rev. 54 (1938) 818–826.

[38] D. Roy, J.D. Carette, Improvement of the Resolving Power and Transmission of

Electrostatic Spectrometers, J. Appl. Phys. 42 (1971) 3601–3615. doi:doi: 10.1063/1.1660776.

[39] J.H. Moore, C.C. Davis, M.A. Coplan, S.C. Greer, Building Scientific Apparatus, Cambridge University Press, 2009.

[40] A. Khursheed, Scanning Electron Microscope Optics and Spectrometers, World Scientific, 2011.

[41] O. Sise, T.J.M. Zouros, M. Ulu, M. Dogan, First-order focusing and energy resolution optimization of a biased paracentric hemispherical spectrograph, Phys. Procedia. 1 (2008) 467–472. doi:10.1016/j.phpro.2008.07.128.

[42] P. Coxon, J. Krizek, M. Humpherson, I.R.M. Wardell, Escascope - a new imaging photoelectron spectrometer, J. Electron Spectros. Relat. Phenomena. 52 (1990) 821–836. doi:10.1016/0368-2048(90)85067-J.

[43] E.I. Rau, V.N.E. Robinson, An annular toroidal backscattered electron energy analyser for use in scanning electron microscopy, Scanning. 18 (1996) 556–561. doi:10.1002/sca.4950180804.

[44] G.H. Oetjen, W.P. Poschenrieder, Focussing errors of a multiple-focussing time-of-flight mass spectrometer with an electrostatic sector field, Int. J. Mass Spectrom. Ion Phys. 16 (1975) 353–367.

[45] O. Sise, T.J.M. Zouros, M. Ulu, M. Dogan, Comparison of fringing field correction schemes for the 180° hemispherical deflector analyzer, Phys. Procedia. 1 (2008) 473–477.

[46] K. Jost, Fringing field correction for 127 degrees and 180 degrees electron spectrometers, J. Phys. E. 12 (1979) 1001.

[47] H.Z. Sarl-El, Cylindrical Capacitor as an Analyzer I. Nonrelativistic Part, Rev. Sci. Instrum. 38 (1967) 1210–1216. doi:10.1063/1.1721067.

[48] D. Varga, K. Tokési, I. Rajta, Design of an electrostatic electron spectrometer for simultaneous energy and angular distribution measurements, J. Electron Spectros. Relat. Phenomena. 76 (1995) 433–436.

[49] A.A. Trubitsyn, A cylindrical mirror analyser with high energy resolution, J. Electron Spectros. Relat. Phenomena. 73 (1995) 305–310.

[50] K. Siegbahn, N. Kholine, G. Golikov, A high resolution and large transmission electron spectrometer, Nucl. Instruments Methods Phys. Res. Sect. A Accel. Spectrometers, Detect. Assoc. Equip. 384 (1997) 563–574.

[51] V.D. Belov, M.I. Yavor, New type of high-resolution high-transmission energy analyzers based on toroidal mirrors, J. Electron Spectros. Relat. Phenomena. 104 (1999) 47–54. doi:10.1016/S0368-2048(98)00311-9.

[52] N.A. Kholine, D. Cubric, I. Konishi, Spheroidal charged particle energy analysers, (2013).

[53] H.P.N. Nguyen, Electron Energy Spectrometers, National University of Singapore, 2013.

[54] H.Q. Hoang, Electron energy spectrometers for the scanning electron microscope, National University of Singapore, 2011.

[55] A.D. McNaught, A. Wilkinson, Compendium of Chemical Terminology, Blackwell Scientific Publications, 1997, 1997.

[56] J.E. Spencer, H.A. Enge, Split-pole magnetic spectrograph for precision nuclear spectroscopy, Nucl. Instruments Methods. 49 (1967) 181–193.

[57] H.A. Enge, Magnetic spectrographs and beam analyzers, Nucl. Instruments Methods. 28 (1964) 119–130.

[58] C.M. Braams, Edge effect in charged-particle analyzing magnets, Nucl. Instruments Methods. 26 (1964) 83–89.

[59] A. Septier, Focusing of Charged Particles, Academic Press, 1967.

[60] B. Pfreundtner, H. Wollnik, Curvature of the effective field boundary of realistic sector magnets, Proc. SPIE 2522, Electron -Beam Sources Charg. -Particle Opt. 297 (1995).

[61] Lorentz, Integr. Eng. Softw. (n.d.). https://www.integratedsoft.com.

[62] S.B. Kowalski, H.A. Enge, The ion-optical program raytrace, Nucl. Instruments

Methods Phys. Res. Sect. A Accel. Spectrometers, Detect. Assoc. Equip. 258 (1987) 407. doi:http://dx.doi.org/10.1016/0168-9002(87)90921-1.

[63] COSY Infinity, (n.d.). http://bt.pa.msu.edu/index_cosy.htm.

[64] D.J.Manura, D.A.Dahl, SIMION Version 8.0 User Manual, 4th ed., Scientific Instrument Services INc., 2008.

[65] T. Wirtz, P. Phillip, J.-N. Audinot, D. Dowsett, S. Eswara, High-resolution high sensitivity elemental imaging by seondary ion mass spectrometry: from traditional 2D and 3D imaging to correlative microscopy, Nanotechnology. 26 (2015).

[66] L. Bischoff, J. Teichert, Focused Ion Beam Sputtering of Silicon and Related Materials, Forshungszentrum Rossendorf, Rossendorf, 1998.

[67] B. Kasel, The storing Matter Technique: Fundamentals and application to inorganic Materials, University of Luxembourg. The Faculty of Sciences, Technology and Communication, 2014.

[68] P. Sigmund, Sputtering by ion bombardment theoretical concepts, in: S.B. Heidelberg (Ed.), Sputtering by Part. Bombard. I, 1981: pp. 9–71. doi:10.1007/3540105212_7.

[69] R. Behrish, W. Eckstein, Sputtering by particle bombardment, Springer, 2007.

[70] P. Sigmund, Ion Beam Science, Det Kongelige, 2006.

[71] A. Benninghoven, F.G. Rüdenauer, H.W. Werner, Elving, Winefordner, Kolthoff, Secondary ion mass spectrometry: basic concepts, instrumental aspects, applications and trends., John Wiley and Sons, 1987.

[72] H. Tsuge, S. Escho, Angular distribution of sputtered atoms from polycrystalline metal targets, J. Appl. Phys. 52 (1981) 4391.

[73] R.F.K. Herzog, W.P. Poschenrieder, F.G. Satkiewicz, Observation of clusters in a sputtering ion source, Radiat. Eff. 18 (1973) 199–205. doi:10.1080/00337577308232122.

[74] G. Slodzian, Remarks on Some Factors Influencing the Charge State of Sputtered Particles, Phys. Scr. 1983 (1983) 54.

[75] G. Slodzian, Some problems encountered in secondary ion emission applied to elementary analysis, Surf. Sci. 48 (1975) 161–186.

[76] P. Williams, The sputtering process and sputtered ion emission, Surf. Sci. 90 (1979) 588–634.

[77] P. Williams, On mechanisms of sputtered ion emission, Appl. Surf. Sci. 13 (1982) 241–259.

[78] M.L. Yu, K. Mann, Bond Breaking and the Ionization of Sputtered Atoms, Phys. Rev. Lett. 57 (1986) 1476–1479.

[79] M.A. Ray, Baker; J E, C.M. Loxton, J.E. Greene, Quantitative analysis and depth profiling of rare gases in solids by secondary-ion mass spectrometry: Detection of (CsR)+ molecular ions (R=rare gas), J. Vac. Sci. Technol. A Vacuum, Surfaces, Film. 6 (1988) 44–50. doi:10.1116/1.574966.

[80] Y. Gao, A new secondary ion mass spectrometry technique for III-V semiconductor compounds using the molecular ions CsM+, J. Appl. Phys. 64 (1988) 3760–3762. doi:10.1063/1.341381.

[81] T. Wirtz, H.N. Migeon, H. Scherrer, Useful yields of MCsx+ clusters: a cesium concentration-dependent study on the Cation Mass Spectrometer (CMS), Int. J. Mass Spectrom. 225 (2003) 135–153.

[82] P.Philipp, T.Wirtz, H.-N. Migeon, H.Scherrer, Important Increase of Negative Secondary ion sensitivity during SIMS analysis by neutral cesium deposition, Appl. Surf. Sci. 252 (2006) 7205–7207.

[83] H. Gnaser, H. Oechsner, Emission of MCs+ secondary ions from semiconductors by caesium bombardment, Surf. Interface Anal. 21 (1994) 257–260.

[84] W.A. Lamberti, Imaging Secondary Ion Mass Spectrometry, in: N. Yao, Z.L. Wang (Eds.), Handb. Microsc. Nanotechnol., Springer US, Boston, MA, 2005: pp. 207–225.

[85] M.L. Yu, Velocity Dependence of the Ionization Probability of Sputtered Atoms, Phys. Rev. Lett. 47 (1981) 1325–1328.

[86] K. Franzreb, J. Lörincik, P. Williams, Quantitative study of oxygen enhancement of

sputtered ion yields. I. Argon ion bombardment of a silicon surface with O2 flood, Surf. Sci. 573 (2004) 291–309.

[87] M. Bernheim, Slodzian; G, Caesium flooding on metal surfaces and sputtered negative ion yields, J. Phys. Lettres. 38 (1977) 325–328.

[88] T.Wirtz, H.-N. Migeon, Optimization of SIMS analyses performed in the MCSx+ mode by using an in situ deposition of Cs, Appl. Surf. Sci. 231–232 (2004) 743–748.

[89] E. Niehuis, T. Heller, H. Feld, A. Benninghoven, High-Resolution TOF Secondary Ion Mass Spectrometer BT - Ion Formation from Organic Solids (IFOS III): Mass Spectrometry of Involatile Material, in: A. Benninghoven (Ed.), Springer Berlin Heidelberg, Berlin, Heidelberg, 1986: pp. 198–202. doi:10.1007/978-3-642-82718-1_37.

[90] E. Niehuis, T. Heller, H. Feld, A. Benninghoven, High Resolution TOF Secondary Ion Mass Spectrometer BT - Secondary Ion Mass Spectrometry SIMS V: Proceedings of the Fifth International Conference, Washington, DC, September 30 – October 4, 1985, in: A. Benninghoven, R.J. Colton, D.S. Simons, H.W. Werner (Eds.), Springer Berlin Heidelberg, Berlin, Heidelberg, 1986: pp. 188–190. doi:10.1007/978-3-642-82724-2_48.

[91] J.C. Vickerman, D. Briggs, TOF-SIMS: Materials Analysis by Mass Spectrometry, SurfaceSpectra/IM Publications, 2013.

[92] T.W. Burgoyne, G.M. Hieftje, An introduction to ion optics for the mass spectrograph, Mass Spectrom. Rev. 15 (1996) 241–259. doi:10.1002/(SICI)1098-2787(1996)15:4<241::AID-MAS2>3.0.CO;2-I.

[93] T. Matsuo, M. Ishihara, A new mass spectrograph, J. Am. Soc. Mass Spectrom. 4 (1993) 372–386. doi:http://dx.doi.org/10.1016/1044-0305(93)85002-F.

[94] G. Münzenberg, Development of mass spectrometers from Thomson and Aston to present, Int. J. Mass Spectrom. 349–350 (2013) 9–18.

[95] H.-N. Migeon, F. Saldi, Y. Gao, M. Schuhmache, Ion microscope and ion microprobe analysis under oxygen , cesium and gallium bombardment, Int. J. Mass Spectrom. Ion Process. 143 (1995) 51–63.

[96] M.T.Bernius, Y. Ling, G.H.Morrison, Improved Spatial Resolution of the CAMECA IMS-3f Ion Microscope, Second. Ion Mass Spectrom. (SIMS V- Proceedings). (1986).

[97] M.T. Bernius, Y. Ling, G.H. Morrison, High Resolution Imaging with the Stigmatic Ion Microscope, J. Appl. Phys. 60 (1986) 1904–1912.

[98] H.-N. Migeon, M. Schumacher, J.J.L. Goux, B. Rasser, Three -dimensional analysis of trace elements with the CAMECA IMS 4F, Anal. Chemie. (1989) 333–334.

[99] Physical principles IMS 6F / IMS 1270, in: IMS6F User's Guid., Cameca, France, 1995.

[100] G.Slodzian, Microanalizers Using Secondary Ion Emision, in: A.L. Septier (Ed.), Appl. Charg. Part. Opt. Part B. Adv. Electron. Electron Phys. 13B, Supplement, 1980.

[101] M.T.Bernius, Y. Ling, G.H.Morrison, High resolution imaging with the stigmatic ion microscope, J. Appl. Phys. 60 (1986) 1904–1912.

[102] F. Vanhaecke, P. Degryse, Isotopic Analysis: Fundamentals and Applications Using ICP-MS, Wiley, 2012.

[103] F.A. Stevie, L. Sedlacek, P. Babor, J. Jiruse, E. Principe, K. Klosova, FIB-SIMS quantification using TOF-SIMS with Ar and Xe plasma sources, Surf. Interface Anal. 46 (2014) 285–287. doi:10.1002/sia.5483.

[104] N. Klingner, R. Heller, G. Hlawacek, J. von Borany, J. Notte, J. Huang, S. Facsko, Nanometer scale elemental analysis in the helium ion microscope using time of flight spectrometry, Ultramicroscopy. 162 (2016) 91–97. doi:10.1016/j.ultramic.2015.12.005.

[105] J.A. Whitby, F. Östlund, P. Horvath, M. Garbuerac, J.L. Riesterer, Utke; I, Hohl; M, L. Sedlacek, J.Jiruse, V.Friedli, M.Bechelany, J.Michler, High Spatial Resolution Time-of-Flight Secondary Ion Mass Spectrometry for the Masses: A Novel Orthogonal ToF FIB-SIMS Instrument with In Situ AFM, Adv. Mater. Sci. Eng. 2012 (2012).

[106] Midwest Tungsten Service, (n.d.). https://www.tungsten.com/.

[107] R. Andrzejewski, R. Barrahama, D. Dowsett, T. Wirtz, FLOATING MAGNET FOR A MASS SPECTROMETER, WO/2017/137390, 2017.

[108] J. Lorincik, K. Franzreb, P. Williams, SIMION modeling of ion optical effects in

Cameca ion microanalyzers: simulation of ion transmission losses, Appl. Surf. Sci. 231 (2004) 921–925.

[109] M.K. Passarelli, N. Winograd, Lipid imaging with time-of-flight secondary ion mass spectrometry (ToF-SIMS), Biochim. Biophys. Acta - Mol. Cell Biol. Lipids. 1811 (2011) 976–990. doi:10.1016/j.bbalip.2011.05.007.

[110] D. Touboul, F. Kollmer, E. Niehuis, A. Brunelle, O. Laprévote, Improvment of Biological Time-of-Flight-Secondary Ion Mass spectrometry Imaging with Bismuth Cluster Ion Source, Am. Soc. Mass Spectrom. 16 (2015) 1608–1618.

[111] M.J. Van Bruggen, Multi-electron beam system for high resolution electron beam induced deposition, Technische Universiteit Delf, 2008.

[112] T.H.P. Chang, M. Mankos, K.Y. Lee, L.P. Muray, Multiple electron-beam lithography, Microelectron. Eng. 57–58 (2001) 117–135. doi:10.1016/S0167-9317(01)00528-7.

[113] N. Shimazu, K. Saito, F. Minpei, An Approach to a High-Throughput E-Beam Writer with a Single-Gun Multiple-Path System, Jpn. J. Appl. Phys. 34 (1995) 6689.

[114] G. Winograd, V. Krishnamurthi, R. Garcia, L.H. Veneklasen, M. Mankos, F. Pease, Demonstration of multiblanker electron-beam technology, J. Vac. Sci. Technol. B Microelectron. Nanom. Struct. Process. Meas. Phenom. 18 (2000) 3052–3056. doi:10.1116/1.1321757.

[115] I.L. Berry, A.A. Mondelli, J. Nichols, J. Melngailis, Programmable aperture plate for maskless high-throughput nanolithography, J. Vac. Sci. Technol. B Microelectron. Nanom. Struct. Process. Meas. Phenom. 15 (1997) 2382–2386. doi:10.1116/1.589652.

[116] E. Slot, MAPPER: high throughput maskless lithography, Proc. SPIE 6921, Emerg. Lithogr. Technol. XII. 6921 (2008) 9. doi:10.1117/12.771965.

[117] Y. Zhang, A 100-electron-beam source froma high brightness Schottky emitter for fast patterning applications, Technische Universiteit Delft, 2008.

[118] Computar, (n.d.). https://computar.com/.

[119] IMS 6F7IMS 1270 User's Guide, (1995).

[120] R.L. Hervig, F.K. Mazdab, P. Williams, Y. Guan, G.R. Huss, L.A. Leshin, Useful ion yields for Cameca IMS 3f and 6f SIMS: Limits on quantitative analysis, Chem. Geol. 227 (2006) 83–99.

[121] M.L. Taylor, R.D. Franich, A. Alves, P. Reichart, D.N. Jamieson, P.N. Johnston, Ion transmission through nano-apertures, Nucl. Instruments Methods Phys. Res. Sect. B Beam Interact. with Mater. Atoms. 249 (2006) 752–755. doi:https://doi.org/10.1016/j.nimb.2006.03.132.

[122] D.C. Olivier, Development of a Versatile High-Brightness Electron Impact IonSource for Nano-Machining , Nano-Imaging and Nano-Analysis, University Paris Saclay, 2016.

[123] A. Mohammadi-Gheidari, C.W. Hagen, P. Kruit, Multibeam scanning electron microscope: Experimental results, J. Vac. Sci. Technol. B, Nanotechnol. Microelectron. Mater. Process. Meas. Phenom. 28 (2010) C6G5-C6G10. doi:10.1116/1.3498749.

[124] O. Kamimura, S. Tanimoto, H. Ohta, Y. Nakayama, M. Sakakibara, Y. Sohda, M. Muraki, S. Gotoh, M. Hosoda, Y. Someda, K. Tamamori, F. Hirose, K. Nagae, K. Kato, M. Okunuki, Optical properties of a multibeam column with a single-electron source, J. Vac. Sci. Technol. B Microelectron. Nanom. Struct. Process. Meas. Phenom. 25 (2007) 140–146. doi:10.1116/1.2429674.

[125] J. Malherbe, F. Penen, M.-P. Isaure, J. Frank, G. Hause, D. Dobritzsch, E. Gontier, F. Horréard, F. Hillion, D. Schaumlöffel, A New Radio Frequency Plasma Oxygen Primary Ion Source on Nano Secondary Ion Mass Spectrometry for Improved Lateral Resolution and Detection of Electropositive Elements at Single Cell Level, Anal. Chem. 88 (2016) 7130–7136. doi:10.1021/acs.analchem.6b01153.

[126] M.M. Lyra da Cunha, S. Trepout, C. Messaoudi, T.-D. Wub, R. Ortega, J. Guerquin-Kern, S. Marco, Overview of chemical imaging methods to address biological questions, Micron. 84 (2016) 23–36.

[127] O. Sise, M. Ulu, M. Dogan, Aberration coefficients of multi-element cylindrical electrostatic lens systems for charged particle beam applications, Nucl. Instruments Methods Phys. Res. Sect. A Accel. Spectrometers, Detect. Assoc. Equip. 573 (2007) 329–339.

[128] P.B. Norton, J.J. Esposito, E.B. inc., The new encyclopaedia Britannica, 15th ed., Encyclopaedia Britannica, 1994.

[129] O. Sise, M. Ulu, M. Dogan, Characterization and modeling of multi-element electrostatic lens systems, Radiat. Phys. Chem. 76 (2007) 593–598. doi:10.1016/j.radphyschem.2005.11.037.

[130] C. C.Farnell, C. C.Farnell, S.C.Farnell, J.D.Williams, Electrostatic analyzers with application to electric propulsion testing, Int. Electr. Propuls. Conf. Publ. (2013).

[131] R. Andrzejewski, New methods for high-resolution ion beam analysis, Universidad Autónoma de Madrid, 2008.

[132] Y. Liao, Practical Electron Microscopy and Database, Second, GlobalSino, 2007.

[133] K.Wittmaack, Local SiO2 formation in silicon bombarded with oxygen above the critical angle for beam-induced oxidation: new evidence from sputtering yield ratios and correlation with data obtained by other techniques, Surf. Interface Anal. (2000) 721–725.

[134] K. Wittmaack, Energy dependence of the secondary ion yield of metals and semiconductors, Surf. Sci. 53 (1975) 626–635.

[135] J.H. Batey, The physics and technology of quadrupole mass spectrometers, Vacuum. 101 (2014) 410–415. doi:https://doi.org/10.1016/j.vacuum.2013.05.005.

[136] V.S. Edmond de Hoffmann, Mass Spectrometry: Principles and Applications, 3rd Editio, John Wiley & Sons Ltd., 2007.

[137] B.W. SINHA, P. PHOPPE, Ion microprobe analysis: Basic principles, state-of-the-art instruments and recent applications with emphasis on the geosciences, in: Frank E. Brenker and Guntram Jordan (Ed.), EMU Notes Mineral. Approaches Earth Planet. Sci., Mineralogical Society of America, 2010.

[138] J.M. Gourgout, Cameca S.A., Cameca News. N°2 (1977).

[139] E. Hoffman, V. Stroobant, Mass Spectrometry: Principles and Appplications, Third, John wiley & Sons Ltd, 2007.

[140] H. Liebl, Ion gun systems for submicron SIMS, Second. Ion Mass Spectrom. SIMS IV Proc. Fourth Int. Conf. Osaka, Japan, Novemb. 13–19, 1983. (2012).

9 Glossary:

Abbreviation	Meaning
AES	Auger Electron Spectroscopy
AC/DC	Alternate/Direct Current
BEM	Boundary Element Method
CA	Contrast Aperture
CAD	Computer Aided Design
CCD	Charged Couple Device
CDM	Charged Density Method
CHA	Cylindrical Hemispherical Analyser
CMA	Cylindrical Mirror Analyser
CPO	Charged Particle Optics
cps	counts per second
D-SIMS	Dynamic-SIMS
EDX	Energy Dispersive X-ray Spectroscopy
EELS	Electron Energy Loss Spectroscopy
EFB	Effective Field Boundary
ESA	Electrostatic Spherical Analyser
FBW	Full Base width
FC	Faraday Cup
FDM	Finite Boundary Method
FIB	Focused Ions Beam
FOFEM	First Order Finite Element Method
FOV	Field of View
FS	Phosphor Screen
FWHM	Full Width at Half Maximum
FW50	Full Width containing 50% of the particles

HDA	Hemispherical Deflector Analyser
HIM	Helium Ion Microscope
IVM	Infinity Velocity Method
LIST	Luxembourg Institute of Science and Technology
LMIS	Liquid Metal Ion Source
MCP	Micro Channel Plate
MC_S	Clusters of the element M plus Caesium C_S
MD	Molecular Dynamics
MISR	Matrix Isotope Species Ratio
PA	Potential Array
PMA	Parallel Mirror Analyser
ppm/ppb	parts per million/part per billion
RSF	Relative Sensitivity Factors
SEA	Spheroid Energy Analyser
SEM	Scanning Electron Microscopy
SIMS	Secondary ion Mass Spectrometry
SMA	Spherical Mirror Analyser
SOFEM	Second order Finite Element Method
SOR	Successive Over Relaxation
SPM	Scanning Electron Microscopy
TEM	Transmission Electron Microscopy
TMA	Toroidal Mirror Analyser
TOF	Time of Flight
TRIM	Transport of Ion in Matter
XPS	X-ray Photoelectron Spectroscopy
WD	Working Distance

9. Glossary

Symbol	**Meaning**
EA	Electron Afinity
α	Angle in the plane of deflection
α_0, φ	Particle trajectory angle
$\vec{B}$	Magnetic Field
β	Angle perpendicular to the deflection plane
β_x	Ionization probability of certain element X
C_c	Chromatic Aberration Coefficient
C_s, C_{s2}, C_{s3}	Spherical Aberration Coefficients
c	Toroidal coefficient
d	Gap distance
D	Dispersion
δl	distance difference on the optical axis
Δr_{sph}, Δr_{chr},	Sphericaδ and Chromatic aberration disc radius
ΔE, δE	Difference in energy
$\vec{E}$, E_r	Electric Field, radial component
E_0	Central energy
ε_0	Electric Constant
ϵ_n, ϵ_p	parameters depending on the local properties
ϕ	Work function
I	Ionization Potential
m/q	Mass to charge ratio
M_L	Linear Magnification
I_x	Intensity current of certain element X
N_x	Number of detected ions
ns	Number of removed atoms
ni	Number of incident atoms

Φ	Potential
S	Sputter Yield
T_x	Transmission coefficient of the secondary ions
UY	Useful Yield
L1, L2, L3, L4	Lenses of the primary optics 1, 2, 3, 4
r_e	Radius of the optical axis
R_e	Radius in radial plane
ρ_c	Charge density
ρ_x	Concentration of certain element X
v	Particles velocity
V1, V2, V3	Potential for electrodes 1, 2 ,3
V_s	Source Potential
W	Trace width
W_S	Trace width of the exit slit
W_A	Trace width of the spherical aberration
$\dot{z}$	Velocity in z direction

10 List of Figures

Chapter 2

Chapter 3

Chapter 4:

Chapter 5:

Chapter 2:

Chapter 3:

Chapter 4:

Chapter 5:

université PARIS-SACLAY | ÉCOLE DOCTORALE PHENIICS

Titre : Recherche sur l'amélioration de la performance des instruments SIMS

Mots clés : SIMS, sphéroïde, multifaisceaux

Résumé : Les instruments de spectrométrie de masse à ionisation secondaire (SIMS) doivent être améliorés afin de satisfaire les exigences et tendances dans de nombreux domaines qui demandent des outils d'analyse pouvant cartographier les échantillons à la fois avec une excellente résolution et une haute sensibilité chimique, mais également avec des temps d'analyse plus court. Les objectifs de cette thèse sont : rechercher à améliorer la résolution en masse des spectromètres de masse à double focalisation en remplaçant le secteur sphérique standard par une nouvelle géométrie sphéroïde ayant de meilleures propriétés de focalisation, et d'étudier la réduction du temps d'analyse en imagerie SIMS, par la preuve de concept du système SIMS à multifaisceaux d'ions.
Une comparaison dans une configuration Nier-Johnson entre le secteur sphérique et le sphéroïde, a montré que le faisceau présente une élargissement du enveloppe à la sortie de l'aimant nuisant à la résolution de masse dans la configuration sphéroïde. Avec un aimant spécialement conçu pour l 'optique sphéroïde, le performance pourrai être améliorée.. Une comparaison des performances entre les secteurs sphérique et hybride dans une configuration Mattauch-Herzog a montré que lorsque la double condition de focalisation est optimisée, une meilleure résolution de masse pourrait être obtenue avec la géométrie sphéroïde. La preuve du concept d'une sonde multi-faisceaux pour minimiser le temps d'acquisition a été achevée par simulations et expérimentalement dans l'IMS 6F de Cameca où une ouverture à trous multiples était montée dans la colonne principale, générant 9 et 16 faisceaux de tailles comprises entre 4 um à 10 um. Des images d'une grille AlCu ont été obtenues en balayant l'échantillon par le système de multifaisceaux d'ions.

Title: Investigation of the enhancement of the performance of the SIMS instruments

Keywords : SIMS, spheroid, multi-beams

Abstract: Secondary ion mass spectrometry (SIMS) instruments need to be improved in order to satisfy the demands of trends in many fields that require analytical tools that can map samples with both excellent resolution and high-sensitivity chemical information, but also with shorter time of analysis. The objectives of this thesis are: investigate the enhancement of the mass resolution of double focusing mass spectrometers by replacing the standard spherical sector with a novel spheroid geometry which has better focusing properties, and to investigate the reduction of the time of analysis in imaging SIMS by the proof-of-concept of the SIMS multi-ion- beam system.
A comparison in a Nier-Johnson configuration between the spherical sector and the spheroid, showed that the beam presents a broadening of the envelope at the exit of the magnet harming the mass resolution in the last case. With a magnet especially designed for the spheroid optics the performance could be improved. A comparison of the performances between the spherical and hybrid sectors simulated in a Mattauch-Herzog configuration, showed that when the double focusing condition is properly satisfied, better mass resolution could be achieved with the spheroid geometry. The proof-of-concept of the multi-ion-beam to reduce drastically the time of analysis was done by simulations and experiments in the Cameca IMS 6F, where a multi-hole aperture was mounted in the primary column generating 9 and 16 beams of sizes between 4 µm to 10 µm. Images of an AlCu grid were obtained when the multi-ion-beam system was scanned over the sample.

Université Paris-Saclay
Espace Technologique / Immeuble Discovery
Route de l'Orme aux Merisiers RD 128 / 91190 Saint-Aubin, France